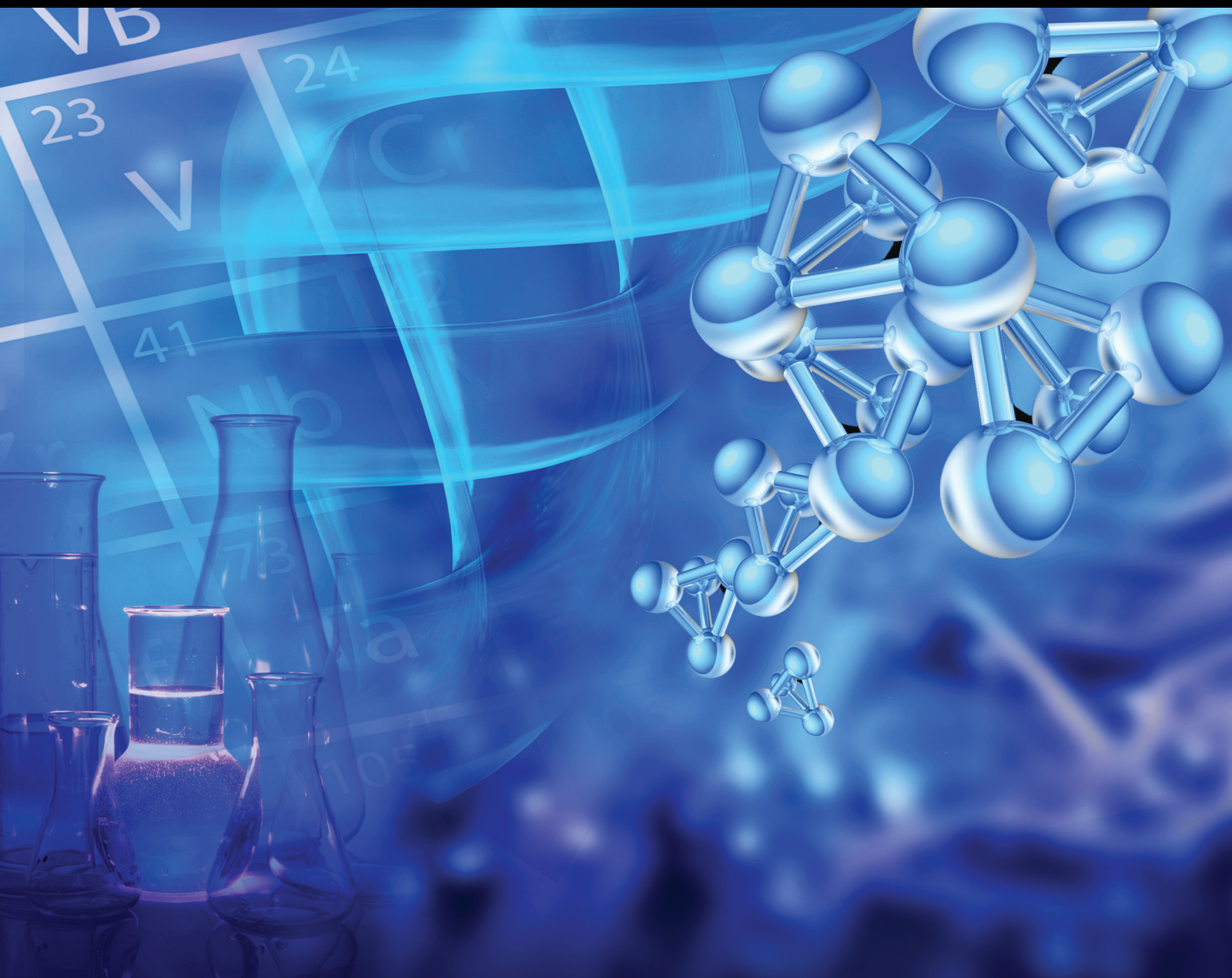


Bioinorganic Chemistry and Applications

Anticancer and Antimicrobial Properties of Inorganic Compounds/Nanomaterials

Lead Guest Editor: Rais A. Khan

Guest Editors: Aurel Tabacaru, Farman Ali, and Bon H. Koo





Anticancer and Antimicrobial Properties of Inorganic Compounds/Nanomaterials

Bioinorganic Chemistry and Applications

Anticancer and Antimicrobial Properties of Inorganic Compounds/Nanomaterials

Lead Guest Editor: Rais A. Khan

Guest Editors: Aurel Tabacaru, Farman Ali, and Bon H. Koo



Copyright © 2019 Hindawi. All rights reserved.

This is a special issue published in "Bioinorganic Chemistry and Applications." All articles are open access articles distributed under the Creative Commons Attribution License, which permits unrestricted use, distribution, and reproduction in any medium, provided the original work is properly cited.

Editor-in-Chief

Francesco Paolo Fanizzi Fanizzi, University of Salento, Italy

Editorial Board

Patrick J. Bednarski, Germany
Viktor Brabec, Czech Republic
Ian S. Butler, Canada
Luigi Casella, Italy
Zhe-Sheng Chen, USA
Anastasios Keramidas, Cyprus
Concepción López, Spain

Guillermo Mendoza-Diaz, Mexico
Albrecht Messerschmidt, Germany
Elena R. Milaeva, Russia
Demetrio Milea, Italy
Giovanni Natile, Italy
Massimiliano F. Peana, Italy
Spyros P. Perlepes, Greece

Claudio Pettinari, Italy
Enrico Rizzarelli, Italy
Jacopo Sgrignani, Switzerland
Imre Sovago, Hungary
Marie Stiborova, Czech Republic
Konstantinos Tsipis, Greece

Contents

Anticancer and Antimicrobial Properties of Inorganic Compounds/Nanomaterials

Rais Ahmad Khan , Aurel Tăbăcaru , Farman Ali, and Bon H. Koo
Editorial (2 pages), Article ID 6019632, Volume 2019 (2019)

Encapsulation of Gold Nanorods with Porphyrins for the Potential Treatment of Cancer and Bacterial Diseases: A Critical Review

Nthabeleng Hlapisi , Tshwafo E. Motaung , Linda Z. Linganiso, Oluwatobi S. Oluwafemi, and Sandile P. Songca
Review Article (27 pages), Article ID 7147128, Volume 2019 (2019)

Synthesis and Antibacterial Activity of Polyoxometalates with Different Structures

Jingmin Gu , Lei Zhang, Xiaofeng Yuan, Ya-Guang Chen , Xiuzhu Gao, and Dong Li 
Research Article (6 pages), Article ID 9342326, Volume 2018 (2019)

Anticancer Potential of Green Synthesized Silver Nanoparticles Using Extract of *Nepeta deflersiana* against Human Cervical Cancer Cells (HeLA)

Ebtesam S. Al-Sheddi, Nida N. Farshori , Mai M. Al-Oqail, Shaza M. Al-Massarani , Quaiser Saquib, Rizwan Wahab, Javed Musarrat, Abdulaziz A. Al-Khedhairi, and Maqsood A. Siddiqui
Research Article (12 pages), Article ID 9390784, Volume 2018 (2019)

Cytotoxic and Bactericidal Effect of Silver Nanoparticles Obtained by Green Synthesis Method Using *Annona muricata* Aqueous Extract and Functionalized with 5-Fluorouracil

María del Carmen Sánchez-Navarro, Claudio Adrian Ruiz-Torres , Nereyda Niño-Martínez, Roberto Sánchez-Sánchez, Gabriel Alejandro Martínez-Castañón , I. DeAlba-Montero, and Facundo Ruiz 
Research Article (8 pages), Article ID 6506381, Volume 2018 (2019)

Synthesis, Characterization, and Antimicrobial Activity of Novel Sulfonated Copper-Triazine Complexes

Supun Katugampala, Inoka C. Perera, Chandrika Nanayakkara, and Theshini Perera 
Research Article (7 pages), Article ID 2530851, Volume 2018 (2019)

Exploration on the Interaction Ability of Antitumor Compound

Bis-[2,6-difluoro-*N*-(hydroxyl-κO)benzamido-κO]dibutyltin(IV) with Human Peroxisome Proliferator-Activated Receptor hPPAR γ

Jiaqi Mai , Yunlan Li , Xiaozhi Qiao, Xiaoqing Ji, and Qingshan Li 
Research Article (10 pages), Article ID 3063271, Volume 2018 (2019)

Synthesis, Structural Analysis, and Biological Activities of Some Imidazolium Salts

Gühergöl Uluçam  and Murat Turkyilmaz
Research Article (12 pages), Article ID 1439810, Volume 2018 (2019)

Editorial

Anticancer and Antimicrobial Properties of Inorganic Compounds/Nanomaterials

Rais Ahmad Khan ¹, Aurel Tăbăcaru ², Farman Ali,³ and Bon H. Koo⁴

¹Department of Chemistry, College of Science, King Saud University, Riyadh 11451, Saudi Arabia

²Department of Chemistry, Physics, and Environment, Faculty of Sciences and Environment,

“Dunarea de Jos” University of Galati, 111 Domneasca Street, Galati 800201, Romania

³Department of Applied Chemistry, Aligarh Muslim University, Aligarh 202001, India

⁴School of Materials Science and Engineering, Changwon National University, Changwon 51140, Republic of Korea

Correspondence should be addressed to Rais Ahmad Khan; krais@ksu.edu.sa and Aurel Tăbăcaru; aurel.tabacaru@ugal.ro

Received 20 March 2019; Accepted 20 March 2019; Published 9 June 2019

Copyright © 2019 Rais Ahmad Khan et al. This is an open access article distributed under the Creative Commons Attribution License, which permits unrestricted use, distribution, and reproduction in any medium, provided the original work is properly cited.

The field of bioinorganic chemistry has emerged after a serendipitous discovery of cisplatin by Rosenberg in 1962. Cisplatin is called “penicillin of cancer” because of its wide application and was a first chemotherapeutic drug. After this, a new field of drug formulation with metal center/core was sparked and investigated. Interestingly, it became the promising alternative for the treatment of various diseases like cancer, microbial, quorum sensing, and biofilm-associated infectious disease. The field of metallodrugs has also evolved with the emergence of nanomaterials as therapeutic anticancer and antibacterial agents. These molecules have also shown significant potential to act as potential drug candidates in different prospects from chemotherapy to diagnostics to drug delivery in various diseases. Nanomaterials possess unique physical and chemical properties. The fabrication of nanomaterials gives rise to controlled size, shape, compositions, charge, aggregation, and solubility. This special issue includes a collection of original papers covering aspects related to the synthesis and characterization of various metal-based compounds and nanomaterials with anticancer and antimicrobial properties.

The critical review by N. Hlapisi et al. explores the utilization of gold nanorods, as delivery and photothermal agents, and porphyrins, as photosensitizers, in the treatment of cancer and bacterial diseases, delving into ways of incorporating both photothermal and photodynamic therapies with the scope of producing less toxic, more efficient, and specific compounds for the treatment. The excellent imaging

and sensing properties shown by gold nanorods qualify them as excellent for photothermal therapy. On the other hand, porphyrin and nanorod conjugates show excellent properties as photosensitizers due to the fact that they have more than one absorption band on the near infrared region; hence, they can be manipulated and are used to penetrate deeper into tissue for photodynamic therapy.

The new inorganic-organic hybrid compound, $[\{\text{Cu}(\text{phen})_2\}_2(\text{H}_4\text{W}_{12}\text{O}_{40})]$, was synthesized and structurally characterized by D. Li et al. The Keggin anion $\text{H}_4\text{W}_{12}\text{O}_{40}^{4-}$ from the constitution of this compound was grafted with two coordination units $\{\text{Cu}(\text{phen})_2\}$, forming an electrically neutral molecule. The antibacterial activity of several polyoxometalate compounds with different anionic structures, also including the new compound, was studied. The results showed that the new polyoxometalate-based compound (POM) could inhibit the growth of *Enterococcus faecalis* FA2 strains and that the antibacterial activity of the polyoxometalate compounds is dependent on the component elements of POM but is less relative with the anion structures.

In the study of N. N. Farshori et al., silver nanoparticles (ND-AgNPs) were synthesized using an aqueous extract of *Nepeta deflersiana* plant, and their morpho-structural features were revealed by ultraviolet-visible spectroscopy, Fourier transforms infrared spectroscopy, X-ray diffraction, transmission electron microscopy, scanning electron microscopy, and energy dispersive spectroscopy. The results

obtained from these various characterization tools showed that the average size of synthesized AgNPs was 33 nm and in face-centered-cubic structure. The anticancer potential of ND-AgNPs was investigated against human cervical cancer cells (HeLa). The cytotoxic response was assessed by 3-(4,5-dimethylthiazol-2-yl)-2,5-diphenyltetrazolium bromide (MTT), neutral red uptake (NRU) assays, and morphological changes. The influence of cytotoxic concentrations of ND-AgNPs on oxidative stress markers, reactive oxygen species (ROS) generation, mitochondrial membrane potential (MMP), cell cycle arrest, and apoptosis/necrosis was also studied. The cytotoxic response observed was in a concentration-dependent manner. Furthermore, the results also showed a significant increase in ROS and lipid peroxidation (LPO), along with a decrease in MMP and glutathione (GSH) levels. The cell cycle analysis and apoptosis/necrosis assay data exhibited ND-AgNPs-induced SubG1 arrest and apoptotic/necrotic cell death. The biosynthesized AgNPs-induced cell death in HeLa cells suggested the anticancer potential of ND-AgNPs, thus suggesting their potential use in the treatment of cervical cancer cells.

Another green method to obtain silver nanoparticles, with cytotoxic and bactericidal properties, was reported by F. Ruiz et al., who used the *Annona muricata* aqueous extract, along with the functionalization with 5-fluorouracil (5-FU). The processes of reduction, nucleation, and functionalization of the obtained AgNPs were analyzed by UV-Vis absorption spectroscopy, and it was found that they are a function of the contact time of the metal ions with the extract. The morpho-structural characterization of AgNPs carried out by transmission electron microscopy revealed their quasispherical shape with an average particle size of 10.87 nm. The recorded Z-potential had a value of -27.3 ± 1.22 mV, demonstrating repulsion between the particles and good colloidal stability of the nanomaterials. The antibacterial properties of the synthesized nanomaterials showed significant inhibition against *Enterococcus faecalis*, *Staphylococcus aureus*, and *Escherichia coli*. The cytotoxicity of the AgNPs at 24 and 48 hrs displayed an increment in cell viability associated with the particle functionalization by 5-FU, and only a few dead cells at 24 hrs were observed in the fluorescence microscopy images.

The research article of T. Perera et al. focuses on the synthesis, characterization, and antimicrobial activity of four novel water-soluble copper-triazine derivatives in search of potent antibacterial and antifungal drug leads. As such, 3-(2-pyridyl)-5,6-diphenyl-1,2,4-triazine-4,4'-disulfonic acid monosodium salt (L_1 , ferrozine) and 3-(2-pyridyl)-5,6-di(2-furyl)-1,2,4-triazine-5,5'-disulfonic acid disodium salt (L_2 , ferene) have been used as ligands to study the complexation towards copper(II). The synthesized complexes, $[\text{CuCl}_2(\text{ferrozine})] \cdot 7\text{H}_2\text{O} \cdot \text{MeOH}$ (1), $[\text{CuCl}_2(\text{ferrozine})_2] \cdot 5\text{H}_2\text{O} \cdot \text{MeOH}$ (2), $[\text{CuCl}_2(\text{ferene})] \cdot \text{H}_2\text{O} \cdot \text{MeOH}$ (3), and $[\text{CuCl}_2(\text{ferene})_2] \cdot \text{H}_2\text{O} \cdot \text{MeOH}$ (4), have been characterized spectroscopically, and preliminary bioassays have been carried out. Complexes (1) and (2) have shown antibacterial activity for both *Staphylococcus aureus* and *Escherichia coli* at 1 mg/disc concentration, and ferrozine has shown a larger inhibition zone against the clinical sample of *Candida*

albicans at 1 mg/disc concentration in comparison with the positive control, fluconazole.

This study of Q. Li et al. analyzed the interaction between the novel patent diorganotin(IV) compound bis-[2,6-difluoro-N-(hydroxyl- κ O)benzamido- κ O] (DBDF2,6T) and the hPPAR γ protein under physiological condition with the methods of fluorescence quenching, 3D fluorescence, DARTS, ultrafiltration-LC, and computer molecular docking. According to the experimental spectroscopic data, DBDF2,6T could interact with the hPPAR γ protein and formed a nonradiative ground-state complex of hPPAR γ -DBDF2,6T, mainly through hydrophobic force. The experiments of DARTS and ultrafiltration-LC preliminarily proved the possibility of DBDF2,6T to be an agonist compound to hPPAR γ protein. Considering the anticancer activity of DBDF2,6T and various physiological functions performed by agonists of PPAR γ protein, the authors concluded that DBDF2,6T had a possibility to interact with the hPPAR γ protein as an agonist and finally inducing physiological effects such as anticancer activity.

The novel imidazole salts 1,3-bis(2-hydroxyethyl) imidazolium bromide (L_A), 3-(2-ethoxy-2-oxoethyl)-1-(3-aminopropyl)-1H-imidazol-3-ium bromide (L_B), 1,3-bis(2-carboxyethyl)-4-methyl-1H-imidazol-3-ium bromide (L_C), and 3-(2-carboxyethyl)-1-(3-aminopropyl)-1H-imidazol-3-ium bromide (L_D), along with their synthesis and characterization, were reported by G. Uluçam and M. Turkyilmaz. The antimicrobial and cytotoxic activities of the synthesized salts on some specific bacteria and cancer cell lines were measured using spectrophotometric methods, showing that L_A exhibited better inhibition than the selected antibiotic on *Bacillus cereus*, while it is active on the selected bacteria and the yeast together with L_B . On the cytotoxicity evaluation, L_C showed considerable inhibition effect on HeLa, as L_D manifested on Hep G2. Although their IC_{50} doses are quite high in comparison with the similar chemicals in the literature, the cytotoxicity of L_C and L_D is affirmed by not causing harmful effect on the healthy MEF cells as much as they do on the cancer cell lines.

We hope that this special issue would shed light on the use of metal-based compounds and nanomaterials as potential candidates for anticancer and antimicrobial properties and attract the attention of the scientific community to further challenges and investigations in this field.

Conflicts of Interest

The Guest Editors declare no conflicts of interest.

Acknowledgments

We would like to express our sincere appreciation to all the authors for having brought interesting and significant contributions, as well as to all the reviewers for their support and constructive criticisms in making this special issue possible.

Rais Ahmad Khan
Aurel Tăbăcaru
Farman Ali
Bon H. Koo

Review Article

Encapsulation of Gold Nanorods with Porphyrins for the Potential Treatment of Cancer and Bacterial Diseases: A Critical Review

Nthabeleng Hlapisi ¹, Tshwafo E. Motaung ¹, Linda Z. Linganiso,¹
Oluwatobi S. Oluwafemi,^{2,3} and Sandile P. Songca⁴

¹Department of Chemistry, University of Zululand, X1001, KwaDlangezwa, KwaZulu-Natal, South Africa

²Department of Applied Chemistry, University of Johannesburg, P.O. Box 17011, Doornfontein, Johannesburg 2028, South Africa

³Centre for Nanomaterials Science Research, University of Johannesburg, Johannesburg, South Africa

⁴Department of Chemistry, University of Kwazulu Natal, Kwazulu Natal, South Africa

Correspondence should be addressed to Nthabeleng Hlapisi; nsisitha@gmail.com and Tshwafo E. Motaung; motaungt@unizulu.ac.za

Received 1 August 2018; Accepted 4 February 2019; Published 30 April 2019

Guest Editor: Rais A. Khan

Copyright © 2019 Nthabeleng Hlapisi et al. This is an open access article distributed under the Creative Commons Attribution License, which permits unrestricted use, distribution, and reproduction in any medium, provided the original work is properly cited.

Cancer and bacterial diseases have been the most incidental diseases to date. According to the World Health Report 2018, at least every family is affected by cancer around the world. In 2012, 14.1 million people were affected by cancer, and that figure is bound to increase to 21.6 million in 2030. Medicine therefore sorts out ways of treatment using conventional methods which have been proven to have many side effects. Researchers developed photothermal and photodynamic methods to treat both cancer and bacterial diseases. These methods pose fewer effects on the biological systems but still no perfect method has been synthesized. The review serves to explore porphyrin and gold nanorods to be used in the treatment of cancer and bacterial diseases: porphyrins as photosensitizers and gold nanorods as delivery agents. In addition, the review delves into ways of incorporating photothermal and photodynamic therapy aimed at producing a less toxic, more efficacious, and specific compound for the treatment.

1. Introduction

Drugs based on metals have since been used during ancient times; however, modern metal-based medicine dates to about 50 years ago through the use of cisplatin; since then, the antitumor activity of these metals has been studied [1–5]. Gold salts and arsenic compounds have been used for the treatment of arthritis and syphilis, respectively. Heavy metals, rhodium, indium, palladium, and noble metals have the ability to be used as therapeutic agents. The noble metal nanoparticles work better when ligands are attached to them as opposed to when they operate singularly as free ligands; in addition, antibiotic compounds can also be bound to the metals, thereby increasing their efficacy or to avoid the resistance by drugs [6, 7]. In their elemental and coordinated states, metals act as various agents: antibiotic, antimalarial, antibacterial, antiviral, antitubercular, antimycotic, antiarthritis, and anti-inflammatory. In their elemental states,

nanoparticle formulations are used as carrier agents for drugs and to toxify bacteria but this toxicity of bacteria in humans is still a subject of research [8]. The specificity and selectivity of target drugs that only hit the affected cells and tissue have been a challenge in the therapeutic field, but the use of receptor nanoparticles has been implemented to overcome this challenge. Other challenges as highlighted by Akhtar et al. [9] are primarily on the basis of the design of a nanocarrier, the drug loading efficiency, how stable the ligands are on the nanoconjugates, maximum receptor-ligand interactions, and the time the targeted receptor would be expressed, the toxicity of the nanoparticle, and immunity to the blood system [10]. Gold nanorods (AuNRs) are used in photodynamic and photothermal therapy for clinical purposes on the basis of their optical and chemical properties. Porphyrin is one of the common photosensitizers used for the treatment of tumors and antibacterial infections. Nanoparticles have been introduced to the clinical field as to

prevent or assist in the traditional methods of treating cancer.

Noble metal nanoparticles have strong electric fields at the surface; hence, the absorption and scattering of electromagnetic radiation by those nanoparticles are enhanced, making them ideal choices in the photothermal cancer therapy. The best option is to use agents that are active at the near-infrared region for minimal light extinction by the intrinsic chromophores in the tumor tissues. AuNRs with suitable aspect ratios have the ability to absorb and scatter light in the NIR (650–900 nm), hence used in molecular imaging and photothermal cancer therapy. Solid tumors have leaky blood vessels with cell junction gaps from 100 nm to 780 nm, and this permeable vasculature allows for the extravasation of gold nanoparticles into the tumor matrix. The optimal aspect ratio as experimentally obtained by Singh et al. for *ex vivo* experiments was determined as 4.0 ± 0.06 as per TEM results. The aspect ratio resulted in the SPR peak of the AuNR to be around 808 nm which is in the NIR and allows for deep optical tissue penetration [11].

Some scientists however argue for the use of nanoparticles as tumor-targeted delivery systems in the clinical environment. An example is seen where Van de Meel et al. [12] state that the “unappreciation” of nanomedicine is due to clinical trials practised on mice as opposed to humans and that only 0.7% of the researched nanomedication even reaches clinical trials. He however concluded that researchers should focus not only on the understanding of the biology and chemistry behind nanocarriers but also on the idealistic “disease-driven” approach on their potential.

The use of gold nanoparticles has been of interest lately due to their impeccable properties as carrier agents of drugs; the properties include the fact that a wide range of organic molecules can adhere and be bonded to the nanoparticles, they have low levels of toxicity, their absorption is very tunable, and they have small sizes and high surface area to the volume ratio. These properties however ideally work when the surface of the gold particles is modified and tuned to suit the use [13]. Gold nanoparticles are biologically inert, have high dispersity, are noncytotoxic, are biocompatible, and are optically tunable [14]. The treatment of cancer has traditionally made use of the systematic delivery of an anticancer agent which unfortunately leads to the accumulation of the agent to the tumor cell; a new method has however been developed which ensures that the anticancer agent is delivered through the lymphatic network. Oladipo et al. used the polymeric AuNRs (PAuNRs) to deliver drugs from an accessory lymph node to a proper auxiliary lymph node containing a tumor in order to treat lymph node metastases [15]. Coating of nanoparticles with alkane thiols monolayer has become of great attraction as resulting nanoconjugates have unique optical and electronic properties that depend and can be controlled by the particle size and the nature of the protecting molecules [16].

Gold nanoparticles possess unique optical properties. AuNRs particularly have two distinctive absorption bands: one is caused by light absorbed on the short axis (transverse) and another due to light absorbed on the long axis (longitudinal). The ability of the AuNRs to be optically

controlled and the fact that they are very sensitive to changes in the local environment makes them excellent materials for sensing, photothermal therapy, and imaging [17]. AuNRs applications are vast; they can be used in biomedical technologies, plasmon-enhanced spectroscopies, and optical and optoelectronic devices. AuNRs exhibit special optical properties in cancer diagnostics and treatment. Their advantages however still bring a few questions: their toxicity in the blood system, their biodistribution, and their fate *in vivo*. Still to be explored is a further optical control of gene delivery and use of nanorods for *in vivo* spectroscopic tumor detection combined with organic dye molecules [18].

Photodynamic therapy is one of the most effective regimens in the treatment of cancer, precancerous inductions, actinic keratosis, infections, dermatology, cardiovascular illness, and wound healing. For photodynamic therapy to successfully proceed, three elements have to be present: oxygen, a photosensitizer, and light [19]. Porphyrins are photosensitizers which selectively accumulate in tumor cells, releasing cytotoxic substances and hence destroy the cancerous cells with minimal harm to the surrounding healthy cells. Exposure of a photosensitizer to photoactivating light enhances the destruction of malignant tissues. Clinically, common photosensitizers used are the haematoporphyrin derivative (HPD) and the Photofrin II, which is a purified form of HPD [20]. Porphyrin is a naturally occurring heterocyclic compound shown in Figure 1 [21].

Heterocyclic compounds occur widely in nature in compounds such as hemes and chlorophylls. These compounds are used in medicines, pharmaceutical, agrochemical, and energy materials. Polyheteroatomic heterocycles are used in clinical therapy as they allow for direct interactions with the biological targets which are often not possible with single heterocyclic compounds [22]. Porphyrins are heterocyclic compounds with semiconducting properties; these compounds can be used for a number of applications: artificial photosynthesis, catalysis, molecular electronics, sensors, nonlinear optics, and solar cells. The functionality of porphyrins depends on their crystallography, which depends on the plane of the macrocycle and the conjunction of the pi-bonding to the adjacent macrocycle or how the macrocycles are interconnected with the ligands by covalent bonds. The modification of the basic porphyrin structure enhances its semiconductivity property and hence its ability to be used as a photosensitizer. Porphyrins also have the tumor-localizing ability [23].

Encapsulation of gold nanorods with porphyrin has been achieved before to obtain novel multifunctional nanoparticles. The porphyrin structures were, for example, doped with silica shells to protect them from the external bioenvironment [24]. The resulting multifunctional nanoparticles are good candidates for both photosensitization and two-photon imaging and also image-guided therapy.

The use of imaging therapy has many advantages over conventional therapy. The merits of two imaging therapy include the bioimaging that provides for deeper penetration (light) and has a 3D imaging capability. Metal nanoparticles especially gold nanorods have shown an excitingly good

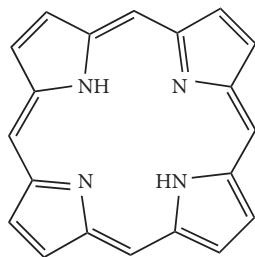


FIGURE 1: Structure of porphyrin.

promise in two-photon imaging. They have high two-photon luminescence which is approximately 58 times greater than that of a single rhodamine molecule [25]. The biological transparency window is around 6000–10000 nm which coincides with the longitudinal plasmon band of the gold nanorods. The nanorods alone however lack the targeting ability, hence with combination with porphyrins will create a more specific selective multifunctional compound.

The purpose of this study is to revise the coating performed on nanorods with porphyrin for further modification for the treatment of cancer and bacteria using photodynamic and photothermal therapy [26–29].

2. Literature Review

2.1. Gold Nanoparticles. Generally, metal nanoparticles have been used for cancer diagnosis and treatment for the past decades [30–34]. Multifunctional nanoparticles have specifically been used for a number of aspects such as targeting, imaging, and therapy as a way to overcome challenges imposed by conventional treatment (radiotherapy, chemotherapy, and surgery). Amongst all, the use of iron oxide nanoparticles received overwhelming attention primarily due to super magnetic properties for magnetic resonance imaging (MRI). In fact, magnetic nanoparticles other than gold and carbon nanoparticles could be degraded to the respective metal cations in the body especially in acidic media, increasing the toxicity of the long-term nanoparticles residing in the body [35]. Certain metal nanoparticles interact with light, and that proved to be an opportunity for biophonic nanomedicine [36, 37]. One of the main fields that use nanoparticles (NPs) is the image-guided therapy; it uses multifunctional nanoparticles based on surface plasmon resonance absorption property which is tunable in the near-infrared region [38, 39]. Typical examples are gold nanorods, for which optical properties could be explained better by the Mie–Gans theory [40]. The sensitivity of the plasmon resonance frequency of the nanorods towards the refractive index of its surroundings makes them suitable for use in biological sensing. They are also proven to be very sensitive to thermal environments and possess nonlinear optical response properties [41, 42]. Synthesis of the nanorods is one of the main parameters that are controlled for optimization of properties [43]. An important technology investigated in this review as a promising factor for the image-guided therapy and diagnosis is the passivation of gold nanorods [44, 45].

Gold nanoparticles have different shapes ranging from spherical, suboctahedral, octahedral, decahedral, icosahedral multiple twinned, irregular shaped, tetrahedral, nanotriangles, nanoprisms, hexagonal platelets, and nanorods [46–48]. Fluorescent nanoparticles have good biocompatibility for molecular imaging and metabolites used for cellular functions in cancer. On the other hand, nanorods show special optical and chemical properties for biological applications. They also have unique anisotropic geometry for tuneable absorption in the visible and near-infrared region. These phenomena make them useful for biosensing, photothermal therapy, and gene delivery [49–52]. Generally, nanoparticles are used for their light scattering and absorbing abilities, and scattering is more important for microscopy and optical coherence tomography (OCT) [53].

The effects of the nanoparticles can be detected using various imaging apparatus: magnetic resonance imaging, nuclear imaging, and photoacoustic imaging. After the administration of the nanoparticle to the tumor cell, they land on a solid target tissue, and their activity can be changed by an external stimulus. An example is photothermal therapy, in which the light energy is converted to heat energy for damaging the cancer cells [54, 55]. The dependence of the excitation of the noble metal nanorod energy lies in the dimensions of the nanorods and its environment. This enhances tunable optical properties which can be demonstrated by the Mie–Gans theory. It states that there is a direct dependence of the geometry end cap of the nanoparticles and the particles' size, which affects the peak position in the absorption spectra. For AuNRs, this gives rise to the two absorption bands by the longitudinal band and the transverse band [56–58].

2.1.1. Properties of Gold Nanorods. The optical properties of AuNRs are of great importance and make them excellent to use in therapy. In the past, the use of gold nanoparticles was limited to additives for aesthetic purposes, but emerging studies indicated that the peculiar optical properties at nanoscale of the particles brought other dimensions. For instance, the increase in rod length of the gold nanorod increases the longitudinal band red shift and the extinction coefficient [59, 60], as shown in Figure 2 [60, 62–66]. As a result, the nanostructures are used in sensing, imaging, and photothermal therapy. One property which qualifies the nanorods to be used in as biological sensors is that their absorption band changes with the refractive index of the local material. This phenomenon allows for very accurate sensing. They are often identified by their aspect ratio and are cylindrical rods with a width less than 10 nm to over 40 nm and length to several nanometers; an example is seen in Figure 3. For one to fully comprehend the unique features of nanorods, the robust extinction coefficient for predicting the concentration at an absorbance has to be known. The AuNRs are effective for the detection of sequences of infectious agents for diseases like HIV-1 [68].

AuNRs absorb at the near-infrared region where the maximum radiation through the tissue occurs, hence used for *in vivo* imaging and photothermal therapy. Nanorods

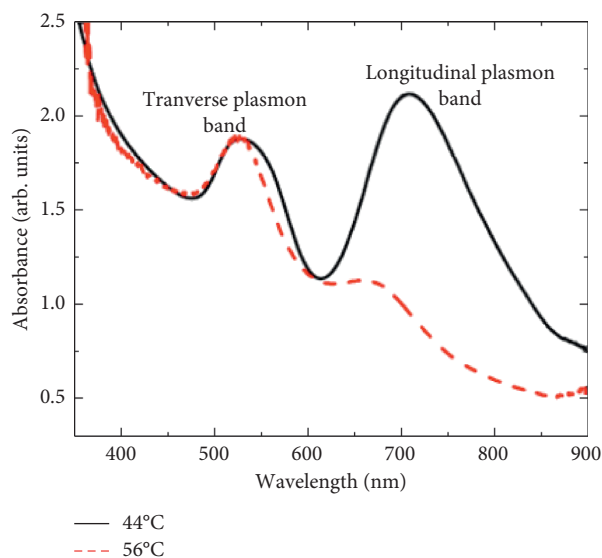


FIGURE 2: UV-Vis spectrum of AuNRs at different preparation temperatures [61].

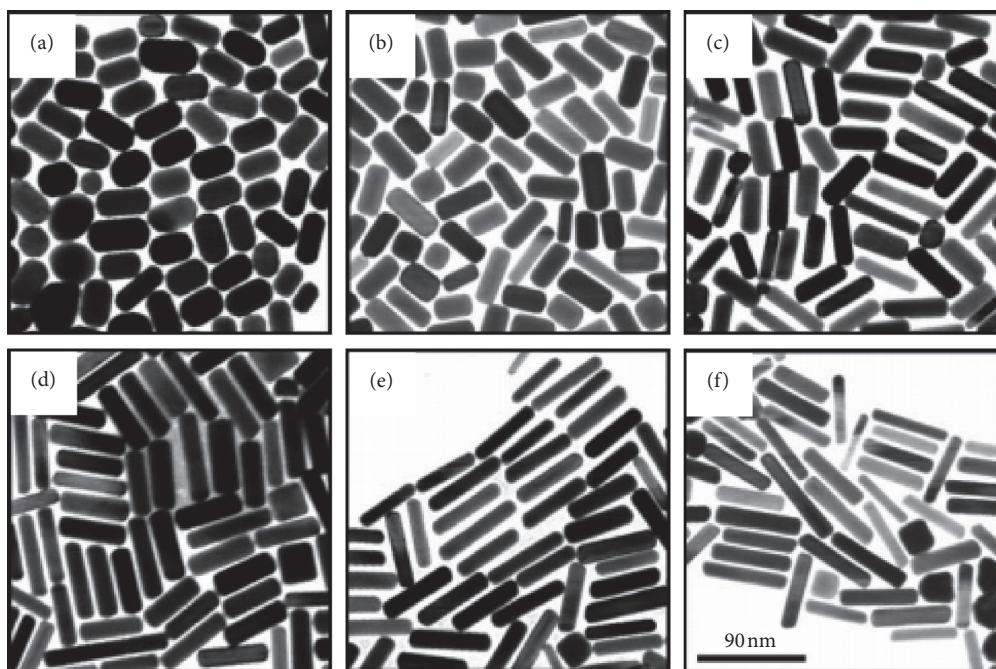


FIGURE 3: Illustration of gold nanorods of different aspect ratios in AgNO_3 growth solution with concentration (a) 0.03, (b) 0.05, (c) 0.075, (d) 0.1, (e) 0.125, and (f) 0.15 mmol^{-1} [67].

exhibit two bands of surface plasmon resonance (SPR), which are a product of the conduction band along their long and short axes. On the visible region, the transverse band and the longitudinal band occur on the near-infrared region (NIR) [69–72]. Tailoring of the nanorods during synthesis enables the absorption bands to be of desired wavelength in the near-infrared region, and this can be attributed to the fact that the longitudinal length of the nanorods can be tuned via its aspect ratio. Their luminous energy can be converted into heat energy which is influenced by the

maximum penetration of light in tissues favorable for photothermal therapy [73–76]. AuNRs have a higher distinct local field enhancement resulting in a significant surface-enhanced Raman spectroscopy (SERS) activity. Their modifiable surface area enables the incorporation of drugs for use as drug delivery agents [77–79].

The distinctive optical and electrical properties of AuNRs depend on size and aspect ratio. For the nanorods to efficiently work, several aspects need to be addressed: improvement of the synthesis of AuNRs in terms of reproducibility and

efficiency, full understanding of the direct characterization of nanorod geometry functionalization, and lastly, to find a cost-effective and sensitive method that would be used for nanorod sensing. Another important aspect is coating which also depends on synthesis that may lead to covalent or noncovalent bonds at the interface [80–82].

X-ray diffraction (XRD) shows a face-centred cubic close packing arrangement of gold nanorods in specific areas. The XRD peaks are very consistent with ones of metallic gold. Sharp peaks resembling ones of gold are observed in Figure 4, hence confirming the crystalline nature of the gold nanorods. Figure 4 shows an XRD pattern of gold nanorods [83].

Various diffraction patterns are presented at 2θ with values 38.4° , 44.4° , and 64.6° which correspond to the following diffraction planes: (111), (200), and (220), respectively. The peaks perfectly index to a cubic face-centred structure of a gold metal. The XRD showed a lattice constant of $a = 4.082 \text{ \AA}$ which is in agreement with 4.079 \AA , which is the standard diffraction pattern of a cubic gold metal (CAS: 7440-57-5) by Pallares [83].

2.1.2. Synthesis of Gold Nanorods. The nanorods are mainly synthesized using the wet chemical method and the hard template directed (an example in Figure 5) method [84, 85]. The wet chemical techniques involve the reduction of metal ions at gold surfaces in the presence of various surfactants; the technique however produces hybrids of nanospheres and other shapes clearly dominated by rods and that affects the ideal optical response of the gold nanorods. For high purity nanorods, the hard template directed methods are utilized by making use of the polycarbonate membrane and the anionic aluminum oxide (AAO) as templates [86, 87]. A typical example of the wet chemical method is the synthesis of AuNRs by seeding. In this method, a spherical seed of nanoparticles is added to a gold salt solution containing ascorbic acid, silver nitrate, and cetyltrimethylammonium bromide (CTAB) which then produces nanoparticles with a rod-like shape, as shown in Figures 5 and 6 [88]. CTAB enhances the rod-like shape of nanoparticles by preferably binding to the sides of the nanoparticles, and the concentration of gold nanoparticles is reduced slowly by the growth of the nanorods particles. Variation of silver nitrate concentration is used for the alteration of the rod length. The synthesis is followed by the centrifugation with distilled water to purify the nanoparticles by removing excess CTAB which is cytotoxic, unreacted metal ions, and the ascorbic acid.

The hard template directed method includes photochemical and electrochemistry methods, from which nanorods are grown in an electrolyte solution under regulated current between two electrolytes [89–92]. A gold metal plate acts as an anode and a platinum plate as a cathode. Both electrodes are immersed into an electrolytic solution containing a cationic surfactant.

The solution normally is placed in an ultrasonic bath to avoid aggregation of the gold nanoparticles before the addition of acetone and cyclohexane to the electrolyte

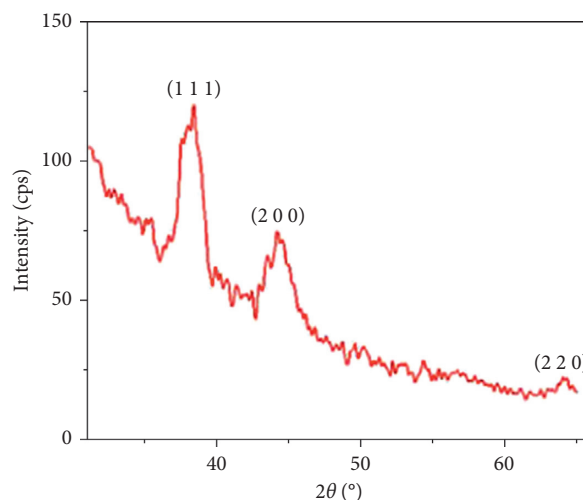


FIGURE 4: XRD pattern of gold nanorods as prepared by the sonoelectrochemical method [83].

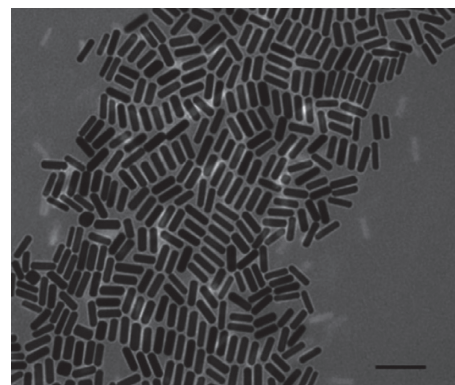


FIGURE 5: AuNRs prepared in the presence of a direction agent CTAB. Scale: 100 nm (TEM micrograph).

solution. Another electrochemical method can be used where the metal (gold) can be electrochemically deposited inside a nanoporous polycarbonate template of alumina membranes, as shown in Figure 7 [94]. In photochemical methods, gold salt is irradiated with UV light in the presence of CTAB and tetradodecylammonium bromide.

2.1.3. The Seed-Mediated Method/Green Method Synthesis.

Although the synthesis of AuNRs using the template method has been perfected and produces the AuNRs, other methods are also used as greener methods to give comparable results as the template method. Gole and Murphy [95] used the seed-mediated method as the alternative route to the template method. In this method as summarized in Figure 8, gold seeds of size 3–4 nm are initially synthesized by chemical reduction using a strong reduction agent (sodium borohydride) in the presence of a capping agent (citrate). Following the step, the seeds are added to the solution of more metal salt, a weak reducing agent, and a surfactant directing agent (CTAB). The method generally results in monodisperse, stable gold nanorods with different aspect ratios.

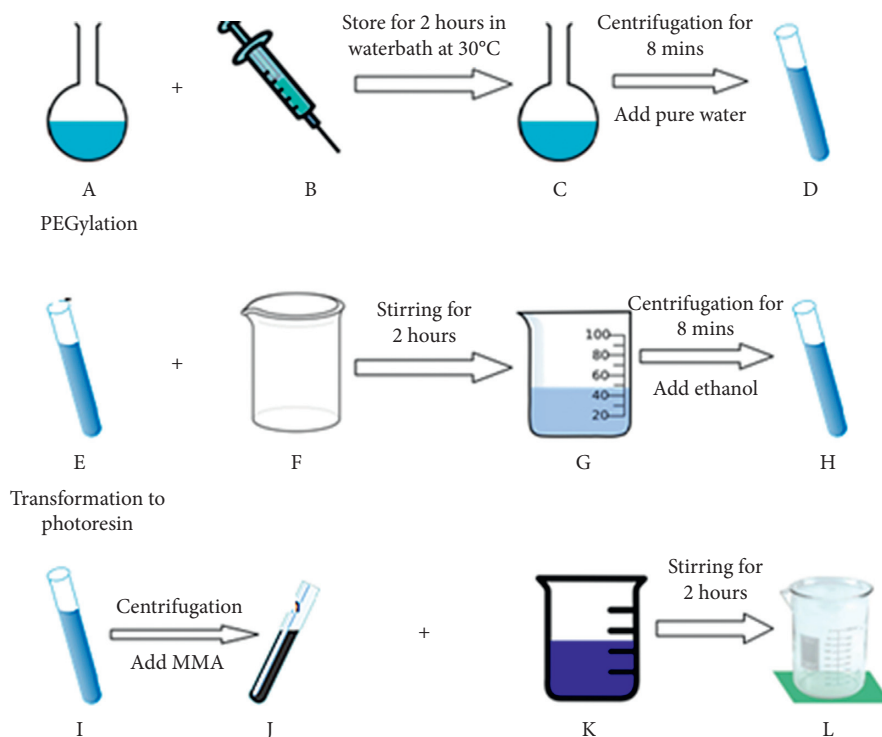


FIGURE 6: (A) Growth solution: CTAB, HAuCl_4 , AgNO_3 , H_2SO_4 , and AA. (B) Seed solution: CTAB, HAuCl_4 , and NaBH_4 . (C) Gold nanorods dispersed in pure water. (D) Redispensation of gold nanorods in pure water. (E) Gold nanorods dispersing in water. (F) mPEG-SH solution. (G) Gold nanorods wrapped in mPEG-SH, in pure water. (H) Gold nanorods wrapped in mPEG-SH, dispersing in ethanol. (I) Gold nanorods dispersing in ethanol. (J) Gold nanorods dispersing in MMA. (K) Photopolymerisation resin. (L) Gold nanorods dispersing in photoresin.

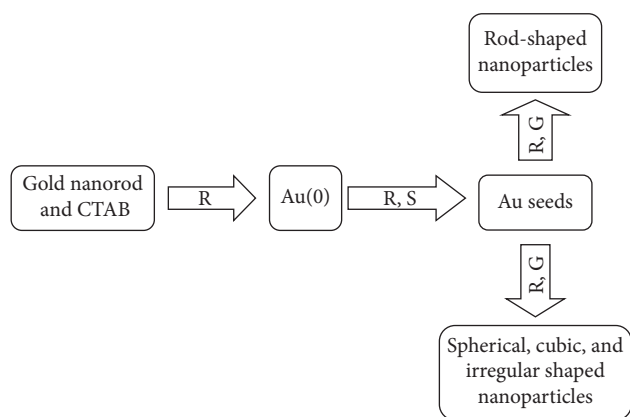


FIGURE 7: Illustration of the template method to synthesize gold nanorods and reduction of Au(I). S, forming Au seeds; G, growth of the Au seeds [93].

Moreover, another alternative green method is to synthesize gold nanorods without the use of CTAB but using gelatin as a capping agent. The method was reported to have resulted in higher media stability and enhance photostability [96].

2.1.4. Characterization of Gold Nanorods. Recent developments are done to develop nanotechnologies for specific drug delivery and multimodal activities [96–98]. Due to their distinctive chemical, physical, and photonic properties, AuNRs

have been used for cancer therapy, diagnostic, and therapeutic applications. Ali et al. stated that the low resolution from some equipment limits crucial information about the nanorods [99]. Many researchers characterised the nanoparticles by using electron microscopy (EM), atomic force microscopy (AFM), dynamic light scattering (DLS) and static light scattering (SLS), X-ray diffraction (XRD), and the Fourier-transform infrared spectroscopy (FTIR), as indicated in Table 1 [112–114].

Table 1 shows the properties, synthesis, characterization, and applications of AuNRs.

2.1.5. Application of the Gold Nanorods. A lot of studies indicated that the nanoparticles have the potential to be consumed as drug carriers, used in the detection and treatment of tumors, monitoring of treatment response, and to guide the therapeutic regimens [115, 116]. In addition, plasmon resonant gold nanorods are used as multifunctional agents for image-guided therapies. As the carriers, they promote the circulation time of drugs to take longer and improve and ensure that drugs do not degrade until they reach their targets. In the event of a tumor, the drug would land on the target still effective for an uptake through permeability, retention effect, and the receptor-mediated endocytosis. The large surface to volume ratio of nanocarriers helps them carry agents for chemotherapy, anti-angiogenic, or gene therapy delivered to tumor sites for enhanced treatment [117, 118].

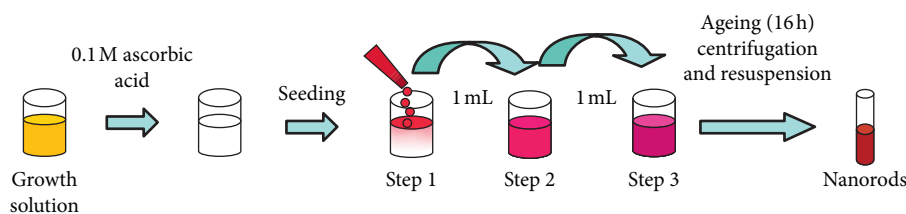


FIGURE 8: The general scheme used for the three step seed-mediated method [95].

TABLE 1: Summary of properties, synthesis, characterization, and applications of AuNRs

Synthesis	Characterization	Limitation	Application
Wet chemical synthesis [100–102], template method [103–105]	SEM, TEM	Limited yield due to the CTAB bilayer	Sensing, photothermal therapy, imaging
Electrochemical route [106–108]	TEM	N/A	Sensing, photothermal therapy, imaging
Seed-mediated method [109–111]	TEM, ETEM	N/A	Sensing, photothermal therapy, imaging

The versatility of nanoparticles enables them to be used in various ways. For example, in therapy, one way is for the treatment of ovarian cancer. This required a coat with thioglucose, sensitizers to produce ROS to damage the cancer cells [119–122]. The use of the nanorods over nanospheres or any other nanoshapes is also due to narrower line widths at more or less the same resonance frequencies because of reduced radiation-damping effects. In fact, nanorods have the ability to emit two-photon luminescence (TPL) signals that are used for single photon detection, which is suitable for biological imaging purposes [123–125].

The use of AuNRs however has a few challenges. For example, under intense illumination, the shape of the rod changes to a nanosphere and longitudinal NIR resonance loss. This normally happens in the photothermal therapy. A coating with thermally stable material was effective to overcome the shape change [100, 101, 126]. The modifications of gold nanoparticles for clinical value are of great importance, taking note of uptake and cell targeting. Theranostic systems have been founded from many building blocks, including hybrid, organic and or inorganic nanoparticles, superparamagnetic iron oxide, and plasmonic gold nanoparticles, which have been extensively studied due to their unique physical properties. The hybrid of these particles can be used for *in vitro* or *in vivo* imaging, magnetic targeting, and photothermal therapy. The coating/passivation or functionalization of the gold nanoparticles has currently received enormous attention due to more multifunctional competitive applications [102, 103].

2.1.6. Passivation of Gold Nanorods. The significance of magnetic nanoparticles has been growing due to use in more important and exciting applications like use in biomedical diagnosis, catalysis, and photoluminescent materials. Due to their unstable nature to the surrounding environment, their applications are inhibited as they readily oxidise on exposure to air due to their large surface areas. Methods have been developed to increase oxygen resistance on metal nanoparticles such as plasma spraying, phosphating, and electrolyte deposition [104–107]. Consideration has to be made

when encapsulating metal nanoparticles so as not to increase the thickness of the metal and hence interfering with the bulk metallic properties of the metal. One of the most ideal methods of passivation is the atomic layer deposition (ADL) method, which provides an ultrathin layer on the metal nanoparticle [108–111]. This method however does not guarantee the conformation of the geometry of the nanoparticles, hence only excellent for application in which precise morphology is not required [127, 128]. One of the methods used for the stabilization of metal nanoparticles is the attachment to dendrimers, ensuring and controlling the stability, size, and solubility of nanoparticles in a range of less than 1–5 nm diameter [129–131]. Examples of dendrimers include PAMAM and PPI as shown in Figure 9 [132]. Ligands and polymers have been used for the past years for the stabilization of metal nanoparticles and their application in catalysis and biocatalysis; in particular, their use with gold nanoparticles has been reported to yield excellent results.

The optical properties of AuNRs can be changed by slight changes in the shape or size of the nanorod; hence, it is important to ensure a stable environment for them. Sensing, imaging, and biomedical applications of AuNRs all come as a consequence of the ability of the AuNRs to be tunable, which is attributed to their optical properties contributed by their rod-like shape. Murphy et al. elaborates on the interfacial chemistry of nanorods [133]; three interfaces occur on the surface of nanorods, the gold-surfactant interface, hydrophobic surfactant bilayer, and a surfactant interface. These interfaces help in altering the nanorod properties in terms of stability, against aggregation and toxicity and how easily they can be assembled. Lastly, the solvent accessible interface provides a platform or directs how the nanorod can interact with other particles, macromoles, and living cells [134–136].

A common method of the synthesis of AuNRs uses CTAB, which makes the functionalization of AuNRs using ligands a challenge. During the synthesis using this method, a double layer of CTAB is formed for the passivation; this layer is a problem in terms of bioconjugation, adsorption of DNA nonspecifically, cytotoxicity, and the stability of the

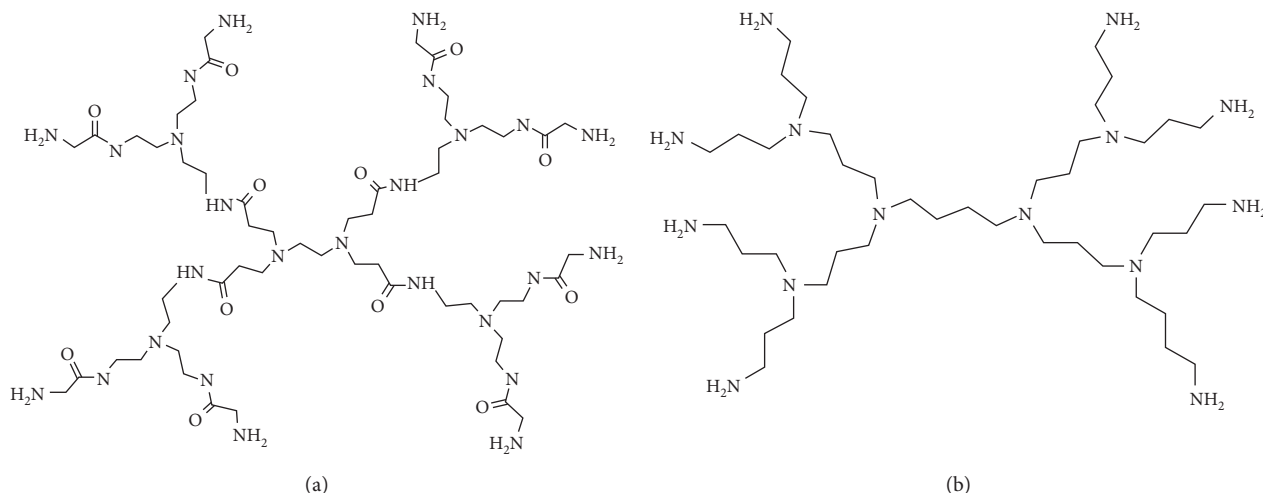


FIGURE 9: (a) A G1 PAMAM dendrimer and (b) G1 PPI dendrimer.

nanorod and hence limits the use of these AuNRs for biological applications [137–140]. Absorption associated with AuNRs enables them to be used for dark-field light scattering observation or biological media. Even though CTAB is very toxic to the biological environment, complete removal from the AuNRs would yield unstable AuNRs in colloidal dispersion forming aggregates. To obtain functional AuNRs, CTAB has to be replaced by amphiphilic molecules. Cationic cerasone-forming lipids and cationic nonsilylated lipids are used to passivate AuNRs [141]. Moreover, the amphiphilic molecules were added as to overcome the shortcomings brought by CTAB especially the fact that it has high cytotoxicity preparation of phosphatidylcholine passivated AuNRs (PC-AuNRs) which have low cytotoxicity and efficiently used as photosensitizers using pulsed light [142]. The pulsed light however reshapes the nanorods into nanospheres, hence no absorption spectra at the near-IR region. This helps in the damage of only tumor cells not healthy cells even with successive irradiation. The combination of photosensitizers and light induces the selectivity for tumors from healthy cells and also use of light produces heat just around the photosensitizer, hence the destruction of cells. Figure 10 [119] shows the absorption spectra of a PC-AuNRs in solution. It shows a normal NR spectrum with two SP peaks: ~900 nm for the LSPR and ~520 for the TSPR.

Ferric acid at room temperature as an etching agent for AuNRs is also used to passivate gold nanorods. The method used decreased the length of the AuNRs but not their diameter due to the oxidation of AuNRs by ferric ions, the shortening of only the length helps in the provision of the nanorod's desired aspect ratios and selective optical and also selectively removes other nanostructures. The shortening in length of the nanorods was monitored by TEM and the UV-vis absorption spectroscopy, and the results showed the reduction of electron potential of the gold species by halide ions and acceleration in oxidation of the AuNRs by ferric ions [121].

Other ways to encapsulate the particles include polyelectrolyte coatings such as poly(diallyldimethylammonium

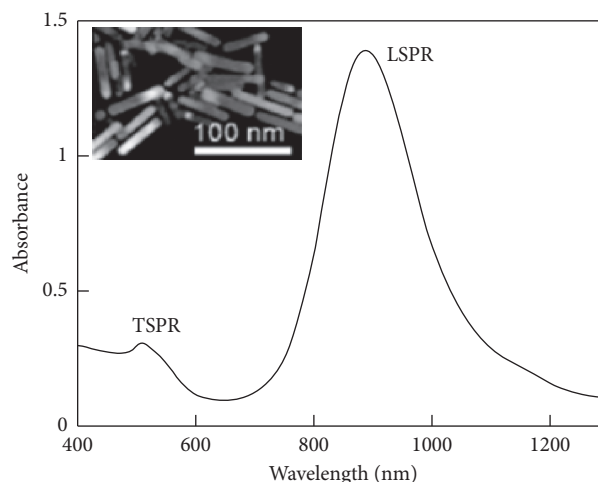


FIGURE 10: PC-AuNRs absorption spectrum, 0.5 nM Au nanorods (TEM image of PC-NRs).

chloride) (PDADMAC), poly(4-styrenesulfonic acid) (PSS), poly(acrylic acid) (PAA), or poly(allylamine) hydrochloride (PAH); these molecules reduce the interaction of CTAB with cells. PEGyated AuNRs are also used, which to some extent replace the CTAB in the molecule hence reducing toxicity [122]. Figure 11 illustrates the encapsulation with polymer-based molecules.

The treatment of particles with PEG-SH replaces the CTAB in the molecules which is toxic, replaces it with PEG (polyethylene glycol), and it also enhances the particles to be more stable under different conditions. Takahashi et al. stated that the PEG as a linker to attach antibodies is still a field to be explored further [91]. Lastly, a hydrophobic polymeric precursor, polyvinyl acetate (PVA) which changes into polyvinyl alcohol which is hydrophilic, is used to replace the nonbiocompatible and toxic CTAB [143].

AuNRs perform adequately in their retained shape; hence, a suitable coat has to be used for such. CTAB is the main inhibitor in AuNRs application due to instability; hence, thiol monolayers are used which provide for better

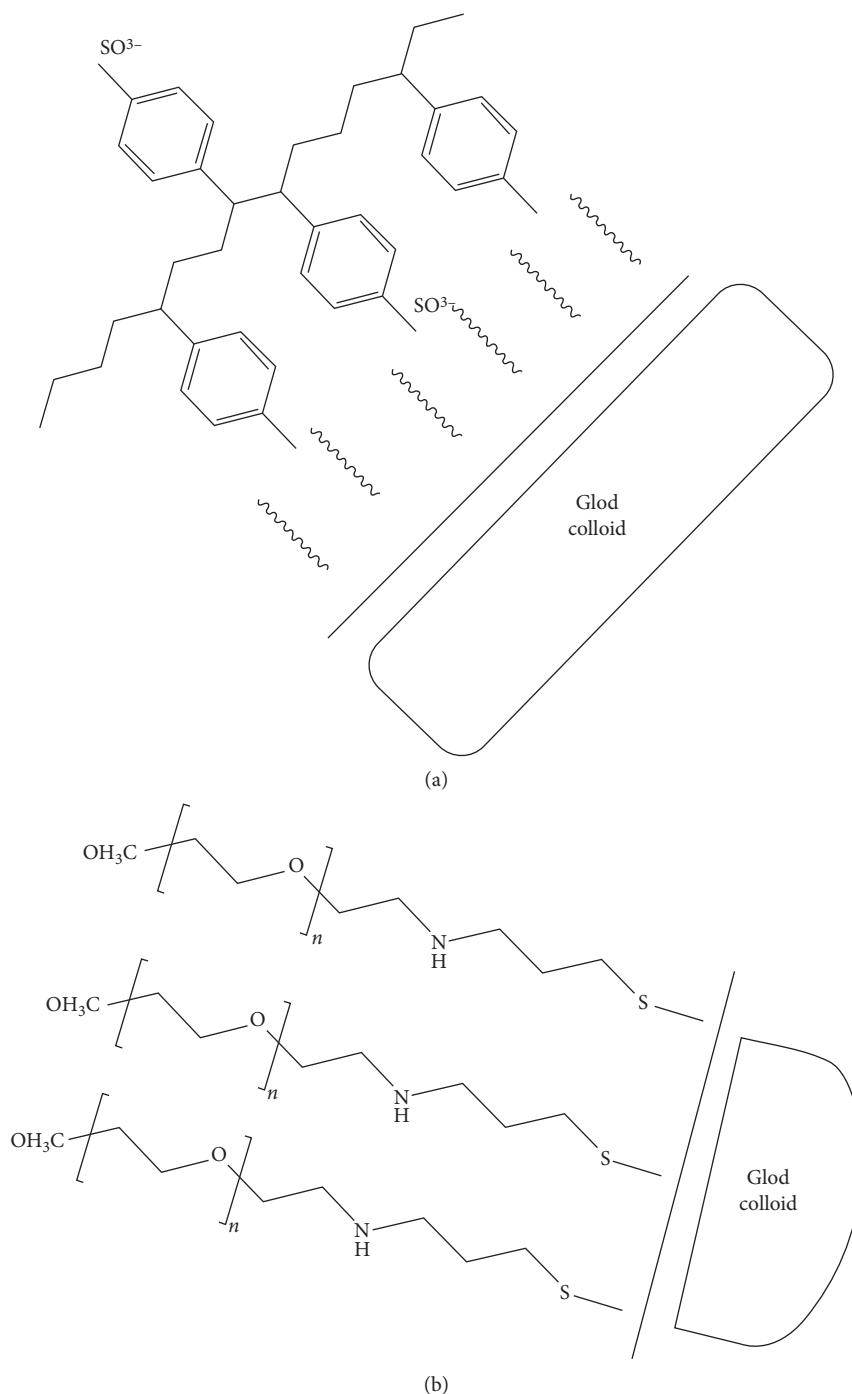


FIGURE 11: Surface modification of AuNRs. (a) PSS, encapsulation occurs on the CTAB bilayer through electrostatic adsorption. (b) mPEG-SH, replacement of the CTAB by PEG by the gold sulphur binding [123].

stability and organic media for compatibility [144]. Polymer (including porphyrin) coated nanorods are used as either ionic or cationic molecules with different charge densities, and these also give a promising future as biological delivery agents [145, 146].

2.1.7. The Replacement of Quantum Dots over Gold Nanorods. Quantum dots (QDs) are nanocrystals with semi-conducting properties. These materials comprise elements

from Group II to VI or III to V, and their sizes range from 2 nm to 19 nm. QDs such as AuNRs have unique optical and chemical properties [147]. These materials have an excellent future in biomedical imaging and detection; however, due to the heavy metals and colloidal instability, these pose limitation in terms of their use in diagnosis and therapy for both cancer and other diseases. Moreover, QDs still have questions pertaining to their cytotoxicity and their size increase after coating. The materials also show impressive results in imaging tumor neovasculature which

is done late after clinical diagnosis of the development of the cancer. Gold nanorods have very high absorption spectra in the NIR; this is where light penetration into the tissue is very high, around 10 cm deep. Gold nanorods relative to quantum dots are easy to synthesize, they have tunable optical properties, and they can also be multifunctional [11].

2.2. Porphyrins. Porphyrins and metalloporphyrins are tetraazamacrocyclic compounds found in nature, and the compounds participate in important biological processes such as photosynthesis. Importantly, the ability of a porphyrin photosensitizer to be located in a biological medium depends strongly on their peripheral substituent groups as well as their axial ligand; the two factors determine solubility, chemical affinity, redox potential, and other properties [148–150].

2.2.1. Synthesis of Porphyrin and Characterization. Porphyrins exist as two types, β -substituted and mesosubstituted porphyrins, as illustrated in Figure 12 [151], where the β -substituted porphyrins mirror naturally occurring porphyrins while mesosubstituted are synthesized. Meso-substituted porphyrins are widely used in biomedical and material chemistry [152].

The synthesis of the mesosubstituted porphyrins from nonporphyrins follows basic steps which are seen in the methods described here. The first synthesis was performed by Rothermund in 1936, and the method starts with the reaction of an aldehyde and pyrrole with both reactants at high temperature and concentration in a bomb reactor with no added oxidant. The addition of zinc acetate to the reaction only increases the yield of tetraphenylporphyrins twofold, but this is not observed with any other porphyrins [153–157].

Another method was developed by Adler and Longo so as to modify the Rothermund method by increasing the yields. The method was developed around the 60s and uses high temperature and concentration, but unlike the Rothermund method, it takes place in the presence of air under reflux in propionic acid. The method allows for synthesis of various porphyrins at relatively higher yields but polymerized pyrrole yield also increases, hence reduced porphyrin yields because it contaminates the product. The porphyrin can be isolated in two ways: treating with DDQ (2,3-dichloro-5,6-dicyano-1-4-benzoquinone) and refluxing with toluene or by using column chromatography. Scheme 1 illustrates the synthesis by the Adler–Longo method [158]. Figures 13 and 14 show a reported method scheme as performed by Lindsey in 1987.

The Adler–Longo reaction is used to react substituted benzaldehydes with pyrroles to produce the corresponding porphyrins in yields of about 20%. The method provides crystalline and pure product relative to the Rothermund reaction product, and it can also be used with different aldehydes to produce porphyrins but it poses certain problems; the high temperatures and concentrations hinder the synthesis of porphyrins with sensitive functional

groups [144, 160, 161]. The reaction method as established by Alder, Longo, and Shergalis shows that before the porphyrin is cyclised, it goes through a carbinol step as shown in Figure 15 [162].

Due to the drawbacks brought by the Adler–Longo method, the Lindsey method was developed. The method synthesizes porphyrins under milder conditions and is a two-step one-flask reaction. The method enhances the Adler–Longo method, in that porphyrins that cannot be synthesized by the latter can be synthesized by the Lindsey method; this method can yield porphyrins from some sensitive aldehydes. In this method, pyrrole, benzaldehyde, triethylorthoacetate, and a water quencher are stirred at room temperature at equimolar concentrations with boron triflate in dichloromethane (DCM). After an interval of 30–40 minutes, formation of porphyrinogen occurs. DDQ is added to oxidise the porphyrinogen to produce the porphyrin in a yield of 30–40%. Figure 16 [163] shows the reaction path from an aldehyde to a porphyrin. Figure 14 illustrates a reaction scheme for the formation of porphyrinogen [164–171].

2.2.2. Modifications in the Structure

(1) First-, Second-, and Third-Generation Photosensitizers. Photofrin has intrigued synthesis of a lot of other photosensitizers such as photoheme which is used to treat lung, skin, and breast cancer, and these are the first-generation photosensitizers [172–184]. Second-generation photosensitizers were developed so as to improve on first-generation photosensitizers. These photosensitizers are chemically pure and absorb light at around 650 nm, and they have relatively less skin photosensitivity. A lot of research has been conducted and shows that the sensitising efficiency of a compound increases with decreasing polarity [185]. The use of Photofrin has triggered the synthesis of more porphyrin-based photosensitizers mainly to produce the ideal photosensitizer. Numerous new porphyrin-based photosensitizers have been produced: first- and second-generation photosensitizers including hematoporphyrin monomethyl ether (HMME), photocarcinogen (PsD-007), second-generation hematoporphyrin derivatives (HiPorphyrin), and 5-ALA (aminolevulinic acid hydrochloride) [186]. The activation of a porphyrin and its derivatives by light triggers its relaxation to the ground state in three ways: nonradiative decay, emitting a photon, or by the transfer of energy [187–189]. Photofrin, which is the purified form of hematoporphyrin, was the first accepted photosensitizer for PDT, for the treatment of various cancers. Photofrin has certain properties required for an ideal photosensitizer but it has a few challenges; it has a weak long wavelength at 630 nm which is below the wavelength for maximum tissue penetration of deep tumors; secondly, it has a long photosensitivity to the skin. The surface of porphyrins can also be modified by different methods including surfactant-resistant, ionic, mixed porphyrin, sonic cation-assisted, and metal coordination self-assembly [190–192].

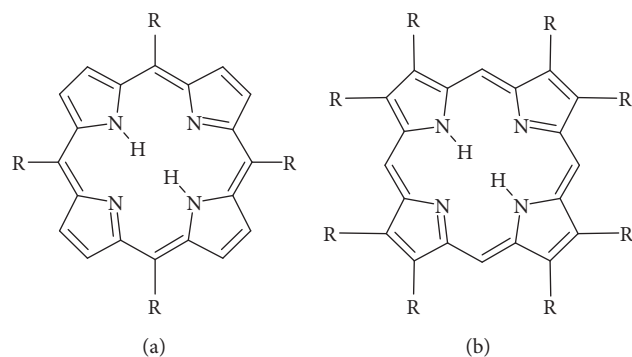


FIGURE 12: Structures of the (a) mesosubstituted and (b) β -substituted porphyrins.

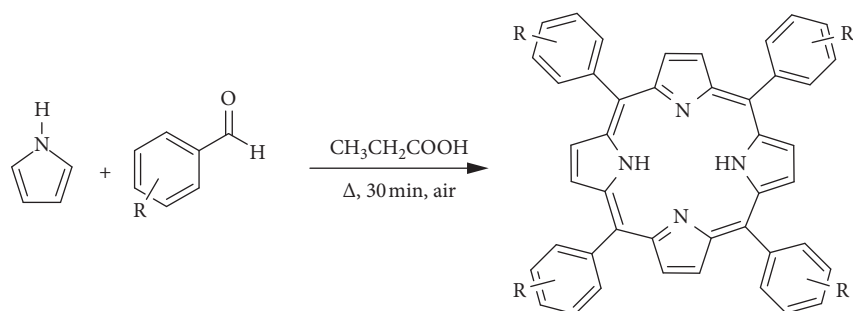


FIGURE 13: Synthesis of mesosubstituted tetraphenylporphyrin in open air [158].

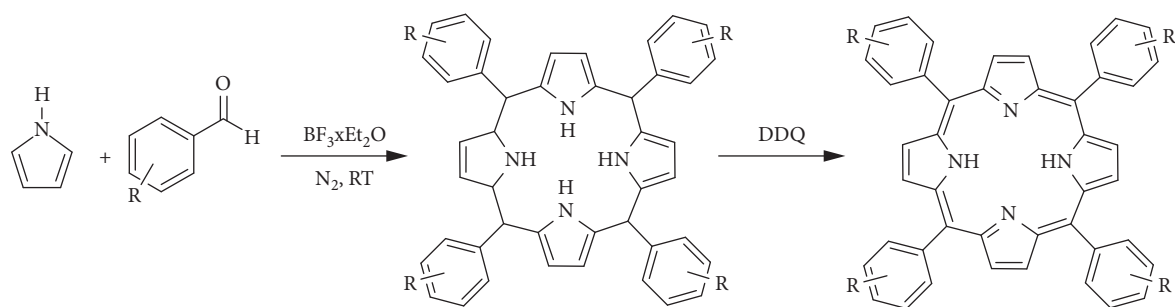


FIGURE 14: Schematic method as by Linsley in 1987 [159].

2.2.3. Modification of Porphyrins. Porphyrins can be modified by expanding their pi-electron conjugation. This is achieved by increasing the heterocyclic rings or bridging carbons around the porphyrin framework. The resulting chromophores absorb strongly in the red region, 650–800 nm as opposed to the 18 pi-electrons in normal porphyrins [193–195]. Modification to the porphyrin structure enhances the absorbing ability of the porphyrin; for example, the reduction of the ring produces a ring of chlorine which absorbs around 660 nm in the red spectra. This allows for the modulation of the light-activated analysis [196].

2.2.4. Porphyrin in Photosensitization. The use of two-photon imaging over conventional imaging has many advantages including the deeper light penetration, 3D image capability, low background fluorescence, and reduced damage to the surrounding tissue. The use of gold nanorods

as contrast agents of two-photon imaging is very essential due to the fact that they exhibit high two-photon luminescence which is 58x more than that of a rhodamic molecule [197, 198]. In the two-photon imaging, mesoporous silica nanoparticles have been used, so as to evade the shortcomings of photosensitizer delivery systems; they are used as carriers in chemical catalysis, drug delivery, and cell labelling. Mesoporous silica nanoparticles have high pore volume and surface area, hence ease for the production of singlet oxygen which is easily released from the matrix. The structures also show high biocompatibility and tolerance to most organic solvents; these compounds are also easily functionalized for targeting tumor cells *in vivo* [199–206].

2.2.5. Application of Porphyrins. The application of porphyrins is based on their peculiar characteristics including that they have rigid and planar geometries, photothermal,

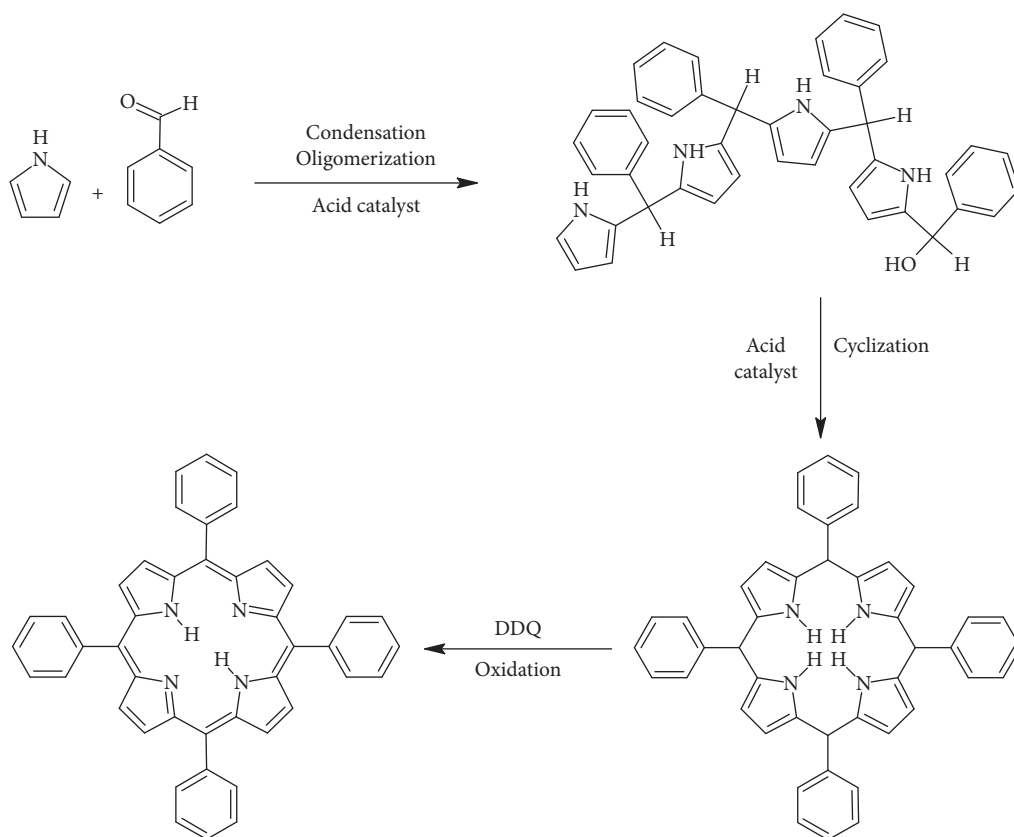


FIGURE 15: Reaction transformation from an aldehyde to a porphyrin.

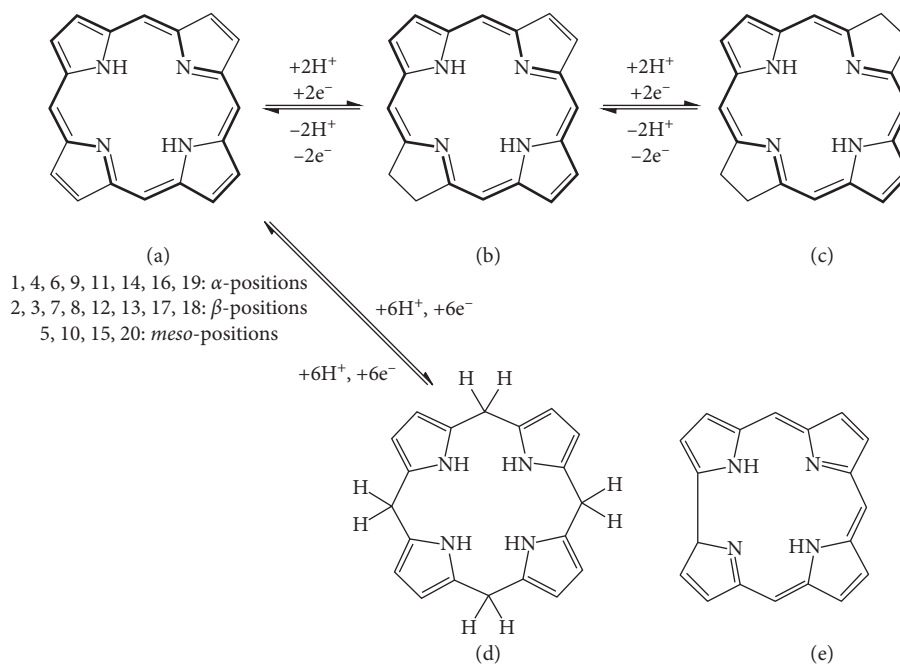


FIGURE 16: (d) The tetrapyrrole derivative porphynogen, a synthetic precursor of the porphyrin ligand. (a) Porphyrin. (b) Chlorin. (c) Bacteriochlorin. (d) Porphyrinogen. (e) Corrin.

and spectroscopic properties that can be tailored readily; they are multifunctional, biocompatible, and serve as electron donors [207, 208].

Photodynamic therapy is used for the treatment of tumor and malignant diseases. Its basis is on the administration of the photosensitizer which is followed by

irradiation of light at a specific wavelength, and this results in reactive species like radicals or singlet oxygen which ultimately destroy the tumor cells; this phenomenon is illustrated in Figure 17 [209]. The selectivity of PDT depends on the concentration of the photosensitizer, on the normal and tumor cells, and on the exposure to light of the side being treated [210].

New antibacterial approaches include the use of photosensitizers activated with visible light; as in PDT, the photosensitizers accumulate in microbial cells to induce phototoxic reactions. The excited PS in the triplet state in the presence of oxygen induces the production of reactive oxygen species (ROS), which then continually induces further reactions in the bacterial cell wall and the lipid membranes. Maich [211] reports that a specific photosensitizer with the ability to only target the bacteria without causing harm to the surrounding environment is still a challenge [212].

The low-dark toxicities of porphyrin macrocycles and the fact that porphyrins selectively localize on a wide range of tumors have led to them being one of the best photosensitizers relative to other macrocycles. Porphyrins and compounds based on porphyrins strongly absorb in the visible part of the optical spectrum; they are noncytotoxic in the dark, have high chemical stability, have high affinity for serum proteins, can be modified to have favorable pharmacokinetic properties, and are stable when complexed with different metals but still maintain their *in vivo* tumor localization properties [213, 214].

Most photosensitizers used in PDT and fluorescence diagnosis (FD) are based on the porphyrin structure because generally porphyrin accumulates on cancer cells as opposed to the surrounding nearby healthy cells and because their fluorescing properties are used for the detection of the cancer cells. Therapy resulting from the photosensitizers is based on the production of singlet oxygen when the photosensitizer is exposed to light. A major setback however for PDT is that it does not work best on distal metastasis [215].

Porphyrins and their analogs are adopted in many nanotechnologies due to their supramolecular design, flexibility, robustness, and unique photophysical and chemical properties and are used in technologies such as catalysts, sensors, molecular electronics and solar energy upconversion [216]. Porphyrins also have a visible light absorption and synthetic versatility, thus can be applied to the optoelectronics and act as photosensitizers [217]. Engelmann et al. [218] demonstrates the use of two cationic porphyrins to understand factors influencing the binding of the porphyrins to liposomes and mitochondria and how efficient their photodynamic reaction is in entocytes. The results showed that binding and photodynamic efficiency were inversely proportional to the number of positively charged groups but directly proportional to *n*-octanol/water partition coefficients [219, 220].

2.2.6. Encapsulation of Gold Nanorods with Porphyrins.

The use of nanoparticles has been very impressive, but when used by themselves, they pose certain shortcomings; for example, when entering the blood system, macrophages

and phagocytes readily passivate them leading to accumulation in the liver, spleen, and lymphatic system; this leads to toxicity, causes oxidative stress, and draws out an immune response [220]. Theranostic agents to be developed have to be the ones that contain both therapeutic and imaging properties. A lot of chemotherapeutic agents cannot be used as theranostic agents because they comprise less drug than the imaging doses; moreover, they are not tumor specific; antibodies on the other hand have the ability to be used as theranostic agents but they are relatively expensive. Porphyrins and derivatives however have the ability to fluoresce when excited by light, hence allowing for imaging before or after therapy; these molecules also allow for the attachment of tumor-targeting moieties at peripheral positions for the development of tumor-specific agents [221].

Porphyrins have a very rigid highly stable macrocyclic structure; hence, they are used as ligands in chemistry and biology; moreover when coordinated to metals, they give new characteristics. Metal-porphyrin chemistry is very important in biomimetic and chemical applications [222, 223]. The removal of the internal protons from the “free base” porphyrin gives a tetradentate chelating dianion molecule with an ability to coordinate a metal at the central cavity, as demonstrated in Figure 18. Research reports show that porphyrins can coordinate with lanthanides, some actinides, and a few main group metals [224].

Metals bounded to porphyrins can be in a range of oxidation states; $-2, -6, (d^0 - d^{10})$ spin; $S = 0$ to $S = 5/2$; and a coordination ranging from 4 to 8. Restriction on the metal coordinated with the porphyrin confines them to only have two mutually *trans*-coordination sites as shown in Figure 18 [225]. Peripheral substitution or enhancement of porphyrin is an approach for modifying the steric and electronic factors of metals but rearranging the meridional or facial types is not possible.

The versatility of the porphyrin ligand has led to a very large number of designed porphyrin complexes. Paths followed for the insertion or $M-L_n$ fragment have been explored and depend on the nature of the metal source. Reactions of porphyrins and metals can be of different paths which basically depend on the previous oxidation state of the metal and coordination, reduction, or oxidation of the metal.

The noncovalent interaction of porphyrins and their derivatives are very important in biological systems. Derivatives that possess a positive charge on the mesoposition interact well with DNA, nucleotides, and a lot of aromatic substrates [226]. Neutral porphyrins are reactive but the dications are inert. Metalloporphyrin reactions depend on a number of factors which influence the nature of the reaction, the rate at which the metal incorporates is decreased by the electron withdrawing group in the β -substituent and the solvent in use also influences the reactions [227].

Two photon-imaging systems have attracted a lot of research due to a number of advantages including the fact that there is enhanced penetration of light in the tissue or cells. The systems also have low fluorescence, and the photodamage on the living cells is reduced with their use. Using photodynamic therapy to treat cutaneous malignant

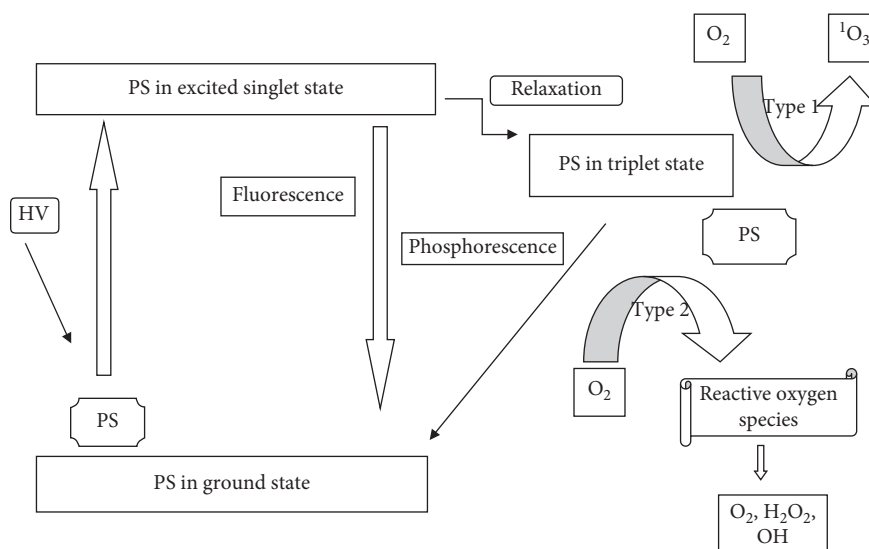


FIGURE 17: Schematic representation of a photosensitizer before and after excitation.

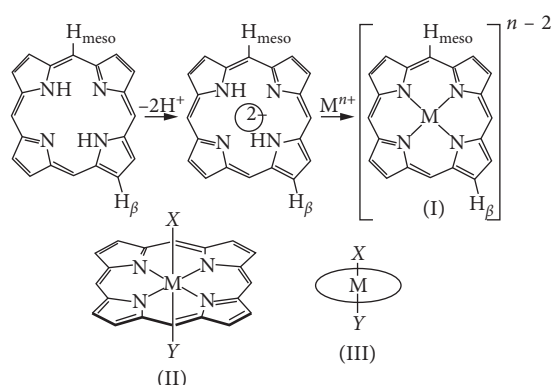


FIGURE 18: Schematic mechanism of a porphyrin complex presenting a tetra-coordinated metal in its tetrapyrrolic core. (i) Metal *trans*-coordinated to two ligands. (ii) Simplified presentation.

and intraperitoneal tumors has been researched to be one of the excellent pathways to use. The method however uses photosensitizers which currently have a lot of pitfalls, problems that can be solved by development of a new improved photosensitizer or enhancing the already existing ones. The aim will be to increase the cytotoxicity, selectivity, and protection against degradation.

The encapsulation of porphyrin with silica or an additional entity protects it from biological degradation. Multifunctional nanoparticles have been shown to produce more singlet oxygen than the porphyrin on its own. An example is illustrated by Zhao et al. [228] by using a two-photon imaging system with high photosensitisation and varying different image contrast agents, photosensitizers, and carriers. Here, a multifunctional nanocomposite (AuNRs/mSiO₂HP) was designed and used. The nanoparticles comprise a gold nanorod core with a porphyrin-doped mesoporous silica shell. Results included the fact that the triplet oxygen production was enhanced with the addition of the silica coating as opposed to pure porphyrins. These were

monitored by the incorporation of ADDBA (anthracenediyl-bis(methylene)dimalonic acid), which readily reacts with newly produced singlet oxygen to produce endoperoxide. Endoperoxide on the other hand decreases the ADDBA absorption which is around 350 nm. The absorption spectra of the composite material embedded with ADDBA can be seen in Figure 19 [228].

Research has shown that enhancing the surface of gold nanorods enables them to be versatile, hence can tune their properties to desired use. Using alkyl thiol to encapsulate the gold not only anchors the nanorod but also enhances the stability of the nanorod and fills the space potentially between the gold nanorod and bulky porphyrin molecule so as to provide space to insert C₆₀ fullness molecules which increase stability to the porphyrin-gold nanorod hybrid structure. Work done by Xue and colleagues [229] showed that protection of nanorods with a monolayer of thiols and porphyrins has very interesting result.

Modification of gold nanorods can also be done by incorporation of a porphyrin with an antitumor drug, for example, doxorubicin (DOX) used usually for the treatment of a number of cancers. The goal is to increase and improve on the multidrug resistance, nanotargeted delivery, and the toxicity of the drugs. Multifunctional nanocomposites of meso-tetrakis-(4-sulfonatophenyl) porphyrin (TPPS), gold nanorods, and DOX (DOX@TPPS-AuNRs) were synthesized by Bera and his colleagues [230]. The resulting composite material showed improved cellular uptake by the cells and showed no cell toxicity. Figure 20 [231] shows UV-Vis spectrum of the composite which significantly shows the SPR (surface plasmon resonance) of TPPS-AuNRs at 523 nm, and one of the pure AuNRs is at 525 nm in aqueous solution. The noticeable peak broadening was observed due to the presence of porphyrin which meant that there was a strong association of the gold surface to the porphyrin.

The excellent imaging and sensing properties shown by AuNRs qualify them as excellent for photothermal therapy; on the other hand, porphyrin and derivatives show excellent

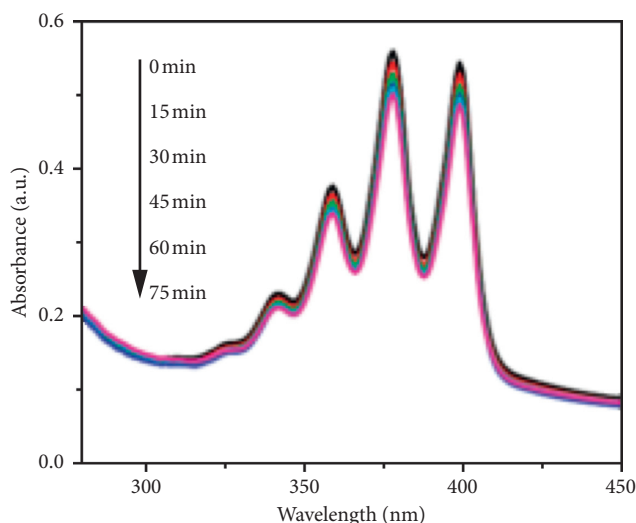


FIGURE 19: Graph showing a decrease in absorption of a composite AuNRs/mSiO₂/HP with ADDBA with increased illumination time.

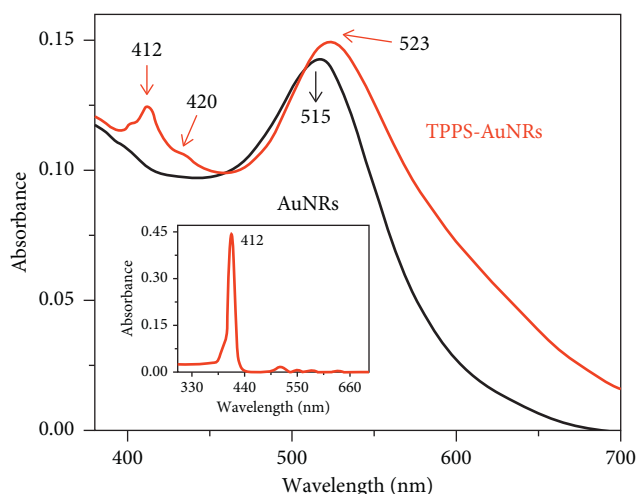


FIGURE 20: UV-Vis spectrum of TPPS-AuNRs and AuNRs.

properties as photosensitizers due to the fact that they have more than one absorption band in the near-infrared region; hence, they can be manipulated to be used to penetrate deeper into the tissue for photodynamic therapy. Photodynamic therapy shows minimal invasion to tissues while photothermal therapy is specific to tumor cells or affected area. Photodynamic therapy limitations are still major issues up to date especially based on singlet oxygen production, selectivity to the target tissue, and the concentration so as not to damage the normal cells [231].

The agglomeration of AuNRs with porphyrins is to increase the specificity and targeting. The system incorporates two modalities: the photothermal and photodynamic stability which will hence increase the chance of tumor and bacterial diseases to be treated. Incorporation of PTT and PDT as a dual technology for cancer and bacterial infections is likely to ensure selectivity and improved efficacy to the system. This study researches and further experiments

on both areas with a view to finding a more specific and less invasive combination technology.

2.3. Phototherapy

2.3.1. Applications of Photodynamic Therapy. Photodynamic therapy (PDT) is the use of a photosensitive agent on tissues to treat cancer or bacterial infections followed by photo-irradiation. This is a clinical treatment used in different diseases [12, 232–234]. It takes place by the administration of a photosensitizer in the body of a patient to accumulate on the tumor. The tumor is irradiated with biothermal light (500–650 nm), leading to an excited photosensitizer [149, 235]. Combination of the excited triplet photosensitizer and molecular oxygen results in a singlet oxygen [¹O₂] which is the main mediator of the destruction of the cell induced by PDT. The generation of the [¹O₂] has a very short life span and a limited diffusion rate, resulting in photo-oxidation of the tumor [236, 237]. A lot of photosensitizing agents have been formed but they have not been tested clinically due to factors such as (a) poor selectivity in terms of the target tissue and the healthy tissue, (b) the absorption spectra at short wavelengths, and (c) high accumulation rates in skin [236].

The use of photodynamic therapy extends to research of quantum dots, porphyrin, and micelles as photosensitizers. The discovery of PDT in the 1900s erupted as a cancer, HIV coronary heart, and psoriasis treatment agent [237–239]. PDT is a modal system which provides binary selectivity, which is accomplished by the increase in accumulation in the target tissue and limiting irradiation. The photosensitizer used in PDT has to be cytotoxic to damage only the affected tissue. An enhancement can be made by attachment to the part which has high affinity to the target tissue [240–243].

The tendency of a photosensitizer used in PDT to accumulate only in cancerous cells or tissue and not on the normal tissue is apparently explained by two reasons. It is taken up mostly by hyperproliferative cells than by normal resting cells, and their uptake by neovascular endothelial cells are accelerated, both of which characteristics can be seen in solid tumors [244, 245].

Photodynamic therapy is used to deactivate microorganisms by not leading to the selection of mutant-resistant chains compared to traditional antibiotics [246, 247]. The use of PDT has been improved by the incorporation of nanoparticles which have been used as delivery agents of the photosensitizer or to improve the inactivation kinetics.

Inorganic nanoparticles such as TiO₂ can also be used and have the capability of inactivating microorganisms [248]. Various developments of tumor target photodynamic therapy have been made; but until now, there is no universal approach due to spontaneous properties of tumors. For the ideal PDT development, the PDT has to be tailored, have an appropriate target strategy, and carefully select the tumor type and the stage of the disease [249].

Photodynamic therapy fundamentally relies on the accumulation of a photosensitizer of a tumor cell or tissue after administration [250, 251]. This phenomenon involves the

production of reactive oxygen and free radicals which are cytotoxic, and the main source of the photobiological activity is however the [$^1\text{O}_2$] which causes damage of cells either by apoptosis or necrosis [252, 253].

The use of supraparamagnetic iron oxide nanoparticles as MRI contrast agents for brain tissue has been proven very effective. Nanomaterials are used as delivery agents across the blood-brain barrier and to specifically transport drugs to cellular compartments such as the nucleus [254, 255].

Antimicrobial photodynamic therapy (aPDT) has been an effective treatment to damage bacteria. Enhancing antimicrobial photodynamic therapy (aPDT) with nanoparticles is a growing field to minimize the use of antibiotics to treat infectious diseases. The technology has many advantages including the increment of [$^1\text{O}_2$] yield of the photosensitizer [256]. A model was made by Hashimoto et al. [257] based on a burned wound and blood stream infection for the verification of aPDT. Two wavelengths were tested *in vitro*, blue and LEDs on a pathogen with resistance to antibiotics and using HB: La^{3+} as a photosensitizer. Experiments were also done *in vivo* on mice; both experiments proved that aPDT can be used in the treatment of bacteria in burned patients using PDT [258].

2.3.2. Mechanism of PDT Cytotoxicity. Singlet oxygen has a relatively short lifetime (see Figure 15), i.e., 810–320 nanoseconds, thereby making its diffusion to be limited to 10–55 nm in cells, the implication being that cells only near the photosensitizer will be damaged [259, 260].

2.3.3. Photodynamic Therapy Using Porphyrin. Photodynamic therapy is the recommended method to treat cancer in the developing countries due to its relative inexpensiveness and user-friendliness [260]. In addition, Chen and Zhang [261] proposed an innovation in which luminescent nanoparticles *in vivo* were used instead of supporting the PDT with external light. The use of these nanoparticles apparently reduces potential damage to the surrounding healthy cells with reasonable costs. The method normally combines both radiotherapy and photodynamic therapy through the attachment of luminescent nanoparticles with photosensitizers such as porphyrin [262]. No external light source is required for this treatment but rather exposure of the photosensitizer to ionizing radiation. The combination enhances the efficiency to damage cancer cells and reduce radiation. Nonetheless, the radiation has to be sufficient enough to produce enough light for PDT, and the prediction of level radiation is usually difficult [263, 264].

2.3.4. Applications of Photothermal Therapy. Photothermal therapy (PTT) is a treatment minimally invasive which occurs by conversion of photon energy to heat energy [265]. The selectivity of the therapy is obtained by the control of incident radiation used and accompanied by the conduct of some proactive molecules or nanoparticles. The photoexcitation relaxation of the particles induces heat transfer to the surrounding affected environment [266, 267].

Nanomaterials with photothermal effects are of great interest to researchers especially in the biological imaging and therapeutics. Nanorods and nanocages possess photothermal properties, hence their use in MRI imaging, infrared thermal imaging, and photothermal ablation of cancer tissues [19, 268–274].

2.3.5. Photothermal Therapy Using Gold Nanorods. Gold nanorods (AuNRs) attracted researchers due to their easy and quick synthesis and simplified bioconjugation, high and strong absorption through their cross-section, and the fact that their optical extinction is tuneable [275–279]. Varying the aspect ratios of the AuNRs influences longitudinal plasmon absorbance shift throughout the visible region [95, 280–285]. AuNRs scatter light through paths of extensive elastic scattering and intensive light scattering of molecular vibrations near the metal surface. The effect is called surface-enhanced Raman scattering (SERS) which is a result of oscillations around the nanoparticle upon radiation [286–289]. These phenomena qualified gold nanorods as chemical sensors as indicated in Figure 21.

In addition, many researchers used gold nanorods as photothermal agents to damage *Pseudomonas aeruginosa*, a Gram-negative pathogen [291–295]. Their work represented gold nanorods which absorbed light at 785 nm and were conjugated to antibodies specific to bacteria. The results positively indicated 75% destruction of infected cells.

2.3.6. Photothermal and Photodynamic Therapy. Recent research has been on nanocomposites based on plasmonic nanoparticles and fluorescent or photodynamic dyes. These are then used for simultaneous therapy and diagnosis [95, 282, 283]. Metal nanoparticles used in the methods are combined with photodynamic drugs using cross-linking procedures or by the use of electrostatic interactions [296–300].

The combination for simultaneous therapeutic purposes was fairly researched. Teretyvk et al. [301] incorporated PDT and PTT by the use of fabricated AuNRs/ SiO_2 -HP composite nanoparticles which successfully decreased large tumor volumes and to damaged solid tumor cells, using the steps (see Figure 22) to fabricate the gold nanorod. On the other hand, Liu et al. [303] synthesized MoS_2 nanosheets which are water-soluble and functionalized them with lipoic acid terminated polyethylene glycol (LA-PEG) to obtain MoS_2 -PEG. These are apparently stable in physiological solutions and also have the ability to be loaded with photosensitizers. Results of the nanocomposites formed using Ce_6 as a photosensitizer in PTT and PDT *in vivo* showed an enhanced tumor necrosis. Jang et al. [304, 305] proposed that for PTT and PDT to work effectively, the distance between the gold nanorod and the photosensitizer must be manipulated. They used an AuNRs- AlPcS_4 composite, and his results proved that the nanocomposite was effective for NIR fluorescence imaging for affected cancer sites and to improve *in vivo* therapeutic efficacy [298, 306–310].

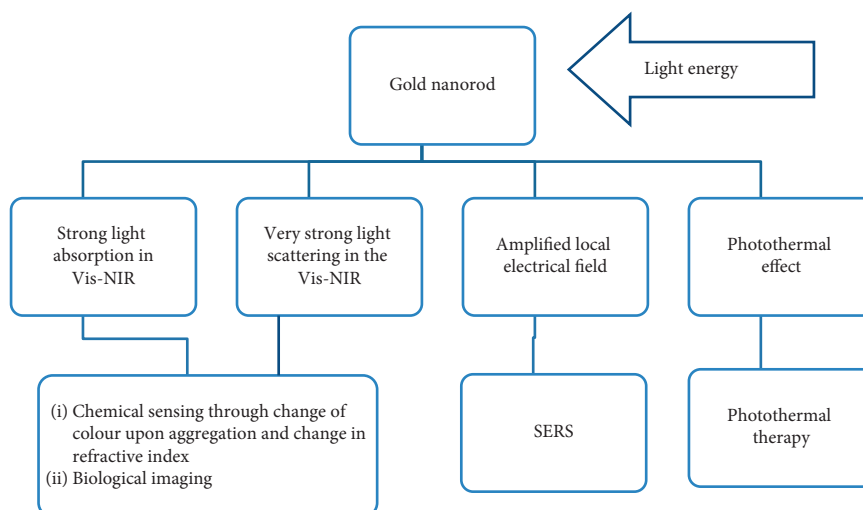


FIGURE 21: AuNRs effects and applications [290].

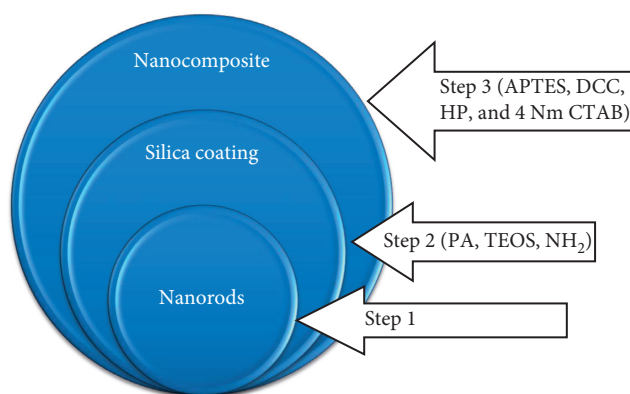


FIGURE 22: Scheme of the fabrication of AuNRs/SiO₂-HP. IPA, isopropyl alcohol; TEOS, tetraethyl orthosilicate; APTES, 3-aminopropyltriethoxysilane; HP, hematoporphyrin; DCC, dicyclo-carbodiimide; CTAB, cetyltrimethylammonium bromide [302].

3. Conclusions and Future Developments

The excellent imaging and sensing properties shown by gold nanorods qualify them as excellent for photothermal therapy. On the other hand, porphyrin and derivatives show excellent properties as photosensitizers due to the fact that they have more than one absorption band on the near-infrared region; the phenomena allow for the penetration deeper into the tissue, and hence, they have excellent use in photodynamic therapy. Photodynamic therapy shows minimal invasion to tissues while photothermal therapy is specific to tumor cells or affected area.

Photodynamic therapy limitation is still an issue up to date especially based on singlet oxygen production, selectivity to the target tissue, and the concentration so as not to damage the normal cells. Despite efforts of several researchers, an ideal photosensitizer is still not discovered, one that is safe and selective and the other that does not cause skin photosensitivity and pain. Many photosensitizers used recently have very low water solubility and tend to aggregate

under physiological conditions; moreover for clinical applications, the target tissue is still not recognised.

Incorporation of PTT and PDT as a dual technology for cancer and bacterial infections ensures selectivity and improved efficacy to the system. Previous attempts have been made using and varying different porphyrin or derivatives for photodynamic therapy or using different noble metals or carbon nanotubes for photothermal therapy or incorporating the two therapies but no ideal photosensitizer or an ideal specific drug which damages only the cancer cells has been discovered. This review is aimed at giving and overviewing of the studies made on the application of photothermal and photodynamic therapy by encapsulating gold nanorods with porphyrin for better cancer and bacterial therapy. A thorough research and further experimentation will be made on both so as to find a more specific and less invasive technology.

Conflicts of Interest

The authors declare that they have no conflicts of interest.

References

- [1] P. a. Ma, H. Xiao, C. Li et al., "Inorganic nanocarriers for platinum drug delivery," *Materials Today*, vol. 18, no. 10, pp. 554–564, 2015.
- [2] F. Foroutan, N. H. de Leeuw, R. A. Martin et al., "Novel sol-gel preparation of (P₂O₅)_{0.4} - (CaO)_{0.25} - (Na₂O)_x - (TiO₂)_(0.35-x) bioresorbable glasses (X = 0.05, 0.1, and 0.15)," *Journal of Sol-Gel Science and Technology*, vol. 73, no. 2, pp. 434–442, 2015.
- [3] Y. Wang and Y. Sun, "Insulin-like growth factor receptor-1 as an anti-cancer target: blocking transformation and inducing apoptosis," *Current Cancer Drug Targets*, vol. 2, no. 3, pp. 191–207, 2002.
- [4] G. Barrera, "Oxidative stress and lipid peroxidation products in cancer progression and therapy," *ISRN Oncology*, vol. 2012, Article ID 137289, 21 pages, 2012.
- [5] J. Abtahi, F. Agholme, O. Sandberg, and P. Aspenberg, "Effect of local vs. systemic bisphosphonate delivery on

- dental implant fixation in a model of osteonecrosis of the jaw," *Journal of Dental Research*, vol. 92, no. 3, pp. 279–283, 2013.
- [6] A. Accardo, D. Tesaro, and G. Morelli, "Peptide-based targeting strategies for simultaneous imaging and therapy with nanovectors," *Polymer Journal*, vol. 45, no. 5, pp. 481–493, 2013.
- [7] I. Ramos-Álvarez, P. Moreno, S. A. Mantey et al., "Insights into bombesin receptors and ligands: highlighting recent advances," *Peptides*, vol. 72, pp. 128–144, 2015.
- [8] S. Medici, M. Peana, V. M. Nurchi, J. I. Lachowicz, G. Crisponi, and M. A. Zoroddu, "Noble metals in medicine," *Coordination Chemistry Reviews*, vol. 284, pp. 29–350, 2015.
- [9] M. J. Akhtar, M. Ahamed, H. A. Alhadlaq, S. A. Alrokayan, and S. Kumar, "Targeted anticancer therapy: overexpressed receptors and nanotechnology," *Clinica Chimica Acta*, vol. 436, pp. 78–92, 2014.
- [10] A. Accardo, L. Aloj, M. Aurilio, G. Morelli, and D. Tesaro, "Receptor binding peptides for target-selective delivery of nanoparticles encapsulate drugs," *International Journal of Nanomedicine*, vol. 9, pp. 1537–1557, 2014.
- [11] M. Singh, D. C. C. Harris-Birtill, Y. Zhou et al., "Application of gold nanorods for photothermal therapy in *ex vivo* human oesophagogastric adenocarcinoma," *Journal of Biomedical Nanotechnology*, vol. 12, no. 3, pp. 481–490, 2016.
- [12] R. Van De Meel, T. Lammers, and W. E. Hennink, "Cancer nanomaterials: oversold or unappreciated?," *Expert Opinion Drug Delivery*, vol. 14, no. 1, pp. 1–5, 2016.
- [13] D. Pissuwan, T. Niidome, and M. B. Cortie, "The forthcoming applications of gold nanoparticles in drug and gene delivery systems," *Journal of Controlled Release*, vol. 149, no. 1, pp. 65–71, 2008.
- [14] A. K. Khan, R. Rashid, G. Murtaza, and A. Zahra, "Gold nanoparticles: synthesis and application in drug delivery," *Journal of Pharmacy Research*, vol. 13, no. 7, pp. 1169–1174, 2014.
- [15] A. O. Oladipo, O. S. Oluwafemi, S. P. Songca et al., "A novel treatment for metastatic lymph nodes using lymphatic delivery and photothermal therapy," *Scientific Reports*, vol. 3, no. 7, p. 45459, 2017.
- [16] J. Ohyama, K. Hitomi, Y. Yasuhiro et al., "One-phase synthesis of small gold nanoparticles coated by a horizontal porphyrin monolayer," *Chemical Communications*, vol. 47, pp. 6300–6302, 2008.
- [17] D. Camestratic, *Synthesis of Polyheteroatomic Heterocycles; Relevance in Microwave Assisted Reactions*, Instituto Superior Técnico, Universidade Técnica de Lisboa, Lisbon, Portugal, 2014.
- [18] L. P. Cook, G. Brewer, and W. Wong-Ng, "Structural aspects of porphyrins for functional materials applications," *Crystals*, vol. 7, no. 7, pp. 1–22, 2017.
- [19] X. Huang, I. H. El-Sayed, W. Qian, and M. A. El-Sayed, "Cancer cell imaging and photothermal therapy in the near infra-red region by using gold nanorods," *Journal of the American Chemical Society*, vol. 128, no. 6, pp. 2115–2120, 2006.
- [20] A. Brioude, X. C. Jiang, and M. P. Pileni, "Structural aspects of porphyrins for functional materials applications," *Crystals*, vol. 109, no. 27, pp. 13138–13142, 2005.
- [21] X. Huang, S. Neretina, and M. A. El-Sayed, "Gold nanorods: from synthesis and properties to biological and biomedical application," *Advanced Materials*, vol. 21, no. 48, pp. 4880–4910, 2009.
- [22] H. Liang, H. Tian, M. Deng, and X. Chen, "Gold nanoparticles for cancer theranostics," *Chinese Journal of Chemistry*, vol. 33, no. 9, pp. 1001–1010, 2015.
- [23] G. Awah and Y. You, "Boron dipyrromethane (BODIPY)-based photosensitizers for photodynamic therapy," *RSC Advances*, vol. 2, pp. 11169–11183, 2012.
- [24] P. Wolf, E. Rieger, and H. Kerl, "Topical photodynamic therapy with endogenous porphyrins after applications of S-aminoleulinic acid," *Journal of the American Academy of Dermatology*, vol. 28, pp. 17–21, 1995.
- [25] Z. Song, A. O. Adeyemo, J. Baker et al., "Structure of porphyrin TPPS4 and its interaction with metal ions as elucidated by ¹H NMR and UV-visible spectra," *Georgia Journal of Science*, vol. 69, no. 2-3, pp. 89–101, 2011.
- [26] J. Winther, "Porphyrin photodynamic therapy in an experimental retinoblastoma model," *Ophthalmic Paediatric Genet*, vol. 8, no. 1, pp. 49–52, 1997.
- [27] V. Delic, J. W. D. Griffin, S. Zivkovic et al., "Individual amino acid supplementation can improve energy metabolism and decrease ROS production in neuronal cells overexpressing alpha-synuclein," *Neuromolecular Medicine*, vol. 19, no. 2-3, pp. 322–344, 2017.
- [28] R. W. Wagner, "Synthesis and excited-state photodynamics of a molecular square containing four mutually coplanar porphyrins," *Journal of Organic Chemistry*, vol. 63, no. 15, pp. 5042–5049, 1998.
- [29] D. Fenyo, B. T. Chait, T. E. Johnson, and J. S. Lindsey, "Laser desorption mass spectrometry of synthetic multiporphyrin arrays," *Journal of Porphyrins and Phthalocyanines*, vol. 1, no. 1, pp. 93–99, 1997.
- [30] E. C. A. Ojadi, H. Linschitz, M. Gouterman et al., "Sequential protonation of meso-(dimethylamino)phenyl porphyrins: charge-transfer excited states producing hyperporphyrins," *Journal of Physical Chemistry*, vol. 97, no. 50, pp. 13192–13197, 1993.
- [31] J. Li, A. Ambrose, S. I. Yang et al., "Template-directed synthesis, excited-state photodynamics, and electronic communication in a hexameric wheel of porphyrins," *Journal of the American Chemical Society*, vol. 121, no. 38, pp. 8927–8940, 1999.
- [32] S. Jain, D. G. Hirst, and J. M. O'Sullivan, "Gold nanoparticles as novel agents for cancer therapy," *British Journal of Radiology*, vol. 85, no. 1010, pp. 101–113, 2012.
- [33] W. Cai, T. Gao, H. Hong et al., "Applications of gold nanoparticles in cancer nanotechnology," *Nanotechnology*, vol. 1, pp. 17–32, 2008.
- [34] M. Marsh, E. Schelew, S. Wolf et al., "Gold nanoparticles for cancer treatment," *Physics*, pp. 1–9, 2009.
- [35] P. K. Jain, I. H. EL-Sayed, and L. A. EL-Sayed, "Au nanoparticles target cancer," *Nano Today*, vol. 2, no. 1, pp. 18–29, 2007.
- [36] S. Link and M. A. El-Sayed, "Shape and size dependence of radiative, non-radiative and photothermal properties of gold nanocrystals," *International Reviews in Physical Chemistry*, vol. 19, no. 3, pp. 409–453, 2000.
- [37] M. K. Yu, J. Park, and S. Jon, "Targeting strategies for multifunctional nanoparticles in cancer imaging and therapy," *Theranostics*, vol. 2, no. 1, pp. 1–42, 2012.
- [38] O. V. Salata, "Applications of nanoparticles in biology and medicine," *Journal of Nanobiotechnology*, vol. 2, p. 3, 2004.
- [39] W. H. De Jong and P. J. A. Borm, "Drug delivery and nanoparticles: applications and hazards," *International Journal of Nanoscience*, vol. 3, no. 2, pp. 133–149, 2008.

- [40] J. Conde, G. Doria, and P. Baptista, "Nobel metal nanoparticles applications in cancer," *Journal of Drug Delivery*, vol. 2012, Article ID 751075, 12 pages, 2012.
- [41] H. C. Huang, S. Barua, G. Sharma, S. K. Dey, and K. Rege, "Inorganic particles for cancer imaging and therapy," *Journal of Controlled Release*, vol. 155, no. 3, pp. 344–357, 2011.
- [42] M. P. Melancon, M. Zhou, and C. Li, "Cancer theranostics with near-infrared light-activatable multinodal nanoparticles," *Accounts of Chemical Research*, vol. 44, no. 10, pp. 947–956, 2011.
- [43] C. D. Chen, S. F. Cheng, L. K. Chau, and C. R. Chris Wang, "Sensing capability of localized surface plasmon resonance of gold nanorods," *Biosensors & Bioelectronics*, vol. 22, no. 6, pp. 926–932, 2007.
- [44] W. Lu, H. Wang, J. Zhang et al., "Gold nanorods: synthesis growth mechanism and purification," *Process Chemistry*, vol. 27, pp. 785–793, 2015.
- [45] H. Takahashi, T. Niidome, A. Nariai, Y. Niidome, and S. Yamada, "Gold nanorod: sensitized cell-death microscopic observation of single living cells irradiated by pulsed near-infrared laser light in the presence of gold nanorods," *Chemistry Letters*, vol. 35, no. 5, pp. 500–502, 2006.
- [46] J. W. Hotchkiss, A. B. Lowe, and S. G. Boyes, "Surface modification of gold nanorods with polymers synthesized by reversible addition-fragmentation chain transfer polymerization," *Chemistry of Materials*, vol. 19, no. 1, pp. 6–13, 2007.
- [47] R. Narayanan, "Nanoparticles of different shapes for biosensor applications. Functional nanoparticles for bioanalysis," *Nanomedicine, and Bioelectronic Devices*, vol. 1, pp. 281–292, 2012.
- [48] G. Doria, J. Conde, B. Veigas et al., "Noble metal nanoparticles for biosensing applications," *Sensors*, vol. 12, no. 2, pp. 1657–1687, 2012.
- [49] M. Holzinger, A. Goff, and S. Cosnier, "Nanomaterials for biosensing applications: a review," *Frontiers in Chemistry*, vol. 2, pp. 63–66, 2014.
- [50] A. Ahmed, M. Ahamad, L. B. Swami, and S. Ikram, "A review on plants extract mediated synthesis of silver nanoparticles for antimicrobial applications: a green expertise," *Journal of Advanced Research*, vol. 7, no. 1, pp. 17–28, 2016.
- [51] W. Chen, S. Zhang, Y. Yu, H. Zhang, and Q. He, "Structural-engineering rationales of gold nanoparticles for cancer theranostic," *Advanced Materials*, vol. 28, no. 39, pp. 8567–8585, 2016.
- [52] Z. Zhang, J. Wang, and C. Chen, "Gold nanorods based platforms for light-mediated theranostic," *Theranostics*, vol. 3, no. 3, pp. 223–239, 2012.
- [53] D. Sharma, S. Kanchi, and K. Bisetty, "Biogenic synthesis of nanoparticles," *Arabian Journal of Chemistry*, vol. 11, pp. 1–25, 2015.
- [54] Q. Zhang, N. Iwakuma, P. Sharma et al., "Gold nanoparticles as a contrast agent for in-vivo tumor imaging and photoacoustic tomography," *Nanotechnology*, vol. 20, no. 39, pp. 1–9, 2009.
- [55] M. Sguizzato, E. Esposito, M. Drechsler et al., "Nanotechnology containing solid lipid nanoparticles as a tool for anticancer drug delivery: preliminary studies," *Journal of Chemistry*, vol. 2017, Article ID 3206298, 6 pages, 2017.
- [56] M. I. Tomey, J. Narula, and J. C. Kovacic, "Advances in the understanding of plaque composition and treatment options," *Journal of the American College of Cardiology*, vol. 63, no. 16, pp. 1604–1606, 2014.
- [57] S. W. Prescott and P. Mulvaney, "Gold nanorod extinction spectra," *Journal of Applied Physics*, vol. 99, no. 103, pp. 1–8, 2008.
- [58] E. K. Payne, K. L. Shuford, S. Park, G. C. Schatz, and C. A. Mirkin, "Multipole plasmon resonances in gold nanorods," *Journal of Physical Chemistry*, vol. 110, no. 5, pp. 2150–2154, 2006.
- [59] M. Liu, P. H. Yang, and J. Y. Cai, "Optical properties and biomedical application of gold nanorods," *Microbiology and Immunology*, vol. 36, no. 11, pp. 1402–1407, 2009.
- [60] K. Park, S. Biswas, S. Kanel, D. Nepal, and R. A. Vaia, "Engineering the optical properties of gold nanorods: independent tuning of surface plasmon energy, extinction coefficient, and scattering cross section," *Journal of Physical Chemistry*, vol. 118, no. 11, pp. 5918–5926, 2014.
- [61] A. M. Funston, C. Novo, T. J. Davis, and P. Mulvaney, "Plasmon coupling of gold nanorods at short distances in different geometries," *Nano Letters*, vol. 9, no. 4, pp. 1651–1658, 2009.
- [62] T. Ye, Z. Dai, F. Mei et al., "Synthesis and optical properties of gold nanorods with controllable morphology," *Journal of Physics: Condensed Matter*, vol. 28, no. 43, article 434002, 2016.
- [63] Y. Liu, E. N. Mills, and R. J. Composto, "Tuning optical properties of gold nanorods in polymer films through thermal reshaping," *Journal of Materials Chemistry*, vol. 19, no. 18, pp. 2704–2709, 2009.
- [64] Y. R. Toh, P. Yu, X. Wen, J. Tang, and T.-s. Hsieh, "Induced pH-dependent shift by local surface plasmon resonance in functionalized gold nanorods," *Nanoscale Research Letters*, vol. 8, no. 1, p. 103, 2013.
- [65] C. A. Peng and S. Pachpinde, "Longitudinal plasmonic detection of glucose using gold nanorods," *Nanomaterials and Nanotechnology*, vol. 4, no. 9, pp. 1–5, 2013.
- [66] B. Sadeghi, *Synthesis and Application of Nanorods: Nanotechnology and Nanomaterials*, Chapter 6, IntechOpen, London, UK, 2012.
- [67] P. Wang, M. Liu, G. Gao et al., "From gold nanorods to nanodumbbells: a different way to tailor surface plasmon resonances by a chemical route," *Journal of Materials Chemistry*, vol. 22, pp. 24006–24011, 2012.
- [68] S. K. Sharma, P. Mroz, T. Dai, Y.-Y. Huang, T. G. S. Denis, and M. R. Hamblin, "Photodynamic therapy for cancer and for infections: what is the difference?," *Israel Journal of Chemistry*, vol. 52, no. 8-9, pp. 691–705, 2012.
- [69] L. Feng, Z. Xuana, J. Mac et al., "Preparation of gold nanorods with different aspect ratio and the optical response to solution refractive index," *Journal of Experimental Nanoscience*, vol. 10, no. 4, pp. 258–26, 2015.
- [70] E. T. Castellana, R. C. Gamez, M. E. Gómez, and D. H. Russell, "Longitudinal surface plasmon resonance based gold nanorod biosensors for mass spectrometry," *Langmuir*, vol. 26, no. 8, pp. 6066–6070, 2010.
- [71] T. A. El-Brollosy, T. Abdallah, M. B. Mohamed et al., "Shape and size dependence of the surface plasmon resonance of gold nanoparticles studied by photoacoustic technique," *European Physical Journal Special Topics*, vol. 153, no. 1, pp. 361–364, 2008.
- [72] A. Sambou, P. D. Tall, K. Talla et al., "Control of the surface plasmon resonance of two configurations of nanoparticles: simple gold nanorod and gold/silica core/shell," *Nanoscience and Nanotechnology Research*, vol. 4, no. 1, pp. 1–6, 2017.

- [73] N. Thioune, N. Lidgi-Guigui, M. Cottat et al., "Study of gold nanorods-protein interaction by localized surface plasmon resonance spectroscopy," *Gold Bulletin*, vol. 46, no. 4, pp. 275–281, 2013.
- [74] J. Cao, T. Sun, and K. T. V. Grattan, "Gold nanorod-based localized surface plasmon resonance biosensors: a review," *Sensors and Actuators B: Chemical*, vol. 195, pp. 332–351, 2014.
- [75] S. Jayabal, A. Pandikumar, H. N. Lim, R. Ramaraj, T. Sun, and N. M. Huang, "A gold nanorod-based localized surface plasmon resonance platform for the detection of environmentally toxic metal ions," *Analyst*, vol. 140, no. 8, pp. 2540–2555, 2015.
- [76] J. Tao, L. Yong-Hua, Z. Rong-Sheng et al., "Effect of aspect ratio distribution on localized surface plasmon resonance extinction spectrum of gold nanorods," *Chinese Physics Letters*, vol. 25, no. 12, pp. 1–4, 2008.
- [77] V. S. Marangoni, J. Cancino-Bernardi, and V. Zucolotto, "Synthesis, physico-chemical properties and biomedical applications of gold nanorod—a review," *Journal of Biomedical Nanotechnology*, vol. 12, no. 6, pp. 1136–1158, 2016.
- [78] B. M. Geilich, A. L. van de Ven, G. L. Singleton, L. J. Sepúlveda, S. Sridhar, and T. J. Webster, "Silver nanoparticle-embedded polymersome nanocarriers for the treatment of antibiotic-resistant infections," *Nanoscale*, vol. 7, no. 8, pp. 3511–3519, 2015.
- [79] H. Takahashi, Y. Niidome, T. Niidome, Y. Niidome, and S. Yamada, "Photothermal reshaping of gold nanorods prevents further cell death," *Langmuir*, vol. 17, no. 17, pp. 4431–4435, 2006.
- [80] L. Vigderman, B. P. Khanal, and E. R. Zubarev, "Functional gold nanorods: synthesis, self-assembly, and sensing applications," *Advanced Materials*, vol. 24, no. 36, p. 5016, 2012.
- [81] Y. Wang, K. C. L. Black, H. Luehmann et al., "Comparison study of gold nano hexapods, nanorods and nanocases for photothermal cancer treatment," *ACS Nano*, vol. 7, no. 3, pp. 2068–2077, 2013.
- [82] J. Li, B. Zhu, Z. Zhu et al., "Simple and rapid functionalization of gold nanorods with oligonucleotides using an mPEG-SH/tween 20-assisted approach," *Langmuir*, vol. 31, no. 28, pp. 7869–7876, 2015.
- [83] R. M. Pallares, X. Su, S. H. Lim et al., "Fine-tuning gold nanorod dimensions and plasmonic properties using the Hofmeister effects," *Journal of Materials Chemistry C*, vol. 00, no. 1, pp. 1–3, 2015.
- [84] K. Liu, Y. Zheng, X. Lu et al., "Biocompatible gold nanorods: one-step surface functionalization, highly colloidal stability, and low cytotoxicity," *Langmuir*, vol. 31, no. 17, pp. 4973–4980, 2015.
- [85] R. G. Rayavarapu, W. Petersen, L. Hartsuiker et al., "In vitro studies of polymer-coated gold nanorods," *Nanotechnology*, vol. 21, no. 14, article 145101, 2015.
- [86] Z.-C. Xu, C.-S. Shen, C.-W. Xiao et al., "Wet chemical synthesis of gold nanoparticles using silver seeds: a shape control from nanorods to hollow spherical nanoparticles," *Nanotechnology*, vol. 18, no. 11, pp. 115608–115613, 2007.
- [87] B. D. Busbee, S. O. Obare, and C. J. Murphy, "An improved synthesis of high-aspect-ratio gold nanorods," *Advanced Materials*, vol. 15, no. 5, pp. 414–416, 2003.
- [88] D. P. Sprünken, H. Omi, K. Furukawa et al., "Influence of the local environment on determining aspect distribution of gold nanorods," *Journal of Physical Chemistry*, vol. 111, no. 39, pp. 14299–14306, 2007.
- [89] L. Scarabelli, A. Sánchez-Iglesias, J. Pérez-Juste et al., "A 'Tips and Tricks' practical guide to the synthesis of gold nanorods," *Journal of Physical Chemistry Letters*, vol. 6, no. 21, pp. 4270–4279, 2015.
- [90] P. Wattanakull, MC Killingsworth, and D. Pissuwan, "Biological responses of T cells encapsulated with poly-electrolyte-coated gold nanorods and their cellular activities in a co-culture system," *Applied Nanoscience*, vol. 7, no. 8, pp. 667–679, 2017.
- [91] H. Takahashi, T. Niidome, A. Nariai, Y. Niidome, and S. Yamada, "Photothermal reshaping of gold nanorods prevents further cell death," *Nanotechnology*, vol. 17, no. 17, pp. 4431–4435, 2006.
- [92] C. Kinnear, D. Burnand, M. J. Clift, A. F. M. Kilbinger, B. Rothen-Rutishauser, and A. Petri-Fink, "Polyvinyl alcohol as a biocompatible alternative for the passivation of gold nanorods," *Journal of the American Chemical Society*, vol. 53, no. 46, pp. 12613–12617, 2014.
- [93] J. Stone, S. Jackson, and D. Wright, "Biological applications of gold nanorods," *Wiley Interdisciplinary Reviews: Nanomedicine and Nanobiotechnology*, vol. 3, no. 1, pp. 100–110, 2011.
- [94] T. A. Larson, B. James, A. Jesse, and K. Sokolov, "Hybrid plasmonic magnetic nanoparticles as molecular specific agent for MRI/optical imaging and photothermal therapy of cancer cells," *Nanotechnology*, vol. 18, no. 32, pp. 1–9, 2007.
- [95] A. Gole and C. J. Murphy, "Seed-mediated synthesis of gold nanorods: role of the size and nature of the seed," *Chemistry of Materials*, vol. 16, no. 19, pp. 3633–3640, 2004.
- [96] O. S. Oluwafemi, "Synthesis of gelatin stabilized high aspect ratio gold nanorods with enhanced biological stability as effective photothermal agents for cancer therapy," *Trends in Green Chemistry*, vol. 3, no. 3, p. 1, 2017.
- [97] H. Ke, J. Wang, Z. Dai et al., "Gold-nanoshelled microcapsules: theranostic agent for ultrasound contrast imaging and photothermal therapy," *Angewandte Chemie International Edition*, vol. 50, no. 13, pp. 3017–3021, 2011.
- [98] J. Becker, I. Zins, A. Jakab, Y. Khalavka, O. Schubert, and C. Sönnichsen, "Plasmonic focusing reduces ensemble linewidth of silver-coated gold nanorods," *Nano Letters*, vol. 8, no. 6, pp. 1719–1723, 2008.
- [99] H. S. Ali, S. Ahmed, and G. A. Khan, "Gold nanoparticles in cancer therapy and diagnosis," *Pharmaceutical Research*, vol. 28, no. 2, pp. 237–259, 2011.
- [100] A. Fernandez-Fernandez, R. Manchanda, and A. J. McGoron, "Theranostic applications of nanomaterials in cancer: drug delivery, image-guided therapy and multifunctional platforms," *Applied Biochemistry and Biotechnology*, vol. 165, no. 7–8, pp. 1628–1651, 2011.
- [101] F. Geng, K. Song, and J. Z. Xing, "Thio-glucose bound gold nanoparticles enhance radio-cytotoxic targeting of ovarian cancer," *Nanotechnology*, vol. 22, no. 28, article 285101, 2011.
- [102] T. Wolfe, D. Chatterjee, J. Lee et al., "Targeted gold nanoparticles enhance sensitization of prostate tumors to megavoltage radiation therapy in vivo," *Nanotechnology*, vol. 11, no. 5, pp. 1277–1283, 2015.
- [103] W. Xu, T. Luo, P. Li et al., "RGD-conjugated gold nanorods induce radiosensitization in melanoma cancer cells by downregulating $\alpha_v\beta_3$ expression," *International Journal of Nanomedicine*, vol. 7, pp. 915–924, 2012.
- [104] D. Kumar, I. Mutreja, K. Chitcholtan, and P. Sykes, "Cytotoxicity and cellular uptake of different sized gold nanoparticles in ovarian cancer cells," *Nanotechnology*, vol. 28, no. 47, article 475101, 2017.

- [105] T. B. Huff, L. Tong, Y. Zhao, M. N. Hansen, J.-X. Cheng, and A. Wei, "Hyperthermia effect of gold nanorods on tumor cells," *Nanomedicine*, vol. 2, no. 1, pp. 125–132, 2007.
- [106] N. Verellen, D. Denkova, B. D. Clercq et al., "Two-photon luminescence of gold nanorods mediated by higher order plasmon modes," *ACS Photonics*, vol. 2, no. 3, pp. 410–416, 2015.
- [107] T. Wang, D. Halaney, D. Ho et al., "Two-photon luminescence properties of gold nanorods," *Biomed Optical Express*, vol. 4, no. 4, pp. 584–595, 2013.
- [108] L. C. Kennedy, L. R. Bickford, N. A. Lewinski et al., "A new era for cancer treatment: gold nanoparticle-mediated thermal therapies," *Small*, vol. 7, no. 2, pp. 169–183, 2011.
- [109] R. Arvizo, R. Bhattacharya, and P. Mukherjee, "Gold nanoparticles: opportunities and challenges in nanomedicine," *Expert Opinion on Drug Delivery*, vol. 7, no. 6, pp. 753–763, 2010.
- [110] L. F. Hakim, C. L. Vaughn, H. J. Dunsheath et al., "Synthesis of oxidation resistance metal nanoparticles via atomic layer deposition," *Nanotechnology*, vol. 18, no. 34, pp. 1–7, 2007.
- [111] J. G. Thakare, C. Pande, R. S. Mulik, and M. M. Mahapatra, "Mechanical property evaluation of carbon nanotubes reinforced plasma sprayed YSZ-alumina composite coating," *Ceramics International*, vol. 44, no. 6, pp. 1–10, 2018.
- [112] S.-S. Chang, C.-W. Shih, C.-D. Chen et al., "The shape transition of gold nanorods," *Langmuir*, vol. 15, no. 3, pp. 701–709, 1999.
- [113] N. R. Jana, L. Gearheart, and C. J. Murphy, "Wet chemical synthesis of high aspect ratio cylindrical gold nanorods," *Journal of Physical Chemistry*, vol. 105, no. 19, pp. 4065–4067, 2001.
- [114] B. Nikoobakht and M. A. El-Sayed, "Preparation and growth mechanism of gold nanorods (NRs) using seed-mediated growth method," *Chemistry of Materials*, vol. 15, no. 10, pp. 1957–1962, 2003.
- [115] D. H. Kim, A. Wei, and Y. Y. Won, "Preparation of superstable gold nanorods via encapsulation into block copolymer micelles," *ACS Applied Materials & Interfaces*, vol. 4, no. 4, pp. 1872–1877, 2012.
- [116] X. Ye, L. Jin, H. Caglayan et al., "Improved size tunable synthesis of monodisperse gold nanorods through the use of aromatic additives," *ACS Nano*, vol. 6, no. 3, pp. 2804–2817, 2012.
- [117] J. S. Lee and J. Feijen, "Polymersomes for drug delivery: design, formation and characterization," *Journal of Controlled Release*, vol. 161, no. 2, pp. 473–483, 2012.
- [118] K. K. Upadhyay, A. K. Mishra, K. Chuttani et al., "The in vivo behavior and antitumor activity of doxorubicin-loaded poly (γ -benzyl L-glutamate)-block-hyaluronan polymersomes in Ehrlich ascites tumor-bearing BalB/c mice," *Nanomedicine: Nanotechnology, Biology and Medicine*, vol. 8, no. 1, pp. 71–80, 2012.
- [119] A. Gharatape, S. Davaran, R. Salehi, and H. Hamishehkar, "Engineered gold nanoparticles for photothermal cancer therapy and bacteria killing," *RSC Advances*, vol. 6, no. 112, pp. 111482–111516, 2016.
- [120] D. Jaque, L. Martínez Maestro, B. del Rosal et al., "Nanoparticles for photothermal therapies," *Nanoscale*, vol. 6, no. 16, pp. 9494–9530, 2014.
- [121] Z. Bao, X. Liu, Y. Liu, H. Liu, and K. Zhao, "Near-infrared light-responsive inorganic nanomaterials for photothermal therapy," *Asian Journal of Pharmaceutical Sciences*, vol. 11, no. 3, pp. 349–364, 2016.
- [122] Y. Niidome, K. Honda, K. Higashimoto et al., "Surface modification of gold nanorods with synthetic cationic lipids," *Chemical Communications*, vol. 36, pp. 3777–3779, 2007.
- [123] A. Pan, H. Zhang, Y. Li et al., "Disulfide-crosslinked nanomicelles confer cancer-specific drug delivery and improve efficacy of paclitaxel in bladder cancer," *Nanotechnology*, vol. 27, no. 42, article 425103, 2016.
- [124] T. Ci, L. Chen, L. Yu, and J. Ding, "Tumor regression achieved by encapsulating a moderately soluble drug into a polymeric thermogel," *Scientific Reports*, vol. 1, no. 4, p. 5473, 2014.
- [125] B. K. Lee, Y. H. Yun, and K. Park, "Smart nanoparticles for drug delivery: boundaries and opportunities," *Chemical Engineering Science*, vol. 125, pp. 158–164, 2015.
- [126] F. Gomez-Rivera, "Functionalization of gold nanorod-based immunosensors for label-free bio-detection with high sensitivity and specificity," *Society for Advancement of Hispanics/Chicanos and Native Americans in Science*, vol. 28, no. 1, 2014.
- [127] P. Bengtsson and T. Johannesson, "Characterization of microstructural defects in plasma-sprayed thermal barrier coatings," *Journal of Thermal Spray Technology*, vol. 4, no. 3, pp. 245–251, 1995.
- [128] S. Ohnishi, A. Nakasuga, and K. Nakagawa, "Synthesis of copper particles covered with cobalt-catalyzed carbon nanofibers and their application to air-curable conductive paste," *Japanese Journal of Applied Physics*, vol. 56, no. 7S2, pp. 1–7, 2017.
- [129] K. J. Park, J. M. Doub, T. Gougousi, and G. N. Parsons, "Microcontact patterning of ruthenium gate electrodes by selective area atomic layer deposition," *Applied Physics Letters*, vol. 86, no. 5, article 051903, 2005.
- [130] M. Leskela and M. Ritala, "Atomic layer deposition chemistry: recent developments and future challenges," *Angewandte Chemie International Edition*, vol. 42, no. 45, pp. 5548–5554, 2003.
- [131] H. Moshe and Y. Mastai, "Atomic layer deposition on self-assembled monolayers," in *Materials Science—Advanced Topics*, Springer, Berlin, Germany, 2009.
- [132] L. Niinistö, M. Nieminen, J. Päiväsaari, J. Niinistö, M. Putkonen, and M. Nieminen, "Advanced electronic and optoelectronic materials by Atomic Layer Deposition: an overview with special emphasis on recent progress in processing of high-k dielectrics and other oxide materials," *Physica Status Solidi*, vol. 201, no. 77, pp. 1375–1376, 2004.
- [133] C. J. Murphy, L. B. Thompson, A. M. Alkilany et al., "The many faces of gold nanorods," *Journal of Physical Chemistry Letters*, vol. 1, no. 19, pp. 2867–2875, 2010.
- [134] J. Schmidt, A. Merkle, R. Brendel et al., "Surface passivation of high-efficiency silicon solar cells by atomic-layer-deposited Al_2O_3 ," *Progress in Photovoltaics: Research and Applications*, vol. 16, no. 6, pp. 461–466, 2008.
- [135] R. M. Crooks, M. Zhao, L. Sun, V. Chechik, and L. K. Yeung, "Dendrimer-encapsulated metal nanoparticle synthesis, characterization and application to catalysis," *Accounts of Chemical Research*, vol. 34, no. 3, pp. 1–10, 2011.
- [136] Y. Niu and R. M. Crooks, "Dendrimer-encapsulated metal nanoparticles and their applications to catalysis," *Metallocentric Catalysis*, vol. 6, no. 8–10, pp. 1049–1059, 2003.
- [137] C. J. Murphy, L. B. Thompson, A. M. Alkilany et al., "The many faces of gold nanorods," *Journal of Physical Chemistry Letters*, vol. 1, no. 19, pp. 2867–2875, 2010.

- [138] S. Boulos, M. B. Prigozhin, Y. Liu et al., "The gold nanorod-biology interface: from proteins to cells to tissue," *Current Physical Chemistry*, vol. 3, no. 2, pp. 128–135, 2013.
- [139] W. Ahmed, C. Glass, E. S. Kooij, and J. M. van Ruitenbeek, "Tuning the oriented deposition of gold nanorods on patterned substrates nanotechnology," *Nanotechnology*, vol. 25, no. 3, article 035301, 2013.
- [140] M. Zhao and R. M. Crooks, "Intradendrimer exchange of metal nanoparticles," *Chemistry of Materials*, vol. 11, no. 11, pp. 3379–3385, 1999.
- [141] P. A. Oroskar, C. J. J. Jameson, and S. Murad, "Rotational behaviour of PEGylated gold nanorods in a lipid bilayer system," *Molecular Physics*, vol. 115, no. 9–12, pp. 1122–1143, 2016.
- [142] A. Wijaya and K. Humad-Shifferli, "Ligand customization and DNA functionalization of gold nanorods via round-trip phase transfer exchange," *Langmuir*, vol. 24, no. 18, pp. 9966–9969, 2008.
- [143] A. B. Golovin and O. D. Lavrentovich, "Electrically reconfigurable optical metamaterial based on colloidal dispersion of metal nano-rods in dielectric fluid," *Applied Physics Letters*, vol. 95, no. 25, article 254104, 2009.
- [144] A. D. Adler, F. R. Longo, F. Kampas, and J. Kim, "Preparation of metalloporphyrins," *Journal of Inorganic and Nuclear Chemistry*, vol. 32, no. 7, pp. 2443–2445, 1970.
- [145] L.-I. Chen, L. Jiang, Y.-I. Wang, J. Qian, and S. He, "Multilayered polyelectrolyte-coated gold nanorods as multifunctional optical contrast agents for cancer cell imaging," *Journal of Zhejiang University Science B*, vol. 11, no. 6, pp. 417–422, 2006.
- [146] D. Pan, M. Pramanik, A. Senpan, S. A. Wickline, L. V. Wang, and G. M. Lanza, "A facile synthesis of novel self-assembled gold nanorods designed for near-infrared imaging," *Journal of Nanoscience and Nanotechnology*, vol. 10, no. 12, pp. 8118–8123, 2010.
- [147] M. Fang, C.-W. Peng, D.-W. Pang, and Y. Li, "Quantum dots for cancer research: current status, remaining issues and future perspectives," *Cancer Biology & Medicine*, vol. 9, no. 3, pp. 151–163, 2013.
- [148] E. Locatelli, I. Monaco, and M. C. Franchini, "Surface modifications of gold nanorods for applications in nanomedicine," *RSC Advances*, vol. 5, no. 28, pp. 21681–21699, 2015.
- [149] C. Xue, Y. Xu, Y. Pang et al., "Organo-soluble porphyrin mixed monolayer protected gold nanorods with intercalated fullerenes," *Langmuir*, vol. 28, no. 14, pp. 5956–5963, 2012.
- [150] A. Gole and C. J. Murphy, "Polyelectrolyte-coated gold nanorods: synthesis, characterization and immobilization," *Chemistry of Materials*, vol. 17, no. 6, pp. 1325–1330, 2005.
- [151] L. M. Moreira, F. V. dos Santos, J. P. Lyon, M. Maftoum-Costa, C. Pacheco-Soares, and N. S. da Silva, "Photodynamic therapy: porphyrins and phthalocyanines as photosensitizers," *Journal of Chemistry*, vol. 61, no. 10, pp. 741–754, 2008.
- [152] J. Moan, "Porphyrin photosensitization and phototherapy," *Photochemistry and Photobiology*, vol. 43, no. 6, pp. 681–690, 1986.
- [153] R. Karami, A. Mohsenifar, N. S. M. Mesbah et al., "A novel nanobiosensor for the detection of paraoxon using chitosan-embedded organophosphorous hydrolase immobilized on Au nanoparticles," *Preparative Biochemistry and Biotechnology*, vol. 46, no. 6, pp. 559–566, 2015.
- [154] C. Thomas, "Exploring new routes towards photoactive assemblies," *Proquest*, vol. 115, pp. 1–229, 2016.
- [155] S. Kimura, E. Bill, E. Bothe et al., "Phenylthiyl radical complexes of gallium(III), iron(III), and cobalt(III) and comparison with their phenoxy analogues," *Journal of the American Chemical Society*, vol. 123, no. 25, pp. 6025–6039, 2001.
- [156] P. Bhyrappa, M. Sankar, and B. Varghese, "Mixed substituted porphyrins: structural and electrochemical redox properties," *Inorganic Chemistry*, vol. 45, no. 10, pp. 4136–4149, 2006.
- [157] G. T. Babcock, M. K. El-Deeb, P. O. Sandusky, M. M. Whittaker, and J. W. Whittaker, "Electron paramagnetic resonance and electron nuclear double resonance spectroscopies of the radical site in 3121 galactose oxidase and of thioether-substituted phenol model compounds," *Journal of the American Chemical Society*, vol. 114, no. 10, pp. 3121–3134, 1992.
- [158] D. Burdinski, E. Bothe, and K. Wieghardt, "Synthesis and characterization of tris(bipyridyl)ruthenium(II)-modified mono-, di-, and trinuclear manganese complexes as electron-transfer models for photosystem II," *Inorganic Chemistry*, vol. 39, no. 1, pp. 105–116, 2000.
- [159] P. Rothemund, "A new porphyrin synthesis. The synthesis of porphyrin," *American Chemical Society*, vol. 58, pp. 624–625, 1936.
- [160] P. Rothemund and A. R. Menott, "Porphyrin studies. IV. The synthesis of @,y,b-tetraphenylporphine," *Journal of the American Chemical Society*, vol. 63, no. 1, pp. 267–270, 1941.
- [161] P. Rothemund, "Porphyrin studies. III. The structure of the porphine² ring system," *Journal of the American Chemical Society*, vol. 61, no. 10, pp. 2912–2915, 1939.
- [162] N. I. Shvetsov-Shilovskii, R. G. Bobkova, N. P. Ignatova et al., "Compounds of two-coordinated phosphorus," *Journal of the American Chemical Society*, vol. 46, no. 6, pp. 514–529, 1977.
- [163] P. Angrish, *Syntheses of meso-Substituted Porphodimethenes and Porphyrins with Exocyclic Ring Systems*, University of Florida, Tampa, FL, USA, 2003.
- [164] A. D. Adler, F. R. Longo, and W. Shergalis, "Mechanistic investigations of porphyrin syntheses. I. preliminary studies on ms-tetraphenylporphine," *Journal of the American Chemical Society*, vol. 86, no. 15, pp. 3145–3314, 1964.
- [165] A. D. Adler, F. R. Longo, J. D. Finarelli, J. Goldmacher, J. Assour, and L. Korsakoff, "A simplified synthesis for meso-tetraphenylporphine," *Journal of Organic Chemistry*, vol. 32, no. 2, p. 476, 1967.
- [166] R. G. Littler, "Notes on the synthesis of meso-substituted porphyrins from pyrrol carbinols and the mechanisms of the rothemund reaction," *Journal of Heterocyclic Chemistry*, vol. 18, no. 4, p. 833, 1981.
- [167] S. Hiroto, Y. Miyake, and H. Shinokubo, "Synthesis and functionalization of porphyrins through organometallic methodologies," *Chemical Reviews*, vol. 117, no. 4, pp. 2910–3043, 2017.
- [168] J. S. Lindsey, I. C. Schreiman, H. C. Hsu, P. C. Kearney, and A. M. Marguerettaz, "Stepwise syntheses of unsymmetrical tetra-arylporphyrin," *Organic Chemistry*, vol. 52, no. 5, p. 827, 1987.
- [169] H. G. Graham, M. van der Auweraer, J.-C. Chambron et al., "Intramolecular energy transfer in bis-porphyrins containing diimine chelates of variable geometry as spacers," *Chemistry: A European Journal*, vol. 5, no. 7, pp. 2189–2100, 1999.
- [170] H. Du, R.-C. A. Fuh, J. Li, L. Andrew Corkan, and J. S. Lindsey, "PhotochemCAD: a computer aided design and

- research tool in photochemistry," *Photochemistry and Photobiology*, vol. 68, no. 2, pp. 141-142, 1998.
- [171] M. Dommaschk, C. Näther, and R. Herges, "Synthesis of functionalized perfluorinated porphyrins for improved spin switching," *Journal of Organic Chemistry*, vol. 80, no. 17, pp. 8496-8500, 2015.
- [172] G. R. Geier III and J. S. Lindsey, "Investigation of porphyrin-forming reactions. Part 2. Examination of the reaction course in two-step, one-flask syntheses of meso-substituted porphyrins," *Journal of the Chemical Society*, vol. 2, no. 5, pp. 687-700, 2001.
- [173] G. R. Geier III, B. J. Littler, and J. S. Lindsey, "Investigation of porphyrin-forming reactions. Part 3. The origin of scrambling in dipyrromethane aldehyde condensations yielding trans-A2B2-tetraarylporphyrins," *Journal of the Chemical Society*, pp. 701-711, 2001.
- [174] G. R. Geier III, B. J. Littler, and J. S. Lindsey, "Investigation of porphyrin-forming reactions. Part 4.1 Examination of the reaction course in syntheses of porphyrins via dipyrromethanecarbinols," *Royal Society of Chemistry*, pp. 712-718, 2001.
- [175] G. R. Geier III and J. S. Lindsey, "Effects of diverse acid catalysts on the reaction course in the two-step one-flask synthesis of meso-tetraphenylporphyrin," *Royal Society of Chemistry*, vol. 6, no. 3, pp. 159-185, 2002.
- [176] G. Urata, "The chemistry of porphyrins and their precursors on the heme biosynthetic chain," *Nihon Rinsho*, vol. 53, no. 6, pp. 1319-1328, 1995.
- [177] S. K. Pushpan, S. Venkatraman, V. G. Anand et al., "Porphyrin in photodynamic therapy-a search for ideal photosensitizers," *Current Medicinal Chemistry-Anti-Cancer Agents*, vol. 2, no. 2, pp. 187-207, 2002.
- [178] Y. Wu, D. Xing, and W. R. Chen, "Single cell FRET imaging determination pathway of tumor cell apoptosis induced by photofin-PDT," *Cell Cycle*, vol. 5, no. 7, pp. 729-734, 2006.
- [179] K. Moghissi, K. Dixon, M. Stringer, and J. A. C. Thorpe, "Photofin PDT for early stage oesophageal cancer: long term results in 40 patients and literature review," *Thorax*, vol. 6, no. 3-4, pp. 159-166, 2009.
- [180] P. J. Muller and B. C. Wilson, "Photodynamic therapy of brain tumors-a work in progress," *Lasers in Surgery and Medicine*, vol. 38, no. 5, pp. 384-389, 2006.
- [181] B.-H. Li, "Singlet oxygen quantum yields of porphyrin based photosensitizers for photodynamic therapy," *Journal of Innovative Optical Health Sciences*, vol. 1, no. 1, pp. 141-149, 2008.
- [182] K. Stefflova, H. Li, J. Chen, and G. Zheng, "Peptide-based phamacodutation of a cancer-targeted optical imaging and photodynamic therapy agent," *Bioconjugate Chemistry*, vol. 18, no. 2, pp. 379-388, 2007.
- [183] Y.-n. Wen, W.-s. Song, L.-m. An, Y.-q. Liu, Y.-h. Wang, and Y.-q. Yang, "Activation of porphyrin photosensitizers by semiconductor quantum dots via two-photon excitation," *Applied Physics Letters*, vol. 95, article 143702, 2009.
- [184] T. Aida and S. Inoue, "Activation of carbon dioxide with aluminum porphyrin and reaction with epoxide. Studies on (tetraphenylporphinato) aluminum alkoxide having a long oxyalkylene chain as the alkoxide group," *Journal of the American Chemical Society*, vol. 105, no. 5, pp. 1304-1309, 1983.
- [185] M. Adinehnia, U. Mazur, and K. W. Hipps, "Predicting the size distribution in crystallization of TSPP:TMPyP binary porphyrin nanostructures in a batch desupersaturation experiment," *Crystal Growth & Design*, vol. 14, no. 12, pp. 6599-6606, 2014.
- [186] P. Guo, P. Chen, and M. Liu, "One-dimensional porphyrin nanoassemblies assisted via graphene oxide: sheet-like functional surfactant and enhanced photocatalytic behaviours," *ACS Applied Materials & Interfaces*, vol. 5, no. 11, pp. 5336-5345, 2013.
- [187] C. J. Medforth, Z. Wang, K. E. Martin, Y. Song, J. L. Jacobsen, and J. A. Shelnutt, "Selfassembled porphyrin nanostructures," *Chemical Communications*, vol. 21, no. 47, pp. 7261-7277, 2009.
- [188] Y. Arai and H. Segawa, "J-aggregation of protonated meso-tetrakis(sulfonatothienyl)porphyrin isomers: morphological selection of self-assembled nanostructures from structurally similar zwitterionic porphyrins," *Chemical Communications*, vol. 46, no. 24, pp. 4279-4281, 2010.
- [189] Y. Arai, K. Tsuzuki, and H. Segawa, "Homogeneously mixed porphyrin J-aggregates with rod-shaped nanostructures via zwitterionic self-assembly," *Physical Chemistry Chemical Physics*, vol. 14, no. 3, pp. 1270-1276, 2012.
- [190] J. Lee and S. J. Lee, "Microscopic crystalline rods from the self-assembly of mixed porphyrin building blocks," *Inorganic Chemistry Communications*, vol. 14, no. 6, pp. 1014-1017, 2010.
- [191] J. Bozja, J. Sherrill, S. Michielsen, and I. Stojiljkovic, "Porphyrin-base, light-activated antimicrobial materials," *Journal of Polymer Science Part A: Polymer Chemistry*, vol. 41, no. 15, pp. 2297-2303, 2005.
- [192] A. S. Derycke and P. A. de Witte, "Liposomes for photodynamic therapy," *Advanced Drug Delivery Reviews*, vol. 56, no. 1, pp. 17-30, 2004.
- [193] J. C. Leroux, E. Roux, D. Garrec, K. Hong, and D. C. Drummond, "N-isopropylacrylamide copolymers for the preparation of pH-sensitive liposomes and polymeric micelles," *Journal of Controlled Release*, vol. 72, no. 1-3, pp. 71-84, 2001.
- [194] S. H. Joo, J. Y. Park, C. K. Tsung, Y. Yamada, P. Yang, and G. A. Somorjai, "Thermally stable Pt/mesoporous silica core-shell nanocatalysts for high-temperature reactions," *Nature Materials*, vol. 8, no. 2, pp. 126-131, 2009.
- [195] T. Maschmeyer, G. Sankar, F. Rey, and J. M. Thomas, "Heterogeneous catalysts obtained by grafting metallocene complexes onto mesoporous silica," *Nature*, vol. 378, no. 6553, pp. 159-162, 1995.
- [196] N. K. Mal, M. Fujiwara, and Y. Tanaka, "Photocontrolled reversible release of guest molecules from coumarin-modified mesoporous silica," *Nature*, vol. 421, no. 6921, pp. 350-353, 2003.
- [197] E. Aznar, M. D. Marcos, R. Martínez-Mañez et al., "pH- and photo-switched release of guest molecules from mesoporous silica supports," *Journal of the American Chemical Society*, vol. 131, no. 19, pp. 6833-6843, 2009.
- [198] D. M. Huang, Y. Hung, B. S. Ko et al., "Highly efficient cellular labelling of mesoporous nanoparticles in human mesenchymal stem cells: implication for stem cell tracking," *FASEB Journal*, vol. 19, no. 14, pp. 2014-2039, 2005.
- [199] L. Li, C.-K. Tsung, T. Ming et al., "Multifunctional meso-structured silica microspheres from an ultrasonic aerosol spray," *Advanced Functional Materials*, vol. 18, no. 19, pp. 2956-2962, 2008.
- [200] L.-L. Li, H. Sun, C.-J. Fang, J. Xu, J.-Y. Jin, and C.-H. Yan, "Optical sensors based on functionalized mesoporous silica SBA-15 for the detection of multianalytes (H⁺ and Cu²⁺) in water," *Journal of Materials Chemistry*, vol. 17, no. 42, pp. 4492-4498, 2007.

- [201] A. Vinu, N. Gokulakrishnan, V. V. Balasubramanian et al., "Three dimensional ultralarge-pore Ia3d mesoporous silica with various pore diameters and their application in biomolecule immobilization," *Chemistry*, vol. 14, no. 36, pp. 11529–11538, 2008.
- [202] P. Guo, G. Zhao, P. Chen et al., "Porphyrin nanoassemblies via surfactant-assisted assembly and single nanofiber nanoelectronic sensors for high-performance H₂O₂ vapor sensing," *Journal of the American Chemical Society*, vol. 8, no. 4, pp. 3402–3411, 2014.
- [203] T. Hasobe, "Photo- and electro-functional self-assembled architectures of porphyrins," *Physical Chemistry Chemical Physics*, vol. 14, no. 46, pp. 15975–15987, 2012.
- [204] C. Pavani, A. F. Uchoa, C. S. Oliveira, Y. Yamamoto, and M. S. Baptista, "Effect of zinc insertion and hydrophobicity on membrane interaction and PDT activity of porphyrin photosensitizers," *Photochemical and Photobiological Sciences*, vol. 8, no. 2, pp. 233–240, 2008.
- [205] T. Uno, K. Aoki, T. Shikimi, Y. Hiranuma, Y. Tomisugi, and Y. Ishikawa, "Copper insertion facilitates water-soluble porphyrin binding to rA, rU and rA, dT base pairs in duplex RNA and RNA, DNA hybrids," *Biochemistry*, vol. 41, no. 43, pp. 13059–13066, 2002.
- [206] A. B. Ormond and H. S. Freeman, "Dye sensitizers for photodynamic therapy," *Materials*, vol. 6, no. 3, pp. 817–840, 2013.
- [207] T. Maisch, C. Bosl, R. M. Szeimies, B. Love, and C. Abels, "Determination of the environmental efficacy of a new porphyrin-based photosensitizer against MRSA ex-vivo," *Photochemical & Photobiological Sciences*, vol. 6, no. 5, pp. 545–551, 2007.
- [208] T. Maisch, C. Bosl, R. M. Szeimies, N. Lehn, and C. Abels, "Photodynamic effects of novel XF porphyrin derivatives on prokaryotic and eukaryotic cells," *Antimicrob Agents Chemother*, vol. 49, no. 4, pp. 1542–1553, 2005.
- [209] H. Aghaie, M. Keshavarz, K. Zare et al., "Spectroscopic study in the interaction of three water-soluble porphyrins with calf thymus DNA," *Journal of Physical & Theoretical Chemistry*, vol. 1, no. 3, pp. 135–142, 2004.
- [210] E. B. Fleischer, "Structure of porphyrins and metalloporphyrins," *Accounts of Chemical Research*, vol. 3, no. 3, pp. 105–112, 1970.
- [211] T. Maisch, C. Bosl, R.-M. Szeimies, N. Lehn, and C. Abels, "Photodynamic effects of novel XF porphyrin derivatives on prokaryotic and eukaryotic cells," *Antimicrobial Agents and Chemotherapy*, vol. 49, no. 4, pp. 1542–1552, 2005.
- [212] Y. Tian, K. E. Martin, J. Shelnuet et al., "Morphological families of self-assemble porphyrin structures and their photosensitization of hydrogen generation," *Chemical Communications*, vol. 47, pp. 6069–6071, 2011.
- [213] A. Lavi, H. Weitman, R. T. Holmes et al., "The depth of porphyrin in a membrane and the membranes physical properties affect the photosensitizing efficiency," *Biophysical Journal*, vol. 82, no. 4, pp. 2101–2110, 2002.
- [214] J. P. C. Tomé, M. G. P. M. S. Neves, A. C. Tomé et al., "Synthesis and antibacterial activity of new poly-S-lysine-porphyrin conjugates," *Journal of Medicinal Chemistry*, vol. 47, no. 26, pp. 6649–6652, 2004.
- [215] A. Srivatsan, J. R. Missert, S. K. Upadhyay, and R. K. Pandey, "Porphyrin based photosensitizers and corresponding multifunctional nanoplatforms for cancer –imaging and phototherapy," *Journal of Porphyrins and Phthalocyanines*, vol. 19, no. 1–3, pp. 109–134, 2015.
- [216] T. G. Smijs, R. N. van der Haas, J. Lugtenburg et al., "Photodynamic Treatment of the Dermatophyte *Trichophyton Rubrum* and its Mivronidia with Porphyrin Photosensitizers," *Photochemistry and Photobiology*, vol. 80, no. 2, pp. 197–202, 2004.
- [217] F. Würthner, C. C. You, and C. R. Saha-Möller, "Metallo-supramolecular squares: from structure to function," *Chemical Society Reviews*, vol. 33, no. 3, pp. 133–146, 2004.
- [218] F. M. Engelmann, I. Mayer, D. S. Gabrielli et al., "Interaction of cationic meso-porphyrins with liposomes, mitochondria and erythrocytes," *Journal of Bioenergetics and Biomembranes*, vol. 39, no. 2, pp. 175–185, 2007.
- [219] D. K. Cabbiness and D. W. Margerum, "Effect of macrocyclic structures on the rate of formation and dissociation of copper(II) complexes," *Journal of the American Chemical Society*, vol. 92, no. 7, pp. 2151–2153, 1970.
- [220] R. West and A. Hill, *Advances in Organometallic Chemistry*, vol. 58, pp. 289–342, 1st edition, 2001.
- [221] S. H. van Rijt and P. J. Sadler, "Current applications and future potential for bioinorganic chemistry in the development of anticancer drugs," *Drug Discovery Today*, vol. 14, no. 23–24, pp. 1089–1097, 2009.
- [222] P. Comba, H. Rudolf, and H. Wadepohl, "Synthesis and transition metal coordination chemistry of a novel hexadentate bispidine ligand," *Dalton Transactions*, vol. 44, no. 6, pp. 2724–2736, 2015.
- [223] M. Scirish and H. J. Scheureder, "Porphyrin derivatives as water soluble receptors for peptides," *Chemical Communications*, vol. 10, pp. 907–908, 1999.
- [224] F. R. Longo, E. M. Brown, D. J. Quimby, A. D. Adler, and M. Meot-Ner, "Kinetic studies on metal chelation by Porphyrins," *Annals of the New York Academy of Sciences*, vol. 206, no. 1, pp. 420–442, 1973.
- [225] X. Gong, T. Milic, C. Xu, J. D. Batteas, and C. M. Drain, "Preparation and characterization of porphyrin nanoparticles," *Journal of the American Chemical Society*, vol. 124, no. 48, pp. 14290–14291, 2002.
- [226] O. Penon, T. Patiño, L. Barrios et al., "A new pophyrin for the preparation of functionalized water-soluble gold nanoparticle with intrinsic toxicity," *ChemistryOpen*, vol. 4, no. 2, pp. 127–136, 2015.
- [227] K. Záruba, J. Králová, P. Řezanka, P. Poučková, L. Veverková, and V. Král, "Modified porphyrin–brucine conjugated to gold nanoparticles and their application in photodynamic therapy," *Organic and Biomolecular Chemistry*, vol. 8, no. 14, pp. 3202–3206, 2010.
- [228] T. Zhao, H. Wu, S. Q. Yao, Q.-H. Xu, G. Q. Xu, and G. Q. Xu, "Nanocomposites containing gold nanorods and porphyrin-doped mesoporous silica with dual capability of two-photon imaging and photosensitization," *Langmuir*, vol. 26, no. 18, pp. 14937–14942, 2010.
- [229] C. Xue, Y. Xu, Y. Pang et al., "Organo-soluble porphyrin mixed monolayer-protected gold nanorods with intercalated fullerenes," *Langmuir*, vol. 28, no. 14, pp. 5956–5963, 2012.
- [230] K. Bera, S. Maiti, M. Maity, C. Mandal, and N. C. Maiti, "Porphyrin-gold nanomaterial for efficient drug delivery to cancerous cells," *ACS Omega*, vol. 3, no. 4, pp. 4602–4619, 2018.
- [231] D. van Straten, V. Mashayekhi, H. S. de Bruijn, S. Oliveira, and D. Robinson, "Oncologic photodynamic therapy: basic principles, current clinical status and future directions," *Cancers*, vol. 9, no. 2, p. 19, 2017.
- [232] L. G. Levy, "Photosensitizers in photodynamic therapy," *Seminars in Oncology*, vol. 21, no. 150, pp. 4–10, 1994.

- [233] M. Panjehpour, R. C. DeNovo, M. G. Petersen et al., "Photodynamic therapy using Verteporfin (benzoporphyrin derivative monoacid ring A, BPD-MA) and 630 nm laser light in canine esophagus," *Lasers in Surgery and Medicine*, vol. 30, no. 1, pp. 26–30, 2002.
- [234] K. Bera, S. Maiti, M. Maity, C. Mandal, and N. C. Maiti, "Porphyrin-gold nanomaterial for efficient drug delivery to cancerous cells," *ACS Omega*, vol. 3, no. 4, pp. 4602–4619, 2018.
- [235] T. H. Foster, B. R. Giesselman, R. Hu, M. E. Kenney, and S. Mitra, "Intratumor administration of the photosensitizer Pc 4 affords photodynamic therapy efficacy and selectivity at short drug-light intervals," *Translational Oncology*, vol. 3, no. 2, pp. 135–141, 2010.
- [236] Z.-A. Chen, Y. Kuthati, R. K. Kankala et al., "Encapsulation of palladium porphyrin photosensitizer in layered metal oxide nanoparticles for photodynamic therapy against skin melanoma," *Science and Technology of Advanced Materials*, vol. 16, no. 5, pp. 1–14, 2015.
- [237] M. Scholz and M. Didie, "New trends in photodynamic therapy research," *Proceedings of Contributed Papers. Part III*, pp. 46–51, 2012.
- [238] D. Bechet, P. Couleaud, C. Frochot, M.-L. Viriot, F. Guillemain, and M. Barberi-Heyob, "Nanoparticles as vehicles for delivery of photodynamic therapy agents," *Trends in Biotechnology*, vol. 26, no. 11, pp. 612–621, 2008.
- [239] A. C. S. Samia, S. Dayal, and C. Burda, "Quarter dot-based energy transfer: perspectives and potential applications in photodynamic therapy," *Photochemistry and Photobiology*, vol. 82, no. 3, pp. 617–625, 2006.
- [240] T. Dai, B. B. Fuchs, J. J. Coleman et al., "Concepts and principles of photodynamic therapy as an alternative antifungal discovery platform," *Frontiers in Microbiology*, vol. 3, no. 120, pp. 1–13, 2012.
- [241] R. R. Allison, G. H. Downie, R. Cuenca, X.-H. Hu, C. J. H. Childs, and C. H. Sibata, "Photosensitizers in clinical PDT," *Photodiagnosis and Photodynamic Therapy*, vol. 1, no. 1, pp. 27–42, 2004.
- [242] J.-Y. Liu, C. Wang, C.-H. Zhu, Z.-H. Zhang, and J.-P. Xue, "Preparation and in vitro photodynamic activity of glucosylated zinc(II) phthalocyanines as underlying targeting photosensitizers," *Molecules*, vol. 22, no. 845, pp. 1–13, 2017.
- [243] Z. Kautzka, S. Clement, E. M. Goldys, and W. Deng, "Light-triggered liposomal cargo delivery platform incorporating photosensitizers and gold nanoparticles for enhanced singlet oxygen generation and increased cytotoxicity," *International Journal of Nanomedicine*, vol. 12, pp. 969–977, 2017.
- [244] T. Kiesslich, A. Gollmer, T. Maisch, M. Berneburg, and K. Plaetzer, "A comprehensive tutorial on vitro characterization of new photosensitizers for photodynamic antitumor therapy and photodynamic inactivation of microorganisms," *BioMed Research International*, vol. 2013, Article ID 840417, 17 pages, 2013.
- [245] C. J. Gomer, N. Rucker, A. Ferrario, and S. Wong, "New applications of photodynamic therapy," *Radiation Research*, vol. 120, no. 1, pp. 1–18, 1989.
- [246] J. Kou, D. Dou, and L. Yang, "Porphyrin photosensitizers in photodynamic therapy and its applications," *Oncotarget*, vol. 8, no. 46, pp. 81591–81603, 2017.
- [247] J. Zhang, C. Jiang, J. P. F. Longo et al., "An updated overview on the development of new photosensitizers for anticancer photodynamic therapy," *Acta Pharmaceutica Sinica B*, vol. 8, no. 2, pp. 137–146, 2017.
- [248] C. Staneloudi, K. S. Smith, R. Hudson et al., "Development and characterization of novel photosensitizer: scFv conjugates for use in photodynamic therapy of cancer," *Immunology*, vol. 120, no. 4, pp. 512–517, 2007.
- [249] A. Almeida, A. Cunha, N. C. M. Gomes, E. Alves, L. Costa, and M. A. Faustino, "Phage therapy and photodynamic therapy: low environmental impact approaches to inactivate microorganisms in fish farming plants," *Marine Drugs*, vol. 7, no. 3, pp. 268–313, 2009.
- [250] T. Huang, T. Dai, and M. R. Hamblin, "Antimicrobial photodynamic inactivation and photodynamic therapy for infections," *Methods in Molecular Biology*, vol. 635, pp. 155–173, 2010.
- [251] S. Perni, P. Prokopovich, J. Pratten, I. P. Parkin, and M. Wilson, "Nanoparticles: their potential use in antibacterial photodynamic therapy," *Photochemical and Photobiological Sciences*, vol. 10, no. 5, pp. 712–720, 2010.
- [252] N. Shirasu, S. O. Nam, and M. Kuroki, "Tumor targeted photodynamic therapy," *Anticancer Research*, vol. 33, no. 7, pp. 2823–2832, 2013.
- [253] C. M. Allen, W. M. Sharman, and J. E. van Lier, "Current status of phthalocyanines in the photodynamic therapy of cancer," *Phthalocyanines*, vol. 5, no. 2, pp. 161–169, 2009.
- [254] S. Wang, R. Gao, F. Zhou, and M. Selke, "Nanomaterials and singlet oxygen photosensitizers: potential application in photodynamic therapy," *Journal of Materials Chemistry*, vol. 14, no. 4, pp. 487–493, 2004.
- [255] Y. N. Konan, R. Gurny, and E. Allemann, "State of the art in the delivery of photosensitizers for photodynamic therapy," *Journal of Photochemistry and Photobiology*, vol. 66, no. 2, pp. 89–106, 2002.
- [256] R. Bonnett, "Photosensitizers of the porphyrin and phthalocyanine series for photodynamic therapy," *Chemical Society Reviews*, vol. 25, pp. 9–33, 1995.
- [257] M. C. Hashimoto, R. A. Prates, I. T. Kato, S. C. Núñez, L. C. Courrol, and M. S. Ribeiro, "Antimicrobial photodynamic therapy on drug resistant pseudomonas aeruginosa-induced infection: an in vivo study," *Photochemistry and Photobiology*, vol. 88, no. 3, pp. 590–595, 2012.
- [258] E. Paszko, C. Ehrhardt, M. O. Senge, D. P. Kelleher, and J. V. Reynolds, "Nanodrug applications in photodynamic therapy," *Photodiagnosis and Photodynamic Therapy*, vol. 8, no. 1, pp. 14–29, 2011.
- [259] J. Estelrich, M. J. Sánchez-Martín, and M. A. Busquets, "Nanoparticles in magnetic resonance imaging: from simple to dual contrast agents," *International Journal of Nanoscience*, vol. 10, pp. 1727–1741, 2015.
- [260] W. C. M. A. de Melo, A. N. Lee, J. R. Perussi, and M. R. Hamblin, "Electroporation enhances antimicrobial photodynamic therapy mediated by the hydrophobic photosensitizer, hypericin, electroporation enhances antimicrobial photodynamic inactivation," *Photodiagnosis and Photodynamic Therapy*, vol. 10, no. 4, pp. 647–650, 2013.
- [261] W. Chen and J. Zhang, "Using nanoparticles to enable simultaneous radiation and photodynamic therapies for cancer treatment," *Journal of Nanoscience and Nanotechnology*, vol. 6, no. 4, pp. 1159–1166, 2006.
- [262] P. Agostinis, K. Berg, K. A. Cengel et al., "Photodynamic therapy of cancer: an update," *CA: A Cancer Journal for Clinicians*, vol. 61, no. 4, pp. 250–281, 2011.
- [263] A. Casas, H. Fukuda, G. Di Venosa, and A. Batlle, "Photosensitization and mechanism of cytotoxicity induced by

- the use of ALA derivatives in photodynamic therapy," *British Journal of Cancer*, vol. 85, no. 2, pp. 279–284, 2001.
- [264] E. Otake, S. Sakuma, K. Torii et al., "Effect and mechanism of a new photodynamic therapy with glycoconjugated fullerene," *Photochemistry and Photobiology*, vol. 86, no. 6, pp. 1356–1363, 2010.
- [265] J. Usuda, H. Kato, T. Okunaka et al., "Photodynamic therapy (PDT) for lung cancers," *Journal of Thoracic Oncology*, vol. 1, no. 5, pp. 489–493, 2006.
- [266] S. P. Songca and O. S. Oluwafemi, "Photodynamic therapy: a new light for the developing world," *African Journal of Biotechnology*, vol. 12, no. 23, pp. 3590–3599, 2014.
- [267] L. Zou, H. Wang, B. He et al., "Current approaches of photothermal therapy in treating cancer metastasis with nanotherapeutics," *Theranostics*, vol. 6, no. 6, pp. 762–772, 2016.
- [268] W. Chen and J. Zhang, "Using nanoparticles to enable simultaneous radiation and photodynamic therapies for cancer treatment," *Journal of Nanoscience and Nanotechnology*, vol. 6, no. 4, pp. 1159–1166, 2006.
- [269] D. R. Cooper, D. Bekah, and J. L. Nadeau, "Gold nanoparticles and their alternatives for radiation therapy enhancement," *Frontiers in Chemistry*, vol. 2, no. 14, p. 86, 2014.
- [270] E. B. Dickerson, E. C. Dreaden, X. Huang et al., "Gold nanorod assisted near-infrared plasmonic photothermal therapy (PPTT) of squamous cell carcinoma in mice," *Cancer Letters*, vol. 269, no. 1, pp. 57–66, 2008.
- [271] J. Chen, D. Wang, J. Xi et al., "Immuno gold nanocages with tailored optical properties for targeted photothermal destruction of cancer cells," *Nano Letters*, vol. 7, no. 5, pp. 1318–1322, 2007.
- [272] C. M. Pitsillides, E. K. Joe, X. Wei, R. Rox Anderson, and C. P. Lin, "Selective cell targeting with light-absorbing microparticles and nanoparticles," *Biophysical Journal*, vol. 84, no. 6, pp. 4023–4032, 2003.
- [273] I. H. El-Sayed, X. Huang, and M. A. El-Sayed, "Selective laser photo-thermal therapy of epithelial carcinoma using anti-EGFR antibody conjugated gold nanoparticles," *Cancer Letters*, vol. 239, no. 1, pp. 129–135, 2006.
- [274] Q. Tian, J. Hu, Y. Zhu et al., "Sub-10 nm Fe₃O₄@Cu₂-XS core-shell nanoparticles for dual-modal imaging and photothermal therapy," *Journal of the American Chemical Society*, vol. 135, no. 23, pp. 8571–8577, 2013.
- [275] A. L. Mckenziei and J. A. S. Carruth, "Lasers in surgery and medicine," *Physics in Medicine and Biology*, vol. 29, no. 6, pp. 619–641, 1984.
- [276] L. O. Svaasand, C. J. Gomer, and E. Morinelli, "On the physical rationale of laser induced hyperthermia," *Lasers in Medical Science*, vol. 5, no. 2, pp. 121–128, 1990.
- [277] W. Lu, A. K. Singh, S. A. Khan, D. Senapati, H. Yu, and P. C. Ray, "Gold nano-popcon based targeted diagnosis nanotherapy treatment, and in situ monitoring of photothermal therapy response of prostate acancer cells using surface enhanced Raman spectroscopy," *Journal of the American Chemical Society*, vol. 132, no. 51, pp. 18103–18114, 2010.
- [278] S. Lal, S. E. Clare, and N. J. Halas, "Nanoshell-enabled photothermal cancer therapy: impending clinical impact," *Accounts of Chemical Research*, vol. 41, no. 12, pp. 1842–1851, 2012.
- [279] T. B. Huff, M. N. Hansen, Y. Zhao et al., "Controlling the cellular uptake of gold nanorods," *Langmuir*, vol. 23, no. 4, pp. 1596–1599, 2007.
- [280] J. M. Harris and R. B. Chess, "Effect of pegylation on pharmaceuticals," *Nature Reviews: Drug Discoveries*, vol. 2, no. 3, pp. 214–221, 2003.
- [281] J. Pérez-Juste, I. Pastoriza-Santos, L. M. Liz-Marzán, and P. Mulvaney, "Gold nanorods: synthesis, characterization and applications," *Coordination Chemistry Reviews*, vol. 249, no. 17–18, pp. 1870–1901, 2005.
- [282] R. Gans, "Form of ultramicroscopic particles of silver," *Annals of Physics*, vol. 14, pp. 270–284, 1915.
- [283] X. Huang, I. H. El-Sayed, W. Qian et al., "Cancer cells assemble and align gold nanorods conjugated to antibodies to produce highly enhanced, sharp and polarized surface Raman spectra: a potential cancer diagnostic marker," *Nano Letters*, vol. 7, no. 6, pp. 1591–1597, 2007.
- [284] M. Moskovits, "Surface-enhanced spectroscopy," *Reviews of Modern Physics*, vol. 57, no. 3, pp. 783–826, 1985.
- [285] C. Adura, S. Guerrero, E. Salas et al., "Stable conjugates of peptides with gold nanorods for biomedical applications with reduced effects on cell viability," *ACS Applied Materials & Interfaces*, vol. 5, no. 10, pp. 4076–4085, 2013.
- [286] A. M. Alkilany, L. B. Thompson, S. P. Boulos, P. N. Sisco, and C. J. Murphy, "Gold nanodots; their potential for photothermal therapeutics and drug delivery tempered by the complexity of their biological interactions," *Advanced Drug Delivery Reviews*, vol. 64, no. 2, pp. 190–199, 2012.
- [287] K. A. Willets and R. P. Van Duyne, "Localized surface plasmon resonance spectroscopy and sensing," *Annual Review of Physical Chemistry*, vol. 58, no. 1, pp. 267–297, 2007.
- [288] C. L. Haynes and A. M. R. P. Van Duyne, "Surface-enhanced Raman spectroscopy," *Analytical Chemistry*, vol. 77, no. 17, pp. 338A–346A, 2005.
- [289] J. N. Anker, W. P. Hall, O. Lyandres, N. C. Shah, J. Zhao, and R. P. Van Duyne, "Biosensing with plasmonic nanosensors," *Nature Materials*, vol. 7, no. 6, pp. 442–453, 2008.
- [290] E. Y. Lukianova-Hleb, E. Y. Hanna, J. H. Hafner, and D. Lapotko, "Tunable plasmonic nanobubbles for cell therapeutics," *Nanotechnology*, vol. 21, no. 8, article 85102, 2016.
- [291] T. Lammers, S. Aime, W. E. Hennink, G. Storm, and F. Kiessling, "Theranostic nanomedicine," *Accounts of Chemical Research*, vol. 44, no. 10, pp. 1029–1038, 2011.
- [292] N. Khlebtsov, V. Bogatyrev, L. Dykman et al., "Analytical and theranostic applications of gold nanoparticles and multifunctional nanocomposites," *Theranostics*, vol. 3, no. 3, pp. 167–180, 2013.
- [293] J. Wang, M. You, G. Zhu et al., "Photosensitizer–gold nanorod composite for targeted multimodal therapy," *Small*, vol. 9, no. 21, pp. 3678–3684, 2013.
- [294] B. Jang, J. Y. Park, C. H. Tung, I.-H. Kim, and Y. Choi, "Gold nanorod-photosensitizer complex for near-infrared fluorescence imaging and photodynamic/photothermal therapy in vivo," *ACS Nano*, vol. 5, no. 2, pp. 1086–1094, 2011.
- [295] G. Terentyuk, E. Panfilova, V. Khanadeev et al., "Gold nanorods with a hematoporphyrin-loaded silica shell for dual-modality photodynamic and photothermal treatment of tumors in vivo," *Nano Research*, vol. 7, no. 3, pp. 325–337, 2014.
- [296] T. Liu, C. Wang, W. Cui et al., "Combined photothermal and photodynamic therapy delivered by PEGylated MoS₂ nanosheets," *Nanoscale*, vol. 6, no. 19, pp. 11219–11225, 2014.
- [297] S. Hayden, L. A. Austin, R. D. Near et al., "Heterogeneous gold catalysts and catalysis," *Photochemistry and Photobiology*, vol. 269, p. 34, 2013.
- [298] A. M. A. Elhissi, W. Ahmed, I. U. Hassan, V. R. Dhanak, and A. D'Emmanuel, "Carbon nanotubes in cancer therapy and

- drug delivery,” *Journal of Drug Delivery*, vol. 2012, Article ID 837327, 10 pages, 2012.
- [299] Z. Liu, J. T. Robinson, S. M. Tabakman, K. Yang, and H. Dai, “Carbon materials for drug delivery and cancer therapy,” *Materials Today*, vol. 14, no. 7-8, pp. 1-8, 2012.
- [300] J.-W. Kim, E. I. Galanzha, E. V. Shashkov, H.-M. Moon, and V. P. Zharov, “Golden carbon nanotubes as multimodal photoacoustic and photothermal high-contrast molecular agents,” *Nature Nanotechnology*, vol. 4, no. 10, pp. 688-694, 2009.
- [301] G. Terentyuk, E. Panfilova, V. Khanadeev et al., “Gold nanorods with a hematoporphyrin-loaded silica shell for dual-modality photodynamic and photothermal treatment of tumors in vivo,” *Nano Research*, vol. 7, no. 3, pp. 325-337, 2014.
- [302] R. Saito, G. Dresselhaus, and M. S. Dresselhaus, *Physical Properties of Carbon Nanotubes*, Imperial College Press, London, UK, 1998.
- [303] R.-S. Liu, H. M. Chen, and S.-F. Hu, “Synthesis and characterization of long gold nanorods,” *IEEE Transactions on Electrical and Electronic Engineering*, vol. 2, no. 4, pp. 468-472, 2007.
- [304] B. Jang, J.-Y. Park, C.-H. Tung, I.-H. Kim, and Y. Choi, “Gold nanorod-photosensitizer complex for near-infrared fluorescence imaging and photodynamic/photothermal therapy in vivo,” *ACS Nano*, vol. 5, no. 2, pp. 1086-1094, 2011.
- [305] S. G. Bachhav and D. R. Patil, “Synthesis and characterization of polyaniline-multiwalled carbon nanotube nanocomposites and its electrical percolation behavior,” *American Journal of Materials Science*, vol. 5, no. 4, pp. 90-95, 2015.
- [306] C. Xua, G. Wu, Z. Liu, D. Wu, T. T. Meek, and Q. Han, “Preparation of copper nanoparticles on carbon nanotubes by electroless plating method,” *Materials Research Bulletin*, vol. 39, no. 10, pp. 1499-1505, 2004.
- [307] Z. M. Markovic, L. M. Harhaji-Trajkovic, B. M. Todorovic-Markovic et al., “In vivo comparison of the photothermal anticancer activity of graphene nanoparticles and carbon nanotubes,” *Biomaterials*, vol. 32, no. 4, pp. 1121-1129, 2011.
- [308] V. Butkova, A. V. Fokina, V. N. Nevedomskaya et al., “A template method for carbon nanotube production from sugar water,” *Nanotech*, vol. 26, pp. 1-5, 2013.
- [309] G. L. Hornyak, A. C. Dillon, P. A. Parilla et al., “Template synthesis of carbon nanotubes,” *Pergamons*, vol. 12, no. 1-4, pp. 83-88, 1999.
- [310] F. Hekmat, B. Sohrabi, and M. S. Rahmanifar, *Effect of Template on the Structure of Carbon Nanotubes Grown by Catalytic Chemical Vapor Deposition Method*, pp. 1-5, Elsevier, New York, NY, USA, 2017.
- [311] H. S. Ali, S. Ahmed, and G. A. Khan, “Gold nanoparticles in cancer therapy and diagnosis,” *Pharmaceutical Research*, vol. 28, no. 2, pp. 237-259, 2011.
- [312] M. Samim, C. K. Prashant, A. K. Dinda et al., “Synthesis and characterization of gold nanorods and their application for photothermal cell damage,” *International Journal of Nanomedicine*, vol. 6, pp. 1825-1831, 2011.
- [313] R.-S. Liu, H. M. Chen, and S.-F. Hu, “Synthesis and characterization of long gold nanorods,” *IEEE Transactions on Electrical and Electronic Engineering*, vol. 2, no. 4, pp. 468-472, 2007.
- [314] E. C. Dreaden, L. A. Austin, M. A. Mackey, and M. A. El-Sayed, “Size matters: gold nanoparticles in targeted cancer drug delivery,” *Therapeutic Delivery*, vol. 3, no. 4, pp. 457-478, 2012.
- [315] J. Gautier, E. Allard-Vannier, E. Munnier, M. Soucé, and I. Chourpa, “Recent advances in theranostic nanocarriers of doxorubicin based on iron oxide and gold nanoparticles,” *Journal of Controlled Release*, vol. 169, no. 1-2, pp. 48-61, 2013.
- [316] M. Ballauff and Y. Lu, ““Smart” nanoparticles: preparation, characterization and applications,” *Polymer*, vol. 48, no. 7, pp. 1815-1823, 2007.
- [317] T. Ci, L. Chen, L. Yu et al., “Tumor regression achieved by encapsulating a moderately soluble drug into a polymeric thermogel,” *Scientific Reports*, vol. 4, no. 1, p. 5473, 2014.
- [318] R. Zou, X. Guo, J. Yang et al., “Selective etching of gold nanorods by ferric chloride at room temperature,” *CrytEngComm*, vol. 11, pp. 2797-2803, 2009.
- [319] P. Rothmund, “The study of chlorophyll and photosynthesis,” *Journal of the American Chemical Society*, vol. 63, pp. 267-270, 1935.
- [320] Z. C. Sun, Y. B. She, Y. Zhou, X. F. Song, and K. Li, “Synthesis, characterization and spectral properties of substituted tetraphenylporphyrin iron chloride complexes,” *Molecules*, vol. 16, no. 4, pp. 2960-2970, 2011.
- [321] G. R. Geier III and G. S. Lindsey, “Investigation of porphyrin-forming reactions. Part 1. Pyrrole aldehyde oligomerization in two-step, one-flask syntheses of meso-substituted porphyrins,” *Journal of the Chemical Society*, vol. 2, no. 5, pp. 677-686, 2001.
- [322] K. Berg, P. K. Selbo, A. Weyergang et al., “Porphyrin-related photosensitizers for cancer imaging and therapeutic applications,” *Journal of Microscopy*, vol. 288, no. 2, pp. 133-147, 2005.
- [323] E. Fagadar-Cosma, A. Lascu, A. Palade et al., “Hybrid material based on 5-(4-pyridyl)-10,15,20-tris (4-phenoxyphenyl)- porphyrin and gold colloid for CO₂ detection,” *Digest Journal of Nanomaterials and Biostructures*, vol. 11, no. 2, pp. 419-424, 2016.
- [324] J. T. Robinson, K. Welsher, S. M. Tabakman et al., “High performance in vivo near-IR (>1 μm) imaging and photothermal cancer therapy with carbon nanotubes,” *Nano Research*, vol. 3, no. 11, pp. 779-793, 2010.
- [325] V. Kumar, J. Sinha, N. Verma, K. Nayan, C. S. Saimbi, and A. K. Tripathi, “Scope of photodynamic therapy in periodontics,” *Indian Journal of Dental Research*, vol. 26, no. 4, pp. 439-442, 2015.
- [326] P. Li, Y.-W. Shi, B.-X. Li et al., “Photo-thermal effect enhances the efficiency of radiotherapy using Arg-Gly-Asp peptides-conjugated gold nanorods that target α_vβ₃ in melanoma cancer cells,” *Journal of Nanobiotechnology*, vol. 13, no. 1, p. 52, 2015.

Research Article

Synthesis and Antibacterial Activity of Polyoxometalates with Different Structures

Jingmin Gu ¹, Lei Zhang,² Xiaofeng Yuan,³ Ya-Guang Chen ⁴, Xiuzhu Gao,⁵
and Dong Li ^{5,6}

¹College of Veterinary Medicine, Jilin University, Changchun 130062, China

²Animal Science and Technology College, Jilin Agricultural University, Changchun 130117, China

³Department of Pediatrics, Affiliated Hospital of the Changchun University of Chinese Medicine, Changchun 130021, China

⁴Key Laboratory of Polyoxometalates Science of Ministry of Education, Faculty of Chemistry, Northeast Normal University, Changchun 130024, China

⁵Department of Hepatology, The First Hospital, Jilin University, Changchun 130021, China

⁶Department of Immunology, College of Basic Medical Sciences, Jilin University, Changchun 130021, China

Correspondence should be addressed to Dong Li; lidong1@jlu.edu.cn

Received 19 May 2018; Accepted 13 September 2018; Published 9 December 2018

Guest Editor: Rais A. Khan

Copyright © 2018 Jingmin Gu et al. This is an open access article distributed under the Creative Commons Attribution License, which permits unrestricted use, distribution, and reproduction in any medium, provided the original work is properly cited.

A new inorganic-organic hybrid compound, $[\{Cu(phen)_2\}_2(H_4W_{12}O_{40})]$, was synthesized, and its crystal structure was determined. The Keggin anion $H_4W_{12}O_{40}^{4-}$ was grafted with two coordination units $\{Cu(phen)_2\}$, forming an electrically neutral molecule. The antibacterial activity of several polyoxometalate compounds with different anionic structures including the new compound was studied. The results show that the compound **1** can inhibit the growth of *Enterococcus faecalis* FA2 strains and that antibacterial activity of the polyoxometalate compounds is dependent with component elements of POM but is less relative with the anion structures.

1. Instruction

Polyoxometalates (POMs) have been shown to exhibit biological activities *in vitro* as well as *in vivo*, including anticancer and antiviral [1], antibacterial [2, 3], antiprotozoal [4, 5], and antidiabetic activities [6]. In the antibacterial activity study of POMs, Tajima found the enhancement of several beta-lactams antibiotics in antibacterial activity to methicillin-resistant *Staphylococcus aureus* under the synergistic action of polyoxometalates, substituted-type POMs $K_7[PTi_2W_{10}O_{40}] \cdot 6H_2O$, $K_7[BVW_{11}O_{40}]7H_2O$, $[SiFeW_{11}O_{40}]^{6/5-}$ and $[SiCoW_{11}O_{40}]^{6-}$ and lacunary-type POMs $[XW_{11}O_{39}]^{n-}$ ($X = Si, P$) and $[XW_9O_{34}]^{n-}$, and proposed the resistant mechanism [7–12]. Inoue et al. reported the enhancement of antibacterial activity of beta-lactam antibiotics, oxacillin, by polyoxometalates ($K_6[P_2W_{18}O_{62}] \cdot 14H_2O$, $K_4[SiMo_{12}O_{40}] \cdot 3H_2O$, and $K_7[PTi_2W_{10}O_{40}] \cdot 6H_2O$) against methicillin-resistant *Staphylococcus aureus* (MRSA)

and vancomycin-resistant *S. aureus* (VRSA) and also proposed a reaction mechanism [13]. Daima et al. studied synergistic antibacterial action of Ag nanoparticles and POMs which were achieved by the physical damage to the bacterial cells [14]. Li and his colleagues showed the short peptides/HSiW nanofibers had antimicrobial activity to the ubiquitous and clinically relevant bacterium *Escherichia coli* [15]. In recent years, there are also many reports about the antibacterial activity of known and new polyoxometalate derivatives to several bacteria including *Escherichia coli*, *Staphylococcus aureus*, *Paenibacillus* sp., *Bacillus subtilis*, *Clavibacter michiganensis*, *Vibrio* sp., *Pseudomonas putida*, *Helicobacter pylori*, *S. typhimurium*, *Streptococcus B* (*S. agalactiae*), *L. acidophilus*, and amebas [3,16–34]. In these reports, the polyoxometalate derivatives are in the form of simple inorganic salts, inorganic-organic hybrids with various organic groups, films, nanofibers, etc. However, the antibacterial activity of these compounds is not satisfactory

according to the reported data. Nevertheless, the emergence of multidrug-resistant bacterial strains which was partially due to the abuse of conventional antibiotics proved that there is an urgent need for novel therapeutic agents. Therefore, synthesizing and exploring new compounds with high antibacterial activity are still a challenging task of chemists and pharmacologist. To achieve this, the study on influence of the composition and structure of compounds on antibacterial activity is very important, which will play an instructional role in synthesizing and exploring new compounds.

This work is about the synthesis of a new polyoxometalate derivative, $[\text{Cu}_2(\text{phen})_4(\text{H}_4\text{W}_{12}\text{O}_{40})]$, and study on the antibacterial activity of several polyoxometalate compounds with different anionic structures including the new compound.

2. Materials and Methods

2.1. Materials and General Methods. All reagents were purchased commercially and used without further purification. Elemental analyses (C, H, and N) were performed on a Perkin-Elmer 2400 CHN elemental analyzer and that of W and Cu on an ICP-AES analyzer. The IR spectrum was obtained on a Magna-560 FT/IR spectrometer with KBr pellets in the 400–4000 cm^{-1} region. TG analysis was carried out on a DTG-60H thermal analyzer in flowing N_2 with a heating rate of 10 $^\circ\text{C}\cdot\text{min}^{-1}$. SEM images were recorded on Hitachi S-3400N (Hitachi High-Technologies Europe GmbH, Krefeld, Germany).

2.2. Synthesis. Synthesis of $[\text{Cu}_2(\text{phen})_4(\text{H}_4\text{W}_{12}\text{O}_{40})]$ was modified from our previous report [35]: compound **1** was prepared from reaction of $(\text{NH}_4)_6(\text{H}_2\text{W}_{12}\text{O}_{40})\cdot 3\text{H}_2\text{O}$ (0.1 mmol, 0.30 g), $\text{CuCl}_2\cdot 2\text{H}_2\text{O}$ (2.0 mmol, 0.34 g), phenanthroline (0.5 mmol, 0.099 g), succinic acid (0.5 mmol, 0.06 g), and 12 mL water. The starting mixture was adjusted to pH = 2.0 by the addition of hydrochloric acid, and the mixture was stirred for 1 h under air. The final solution was transferred to a 25 mL Teflon-lined autoclave and crystallized at 160 $^\circ\text{C}$ for 96 h. Then, the autoclave was cooled at the rate of 10 $^\circ\text{C}\cdot\text{h}^{-1}$ to room temperature. The resulting green stripe crystals were filtered off, washed with distilled water, and air-dried. Good-quality crystals were sealed for structural determination and further characterization. Elemental analysis calcd for $\text{C}_{48}\text{H}_{32}\text{Cu}_2\text{N}_2\text{O}_{41}\text{W}_{12}$ ($M_r = 3710$) C 1.00, H 12.7619, N 2.48, O 20.68, Cu 3.38, P 1.10, W 58.60 (%); found: C 1.10, H 12.39, N 2.41, O 20.56, Cu 3.39, P 1.09, W 59.05 (%). IR(KBr pellet, cm^{-1}): 3500, 3082, 2370, 2298, 2109, 1994, 1628, 1597, 1524, 1335, 1231, 1085, 948, 781, 750, 708, 667, 593, 530 cm^{-1} .

Compounds **2–6** were prepared in accordance with the methods in Refs. [36–39] and characterized by the IR spectrograph and TGA.

2.3. X-Ray Crystallography. The X-ray diffraction data of compound **1** were collected on a Bruker Smart Apex II diffractometer with graphite monochromatic $\text{Mo K}\alpha$ radiation ($\lambda = 0.71073 \text{ \AA}$) at 293 K with ω scans (Table 1).

TABLE 1: Crystal data and structure refinements for compound **1**.

Formula	$\text{C}_{48}\text{H}_{32}\text{Cu}_2\text{N}_2\text{O}_{40}\text{W}_{12}$
Fw	3710
Crystal system	Monoclinic
Space group	P21/c
$a/\text{\AA}$	26.1828(15)
$b/\text{\AA}$	11.84219(7)
$c/\text{\AA}$	23.3996(13)
$\alpha/^\circ$	90.00
$\beta/^\circ$	113.74(2)
$\gamma/^\circ$	90.00
$V/\text{\AA}^3$	6641.2(7)
Z	4
$D_c/\text{g}\cdot\text{cm}^{-3}$	3.711
F(000)	6600
μ/mm^{-1}	21.419
R_{int}	0.0932
Refine number of reflns/parameters/restraints	13661/991/54
$R_{\text{factor_all}}/[I > 2\sigma(I)]$	0.0871/0.0456
$wR_{\text{factor_ref}}/[I > 2\sigma(I)]$	0.0857/0.0745
Goodness of fit	0.954

Multiscan absorption corrections were applied. The structures were solved by direct methods and refined by full matrix least-squares on F^2 using the SHELXTL crystallographic software package [40]. The positions of hydrogen atoms on the carbon atoms were calculated theoretically. Crystal data and structure refinements for compound **1** are presented in Table 1. Cu-O and Cu-N bond lengths are listed in Table 2. CCDC-1487664 for **1** contains the supplementary crystallographic data for this paper. These data can be obtained free of charge from The Cambridge Crystallographic Data Centre via http://www.ccdc.cam.ac.uk/data_request/cif.

2.4. Antibacterial Experiments. All the isolated bacterial strains were achieved by colony formation on selective salt agar plates containing 6 mg/mL oxacillin. All bacterial strains were stored at -80°C and routinely grown at 37°C . *Staphylococcus aureus* (YB57), *Enterococcus faecalis* (FA2 and FA3), and *Enterococcus faecium* (SA2 and SA3) strains were cultured in brain heart infusion (BHI) broth, while *Staphylococcus aureus* (USA300), *Acinetobacter baumannii* (ABC3), and *Streptococcus pneumoniae* (SP) were cultured in the Luria-Bertani (LB) medium. The polyoxometalates were tested for their antibacterial activities against eight different bacterial strains by the observation of the OD value of culture media. Briefly, bacterial cells were washed and resuspended in sterile PBS, and the colony count was determined. The different polyoxometalates were added to the bacterial suspension (final concentration, 1 mg/mL), and the mixture was incubated overnight at 37°C . The colony count was determined again. Enzyme activity *in vitro* was expressed as the CFU reduction. As a negative control, the bacterial strains were treated with the elution buffer under the same conditions. The results are listed in Table 3.

TABLE 2: Cu-O and Cu-N bond lengths (Å) in **1**.

Bond	Length	Bond	Length
Cu1 N1	2.214(11)	Cu2 N5	1.960(12)
Cu1 N2	1.990(10)	Cu2 N9	2.038(12)
Cu1 N3	1.996(13)	Cu2 N7	1.965(12)
Cu1 N4	1.991(11)	Cu2 N8	2.168(12)
Cu1 O7	2.045(10)	Cu2 O38	2.217(8)

2.5. Scanning Electron Microscopy. Scanning electron microscopy (SEM) was performed to assess the activity of different polyoxometalates on the bacterial strains *in vitro*. The *Staphylococcus aureus* strains USA300 were grown to the exponential growth phase (an OD 600 nm value of 0.6) in the BHI broth at 37°C with shaking at 200 rpm. The bacteria were collected and washed three times (5,000 × g for 1 min at 4°C) with PBS. Different formulations were separately added to *S. aureus* suspensions. Bacterial lysates were harvested by centrifugation (1,100 × g for 1 min) at different time points. Then, the bacterial lysates were fixed with glutaraldehyde and were dehydrated and freeze-dried for SEM.

3. Results and Discussion

3.1. Crystal Structure of **1.** The asymmetric unit of compound **1** consists of one Keggin anion [H₄W₁₂O₄₀]⁶⁻, two Cu²⁺ ions, and four phen molecules. The [H₄W₁₂O₄₀]⁶⁻ anion (Figure 1) contains four edge-shared W₃O₁₃ units which combine together through corner-shared linkage. W-O bonds can be classified into three sets: W-O_t (terminal oxygen atoms) with distances of 1.683(12)–1.740(12) Å, W-O_b (bridging oxygen atoms) with distances of 1.847(12)–2.010(14) Å and W-O_c (central oxygen atoms) with distances of 2.174(12)–2.396(13) Å. That is, the WO₆ octahedra are all distorted. The Keggin anion acts as a bidentate ligand bonding two Cu²⁺ ions (Cu1 and Cu2) with one terminal oxygen atom and one bridge oxygen atom. One W-O_t bond was elongated (1.740(12) Å) due to the coordination of the terminal oxygen atom to Cu ion. Such a POM anion is also called as decorated Keggin anion (Figure 1), very similar to the decoration we reported previously [35].

Two Cu²⁺ ions are all five-coordinated. Cu1 ion displays in a square prism geometry, and the geometry of Cu2 ion is better to be described as triangle bipyramid. The donor atoms bonding to Cu ions come from two phen molecules with chelating coordination mode and the Keggin anion, forming a complex fragment {Cu(phen)₂}²⁺ (Figure 1). Cu-O and Cu-N bond lengths are listed in Table 2. As shown in Table 2, the long bonds belong to the atoms at axial site for Cu1 and triangle plane for Cu2 (Figure S1), resulting from their environment in the crystal. Devi et al. [41] had reported a similar cluster [{Cu(phen)₂}₂(H₂W₁₂O₄₀)]²⁻ in [{Cu(phen)₂}₄(H₂W₁₂O₄₀)]·3H₂O, in which one Cu ion is six-coordinated, different from that of this new compound. The neutral molecules are assembled into three dimensional architecture through CH...O hydrogen bonds (Table S2) and intermolecular interaction force (Figure S2).

TABLE 3: Antibacterial activities of compounds **1–6**.

Type	Code	Compound	Concentration	Bacterial strains
I	1	[{Cu(phen) ₂ } ₂ (H ₄ W ₁₂ O ₄₀)]	1 mg/mL	FA2, ABC3, FA2, FA3, YB57, USA300
	2	[Cu(phen)(H ₂ O)(Mo ₃ O ₁₀)]	1 mg/mL	YB57, USA300
II	3	K ₅ PW ₁₁ TiO ₄₀ ·14H ₂ O	1 mg/mL	SA5, SA1, SP, USA300
III	4	Na ₇ CeW ₁₀ O ₃₅ ·26H ₂ O	1 mg/mL	YB57, USA300
IV	5	K ₁₃ [La(SiW ₁₁ O ₃₉) ₂]·26H ₂ O	1 mg/mL	SA5, SA1, SP, USA300
	6	K ₁₃ [Ce(SiW ₁₁ O ₃₉) ₂]·26H ₂ O	1 mg/mL	SA1, SP, USA300

3.2. Characterization of **1.** The IR spectrum (Figure S3) of **1** shows the vibration absorption bands of CH bond in 3080 cm⁻¹ and of C-C and N-C bonds of phen ring in 1614–1137 cm⁻¹. The vibration absorption bands of compound **1** at 952, 877, 846, and 740 cm⁻¹ should be ascribed to the asymmetric stretching vibrations of W-O_d, W-O_b-W, and W-O_c-W bonds, respectively, consistent with that in Ref. [42]. The TG curve of **1** is shown in Figure S4. Compound **1** is stable below 400°C and then decomposes until 600°C. The lost weight of 20.17% is consistent with the calculated one (20.38% for 2H₂O and 4phen), confirming the chemical formula obtained from elemental analysis and structure analysis.

3.3. Antibacterial Activity of **1–6.** The compounds **1–6** used in antibacterial experiments can be divided into four kinds. **1** and **2** are inorganic-organic hybrids with phenanthroline, and **3** is a mono-substituted Keggin-type compound in which Ti atom occupies one of twelve sites. **4** is a complex of mono-lacunaria Lindquist anion and lanthanides. **5** and **6** are complexes of mono-lacunaria Keggin anions and lanthanides. From Table 3, it can be seen that (1) the new compound **1** is active only to bacterial strains FA2. (2) The compound of molybdenum, **2**, has a wider antibacterial spectrum than that of tungsten (**1**, **3**, **4**, **5**, **6**). (3) The anionic structure has less influence on antibacterial activity. (4) The compounds with cerium element (**4**, **6**) show better antibacterial activity than others.

SEM technique was used to explore the interaction of polyoxometalates with the bacterial strains. SEM images (Figure 2) show the surface morphology of *Staphylococcus aureus* strains USA300 untreated (Figure 2(a)) and treated with **3**, **4**, **5**, and **6** (Figures 2(b)–2(e)). From Figure 2, it can be seen that the surface morphology of *Staphylococcus aureus* strains USA300 treated with polyoxometalates (Figures 2(b)–2(e)) has changed obviously compared with that of untreated one (Figure 2(a)) from smooth globular form to chapping oblate spheroid. The degree of changes in the surface morphology indicates the antibacterial activity of

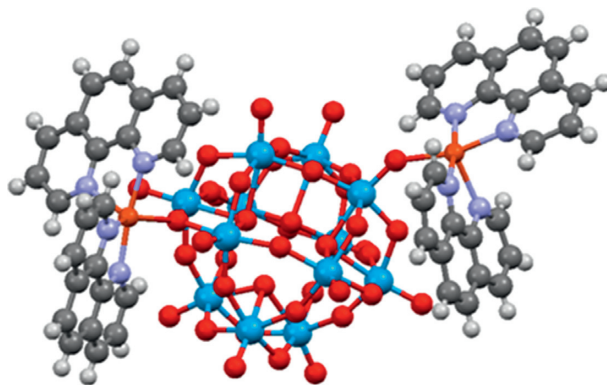


FIGURE 1: Ball-stick representation of the decorated Keggin anion in **1**.

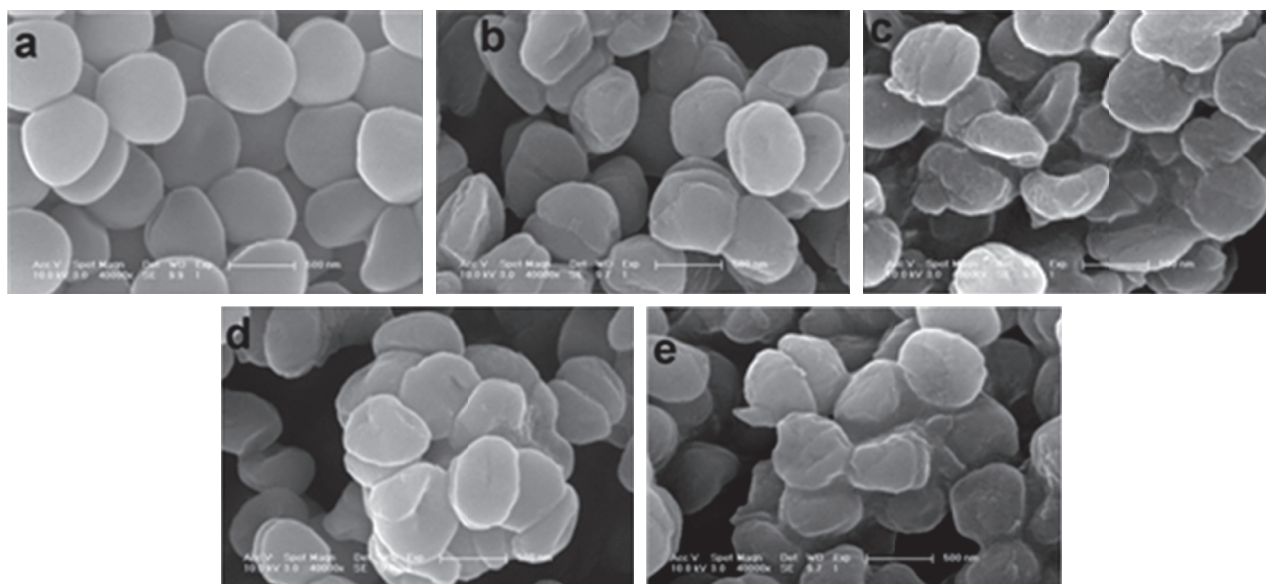


FIGURE 2: SEM images of *Staphylococcus aureus* strains USA300 untreated (a) and treated with **3** (b), **4** (c), **5** (d), and **6** (e).

polyoxometalates. So, a sequence of the activity of polyoxometalates was given according to Figure 2, $4 \approx 6 > 5 > 3$. That is, the compounds with cerium element (**4**, **6**) have better antibacterial activity than others.

4. Conclusion

The bioactivity of polyoxometalates has been known for many years but still has large space to explore. The results of this work on the antibacterial activity of polyoxometalates including the new compound show that antibacterial activity of the compounds is more relative with their component element than with anionic structure, which means that exploration of antibacterial materials should focus on the choice of elements.

In this work, the compounds with Ce elements have better antibacterial activity. So, synthesizing compounds with other lanthanide elements and other compounds with cerium element and examining their antibacterial activity as well as exploring the reaction mechanism of Ce compounds need further investigations.

Data Availability

The data used to support the findings of this study are included within the article.

Conflicts of Interest

The authors declare no conflicts of interest.

Authors' Contributions

Jingmin Gu and Lei Zhang contributed equally to this article.

Acknowledgments

This work was supported by the National Natural Science Foundation of China (No. 81501423) and Norman Bethune Program of Jilin University (No. 2015223). We also like to give our special thanks to Dr. Sadeeq ur Rahman from College of Veterinary Sciences & Animal Husbandry, Abdul

Wali Khan University, Mardan, Pakistan, for generously providing *Enterococcus faecium* strains (SA2 and SA3) and *Streptococcus pneumoniae* strain (SP).

Supplementary Materials

Figure S1: coordination geometries of Cu ions; Figure S2: stacking representation of **1** from three directions of (A) *a*-axis, (B) *b*-axis, and (C) *c*-axis; Figure S3: IR spectrum of **1**; Figure S4: TG plot of **1** in 0–600°C; Table S1: W–O bond lengths (Å); Table S2: CH...O hydrogen bonds in **1**. (Supplementary Materials)

References

- [1] J. T. Rhule, C. L. Hill, and D. A. Judd, "Polyoxometalates in medicine," *Chemical Reviews*, vol. 98, no. 1, pp. 327–357, 1998.
- [2] A. Seko, T. Yamase, and K. Yamashita, "Polyoxometalates as effective inhibitors for sialyl- and sulfotransferases," *Journal of Inorganic Biochemistry*, vol. 103, no. 7, pp. 1061–1066, 2009.
- [3] M. Inoue, K. Segawa, S. Matsunaga et al., "Antibacterial activity of highly negative charged polyoxotungstates, K27 [KAs4W4O140] and K18 [KSb9W21O86], and Keggin-structural polyoxotungstates against *Helicobacter pylori*," *Journal of Inorganic Biochemistry*, vol. 99, no. 5, pp. 1023–1031, 2005.
- [4] T. L. Turner, V. H. Nguyen, C. C. McLauchlan et al., "Inhibitory effects of decavanadate on several enzymes and *Leishmania tarentolae* in vitro," *Journal of Inorganic Biochemistry*, vol. 108, pp. 96–104, 2012.
- [5] Y. Qi, Y. Xiang, J. Wang et al., "Inhibition of hepatitis C virus infection by polyoxometalates," *Antiviral Research*, vol. 100, no. 2, pp. 392–398, 2013.
- [6] K. Nomiyama, H. Torii, T. Hasegawa et al., "Insulin mimetic effect of a tungstate cluster. Effect of oral administration of homo-polyoxotungstates and vanadium-substituted polyoxotungstates on blood glucose level of STZ mice," *Journal of Inorganic Biochemistry*, vol. 86, no. 4, pp. 657–667, 2001.
- [7] T. Yamase, N. Fukuda, and Y. Tajima, "Synergistic effect of polyoxotungstates in combination with beta-lactam antibiotics on antibacterial activity against methicillin-resistant *Staphylococcus aureus*," *Biological and Pharmaceutical Bulletin*, vol. 19, no. 3, pp. 459–465, 1996.
- [8] Y. Tajima, "Purification of a factor that enhances the antibacterial activity of beta-lactams against methicillin-resistant *Staphylococcus aureus*: its identification as undecaphosphotungstate," *Journal of Inorganic Biochemistry*, vol. 68, no. 2, pp. 93–99, 1997.
- [9] Y. Tajima, "Lacunary-substituted undecatungstosilicates sensitize methicillin-resistant *Staphylococcus aureus* to beta-lactams," *Biological and Pharmaceutical Bulletin*, vol. 24, no. 9, pp. 1079–1084, 2001.
- [10] Y. Tajima, "The effects of tungstophosphate and tungstosilicate on various stress promoters transformed in *Escherichia coli*," *Journal of Inorganic Biochemistry*, vol. 94, no. 1–2, pp. 155–160, 2003.
- [11] Y. Tajima, "Effects of tungstosilicate on strains of methicillin-resistant *Staphylococcus aureus* with unique resistant mechanisms," *Microbiology and Immunology*, vol. 47, no. 3, pp. 207–212, 2003.
- [12] Y. Tajima, "Polyoxotungstates reduce the beta-lactam resistance of methicillin-resistant *Staphylococcus aureus*," *Mini-Reviews in Medicinal Chemistry*, vol. 5, no. 3, pp. 255–268, 2005.
- [13] M. Inoue, T. Suzuki, Y. Fujita et al., "Enhancement of antibacterial activity of beta-lactam antibiotics by [P2W18O62]6-, [SiMo12O40]4-, and [PTi2W10O40]7- against methicillin-resistant and vancomycin-resistant *Staphylococcus aureus*," *Journal of Inorganic Biochemistry*, vol. 100, no. 7, pp. 1225–1233, 2006.
- [14] H. K. Daima, P. R. Selvakannan, A. E. Kandjani et al., "Synergistic influence of polyoxometalate surface corona towards enhancing the antibacterial performance of tyrosine-capped Ag nanoparticles," *Nanoscale*, vol. 6, no. 2, pp. 758–765, 2014.
- [15] J. Li, Z. Chen, M. Zhou et al., "Polyoxometalate-driven self-assembly of short peptides into multivalent nanofibers with enhanced antibacterial activity," *Angewandte Chemie International Edition in English*, vol. 55, no. 7, pp. 2592–2595, 2016.
- [16] Y. Feng, Z. Han, J. Peng et al., "Fabrication and characterization of multilayer films based on Keggin-type polyoxometalate and chitosan," *Materials Letters*, vol. 60, no. 13, pp. 1588–1593, 2006.
- [17] K. H. Wu, P. Y. Yu, C. C. Yang et al., "Preparation and characterization of polyoxometalate-modified poly(vinyl alcohol)/polyethyleneimine hybrids as a chemical and biological self-detoxifying material," *Polymer Degradation and Stability*, vol. 94, no. 9, pp. 1411–1418, 2009.
- [18] C. G. Feng, Y. D. Xiong, and X. Liu, "Synthesis, spectroscopy and antibacterial activity of supermolecular compounds of organotitanium substituted heteropolytungstates containing 8-quinolinol," *Guang Pu Xue Yu Guang Pu Fen Xi*, vol. 31, no. 5, pp. 1153–1160, 2011.
- [19] S. Gao, Z. Wu, D. Pan et al., "Preparation and characterization of polyoxometalate–Ag nanoparticles composite multilayer films," *Thin Solid Films*, vol. 519, no. 7, pp. 2317–2322, 2011.
- [20] R. Raza, A. Matin, S. Sarwar et al., "Polyoxometalates as potent and selective inhibitors of alkaline phosphatases with profound anticancer and amoebicidal activities," *Dalton Transactions*, vol. 41, no. 47, pp. 14329–14336, 2012.
- [21] J. He, H. Pang, W. Wang et al., "Uniform M3PMo12O40.nH2O (M = NH4+, K+, Cs+) rhombic dodecahedral nanocrystals for effective antibacterial agents," *Dalton Transactions*, vol. 42, no. 44, pp. 15637–15644, 2013.
- [22] H. K. Daima, P. R. Selvakannan, R. Shukla et al., "Fine-tuning the antimicrobial profile of biocompatible gold nanoparticles by sequential surface functionalization using polyoxometalates and lysine," *PLoS One*, vol. 8, no. 10, Article ID e79676, 2013.
- [23] X. Yu, C. Chen, J. Peng et al., "Antibacterial-active multilayer films composed of polyoxometalate and Methyl Violet: fabrication, characterization and properties," *Thin Solid Films*, vol. 571, pp. 69–74, 2014.
- [24] A. Maalaoui, A. Hajsalem, N. Ratel-Ramond et al., "Synthesis, characterization and antibacterial activity of a novel photoluminescent nb-substituted lindqvist polyoxotungstate based organic cation," *Journal of Cluster Science*, vol. 25, no. 6, pp. 1525–1539, 2014.
- [25] G. Fiorani, O. Saoncella, P. Kaner et al., "Chitosan-polyoxometalate nanocomposites: synthesis, characterization and application as antimicrobial agents," *Journal of Cluster Science*, vol. 25, no. 3, pp. 839–854, 2014.
- [26] L. Grama, A. Man, D.-L. Muntean et al., "Antibacterial activity of some saturated polyoxotungstates," *Romanian Journal of Laboratory Medicine*, vol. 22, no. 1, pp. 111–118, 2014.
- [27] L. De Matteis, S. G. Mitchell, and M. Jesús, "Supramolecular antimicrobial capsules assembled from polyoxometalates and

- chitosan," *Journal of Materials Chemistry B*, vol. 2, no. 41, pp. 7114–7117, 2014.
- [28] H. Liu, Y.-L. Zou, L. Zhang et al., "Polyoxometalate cobalt–gatifloxacin complex with DNA binding and antibacterial activity," *Journal of Coordination Chemistry*, vol. 67, no. 13, pp. 2257–2270, 2014.
- [29] P. Yang, B. S. Bassil, Z. Lin et al., "Organoantimony(III)-containing tungstoarsenates(III): from controlled assembly to biological activity," *Chemistry*, vol. 21, no. 44, pp. 15600–15606, 2015.
- [30] X.-X. Lu, Y.-H. Luo, C. Lu et al., "Assembly of three new POM-based Ag(I) coordination polymers with antibacterial and photocatalytic properties," *Journal of Solid State Chemistry*, vol. 232, pp. 123–130, 2015.
- [31] P. Gull and A. A. Hashmi, "Biological activity studies on metal complexes of macrocyclic schiff base ligand: synthesis and spectroscopic characterization," *Journal of the Brazilian Chemical Society*, vol. 26, no. 7, pp. 1331–1337, 2015.
- [32] P. Yang, Z. Lin, B. S. Bassil et al., "Tetra-antimony(III)-bridged 18-tungsto-2-arsenates(V), [(LSb(III))₄(A- α -As(V)W₉O₃₄)₂](10-) (L = ph, OH): turning bioactivity on and off by ligand substitution," *Inorganic Chemistry*, vol. 55, no. 8, pp. 3718–3720, 2016.
- [33] W. W. Ayass, T. Fodor, Z. Lin et al., "Synthesis, structure, and antibacterial activity of a thallium(III)-containing polyoxometalate, [Tl₂{B- β -SiW₈O₃₀(OH)}₂](12)," *Inorganic Chemistry*, vol. 55, no. 20, pp. 10118–10121, 2016.
- [34] S. Balici, M. Niculae, E. Pall et al., "Antibiotic-like behaviour of polyoxometalates in vitro comparative study: seven polyoxotungstates-nine antibiotics against gram-positive and gram-negative bacteria," *Revista de Chimie*, vol. 67, no. 3, pp. 485–490, 2016.
- [35] H. Wang, H. Liu, T. Shi et al., "Decorated Dawson anion by two different complex fragments of phenanthroline and isonicotinic acid: synthesis and properties," *Journal of Cluster Science*, vol. 28, no. 3, pp. 1041–1049, 2017.
- [36] H.-Y. Wang, T. Shi, and Y.-G. Chen, "Molybdenum-oxygen anionic chain grafted by Cu-phen complex. Synthesis, crystal structure and properties," *Inorganic Chemistry Communications*, vol. 70, pp. 201–204, 2016.
- [37] O. A. Kholdeeva, T. A. Trubitsina, G. M. Maksimov et al., "Synthesis, characterization, and reactivity of Ti(IV)-monosubstituted Keggin polyoxometalates," *Inorganic Chemistry*, vol. 44, no. 5, pp. 1635–1642, 2005.
- [38] R. Peacock and T. Weakley, "Heteropolytungstate complexes of the lanthanide elements. Part I. Preparation and reactions," *Journal of the Chemical Society A: Inorganic, Physical, Theoretical*, pp. 1836–1839, 1971.
- [39] S. Zubairi, S. Ifzal, and A. Malik, "Heteropoly complexes of lanthanum with unsaturated heteropolytungstate ligands," *Inorganica Chimica Acta*, vol. 22, pp. L29–L30, 1977.
- [40] G. Sheldrick, *SHELXL97, Program for Crystal Structure Refinement*, University of Göttingen, Göttingen, Germany, 1997.
- [41] R. N. Devi, E. Burkholder, and J. Zubieta, "Hydrothermal synthesis of polyoxotungstate clusters, surface-modified with M (II)-organonitrogen subunits," *Inorganica Chimica Acta*, vol. 348, pp. 150–156, 2003.
- [42] M. Asami, H. Ichida, and Y. Sasaki, "The structure of hexakis (tetramethylammonium) dihydrogendodecatungstate ennea-hydrate, [(CH₃)₄N]₆[H₂W₁₂O₄₀]·9H₂O," *Acta Crystallographica Section C: Crystal Structure Communications*, vol. 40, no. 1, pp. 35–37, 1984.

Research Article

Anticancer Potential of Green Synthesized Silver Nanoparticles Using Extract of *Nepeta deflersiana* against Human Cervical Cancer Cells (HeLa)

Ebtesam S. Al-Sheddi,¹ Nida N. Farshori ,¹ Mai M. Al-Oqail,¹ Shaza M. Al-Massarani ,¹ Quaiser Saquib,^{2,3} Rizwan Wahab,^{2,3} Javed Musarrat,^{2,3} Abdulaziz A. Al-Khedhairi,² and Maqsood A. Siddiqui^{2,3}

¹Department of Pharmacognosy, College of Pharmacy, King Saud University, Riyadh, Saudi Arabia

²Zoology Department, College of Science, King Saud University, P.O. Box 2455, Riyadh 11451, Saudi Arabia

³Al-Jeraisy Chair for DNA Research, Zoology Department, College of Science, King Saud University, P.O. Box 2455, Riyadh 11451, Saudi Arabia

Correspondence should be addressed to Nida N. Farshori; nidachem@gmail.com

Received 23 May 2018; Accepted 4 October 2018; Published 1 November 2018

Guest Editor: Bon H. Koo

Copyright © 2018 Ebtesam S. Al-Sheddi et al. This is an open access article distributed under the Creative Commons Attribution License, which permits unrestricted use, distribution, and reproduction in any medium, provided the original work is properly cited.

In this study, silver nanoparticles (AgNPs) were synthesized using aqueous extract of *Nepeta deflersiana* plant. The prepared AgNPs (ND-AgNPs) were examined by ultraviolet-visible spectroscopy, Fourier transform infrared (FTIR) spectroscopy, X-ray diffraction (XRD), transmission electron microscopy (TEM), scanning electron microscope (SEM), and energy dispersive spectroscopy (EDX). The results obtained from various characterizations revealed that average size of synthesized AgNPs was 33 nm and in face-centered-cubic structure. The anticancer potential of ND-AgNPs was investigated against human cervical cancer cells (HeLa). The cytotoxic response was assessed by 3-(4, 5-dimethylthiazol-2-yl)-2, 5-diphenyltetrazolium bromide (MTT), neutral red uptake (NRU) assays, and morphological changes. Further, the influence of cytotoxic concentrations of ND-AgNPs on oxidative stress markers, reactive oxygen species (ROS) generation, mitochondrial membrane potential (MMP), cell cycle arrest and apoptosis/necrosis was studied. The cytotoxic response observed was in a concentration-dependent manner. Furthermore, the results also showed a significant increase in ROS and lipid peroxidation (LPO), along with a decrease in MMP and glutathione (GSH) levels. The cell cycle analysis and apoptosis/necrosis assay data exhibited ND-AgNPs-induced SubG1 arrest and apoptotic/necrotic cell death. The biosynthesized AgNPs-induced cell death in HeLa cells suggested the anticancer potential of ND-AgNPs. Therefore, they may be used to treat the cervical cancer cells.

1. Introduction

Nobel metal nanoparticles have attracted the interest of scientific community due to their fascinating applications in the field of biology, material science, medicine, etc [1]. Silver nanoparticles specifically have gained attention due to their unusual physiochemical [2] (chemical stability and electrical conductivity) and biological activities such as antibacterial, antifungal, anti-inflammatory, antiviral, antiangiogenesis, anticancer, and antiplatelet activities [3–5]. In addition,

silver nanoparticles have been used in clothing [6], room spray, laundry detergent, wall paint formulation [7, 8], sunscreens, and cosmetics [9]. Silver nanoparticles also inhibit HIV-1 virus from binding to the host cells *in vitro* [10]. Although a wide variety of metal nanoparticle preparation methods such as UV radiation, laser ablation, lithography, aerosol technologies, and photochemical reduction are available [11–13], the focus is shifting towards green synthesis of nanoparticles, using bacteria [14], yeast [15], fungi [16], and plants [17]. Green synthesis of

nanoparticles reports to be clean, nontoxic, cost effective, and environmentally benign. Among the various biological methods available, the use of microbe-mediated synthesis has limited industrial use, as they require antiseptic conditions. On the contrary, the use of plant extract for the nanoparticles synthesis is valuable due to the ease of scale-up, less biohazardous nature, and avoiding the hideous procedure of maintaining the cell lines [18].

Cancer is a life threatening disease and leads the cases of deaths around the world [19]. According to the WHO, the annual cancer cases are to rise from 14 million in 2012 to 22 million in the next two decades [20]. Thus, the development of potent and effective antineoplastic drugs is one of the most persuaded goals. Among the various approaches, the exploitation of natural products is one of the most successful methods to identify novel hits and leads [21]. *Nepeta deflersiana* Schweinf. (*Labiatae*) is a medicinal plant growing in Saudi Arabia [22]. Traditionally *N. deflersiana* was used as a sedative; the leaf decoction was drunk with tea to release stomach and burn problems [23, 24]. The antimicrobial, anticancer, and antioxidant activities of *N. deflersiana* are documented [25]. Recently, we have reported the positive effects of *N. deflersiana* on human breast and lung cancer cell lines [26]. However, until the present, no published data are available on synthesis of nanoparticles using *N. deflersiana* plant. Herein, we report for the first time (i) the silver nanoparticles (ND-AgNPs) synthesis through a single-step silver ions reduction by *N. deflersiana* plant extract (Figure 1) and (ii) studied the anticancer activity of the biosynthesized silver nanoparticles against human cervical cancer (HeLa) cells.

2. Materials and Methods

2.1. Plant Material, Reagents, and Consumables. *Nepeta deflersiana* (*Lamiaceae*) plants were collected from Shaza Mountains, Saudi Arabia. The identity of the plant was confirmed by Dr. Jakob Thomas, KSU, and a voucher specimen (#15797) was deposited in the herbarium. Cell culture medium, antibiotics-antimycotic solution, trypsin, and FBS were procured from Invitrogen, USA. Plastic wares and other consumables were obtained from Nunc, Denmark. Other chemicals/reagents used in this study were purchased from Sigma, USA.

2.2. Preparation of Plant Extract. The aerial part of *N. deflersiana* was collected and washed several times with distilled water to remove dust and was dried under shade. The air-dried plant was cut into small pieces, macerated in distilled water, filtered under gravity, and the solvent evaporated under reduced pressure using a rotary evaporator. The dried extract was kept at 4°C (Figure 1).

2.3. Synthesis of Silver Nanoparticles. The aqueous extract of *N. deflersiana* (500 mg) was dissolved in 100 ml distilled water. Further 10 ml of the above extract was added to 90 ml of 0.1 M AgNO₃ solution. After 24 h incubation, the solution

turned dark brown, which indicates the formation of AgNPs. The solution was then transferred into a round bottom flask and was heated with continuous stirring at 90°C. After 15 min, the centrifugation was done at room temperature and a speed of 9000 rpm. The black powder obtained after washing thrice with distilled water was dried overnight in an oven at 80°C.

2.4. Characterization of Synthesized Silver Nanoparticles. The optical absorption of green synthesized silver nanoparticles was studied using FTIR (Shimadzu FT-IR Prestige 21) and UV-VIS (Shimadzu UV-VIS 2550, Japan) spectral analysis, respectively. Fourier transmission infrared (FTIR) spectra were recorded using KBr pellets in the range of 4000 to 400 cm⁻¹. The crystalline nature of green synthesized AgNPs was confirmed by XRD pattern. The XRD data were recorded using PANalytical X'Pert X-ray diffractometer using CuK α ($\lambda = 1.54056 \text{ \AA}$). Morphology, size, and electron diffraction pattern were examined by SEM (JSM-7600F, Japan) and TEM (JEM-2100F, Japan) at a voltage 200 kV, respectively. EDX analysis was used to confirm the presence of elemental silver in green synthesized AgNPs.

2.5. Cytotoxicity by MTT Assay. Cytotoxicity of ND-AgNPs was examined by using MTT assay according to the method in [27]. In brief, HeLa cells obtained from American Type Culture Collection, USA, were plated in 96-well plates at a density of 1×10^4 cells/well. Cells were exposed to 1–100 $\mu\text{g/ml}$ ND-AgNPs for 24 h. Following this, MTT was added in the wells, and plates were incubated for 4 h further. The reaction mixture was taken out and 200 $\mu\text{l/well}$ DMSO was added and mixed several times by pipetting up and down. The absorbance of plates was measured at 550 nm. The results were expressed as percentage of control.

2.6. Cytotoxicity by Neutral Red Uptake (NRU) Assay. Cytotoxicity by NRU assay was performed using the procedure [27]. Briefly, HeLa cells were treated with 1–100 $\mu\text{g/ml}$ ND-AgNPs for 24 h. Then, cells were washed with PBS twice and incubated further in 50 $\mu\text{g/ml}$ of neutral red containing medium for 3 h. The cells were washed off with a solution (1% CaCl₂ and 0.5% formaldehyde). The dye was extracted in a mixture of 1% acetic acid and 50% ethanol. The plates were measured at 550 nm. The results were expressed as percentage of control.

2.7. Morphological Analysis. The changes in the morphology were observed under the microscope to determine the alterations induced by ND-AgNPs in HeLa cells treated with 1 $\mu\text{g/ml}$ to 100 $\mu\text{g/ml}$ of ND-AgNPs for 24 h. Images of the cells were grabbed at 20x by using the phase contrast inverted microscope (Olympus CKX 41, USA).

2.8. Glutathione (GSH) Level. The depletion in GSH level was measured following the protocol [28]. In brief, HeLa

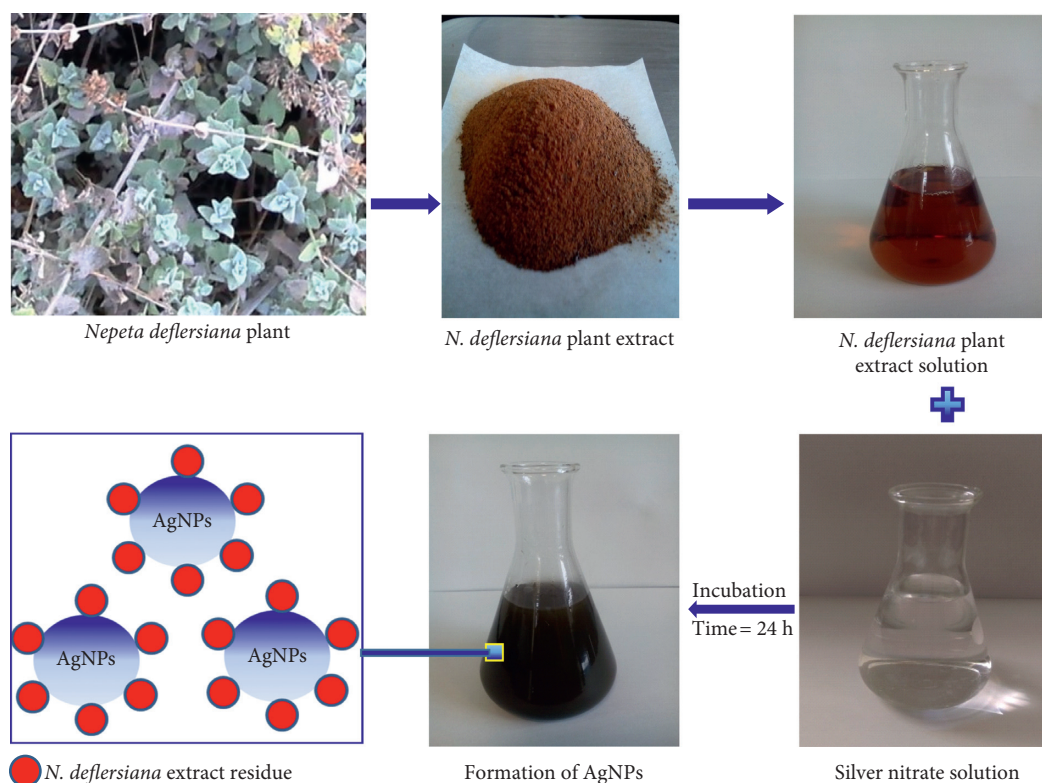


FIGURE 1: Schematic illustration of the green synthesis of silver nanoparticles (ND-AgNPs) using aqueous extract of the *Nepeta deflersiana* plant.

cells exposed to 5–25 $\mu\text{g/ml}$ ND-AgNPs for 24 h were centrifuged, and cellular protein was precipitated in 10% TCA (1 ml). Following this, supernatant was taken by centrifugation at 3000 rpm for 10 min. Then, 2 ml Tris buffer (0.4 M) with EDTA (0.02 M) and 0.01 M 5, 5'-dithionitrobenzoic acid (DTNB) were added in the supernatant. The absorbance was measured at 412 nm after incubating for 10 min at 37°C.

2.9. Lipid Peroxidation (LPO). LPO in ND-AgNPs-exposed HeLA cells were measured following the method [28]. After respective treatment, cells were sonicated in chilled 1.15% potassium chloride solution. Following centrifugation, 1 ml of supernatant was added to 2 ml thiobarbituric acid solution (TCA (15%), TBA (0.7%), and 0.25 N HCl). The resulting solution was then boiled at 100°C for 15 min, and after the centrifugation for 10 min at 1000 \times g, the absorbance was measured at 550 nm.

2.10. ROS Generation. The intracellular ROS generation was measured using 2, 7-dichlorodihydrofluorescein diacetate (DCFH-DA) dye [28]. In brief, HeLA cells were treated with different concentrations (10–50 $\mu\text{g/ml}$) of ND-AgNPs for 24 h. The cells were then with DCFH-DA (5 μM) at 37°C for 1 h. The cell pellet was collected in PBS (500 μl) by centrifugation at 3000 rpm for 5 min. Then, the cells were analysed using flow cytometer.

2.11. Mitochondrial Membrane Potential (MMP). The MMP level in HeLA cells was measured using the method defined by Zhang et al. [29]. In brief, HeLA cells were treated with 10 to 50 $\mu\text{g/ml}$ of ND-AgNPs for 24 h. Then, treated and untreated cells were incubated with rhodamine-123 (5 $\mu\text{g/ml}$) for 1 h at 37°C in dark. Cells were washed twice, and finally, cell pellets were resuspended in PBS (500 μl). MMP was measured by using flow cytometer.

2.12. Cell Cycle Analysis. ND-AgNPs-induced changes in cell cycle were measured using the protocol [30]. In brief, HeLa cells were exposed for 24 h at 10–50 $\mu\text{g/ml}$ ND-AgNPs. After the treatment, cells were fixed in chilled 70% ethanol for 1 h. Then, cells were washed twice by centrifugation, and cells were stained with propidium iodide for 60 min in dark. The stained cells were acquired by flow cytometer.

2.13. Apoptosis Assay. The apoptosis/necrosis induced by ND-AgNPs in HeLA cells were analysed using Annexin-V and 7-AAD Kit (Beckman Coulter) following the manufacturer's protocol. The amount of apoptosis/necrosis in the treated HeLA cells was analysed by flow cytometry following the protocol [31].

2.14. Statistical Analysis. Data were statistically analysed by ANOVA using the post hoc Dunnett's test. Value $p < 0.05$ was considered as a significant level between the exposed

and control sets. The results are presented as mean \pm standard deviation of three experiments.

3. Result and Discussion

3.1. Synthesis and Characterization of ND-AgNPs. Plant extract of *N. deflersiana* was used for the synthesis of ND-AgNPs under facile conditions. The colorless silver nitrate solution (Figure 1) turned dark brown indicating the formation of silver nanoparticles (AgNPs). The occurrence of brown color can be attributed to the surface plasmons [32], arising from the collective oscillations of valance electrons in the electromagnetic field of incident radiation. Figure 2(a) shows the UV-V is spectra of the synthesized AgNPs, giving the plasmon resonance at 400 nm. The characteristic λ max for AgNPs is in the range of 400–500 nm [33]. The position and shape of the surface plasmon absorption is dependent on the shape and size of particles formed, their interparticle distance, and the dielectric constant of the surrounding medium [34, 35]. Similar observations are reported earlier [32, 36]. FTIR measurements were carried out to identify the various functional groups in biomolecules responsible for the reduction of silver ions to AgNPs and capping/stabilization of AgNPs. The band intensities in different region of spectra for *N. deflersiana* extract (Figure 2(b)) and biosynthesized silver nanoparticles (Figure 2(c)) were analysed. The similarities between the two FTIR spectra, with some marginal shifts in peaks clearly indicate the plant extract is also acting as a capping agent. The *N. deflersiana* plant extract showed a number of peaks reflecting a complex nature of the plant extract. The shift in peaks at 3426 cm^{-1} corresponding to NH stretching of amide (II) band or C-O stretching or O-H stretching vibration implicated that their groups may be directly involved in the process of synthesis of AgNPs. Further, peak shifts from 1689 cm^{-1} to 1608 cm^{-1} indicated the possible involvement of C=O stretching or C-N bending in the amide group. Besides, the peak shifts from 1461 cm^{-1} to 1381 cm^{-1} suggest the involvement of C-H or O-H bending vibration of methyl, methylene, or alcoholic group in the reduction of Ag. Moreover, the observed peaks are more characteristic of flavonoids and terpenoids [37] that are present in the *Nepeta* species [25, 26]. It could be speculated that these secondary metabolites are responsible for the synthesis/stabilization of ND-AgNPs.

The crystalline structure of the green synthesized AgNPs was determined by XRD technique. Figure 2(d) displays the XRD pattern of synthesized AgNPs. The Bragg reflection with 2θ values of 37.89, 44.23, 64.26, and 77.24 corresponding to (111), (200), (220), and (311) sets of lattice planes, respectively, is observed. These can be indexed to the face centered cubic (fcc) structure of the synthesized AgNPs. The crystalline size of the AgNPs was determined by using Debye–Scherrer equation [38]:

$$D = \frac{0.9\lambda}{\beta \cos \theta} \quad (1)$$

Where D is the grain size, λ is the wavelength of X-ray (1.54056 \AA), and β is the full width at half maxima of the diffraction peak (in radians).

The average grain size determined by broadening of (111) reflection is estimated to be around 33 nm. Similar results have been reported earlier [39]. The absence of any reflection other than belonging to the silver lattice clearly indicates that the synthesized AgNPs lattice was unaffected by other molecules in the extract of plant. The scanning electron microscopy (SEM) and transmission electron microscopy (TEM) was employed to study the morphological and structural features of synthesized AgNPs. The SEM image (Figure 3(a)) shows that relatively spherical and uniform nanoparticles are formed. Some of the larger particles seen may be due to aggregation of nanoparticles induced by evaporation of solvent during sample preparation [40]. The TEM image (Figure 3(b)) revealed the nanoparticles formed have a narrow size distribution. The average size was about 33 nm, supporting the results of XRD further. Further, the energy-dispersion X-ray (EDX) spectroscopy study was employed to detect the existence of elemental silver. Figure 3(c) shows the EDX image of *N. deflersiana* synthesized AgNPs. The results clearly indicate an intense signal at approximately 2.98 KeV corresponding to the presence of metallic silver nanocrystals, occurring due to surface plasmon resonance (SPR) [41]. The other intense signal at around 0.0–0.5 KeV represents the characteristic absorption for oxygen and carbon. This indicates the presence of *N. deflersiana* plant extract as a capping ligand on the surface of AgNPs.

3.2. Cytotoxicity Assessments of ND-AgNPs by MTT and NRU Assays. The key results obtained by MTT and NRU assays in HeLA cells exposed to $1\text{ }\mu\text{g/ml}$ to $100\text{ }\mu\text{g/ml}$ for 24 h are summarized in Figures 4(a) and 4(b). The results exhibited a concentration dependent decrease in the viability of HeLA cells. The cell viability was recorded as 86% and 29% in ND-AgNPs at $2\text{ }\mu\text{g/ml}$ and $5\text{ }\mu\text{g/ml}$ concentrations, respectively; however, the maximum decrease in cell viability was measured as 9% each at 10, 25, 50, and $100\text{ }\mu\text{g/ml}$ of ND-AgNPs (Figure 4(a)). Like MTT assay, a concentration-dependent decrease in cell viability of HeLA cells exposed to ND-AgNPs was also observed by NRU assay. The cell viability was recorded as 87% and 43% in ND-AgNPs at $2\text{ }\mu\text{g/ml}$ and $5\text{ }\mu\text{g/ml}$ concentrations, respectively; however, the maximum decrease in cell viability was measured as 23% at $100\text{ }\mu\text{g/ml}$ of ND-AgNPs (Figure 4(b)). In this study, the cytotoxicity assessments were performed using two independent end points (MTT and NRU) assays [42]. The MTT, a colorimetric assay is based on the mitochondrial dehydrogenase enzyme of viable cells [43]; however, NRU assay is based on the lysosomal integrity of viable cells [44]. The cytotoxic responses of the ND-AgNPs, suggesting that biosynthesized AgNPs could contribute in search of alternative chemotherapeutic agent. Our results showed more than 50% of cell death even at $5\text{ }\mu\text{g/ml}$ of ND-AgNPs. The cytotoxic effects induced by ND-AgNPs at lower concentrations could be due to the plant components attached to the AgNPs [45]. The results obtained from this study are also very well supported with various evidences

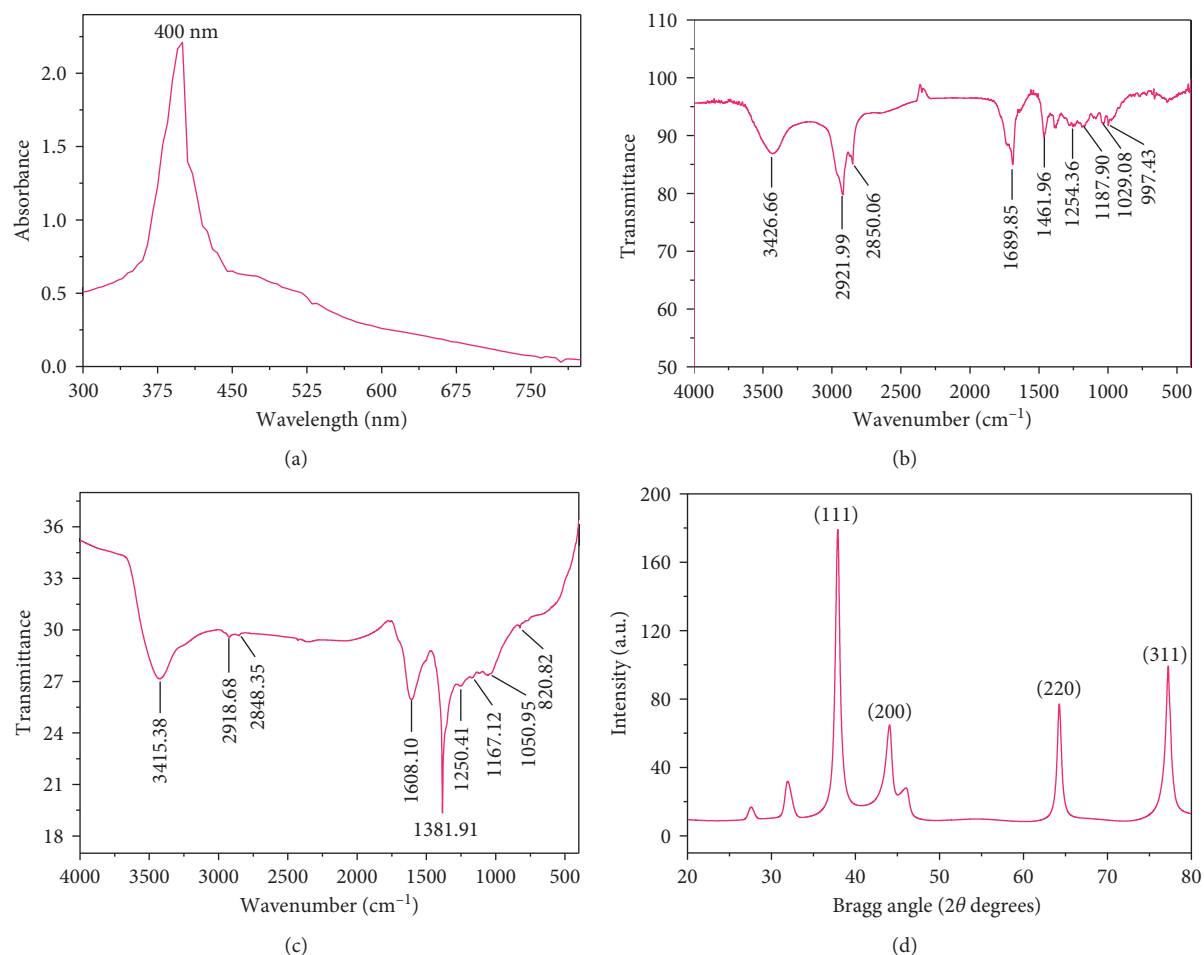


FIGURE 2: Characterization of green synthesized silver nanoparticles (ND-AgNPs) prepared using aqueous extract of the *Nepeta deflersiana* plant. (a) Ultraviolet-visible absorption spectra of synthesized silver nanoparticles (AgNPs). (b) Fourier-transform infrared spectra of *N. deflersiana* extract. (c) Fourier-transform infrared spectra of synthesized silver nanoparticles (ND-AgNPs). (d) X-ray powder diffraction pattern of synthesized silver nanoparticles (ND-AgNPs).

for the cytotoxic effect of biosynthesized AgNPs using *Annona squamosa* leaf extract against the breast cancer MCF-7 cell line [46], *Piper longum* leaf extracts against Hep-2 cancer cell line [47], and *Morinda citrifolia* against HeLa cell lines [48] *in vitro*.

3.3. Morphological Analysis under the Microscope. The alterations observed in the morphology of HeLa cells treated with ND-AgNPs at 1–100 $\mu\text{g}/\text{ml}$ for 24 h are presented in Figure 4(c). There was no significant change observed in the morphology of control HeLa cells. The control cells appeared in normal shape and were attached to the surface. However, the HeLa cells exposed to ND-AgNPs lost their typical shape and cell adhesion capacity, shrank, and decreased the cell density. These kind of changes have also been reported using plant synthesized AgNPs in different cancer cell lines [46], suggesting that the cytotoxic effect of synthesized AgNPs may be due to the antineoplastic nature and their capability *via* numerous molecular mechanism to induce cell death [45].

3.4. Glutathione Depletion and Lipid Peroxidation Level. Figures 5(a) and 5(b) summarize the decrease in glutathione level and increase in the lipid peroxidation in HeLa cells exposed to ND-AgNPs at 5–25 $\mu\text{g}/\text{ml}$ concentrations for 24 h. The results indicate a concentration-dependent decrease in glutathione level. The depletion in the GSH was found to be 40%, 55%, and 69% at 5, 10, and 25 $\mu\text{g}/\text{ml}$, respectively, as compared to control (Figure 5(a)). The effect of ND-AgNPs-induced lipid peroxidation in HeLa cells exposed for 24 h is shown in Figure 5(b). A concentration-dependent statistically significant increase in the LPO level was also observed in HeLa cells. The increase in LPO level was observed as 25%, 56%, and 65% at 5, 10, and 25 $\mu\text{g}/\text{ml}$ concentrations of ND-AgNPs, respectively (Figure 5(b)). Oxidative stress is known to be involved in the nanoparticles-induced cell death [49]. As observed in this study, the decrease in glutathione level and an increase in the level of lipid peroxidation suggest the role of oxidative stress in cell death in HeLa cell line exposed to ND-AgNPs. Our results are very well supported by previous report where a decrease in glutathione level and an increase in lipid

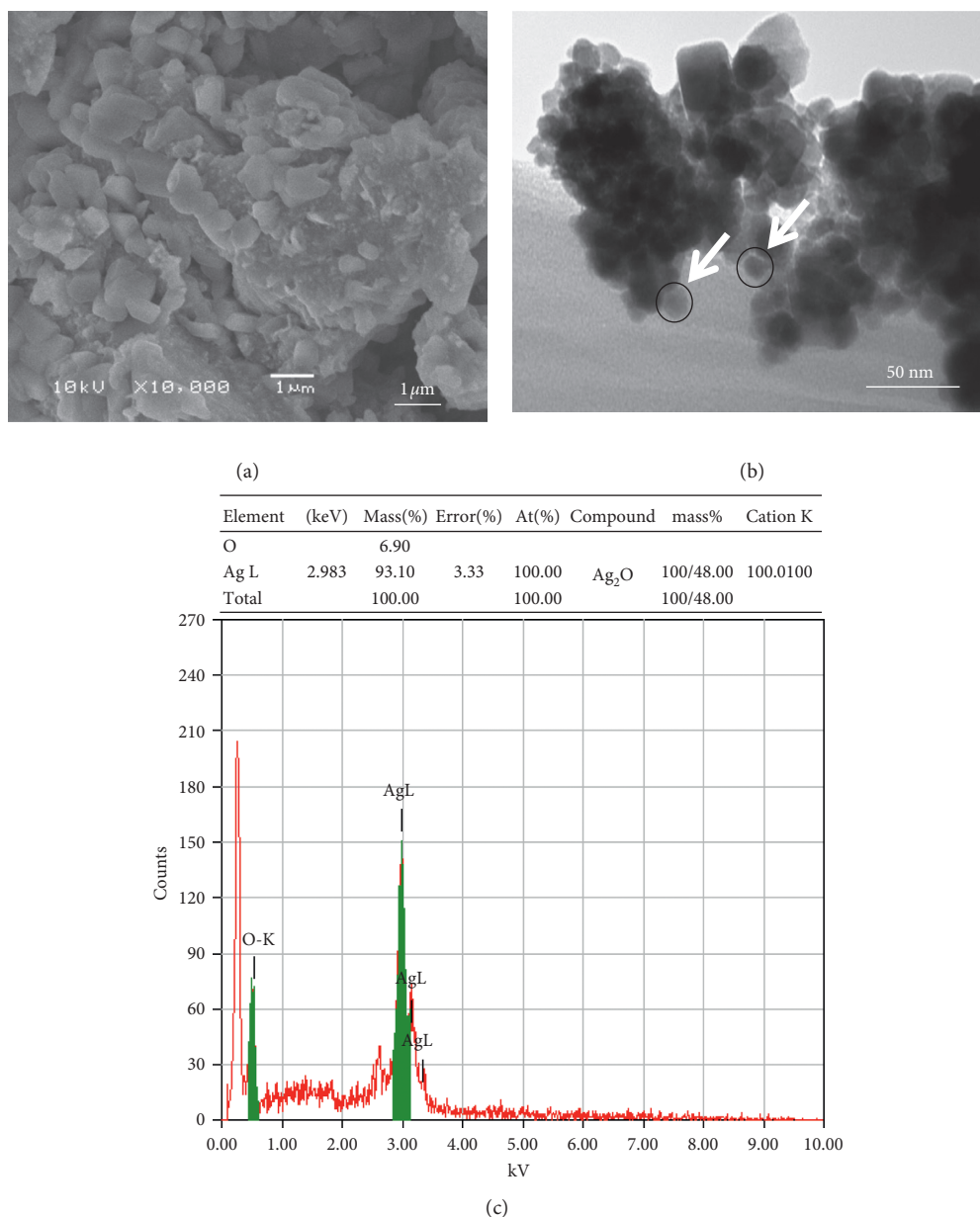


FIGURE 3: (a) SEM image of the green synthesized silver nanoparticles (AgNPs); (b) TEM image of green synthesized silver nanoparticles (ND-AgNPs) at 50 nm; (c) energy-dispersive X-ray spectrum of green synthesized silver nanoparticles (ND-AgNPs).

peroxidation level have been observed due to the exposure of nanoparticles in various cell lines [49, 50].

3.5. Determination of Intracellular Reactive Oxygen Species (ROS). The result obtained from ROS generation in HeLa cells exposed to ND-AgNPs for 24 h is shown in Figures 6(a) and 6(b). A statistically significant induction in ROS generation was measured in HeLa cells exposed to ND-AgNPs at 10, 25, and 50 $\mu\text{g/ml}$ concentrations. As shown in Figures 6(a) and 6(b), an increase of 207%, 167%, and 160% was observed in ROS generation at 5, 10, and 25 $\mu\text{g/ml}$, respectively, as compared to untreated control. Nanoparticles are suggested to induce their toxicity

through oxidative stress by generating reactive oxygen species (ROS) involved in a variety of different cellular processes ranging from apoptosis and necrosis to cell proliferation and carcinogenesis [51]. It has been reported that nanoparticles increase the ROS generation at cellular level. To investigate the potential role of ND-AgNPs in HeLa cell line, intracellular ROS generation was assessed by HDCF-DA dye using flow cytometer. An increase in the ROS level observed in this study established that AgNPs induced ROS generation, which leads to oxidative stress and cell death. Furthermore, consistent with previous reports that plant-synthesized AgNPs have capacity to induce ROS generation that can result in apoptotic cell death [52].

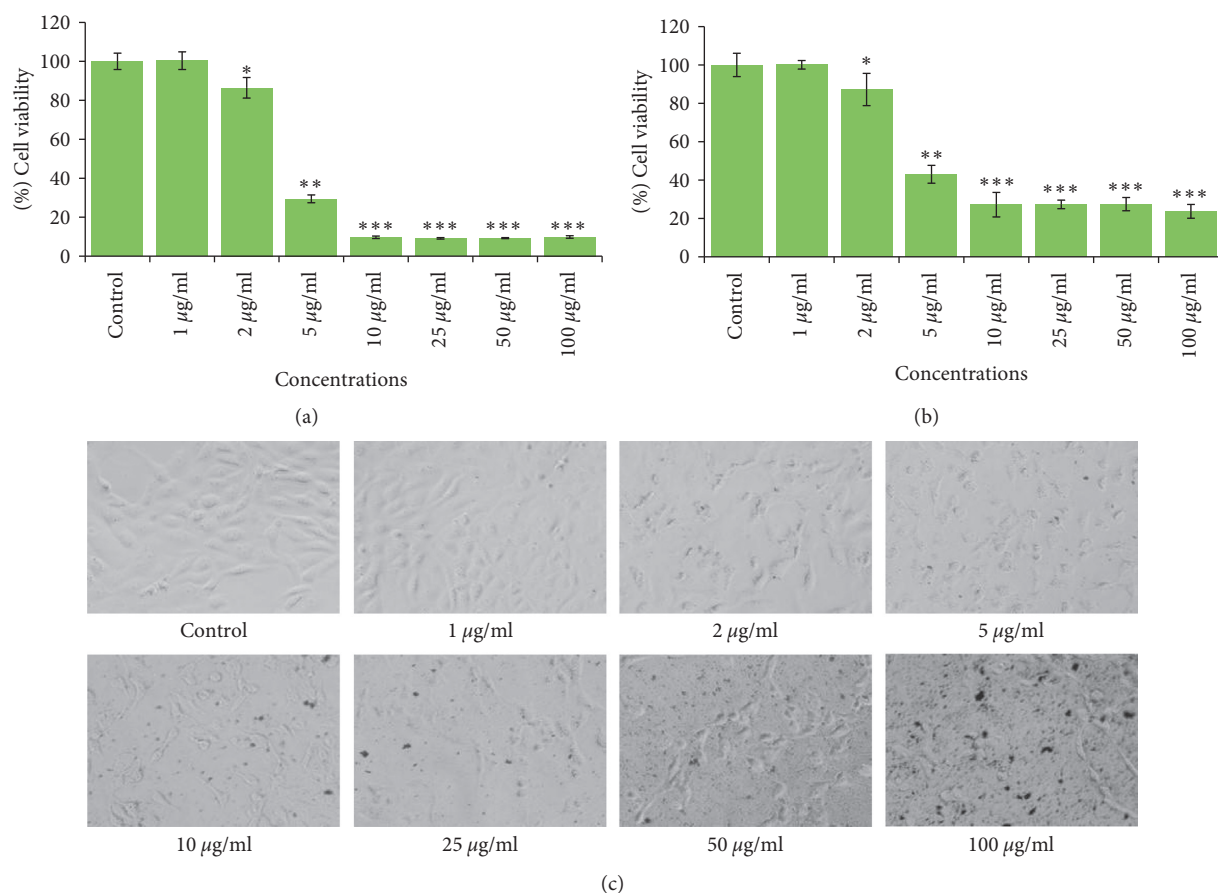


FIGURE 4: Cytotoxicity assessment in HeLA cells following the exposure of various concentrations of ND-AgNPs for 24 h: (a) MTT assay; (b) neutral red uptake assay. (c) Morphological changes. Images were taken using an inverted phase contrast microscope at 20x magnification. * $p < 0.05$, ** $p < 0.01$, *** $p < 0.001$ vs control.

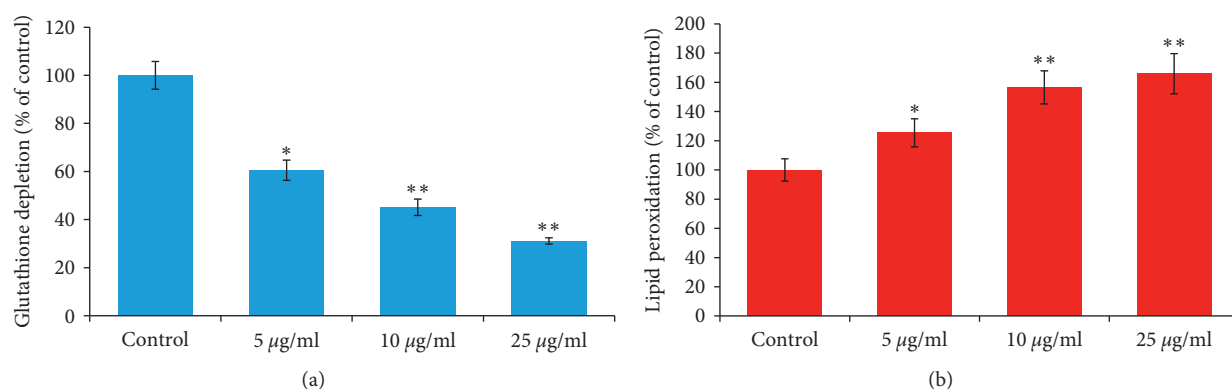


FIGURE 5: ND-AgNPs-induced oxidative stress in HeLA cells exposed for 24 h: (a) glutathione depletion; (b) lipid peroxidation. Results are expressed as the mean \pm S.D. of three independent experiments. * $p < 0.01$, ** $p < 0.001$ vs control.

3.6. *Mitochondrial Membrane Potential (MMP)*. Figures 6(c) and 6(d) illustrate the change in the MMP level. HeLA cells were treated for 24 h at 10–25 µg/ml of synthesized ND-AgNPs. A significant induction in MMP level was found in HeLA cells. The induction in MMP level was found to be 109%, 121%, and 114% at 5, 10, and 25 µg/ml, respectively, compared to control set (Figures 6(c) and 6(d)).

The results of this study suggested that the integrity of mitochondrial membrane might be involved in AgNPs-induced HeLa cell death. It is well documented that the ROS generation at high level can lead to cellular damage by resulting mitochondrial membrane damage, which can then induce toxicity [53, 54]. Based on cationic fluorescent probe Rh123 dye, the induction in MMP level indicated the role of

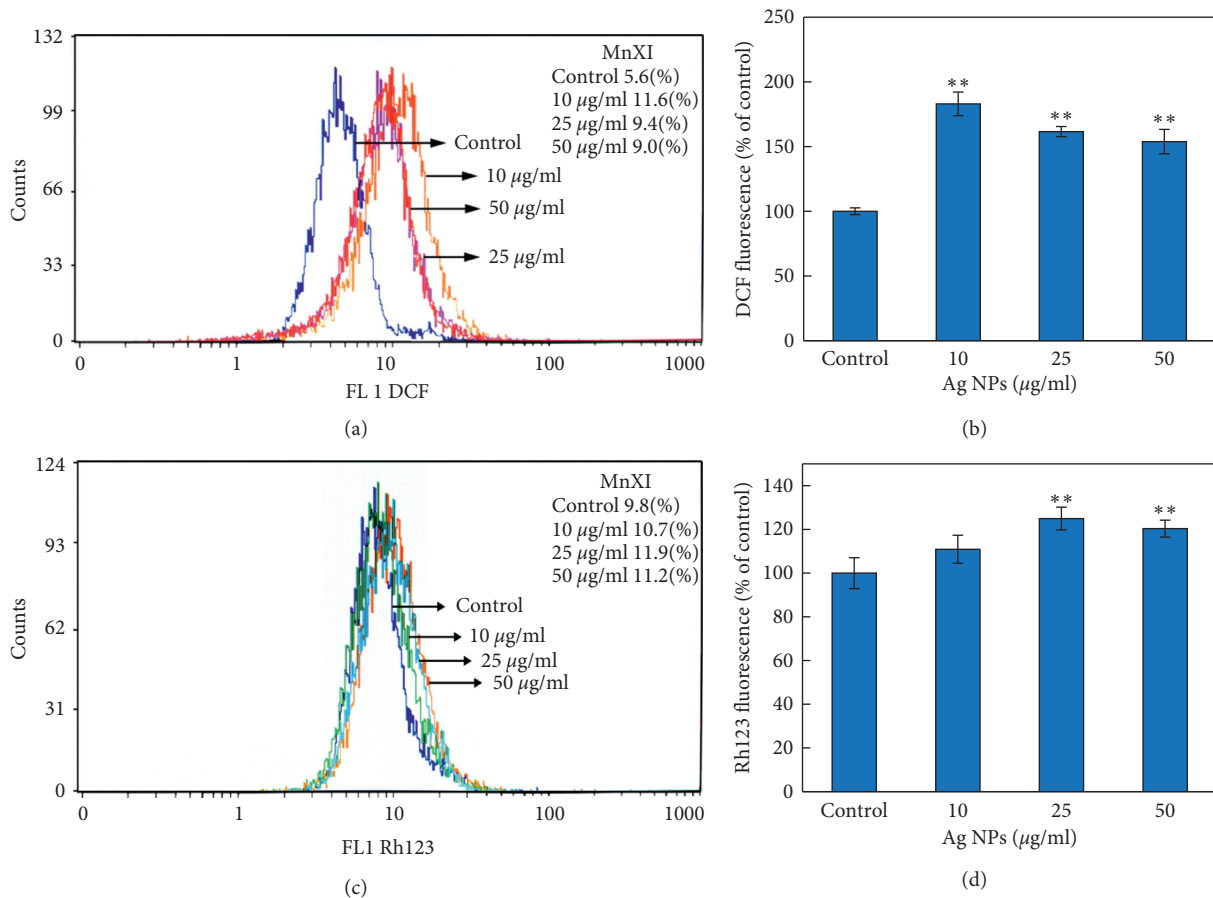


FIGURE 6: Flow cytometric analysis of intracellular ROS generation and mitochondrial membrane potential in HeLA cells exposed to ND-AgNPs for 24 h (a) Representative spectra of fluorescent DCF as a function of ND-AgNPs concentration. (b) Comparative analysis of the fluorescence enhancement of DCF with increasing concentrations of ND-AgNPs. (c) Representative spectra of fluorescence of Rh123 as a function of ND-AgNPs concentrations measured using a flow cytometer. (d) Comparative analysis of the fluorescence enhancement of Rh123 with increasing concentrations of ND-AgNPs. Each histogram represents mean \pm S.D. values of DCF and Rh123 fluorescence obtained from three independent experiments. ** $p < 0.01$ versus control.

reactive oxygen species generation and oxidative stress in the AgNPs-induced HeLA cell death due to free radicals generation [55].

3.7. Cell Cycle Analysis. The results of cell cycle analysis in HeLA cell lines exposed to ND-AgNPs at 10–50 $\mu\text{g/ml}$ for 24 h are represented in Figure 7. The flow cytometric measurement of propidium iodide-stained control and ND-AgNPs-treated HeLA cells showed an increase in apoptotic SubG1 peak. A significant increase in SubG1 arrest was observed at 50 $\mu\text{g/ml}$ concentrations of ND-AgNPs-treated HeLA cells (Figure 7). The increase in the SubG1 (apoptotic) population found in this study suggests that ND-AgNPs-treated HeLA cells were not able to go through G2 checkpoint; therefore, G2/M transition was found to be affected. The apoptosis induction due to the presence of SubG1 peak in the process of cell cycle suggests the role of early and late apoptotic/necrotic pathway [56, 57].

3.8. Apoptosis/Necrosis Assessment Using Annexin V-PE and 7-AAD. The results obtained from the induction of

apoptosis/necrosis using flow cytometry are summarized in Figure 8. The flow cytometry data clearly showed that ND-AgNPs induced cell death in HeLA cells. Based on the Annexin V-PE/7-ADD staining, 94.2% of HeLA control cells were found alive with values of 0.56%, 3.31%, and 1.9% of cells, which are normal process for cells growing in cultures. The HeLA cells exposed to ND-AgNPs significantly increased the late apoptotic and necrotic cells as compared with untreated control cells. An increase in the percentage of apoptotic and necrotic cells was found with the values of 30.3–69.8% and 18.8–25.3% between 10 $\mu\text{g/ml}$ and 50 $\mu\text{g/ml}$ ND-AgNPs concentrations, respectively (Figure 8). Even at lower concentration, i.e., 10 $\mu\text{g/ml}$, ND-AgNPs were found to induce apoptotic and necrotic cell death. It is well known that high amount of ROS generation could lead to apoptotic and necrotic cell death [58]. The excessive ROS generation has been linked with the substantial DNA damage and apoptosis/necrosis [59]. Our results are in well accordance with the recent reports that have shown apoptosis cell death due to the exposure of nanoparticles [60], including the exposure of plant-synthesized silver nanoparticles [52].

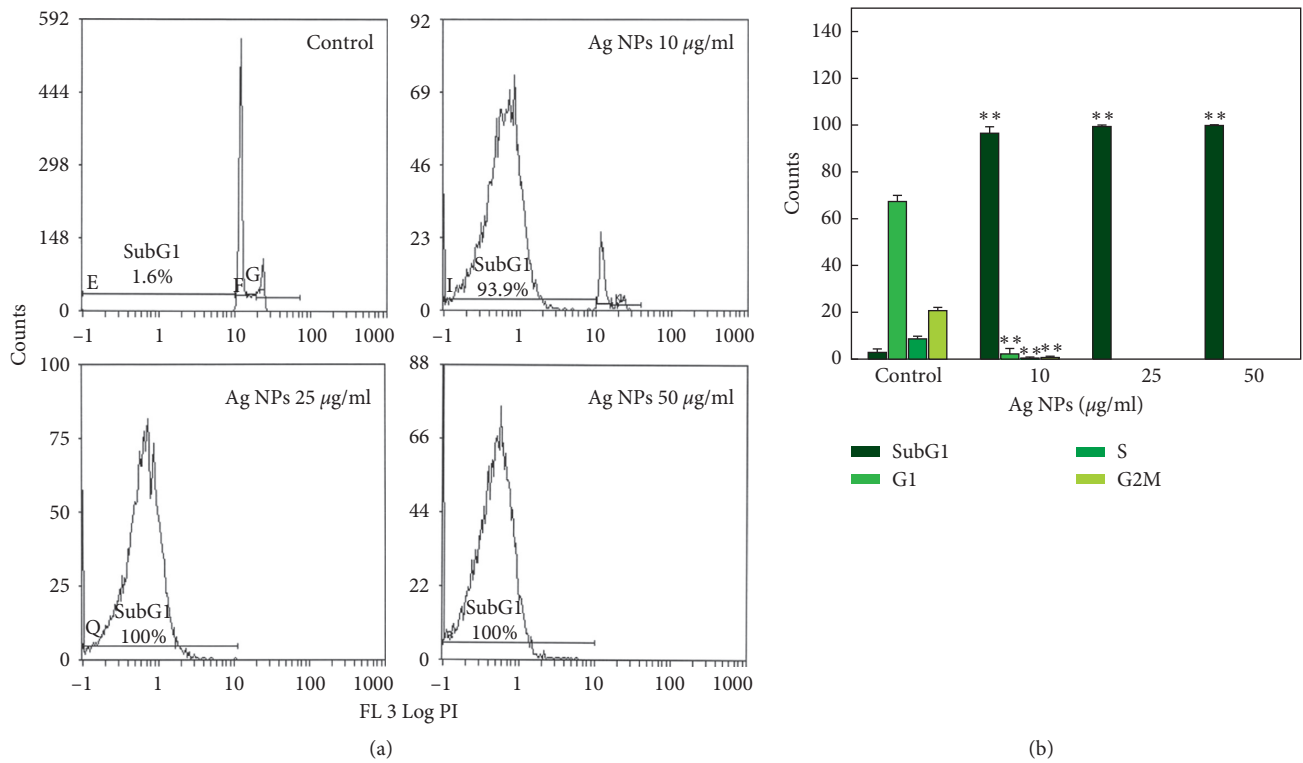


FIGURE 7: Cell cycle analysis in HeLa cells exposed to 10–50 µg/ml concentrations of ND-AgNPs for 24 h. (a) Representative flow cytometric image exhibiting changes in the progression of cell cycle. SubG1 in each micrograph represents the percentage of cells in the SubG1 phase. (b) Each histogram represents the percentage of cells arrested in different phases of cell cycle. Results are expressed as the mean ± S.D. of three independent experiments. ** $p < 0.001$ vs control.

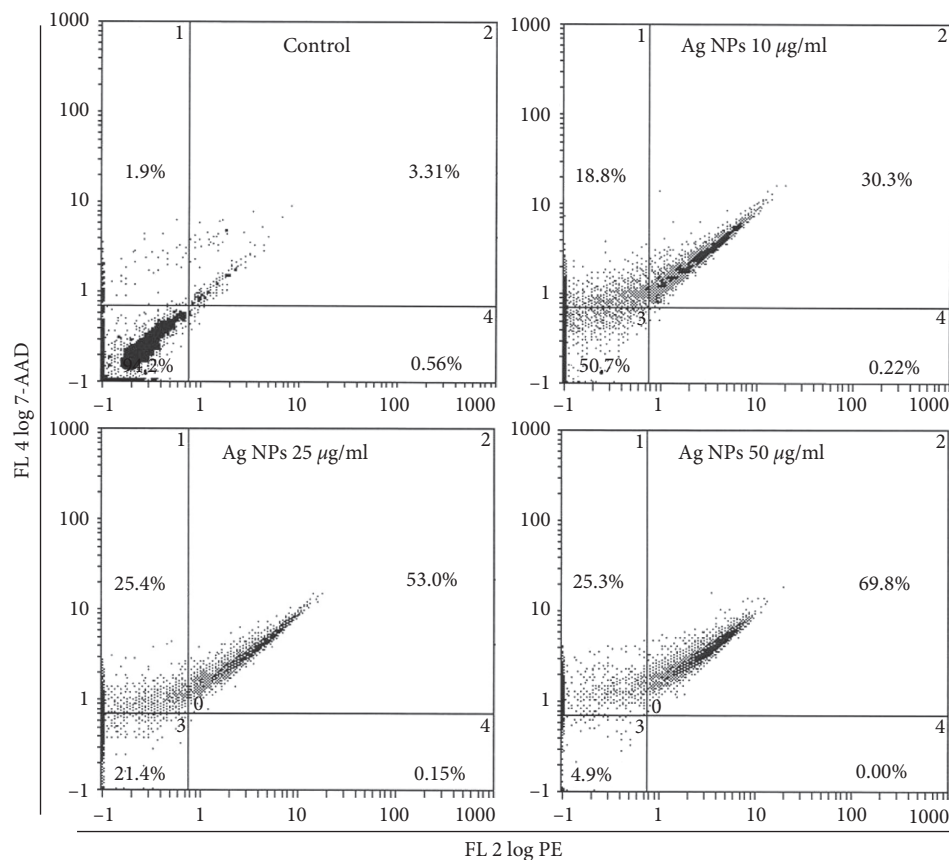


FIGURE 8: Annexin V-PE (phycoerythrin) and 7-AAD (7-amino actinomycin D) assay. Bivariate flow cytometry analysis of HeLa cells treated with different concentrations of ND-Ag NPs. The scatter plots show early apoptotic, late apoptotic, and necrotic cells following 24 h treatment.

4. Conclusions

This investigation demonstrated the biosynthesis of silver nanoparticles (AgNPs) for the first time, via a single-step reduction of silver ions using *Nepeta deflersiana* plant and its anticancer potential against human cervical cancer (HeLa) cells. Our results showed that biosynthesized AgNPs (ND-AgNPs) induced a concentration-dependent cytotoxicity in HeLa cells. ND-AgNPs were also found to induce oxidative stress as observed by the increase in ROS and LPO level and the decrease in GSH level. The increase in the intracellular ROS generation was found eventually to trigger the development of mitochondrial membrane damage and cell cycle alterations. This study also showed that ND-AgNPs have the capacity of inducing apoptosis and necrosis cell death of HeLa cells through SubG1 cell cycle arrest. Thus, our findings suggest the anticancer potential of biosynthesized ND-AgNPs against human cervical cancer cells and could play an important role in the development of new therapeutic agent for the treatment of cancer.

Data Availability

The data used to support the findings of this study are included within the article.

Conflicts of Interest

The authors declare that they have no conflicts of interest.

Acknowledgments

This research project was supported by a grant from the “Research Centre of the Female Scientific and Medical Colleges”, Deanship of Scientific Research, King Saud University.

References

- [1] K. Yokohama and D. R. Welchons, “The conjugation of amyloid beta protein on the gold colloidal nanoparticles surfaces,” *Nanotechnology*, vol. 18, no. 10, pp. 105101–105107, 2007.
- [2] V. K. Sharma, R. A. Yngard, and Y. Lin, “Silver nanoparticles: green synthesis and their antimicrobial activities,” *Advances in Colloid and Interface Science*, vol. 145, no. 1-2, pp. 83–96, 2009.
- [3] K. K. Wong and X. Liu, “Silver nanoparticles—the real “silver bullet” in clinical medicine?,” *MedChemComm*, vol. 1, no. 2, pp. 125–131, 2010.
- [4] D. R. Monteiro, S. Silva, M. Negri et al., “Silver nanoparticles: influence of stabilizing agent and diameter on antifungal activity against *Candida albicans* and *Candida glabrata* biofilms,” *Letters in Applied Microbiology*, vol. 54, no. 5, pp. 383–391, 2012.
- [5] C. Krishnaraj, R. Ramachandran, K. Mohan, and P. T. Kalaichelvan, “Optimization for rapid synthesis of silver nanoparticles and its effect on phytopathogenic fungi,” *Spectrochimica Acta Part A: Molecular and Biomolecular Spectroscopy*, vol. 93, pp. 95–99, 2012.
- [6] F. Martínez-Gutierrez, E. P. Thi, J. M. Silverman et al., “Antibacterial activity, inflammatory response, coagulation and cytotoxicity effects of silver nanoparticles,” *Nano-medicine: Nanotechnology, Biology and Medicine*, vol. 8, no. 3, pp. 328–336, 2012.
- [7] R. Gottesman, S. Shukla, N. Perkas, L. A. Solovoyov, Y. Nitzan, and A. Gedanken, “Sonochemical coating of paper by microbicidal silver nanoparticles,” *Langmuir*, vol. 27, no. 2, pp. 720–726, 2011.
- [8] I. Osório, R. Igreja, R. Franco, and J. Cortez, “Incorporation of silver nanoparticles on textile materials by an aqueous procedure,” *Materials Letters*, vol. 75, pp. 200–203, 2012.
- [9] F. Martínez-Gutierrez, P. L. Olive, A. Banuelos et al., “Synthesis, characterization, and evaluation of antimicrobial and cytotoxic effect of silver and titanium nanoparticle,” *Nano-medicine*, vol. 6, no. 5, pp. 681–688, 2010.
- [10] J. Favero, P. Corbeau, M. Nicolas et al., “Inhibition of human immunodeficiency virus infection by the lectin jacalin and by a derived peptideshowing a sequence similarity with gp120,” *European Journal of Immunology*, vol. 23, no. 1, pp. 179–185, 1993.
- [11] K. Okitsu, A. Yue, S. Tanabe, H. Matsumoto, and Y. Yobiko, “formation of colloidal gold nanoparticles in an ultrasonic field: control of rate of gold (III) reduction and size of formed gold particles,” *Langmuir*, vol. 17, no. 25, pp. 7717–7720, 2001.
- [12] R. R. Naik, S. J. Stringer, G. Agarwal, S. E. Jones, and M. O. Stone, “Biomimetic synthesis and patterning of silver nanoparticles,” *Nature Materials*, vol. 1, no. 3, pp. 169–172, 2002.
- [13] K. B. Narayanan and N. Sakthivel, “Biological synthesis of metal nanoparticles by microbes,” *Advances in Colloid and Interface Science*, vol. 156, no. 1-2, pp. 1–13, 2010.
- [14] D. Mandal, M. E. Bolander, D. Mukhopadhyay, G. Sarkar, and P. Mukherjee, “The use of microorganisms for the formation of metal nanoparticles and their application,” *Applied Microbiology and Biotechnology*, vol. 69, no. 5, pp. 485–492, 2006.
- [15] M. Kowshik, S. Ashtaputre, S. Kharrazi et al., “Extracellular synthesis of silver nanoparticles by a silver-tolerant yeast strain MKY3,” *Nanotechnology*, vol. 14, no. 1, pp. 95–100, 2002.
- [16] P. Mukherjee, A. Ahmad, D. Mandal et al., “Fungus-mediated synthesis of silver nanoparticles and their immobilization in the mycelial matrix: a novel biological approach to nanoparticle synthesis,” *Nano Letters*, vol. 1, no. 10, pp. 515–519, 2001.
- [17] S. Iravani, “Green synthesis of metal nanoparticles using plants,” *Green Chemistry*, vol. 13, no. 10, pp. 2638–2650, 2011.
- [18] K. Kalishwaralal, V. Deepak, S. R. K. Pandian et al., “Bio-synthesis of silver and gold nanoparticles using *Brevibacterium casei*,” *Colloids and Surfaces B: Biointerfaces*, vol. 77, no. 2, pp. 257–262, 2010.
- [19] X. Gao, Y. Lu, L. Fang et al., “Synthesis and anticancer activity of some novel 2-phenazinamine derivatives,” *European Journal of Medicinal Chemistry*, vol. 69, pp. 1–9, 2013.
- [20] S. McGuire, “World cancer report 2014. Geneva, Switzerland: world health organization, international agency for research on cancer, WHO press, 2015,” *Advances in Nutrition*, vol. 7, no. 2, pp. 418–419, 2016.
- [21] D. J. Newman and G. M. Cragg, “Natural products as sources of new drugs over the 30 years from 1981 to 2010,” *Journal of Natural Products*, vol. 75, no. 3, pp. 311–335, 2012.
- [22] M. A. Rahman, J. S. Mossa, M. S. Al-Said, and M. A. Al-Yahya, “Medicinal plant diversity in the flora of Saudi Arabia 1: a report on seven plant families,” *Fitoterapia*, vol. 75, no. 2, pp. 149–161, 2004.

- [23] J. S. Mossa, M. A. Al-Yahya, and I. A. Al-Meshal, *Medicinal Plants of Saudi Arabia*, King Saud University Press, Riyadh, Saudi Arabia, 2000.
- [24] C. Hedge, "Studies in the flora of Arabia 2, some new and interesting species of labiatae," *Notes from the Royal botanic Garden Edinburgh*, vol. 40, no. 2, pp. 63–74, 1982.
- [25] R. A. Mothana, R. Gruenert, P. J. Bednarski, and U. Lindequist, "Evaluation of the in vitro anticancer, antimicrobial and antioxidant activities of some Yemeni plants used in folk medicine," *De Pharmazie*, vol. 64, no. 4, pp. 260–268, 2009.
- [26] M. M. Al-Oqail, E. S. Al-Sheddi, M. A. Siddiqui, J. Musarrat, A. A. Al-Khedhairi, and N. N. Farshori, "Anticancer activity of chloroform extract and subfractions of *Nepeta deflersiana* on human breast and lung cancer cells: an in vitro cytotoxicity assessment," *Pharmacognosy Magazine*, vol. 11, no. 44, pp. 598–605, 2015.
- [27] M. A. Siddiqui, M. P. Kashyap, V. Kumar, A. A. Al-Khedhairi, J. Musarrat, and A. B. Pant, "Protective potential of trans-resveratrol against 4-hydroxynonenal induced damage in PC12 cells," *Toxicology in Vitro*, vol. 24, no. 6, pp. 1592–1598, 2010.
- [28] M. A. Siddiqui, H. A. Alhadlaq, J. Ahmad, A. A. Al-Khedhairi, J. Musarrat, and M. Ahamed, "Copper oxide nanoparticles induced mitochondria mediated apoptosis in human hepatocarcinoma cells," *PLoS ONE*, vol. 8, no. 8, Article ID e69534, 2013.
- [29] Y. Zhang, L. Jiang, L. Jiang et al., "Possible involvement of oxidative stress in potassium bromate-induced genotoxicity in human hepG2 cells," *Chemico-Biological Interactions*, vol. 189, no. 3, pp. 186–191, 2011.
- [30] Q. Saquib, A. A. Al-Khedhairi, M. A. Siddiqui, F. M. Abou-Tarboush, A. Azam, and J. Musarrat, "Titanium dioxide nanoparticles induced cytotoxicity, oxidative stress and DNA damage in human amnion epithelial (WISH) cells," *Toxicology in Vitro*, vol. 26, no. 2, pp. 351–361, 2012.
- [31] Q. Saquib, J. Musarrat, M. A. Siddiqui et al., "Cytotoxic and necrotic responses in human amniotic epithelial (WISH) cells exposed to organophosphate insecticide phorate," *Mutation Research/Genetic Toxicology and Environmental Mutagenesis*, vol. 744, no. 2, pp. 125–134, 2012.
- [32] L. Mulfinger, S. D. Solomon, M. Bahadory et al., "Synthesis and study of silver nanoparticles," *Journal of Chemical Education*, vol. 84, no. 2, p. 322, 2007.
- [33] M. Sastry, K. S. Mayyaa, and K. Bandyopadhyay, "pH dependent changes in theoptical properties of carboxylic acid derivatized silver colloid particles," *Colloids and Surfaces A: Physicochemical and Engineering Aspects*, vol. 127, no. 1–3, pp. 221–228, 1997.
- [34] K. L. Kelly, E. Coronado, L. L. Zhao, and G. C. Schatz, "The optical properties of metal nano particles: the influence of size, shape and dielectric environment," *Journal of Physical Chemistry B*, vol. 107, no. 3, pp. 668–677, 2003.
- [35] A. Rai, A. Singh, A. Ahmad, and M. Sastry, "Role of halide ions and temperature on the morphology of biologically synthesized gold nanotriangles," *Langmuir*, vol. 22, no. 2, pp. 736–741, 2006.
- [36] N. E. El-Naggar, N. A. Abdelwahed, and O. M. Darwesh, "Fabrication of biogenic antimicrobial silver nanoparticles by streptomyces aegyptia NEAE 102 as eco-friendly nanofactory," *Journal of Microbiology and Biotechnology*, vol. 24, no. 4, pp. 453–464, 2014.
- [37] A. K. Jha, K. Prasad, V. Kumar, and K. Prasad, "Biosynthesis of silver nanoparticles using Eclipta leaf," *Biotechnology Progress*, vol. 25, no. 5, pp. 1476–1479, 2009.
- [38] H. Borchert, "Determination of nanocrystal sizes: a comparison of TEM, SAXS, and XRD studies of highly monodisperse CoPt3 particles," *Langmuir*, vol. 21, no. 5, pp. 1931–1936, 2005.
- [39] K. D. Arunachalam, L. B. Arun, S. K. Annamalai, and A. M. Arunachalam, "Potential anticancer properties of bioactive compounds of *Gymnema sylvestre* and its bio-functionalized silver nanoparticle," *International Journal of Nanomedicine*, vol. 10, pp. 31–41, 2015.
- [40] P. V. Kumar, S. V. N. Pammi, P. Kollu, K. V. V. Satyanarayana, and U. Shameem, "Green synthesis and characterization of silver nanoparticles using *Boerhaavia diffusa* plant extract and their anti bacterial activity," *Industrial Crops and Products*, vol. 52, pp. 562–566, 2014.
- [41] K. Mallikarjuna, N. J. Sushma, G. Narasimha, L. Manoj, and B. D. P. Raju, "Phytochemical fabrication and characterization of silver nanoparticles by using pepper leaf broth," *Arabian Journal of Chemistry*, vol. 7, no. 6, pp. 1099–1103, 2014.
- [42] D. R. Nogueira, M. Mitjans, M. R. Infante, and M. P. Vinardell, "Comparative sensitivity of tumor and non-tumor cell lines as a reliable approach for in vitro cytotoxicity screening of lysine-based surfactants with potential pharmaceutical applications," *International Journal of Pharmaceutics*, vol. 420, no. 1, pp. 51–58, 2011.
- [43] T. Mosmann, "Rapid colorimetric assay for cellular growth and survival: application to proliferation and cytotoxicity assays," *Journal of Immunological Methods*, vol. 65, no. 1–2, pp. 55–63, 1983.
- [44] E. Borenfreund and J. A. Puerner, "Short-term quantitative in vitro cytotoxicity assay involving an S-9 activating system," *Cancer Letters*, vol. 34, no. 3, pp. 243–248, 1987.
- [45] M. A. Farah, M. A. Ali, S. M. Chen et al., "Silver nanoparticles synthesized from adenium obesum leaf extract induced DNA damage, apoptosis and autophagy via generation of reactive oxygen species," *Colloids and Surfaces B: Biointerfaces*, vol. 141, pp. 158–169, 2016.
- [46] R. Vivek, R. Thangam, K. Muthuchelian, P. Gunasekaran, K. Kaveri, and S. Kannan, "Green biosynthesis of silver nanoparticles from *Annona squamosa* leaf extract and its in vitro cytotoxic effect on MCF-7 cells," *Process Biochemistry*, vol. 47, no. 12, pp. 2405–2410, 2012.
- [47] S. J. P. Jacob, J. S. Finub, and A. Narayanan, "Synthesis of silver nanoparticles using piper longum leaf extracts and its cytotoxic activity against Hep-2 cell line," *Colloids and Surfaces B: Biointerfaces*, vol. 91, pp. 212–214, 2012.
- [48] T. Y. Suman, S. R. Rajasree, A. Kanchana, and S. B. Elizabeth, "Biosynthesis, characterization and cytotoxic effect of plant mediated silver nanoparticles using *Morinda citrifolia* root extract," *Colloids and Surfaces B: Biointerfaces*, vol. 106, pp. 74–78, 2013.
- [49] M. A. Siddiqui, Q. Saquib, M. Ahamed et al., "Molybdenum nanoparticles-induced cytotoxicity, oxidative stress, G2/M arrest, and DNA damage in mouse skin fibroblast cells (L929)," *Colloids and Surfaces B: Biointerfaces*, vol. 125, pp. 73–81, 2015.
- [50] S. M. El-Sonbaty, "Fungus-mediated synthesis of silver nanoparticles and evaluation of antitumor activity," *Cancer Nanotechnology*, vol. 4, no. 4–5, pp. 73–79, 2013.
- [51] S. J. Soenen and M. De Cuyper, "Assessing cytotoxicity of (iron oxide-based) nanoparticles: an overview of different methods exemplified with cationic magnetoliposomes,"

- Contrast Media and Molecular Imaging*, vol. 4, no. 5, pp. 207–219, 2009.
- [52] A. Stroh, C. Zimmer, C. Gutzeit et al., “Iron oxide particles for molecular magnetic resonance imaging cause transient oxidative stress in rat macrophages,” *Free Radical Biology and Medicine*, vol. 36, no. 8, pp. 976–984, 2004.
- [53] S. Dwivedi, M. A. Siddiqui, N. N. Farshori, M. Ahamed, J. Musarrat, and A. A. Al-Khedhairi, “Synthesis, characterization and toxicological evaluation of iron oxide nanoparticles in human lung alveolar epithelial cells,” *Colloids and Surfaces B: Biointerfaces*, vol. 122, pp. 209–215, 2014.
- [54] I. Nicoletti, G. Migliorati, M. C. Pagliacci, F. Grignani, and C. Riccardi, “A rapid and simple method for measuring thymocyte apoptosis by propidium iodide staining and flow cytometry,” *Journal of Immunological Methods*, vol. 139, no. 2, pp. 271–279, 1991.
- [55] S. Ravi, K. K. Chiruvella, K. Rajesh, V. Prabhu, and S. C. Raghavan, “5-isopropylidene-3-ethylrhodanine induce growth inhibition followed by apoptosis in leukemia cells,” *European Journal of Medicinal Chemistry*, vol. 45, no. 7, pp. 2748–2752, 2010.
- [56] P. V. Asharani, M. P. Hande, and S. Valiyaveetil, “Anti-proliferative activity of silver nanoparticles,” *BMC Cell Biology*, vol. 10, no. 1, pp. 65–79, 2009.
- [57] H. Ciftci, M. Turk, U. Tamer, S. Karahan, and Y. Menemen, “Silver nanoparticles: cytotoxic, apoptotic, and necrotic effects on MCF-7 cells,” *Turkish Journal of Biology*, vol. 37, pp. 573–581, 2013.
- [58] R. Foldbjerg, P. Olesen, M. Hougaard, D. A. Dang, H. J. Hoffmann, and H. Autrup, “PVP-coated silver nanoparticles and silver ions induce reactive oxygen species, apoptosis, and necrosis in THP-1 monocytes,” *Toxicology Letters*, vol. 190, no. 2, pp. 156–162, 2009.
- [59] Y. H. Hsin, C. F. Chen, S. Huang, T. S. Shih, P. S. Lai, and P. J. Chueh, “The apoptotic effect of nanosilver is mediated by a ROS-and JNK-dependent mechanism involving the mitochondrial pathway in NIH3T3 cells,” *Toxicology Letters*, vol. 179, no. 3, pp. 130–139, 2008.
- [60] Y. Pan, S. Neuss, A. Leifert et al., “Size-dependent cytotoxicity of gold nanoparticles,” *Small*, vol. 3, no. 11, pp. 1941–1949, 2007.

Research Article

Cytotoxic and Bactericidal Effect of Silver Nanoparticles Obtained by Green Synthesis Method Using *Annona muricata* Aqueous Extract and Functionalized with 5-Fluorouracil

María del Carmen Sánchez-Navarro,¹ Claudio Adrian Ruiz-Torres ²,
Nereyda Niño-Martínez,² Roberto Sánchez-Sánchez,³
Gabriel Alejandro Martínez-Castañón ², I. DeAlba-Montero,² and Facundo Ruiz ²

¹Facultad de Estomatología, Universidad Autónoma de San Luis Potosí (UASLP), Avenida Manuel Nava 2, Zona Universitaria, 78290 San Luis Potosí, Mexico

²Facultad de Ciencias, Universidad Autónoma de San Luis Potosí (UASLP), Avenida Manuel Nava 6, Zona Universitaria, 78290 San Luis Potosí, Mexico

³Instituto Nacional de Rehabilitación LGII, CENIAQ, Calzada México Xochimilco No. 289, Colonia Arenal de Guadalupe, Delegación Tlalpan, 14389 Ciudad de México, Mexico

Correspondence should be addressed to Claudio Adrian Ruiz-Torres; ruiztorresclaudio@gmail.com and Facundo Ruiz; ruizfacundo1@gmail.com

Received 30 May 2018; Accepted 6 September 2018; Published 15 October 2018

Guest Editor: Aurel Tabacaru

Copyright © 2018 María del Carmen Sánchez-Navarro et al. This is an open access article distributed under the Creative Commons Attribution License, which permits unrestricted use, distribution, and reproduction in any medium, provided the original work is properly cited.

Nanomaterials obtained by green synthesis technologies have been widely studied in recent years owing to constitute cost-effective and environmental-friendly methods. In addition, there are several works that report the simultaneous performance of the reducer agent as a functionalizing agent, modifying the properties of the nanomaterial. As a simple and economical synthesis methodology, this work presents a method to synthesize silver nanoparticles (AgNPs) using *Annona muricata* aqueous extract and functionalized with 5-fluorouracil (5-FU). The processes of reduction, nucleation, and functionalization of the nanoparticles were analyzed by UV-Vis absorption spectroscopy, and it was found that they are the function of the contact time of the metal ions with the extract. The structural characterization was carried out by transmission electron microscopy (TEM) and X-ray diffraction patterns (XRD). The antibacterial properties of the synthesized nanomaterials were tested using minimum inhibitory concentration (MIC) and minimum bactericidal concentration (MBC) against *Enterococcus faecalis*, *Staphylococcus aureus*, and *Escherichia coli* growth.

1. Introduction

The use of nanoparticles as nanodelivery vehicles has received quite great interest in the medical sector in recent years owing to the fact that, by biochemical engineering, it is possible to design multifunctional nanostructured biomaterials to deliver specific drugs to target tumor or cancer cells [1]. The best performance of nanobiomaterials with respect to other types of biomaterials is due to quite high compatibility and adaptability to biological systems, which additionally represents nonviral systems, constituting

promising tools in biomedicine research. A clear example of this fact is silver nanoparticles; due to the application of these types of materials to biological systems, there has been development of numerous nanodelivery vehicles, in view of their intrinsic properties, biocompatibility, and antimicrobial capacity [2]. It is necessary to improve material properties and biocompatibility for a more efficient yield in drug delivery to a specific target, avoiding a wide distribution of the medicine. In light of this, the material functionalization and organometallic science by the development of covalent nets or polymeric functionalization have modified the

interaction of inorganic surface on metallic NPs with the surrounding media, improving their performance in biomedicine [3, 4].

5-Fluorouracil (5-FU) is a potent broadly used anti-metabolite for cancer treatments such as advanced oral cancer [5]. Nevertheless, several limitations exist on its use related to the short half-life, lack of control on selective delivery, and ample diffusion on body, limiting its antitumor applicability. Therefore, through the functionalization of nanostructured materials with 5-FU, it has remarkably improved the utility of the drug and produced novel and proficient tools for oncologic research [6].

Currently, ample spectrum of different methodologies for silver nanobiomaterials obtained and functionalization for biomedical purposes exists [7]. However, in the previous years, a remarkable interest in the green synthesis methods of nanobiomaterials has been rising in response which represents environmental-friendly methods, low-toxic methodologies, cost-effective alternatives, and one-step NP synthesis-functionalization method [8]. In general, nanomaterial synthesis by “green methods” considers three main characteristics according to Raveendran et al. [9] as follows: (1) solvent friendly as a reaction medium; (2) environmentally beneficial reducing agents; and (3) use of nontoxic material as capping agents [9]. In addition, different reports had reported not only the achievement of obtaining nanoparticles by green synthesis but also discussed the medicinal properties of the materials associated with the active ingredients present in the natural extracts used, which has promoted a scientific focus on the biological activities of these kinds of substances [10, 11]. Furthermore, in relation to the information described above, the synthesis of silver nanomaterials through an efficient, economically cheap, and environmentally safe method has become an important research area in nanobiotechnology. Therefore, currently, diverse plant extracts have been used as excellent bioreducing agents in the synthesis of silver nanoparticles (AgNPs) [12, 13].

The extract *Annona muricata*, generally known as guanabana, is largely distributed in tropical areas of South America and North America; all fractions of the *A. muricata* tree are widely used as traditional medicines against human diseases, including cancer and infections. The anti-inflammatory, hypoglycemic, sedative, smooth muscle relaxant, hypotensive, and antispasmodic effects are attributed to the leaves, barks, and roots of *Annona muricata*. The leaves of this plant are also employed against tumors and cancer in South America and tropical Africa [14]. Phytochemical evaluations of the *Annona muricata* plant have shown the presence of alkaloids, megastigmanes, flavonol triglycosides, phenolics, cyclopeptides, essential oils, and some minerals such as K, Ca, Na, Cu, Fe, and Mg [14].

In the present work, the synthesis of silver nanoparticles using *Annona muricata* aqueous extracts as a bioreducing agent is reported. The materials were characterized in terms of their optical properties, crystallinity, morphology, hydrodynamic radius, and surface charge. The antibacterial capacities of the materials were evaluated by their bactericidal effect against oral microorganisms such as *E. Faecalis*, *S. Mutans*, *S. Oralis*, *S. Aureus*, and *E. Coli* by minimum

inhibitory concentration (MIC) and minimum bactericidal concentration (MBC). Moreover, the evaluation of the cytotoxicity of the samples was done by the cellular viability of fibroblast cells using MTT assay and fluorescent microscopy.

2. Materials and Methods

2.1. Reagents. *A. muricata* leaves were purchased from a local supermarket; silver nitrate (AgNO_3) and 5-FU were obtained from Sigma-Aldrich; serological pipettes (5, 10, and 25 mL) and 50 mL centrifuge tubes were purchased from Santa Cruz Biotechnology, Inc.; 25 cm³ cell-culture flask were purchased from Corning®; and 48-well cell-culture cluster were purchased from Costar®.

Dulbecco's Modified Eagle Medium (DMEM), phosphate-buffered saline (PBS) of pH 7.4, fetal bovine serum (FBS), penicillin/streptomycin, and doxorubicin were purchased from Gibco®. The following bacteria were used: *Enterococcus faecalis* (ATCC 29212), *Staphylococcus aureus* (ATCC 29213), and *Escherichia coli* (ATCC 25922). Human fibroblasts were donated by Dr. Roberto Sánchez-Sánchez, biotechnology laboratory of Instituto Nacional de Rehabilitación LGII, CENIAQ (Ciudad de México).

2.2. AgNP Synthesis. The synthesis of the materials was carried out by the use of *Annona muricata* extract as a bioreducing agent based on the previously reported method by Santhosh et al. [15]. Initially, the leaves were washed with deionized water to remove impurities. After being crushed in a blender, 5 g of the powder was previously ground in 125 mL of deionized water and was boiled to the boiling point. After obtaining the infusion of the extract, in a separate vessel, Ag salt was added and the process of reduction and formation of the nanoparticles began, which was evidenced by the immediate color change, indicating the formation of the same ones. The color of the mixture changed from pale brown to dark brown for AgNPs, and no synthetic reagents were required for this synthesis. Finally, the NP sedimentation was induced by centrifugation and washed with ethanol three times.

2.3. Silver NP Functionalization with 5-Fluorouracil. Prior to Ag nanoparticle synthesis and washing, 50 ml of NP solution was taken in a vessel; subsequently, 0.5 g of 5-fluorouracil was added, and the solution was sonicated for 20 min.

2.4. Physical Characterization Methods. UV-Vis absorption spectra were obtained using the S2000 UV-Vis spectrometer (OceanOptics, Inc.). Transmission electron microscopy (TEM) images were obtained at 100 kV using a JEOL-1230. The hydrodynamic radius and Z-potential of the samples were measured with a Nanosizer DLS. Furthermore, the X-ray diffraction (XRD) patterns were obtained using a GBC-Difftch MMA diffractometer with filtered $\text{CuK}\alpha$ ($\lambda = 1.54 \text{ \AA}$) radiation.

2.5. Antibacterial Activity of AgNPs. The antimicrobial activities of the AgNPs were confirmed via minimum inhibitory concentration (MIC) and minimum bactericidal

concentration (MBC) against strains of *E. faecalis* (ATCC 29212), *S. aureus* (ATCC 29213), and *E. coli* (ATCC 25922); they were studied at 0.5 of the McFarland Scale determined with a colorimeter (LaMotte Smart3) according to the standard microdilution method (CLSI M100-S25, January 2015) [16].

2.6. Cytotoxicity Assay. With respect to cytotoxicity assays, human fibroblasts isolated from the dermis were cultured and stored in liquid nitrogen at -196°C , in order to retain the viability of the cells. A cell culture was carried out in 25 cm^3 plates (Costar[®]), until the surface of the culture vessel was covered, waiting for the formation of a monolayer (layer thickness of one cell). Previously, subcultures were carried out for three weeks using the DMEM culture medium (Gibco[®]), which contains specific proteins essential for cell survival, development, and proliferation. Subsequently, the incubation was performed at 37°C under a CO_2 atmosphere using a NUAIRE Autoflow Ir Water-Jacketed CO_2 incubator; medium changes were made and observed on an inverted microscope (Axio-Zeiss). Once the desired cell confluence was obtained, the cultures were treated with trypsin (a proteolytic enzyme that degrades the extracellular matrix and sequesters the calcium ion, which is essential for cell adhesion). In addition, by gentle agitation after 5–7 min, the cells detached, and the cell suspension required to calculate the number of cells present in a certain volume were obtained and analyzed in a Neubauer chamber. Furthermore, 20,000 cells per cm^2 were seeded in 48-well plates and cultured for 24 hrs. With the purpose of material cytotoxicity assays performed with calcein and ethidium homodimer (Thermo[®]), different dilutions of silver nanoparticles synthesized by a green method were made using an extract of *Annona muricata*. The treatment groups used to perform the cytotoxicity test are shown in Table 1:

The viability of human fibroblasts after exposure to AgNPs was evaluated by the amount of viable cells stained by MTT assay. The human fibroblasts were plated in 96-well plates and exposed to AgNPs, AgNPs + 5-FU, 5-FU, and *Annona muricata*. Cells were added into the medium at concentrations of $30\text{ }\mu\text{g/ml}$ (ppm) maintained in a humidified atmosphere at 37°C and 5% CO_2 . After 24 and 48 h, the medium was removed from each well, replaced with a new medium with MTT solution in an amount of 10% of culture volume, and incubated for 4 h at 37°C until a blue-colored formazan product developed. The resulting formazan product was dissolved in DMSO, and the absorbance was measured at 570–690 nm by using a Synergy HTX Multi-Mode Microplate reader (BioTek Instrument, Inc.).

3. Results and Discussion

3.1. Structural Characterization of AgNPs

3.1.1. Ultraviolet-Visible (UV-Vis) Absorption Spectroscopy. The UV-Vis spectra of the materials were made in order to follow the nucleation process of the particles as a function of the contact time with the extract. In Figure 1, a band at 425 nm can be observed, which is associated with the surface

TABLE 1: Treatments and different concentrations used in the cytotoxicity tests carried out in fibroblasts.

Concentrations	C1	C2	C3	C4
<i>Annona muricata</i>	100 $\mu\text{g/mL}$	75 $\mu\text{g/mL}$	50 $\mu\text{g/mL}$	25 $\mu\text{g/mL}$
5-FU	20 $\mu\text{g/mL}$	15 $\mu\text{g/mL}$	10 $\mu\text{g/mL}$	5 $\mu\text{g/mL}$
AgNPs	32 $\mu\text{g/mL}$	24 $\mu\text{g/mL}$	16 $\mu\text{g/mL}$	8 $\mu\text{g/mL}$
AgNPs + 5-FU	23 $\mu\text{g/mL}$	18 $\mu\text{g/mL}$	13 $\mu\text{g/mL}$	8 $\mu\text{g/mL}$

plasmon of silver nanoparticles. The intensity of the band increases as the contact time of the metal ions with the extract is increased, having its maximum intensity at 60 min. Additionally, it is possible to observe a thinning of the band of the final solution with respect to the initial solution. This thinning can be associated to two phenomena; firstly, the influence of the symmetry of the particles and their size distribution on their optical properties has been previously reported, where irregular particles (nonspherical) will show two or more surface plasmon bands, which will result in the widening of the band; this is due to the fact that as the reduction process begins, the nucleation and the generation of the primary particles will take place, which will have irregular shapes and smaller diameters, explaining the blue shift of the band in the initial solutions and a red shift in the final solutions where the process of nucleation and generation of the particles is concluded [17, 18].

On the other hand, due to the fact that the nanoparticle formation process is interrupted, there will possibly be several particle sizes influencing the excitation surface plasmon peak. Finally, another phenomenon involved to this fact is the band of absorption of the extract, which is at 435 nm, affecting the band position and possibly influencing the red shift. In relation to this, the preservation of the organic agent on the surface of silver nanoparticles evidenced its role as a functionalizing agent.

3.1.2. Morphological Characterization: TEM. Figure 2(a) presents the TEM images and histograms of the synthesized materials. AgNPs present a quasi-spherical morphology arranged in isolated clusters. The differential distribution corresponding to this sample displays a particle size range between 4.54 and 16.48 nm with an asymmetrical geometry and a bimodal distribution (Figure 2(b)). The average particle size and coefficient of variation (CV%) calculated for this sample were 10.87 nm and 22.94%, respectively. The statistical parameters obtained are shown in Table 2.

3.1.3. Dynamic Light Scattering (DLS) and Zeta Potential. Table 3 displays the values of particle size and Z-potential obtained for the particles. The acquired value for particle size was 16.46 ± 0.46 , slightly differing from the obtained diameter mean of 10.87 from TEM images analysis, indicating the association of the value corresponding to DLS analysis to the hydrodynamic radius of the particles and corroborating the results shown in size statistical analysis. The measured Z-potential of the sample displays a value of $-27.3 \pm 1.22\text{ mV}$, which represent an electrostatic repulsion between the

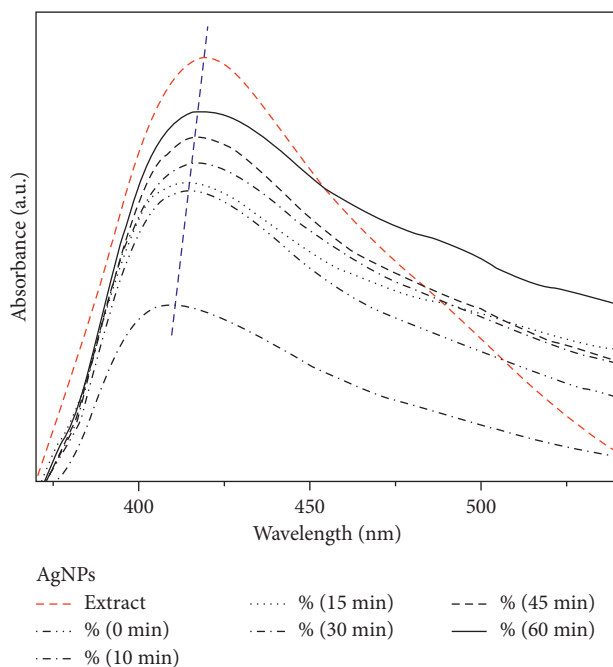


FIGURE 1: UV-Vis absorption spectra of silver nanoparticles at different time periods and their reaction with *A. muricata* extract at 1000 μL .

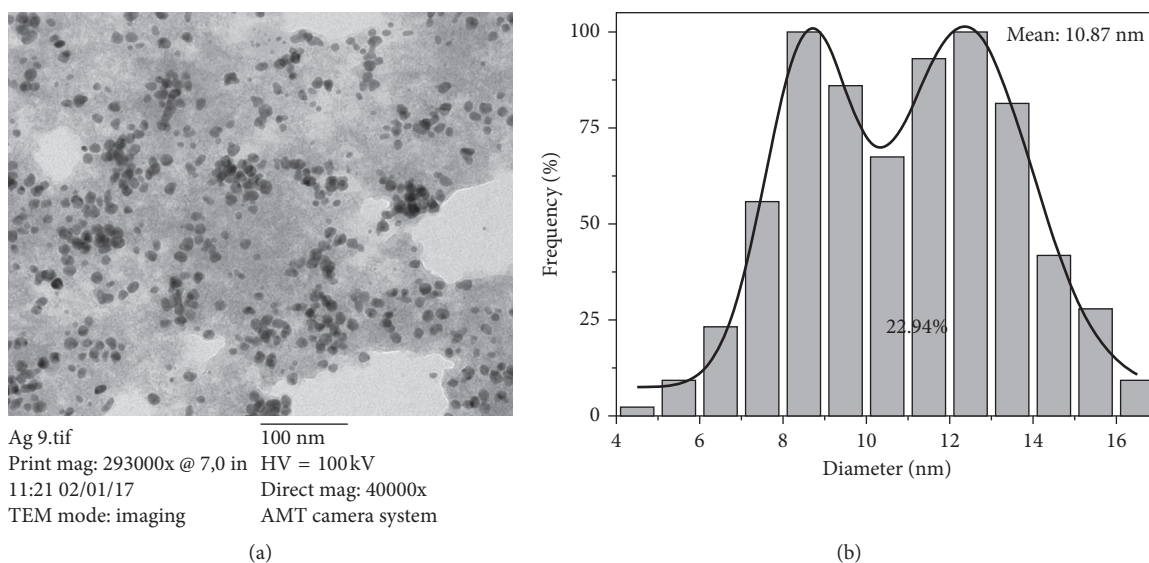


FIGURE 2: (a) TEM photomicrography and (b) differential size distribution of silver nanoparticles biosynthesized using *A. muricata* extract.

TABLE 2: Size distribution statistical parameters of ZVI materials in nm.

Sample	Mean	CV (%)	D10	D50	D90	D50-D10
AgNPs	10.87	22.94	7.12	10.54	13.72	3.42

TABLE 3: Dynamic light scattering (DLS) and zeta potential of Ag sample.

Sample	Particle size (nm)	Z-potential (mV)
AgNPs	16.46 ± 0.46	-27.3 ± 1.22

particles as shown in the TEM image corresponding to this sample, where most of the NPs are well dispersed (Table 3).

3.1.4. X-Ray Diffraction. The X-ray diffractogram corresponding to AgNPs presents the peaks associated with the

Ag cubic phase at 38.23° , 44.18° , 64.74° , 75.51° , and 81.74° , which can be indexed as the (111), (200), (220), (311), and (222) planes (JCPDS File No.: 04-0783), respectively, illustrating with this information the presence of crystalline silver nanoparticles (Figure 3).

3.2. Antimicrobial Activity of AgNPs. In this study, MIC values were obtained for the AgNPs tested against *E. coli* (ATCC 25922), *S. aureus* (ATCC 29213), and *E. faecalis* (ATCC 292129). The results are presented in Table 4, where the MIC of the AgNPs synthesized by *Annona muricata* presents a lower antibacterial activity in comparison with 5-fluoracil, but the functionalization/combination of the silver nanoparticles with 5-fluoracil showed a synergism because all the strains were inhibited at a concentration of 1.95 Dg/ml or less. With respect to the tree strains tested with AgNPs and 5-fluoracil, *Enterococcus faecalis*, which is a facultative anaerobic Gram-positive coccus, shows the lowest sensitivity in comparison with *E. coli* and *S. aureus* [19]; A. Manten and J. I. Terra were the first to report the antibacterial activity of antineoplastic drugs as well as the combination effects between the antibacterial and anti-neoplastic agents [19]. The results corresponding to 5-fluoracil alone displayed similar results compared to the data reported by Gieringer et al. [20], who found that concentrations of 0.8 $\mu\text{g/ml}$ or less inhibit all strains of *Staphylococcus aureus* [20].

3.3. Cytotoxicity Assay

3.3.1. MTT Assay. The cell viability was evaluated by the cytotoxicity test and fluorescent microscopy in order to compare the effects produced on oral fibroblasts by green AgNPs and the presence and absence of 5-FU as the functionalization agent on the nanomaterials.

The results corresponding to the cytotoxicity test show slight differences in cell viability between 24 and 48 hrs of cell exposition to AgNPs. It is possible to observe toxicity for silver nanoparticles at the highest concentrations used (Figure 4). AshaRani et al. [21] report similar results for lung fibroblasts in response to silver NPs exposition, arguing a cytotoxicity dependence on NPs concentration as well as cell-cycle detection [21]. Additionally, Ahmad et al. [22] evaluated the effect of silver and gold nanoparticles obtained by the green synthesis method in murine macrophages using concentrations in the range of 10–1000 $\mu\text{g/mL}$, obtaining less cytotoxicity at a concentration lower than 80 $\mu\text{g/mL}$ [22]. Furthermore, the information presented illustrates a cytotoxicity-effect reduction of the nanomaterials by 5-FU functionalization, evidencing the biocompatibility improvement of the nanobiomaterials.

3.3.2. Fluorescence Microscopy. Corresponding to the fluorescence microscopy analysis, it was observed that, at a lower concentration of treatments, there was more confluence and cell density compared to the control group (Figures 5 and 6). On the other hand, as concentrations increased, alterations in cells morphology and few cell extensions were observed. Moreover, an important characteristic observed at 24 is the presence of few dead cells for AgNPs exposition, indicating the role of the bioextract as a possible cytoprotective agent since it encapsulates the nanoparticles and 5-FU, preventing direct contact with cells, and additionally, the cell cultures remained viable with only

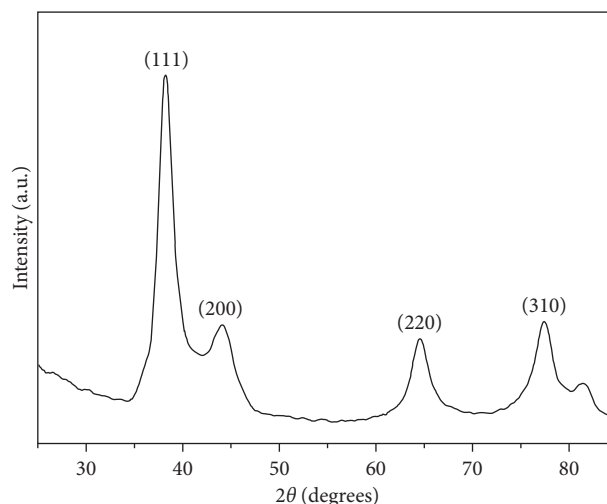


FIGURE 3: X-ray diffraction patterns of the Ag sample.

TABLE 4: Minimum inhibitory concentrations of Ag nanomaterials.

Sample	MIC of silver nanoparticles (mg/ml)		
	<i>E. coli</i> (ATCC 25922)	Bacterial strains <i>S. aureus</i> (ATCC 29213)	<i>E. faecalis</i> (ATCC 29212)
AgNPs	6.68 ± 0.0	13.36 ± 0.0	26.72 ± 0.0
5-Fluorouracil	7.8 ± 0.0	7.8 ± 0.0	15.62 ± 0.0
AgNPs + 5-FU	1.95 ± 0.0	0.97 ± 0.0	0.97 ± 0.0
<i>Annona muricata</i> extract	–a	–a	–a
Amikacin	1 ± 0.0	2 ± 0.0	128 ± 0.0

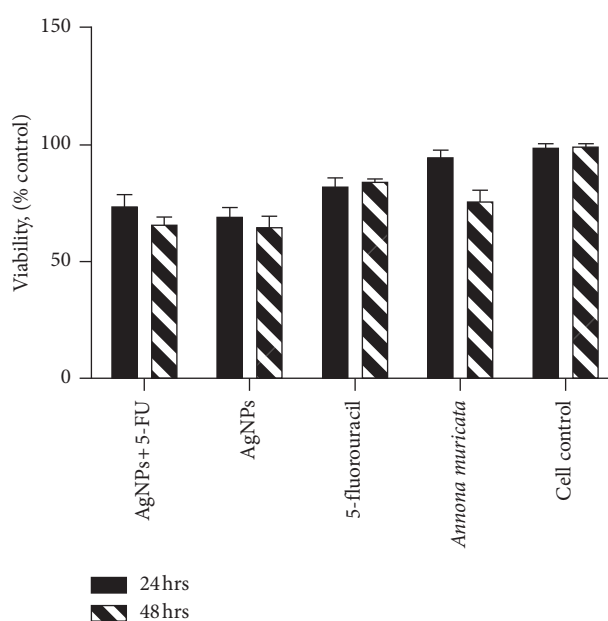


FIGURE 4: Graph of cytotoxicity of fibroblasts exposed to different concentrations of Ag nanoparticles for 24 and 48 hours.

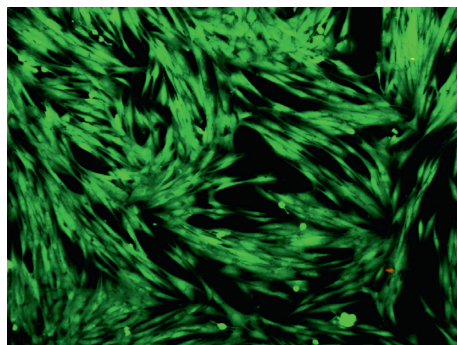


FIGURE 5: Fluorescent microscopy image of the control group of fibroblasts at 24 hrs.

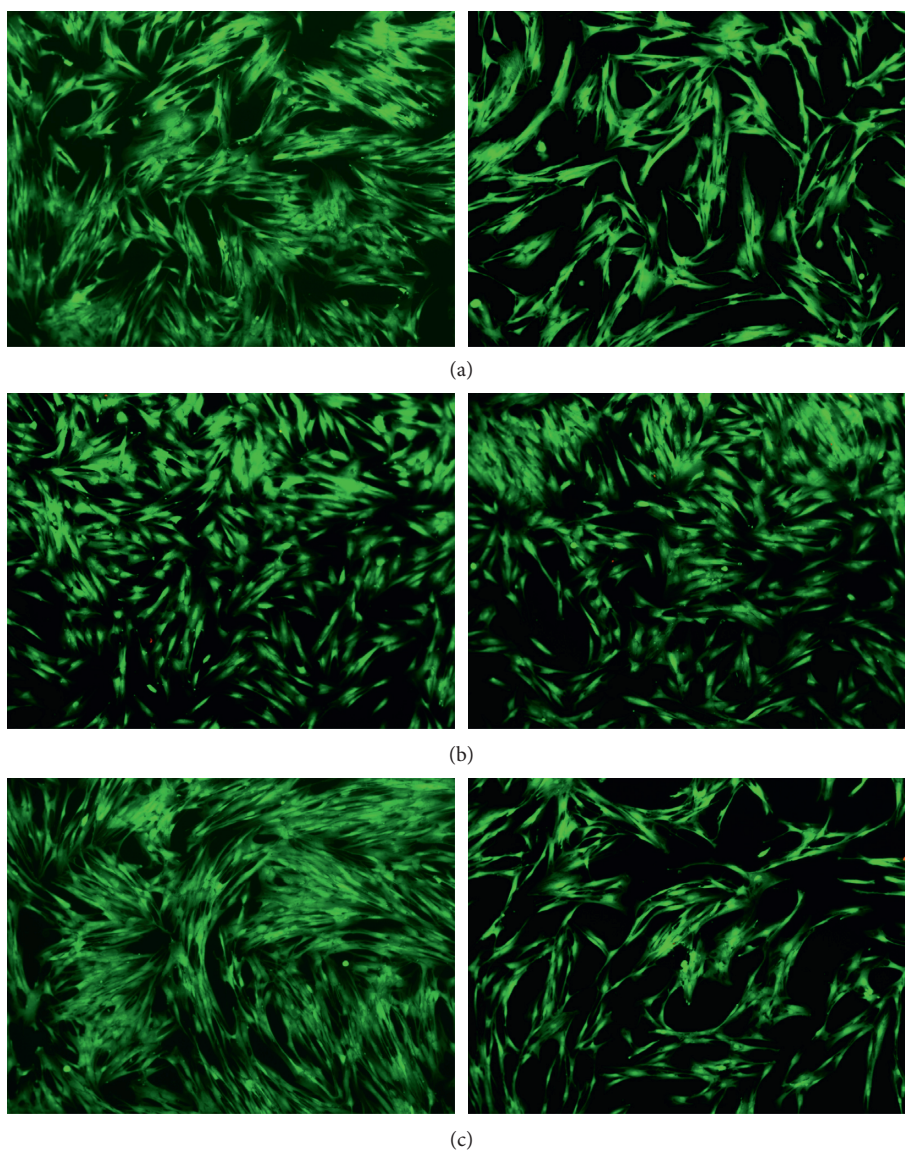


FIGURE 6: Continued.

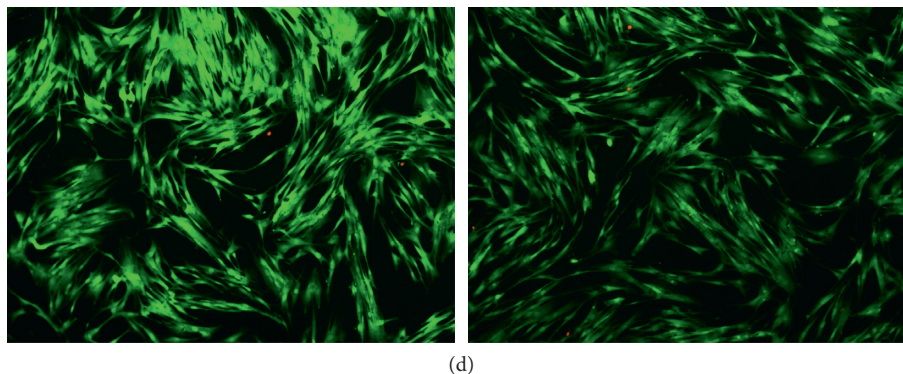


FIGURE 6: Fluorescent microscopy images of cytotoxicity assays in fibroblasts at 24 hrs and with respective concentrations at which it was evaluated (lowest and highest). (a) *A. muricata*. (b) 5-FU group. (c) AgNPs group. (d) Group of AgNPs and 5-FU.

the presence of the extract (Figures 6(b)–6(d)). Similarly, AshaRani et al. [21] previously reported different morphological changes, indicating unhealthy cells, few cell extensions, and restricted propagation patterns with respect to control [21].

4. Conclusions

In this work, it was demonstrated that, in the green synthesis of silver nanoparticles using *Annona muricata* as a bio-reducer, the obtained NPs were characterized in terms of their optical properties, crystallinity, morphology, hydrodynamic radius, and surface charge. The UV-Vis monitoring of the AgNPs formation displayed the nucleation process of the particles and the increasing intensity of the silver characteristic band at 435 nm depending on time reaction. The nanoparticles presented a quasi-spherical shape with an average particle size of 10.87 nm and a hydrodynamic radius of 16.46 ± 0.46 nm. The Z-potential obtained had a value of -27.3 ± 1.22 mV, demonstrating repulsion between the particles and good colloidal stability of the material. The antimicrobial properties of the materials showed a great inhibition against Gram-positive and Gram-negative bacteria. The cytotoxicity of the NPs at 24 and 48 hrs displayed an increment in cell viability associated with the particles functionalization by 5-FU, and only a few dead cells at 24 hrs were observed in the fluorescence microscopy images.

Data Availability

All the data used to support the findings of this study (figures and tables) are included within the article.

Conflicts of Interest

The authors declare that they have no conflicts of interest.

Acknowledgments

This study was supported by Consejo Nacional de Ciencia y Tecnología (CONACyT). DeAlba-Montero would like to thank CONACyT for Scholarship no. 358436, and Claudio

Adrian Ruiz-Torres would like to thank to CONACyT for its support with Scholarship no. 412287.

Supplementary Materials

Schematic illustration representing the synthesis, functionalization, antimicrobial, and cytotoxic effects of silver nanoparticles. (*Supplementary Materials*)

References

- [1] Y.-Y. Tseng, Y.-C. Kau, and S.-J. Liu, “Nanomedicine-the future of cancer treatment: a review,” *Expert Opinion on Drug Delivery*, vol. 13, no. 11, pp. 1533–1544, 2016.
- [2] K. Rani, “Biomedical applications of silver and gold nanoparticles: effective and safe non-viral delivery vehicles,” *Journal of Applied Biotechnology and Bioengineering*, vol. 3, no. 2, article 00059, 2017.
- [3] D. Dhanyalayam, L. Scrivano, O. Ilaria Parisi et al., “Biopolymeric self-assembled nanoparticles for enhanced antibacterial activity of Ag-based compounds,” *International Journal of Pharmaceutics*, vol. 517, no. 1, pp. 395–402, 2017.
- [4] M.-A. Neouze and U. Schubert, “Surface modification and functionalization of metal and metal oxide nanoparticles by organic ligands,” *Monatshefte Für Chemie-Chemical Monthly*, vol. 139, no. 3, pp. 183–195, 2008.
- [5] C. Andreadis, K. Vahtsevanos, T. Sidiras, I. Thomaidis, K. Antoniadis, and D. Mouratidou, “5-Fluorouracil and cisplatin in the treatment of advanced oral cancer,” *Oral Oncology*, vol. 39, no. 4, pp. 380–385, 2003.
- [6] L. Nair, J. Sankar, S. A. Nair, and G. V. Kumar, “Biological evaluation of 5-fluorouracil nanoparticles for cancer chemotherapy and its dependence on the carrier, PLGA,” *International Journal of Nanomedicine*, vol. 6, pp. 1685–1697, 2011.
- [7] D. Dhanya, P. Giuseppe, A. R. Cappello et al., “Phosphonium salt displays cytotoxic effects against human cancer cell lines,” *Anti-Cancer Agents in Medicinal Chemistry*, vol. 17, no. 13, 2017.
- [8] D. MubarakAli, N. Thajuddin, K. Jeganathan, and M. Gunasekaran, “Plant extract mediated synthesis of silver and gold nanoparticles and its antibacterial activity against clinically isolated pathogens,” *Colloids and Surfaces B: Biointerfaces*, vol. 85, no. 2, pp. 360–365, 2011.
- [9] P. Raveendran, J. Fu, and S. L. Wallen, “Completely “green” synthesis and stabilization of metal nanoparticles,” *Journal of*

- the American Chemical Society*, vol. 125, no. 46, pp. 13940-13941, 2003.
- [10] V. Ganesh Kumar, S. Dinesh Gokavarapu, A. Rajeswari et al., "Facile green synthesis of gold nanoparticles using leaf extract of antidiabetic potent cassia auriculata," *Colloids and Surfaces B: Biointerfaces*, vol. 87, no. 1, pp. 159-163, 2011.
- [11] P. Tippayawat, N. Phromviyo, P. Boueroy, and A. Chompoosor, "Green synthesis of silver nanoparticles in aloe vera plant extract prepared by a hydrothermal method and their synergistic antibacterial activity," *PeerJ*, vol. 4, article e2589, 2016.
- [12] S. Patra, S. Mukherjee, A. Kumar Barui, A. Ganguly, B. Sreedhar, and C. R. Patra, "Green synthesis, characterization of gold and silver nanoparticles and their potential application for cancer therapeutics," *Materials Science and Engineering C*, vol. 53, pp. 298-309, 2015.
- [13] M. V. Sujitha and S. Kannan, "Green synthesis of gold nanoparticles using citrus fruits (citrus limon, citrus reticulata and citrus sinensis) aqueous extract and its characterization," *Spectrochimica Acta-Part A: Molecular and Biomolecular Spectroscopy*, vol. 102, pp. 15-23, 2013.
- [14] S. Z. Moghadamtousi, M. Fadaeinasab, S. Nikzad, G. Mohan, H. M. Ali, and H. Abdul Kadir, "*Annona muricata* (Annonaceae): a review of its traditional uses, isolated acetogenins and biological activities," *International Journal of Molecular Sciences*, vol. 16, no. 7, pp. 15625-15628, 2015.
- [15] S. B. Santhosh, R. Yuvarajan, and D. Natarajan, "*Annona muricata* leaf extract- mediated silver nanoparticles synthesis and its larvicidal potential against dengue, malaria and filariasis vector," *Parasitology Research*, vol. 114, no. 8, pp. 3087-3096, 2015.
- [16] Testing Susceptibility, *M100-S24 Performance Standards for Antimicrobial*, SAI Global, Sydney, NSW, Australia, 2013.
- [17] G. A. Martinez-Castanon, N. Niño-Martínez, F. Martínez-Gutierrez, J. R. Martínez-Mendoza, and F. Ruiz, "Synthesis and antibacterial activity of silver nanoparticles with different sizes," *Journal of Nanoparticle Research*, vol. 10, no. 8, pp. 1343-1348, 2008.
- [18] S. Pal, K. T. Yu, and J. M. Song, "Does the antibacterial activity of silver nanoparticles depend on the shape of the nanoparticle? A study of the gram-negative bacterium *Escherichia coli*," *Journal of Biological Chemistry*, vol. 290, no. 42, pp. 1712-1720, 2015.
- [19] A. Manten and J. I. Terra, "Some observations on antagonism between penicillin and antineoplastic antibiotics," *Acta Physiologica et Pharmacologica Neerlandica*, vol. 14, no. 3, pp. 250-258, 1967.
- [20] J. H. Gieringer, A. F. Wenz, H. M. Just, and F. D. Daschner, "Effect of 5-fluorouracil, mitoxantrone, methotrexate, and vincristine on the antibacterial activity of ceftriaxone, ceftazidime, cefotiam, piperacillin, and netilmicin," *Chemotherapy*, vol. 32, no. 5, pp. 418-424, 1986.
- [21] P. V. AshaRani, G. L. Kah Mun, M. P. Hande, and S. Valiyaveetil, "Cytotoxicity and genotoxicity of silver nanomaterials," in *Proceedings of Technical Proceedings of the 2009 NSTI Nanotechnology Conference and Expo NSTI-Nanotech*, pp. 383-386, Houston, TX, USA, May 2009.
- [22] A. Ahmad, F. Syed, A. Shah et al., "Silver and gold nanoparticles from *Sargentodoxa cuneata*: synthesis, characterization and antileishmanial activity," *RSC Advances*, vol. 5, no. 90, pp. 73793-73806, 2015.

Research Article

Synthesis, Characterization, and Antimicrobial Activity of Novel Sulfonated Copper-Triazine Complexes

Supun Katugampala,¹ Inoka C. Perera,² Chandrika Nanayakkara,³ and Theshini Perera ¹

¹Department of Chemistry, University of Sri Jaywardenepura, Nugegoda, Sri Lanka

²Department of Zoology and Environment Science, University of Colombo, Colombo, Sri Lanka

³Department of Plant Science, University of Colombo, Colombo, Sri Lanka

Correspondence should be addressed to Theshini Perera; theshi@sjp.ac.lk

Received 6 April 2018; Revised 5 June 2018; Accepted 8 July 2018; Published 29 August 2018

Academic Editor: Aurel Tabacaru

Copyright © 2018 Supun Katugampala et al. This is an open access article distributed under the Creative Commons Attribution License, which permits unrestricted use, distribution, and reproduction in any medium, provided the original work is properly cited.

Metallotriazine complexes possess interesting biological and medicinal properties, and the present study focuses on the synthesis, characterization, and antimicrobial activity of four novel copper-triazine derivatives in search of potent antibacterial and antifungal drug leads. In this study, 3-(2-pyridyl)-5,6-diphenyl-1,2,4-triazine-4,4'-disulfonic acid monosodium salt (L1, ferrozine) and 3-(2-pyridyl)-5,6-di(2-furyl)-1,2,4-triazine-5,5'-disulfonic acid disodium salt (L2, ferene) have been used as ligands to study the complexation towards copper(II). The synthesized complexes, [CuCl₂(ferrozine)]·7H₂O·MeOH (1), [CuCl₂(ferrozine)₂]·5H₂O·MeOH (2), [CuCl₂(ferene)]·H₂O·MeOH (3), and [CuCl₂(ferene)₂]·H₂O·MeOH (4), have been characterized spectroscopically, and preliminary bioassays have been carried out. FTIR spectroscopic data have shown that N=N and C=N stretching frequencies of complexes have been shifted towards lower frequencies in comparison with that of the ligands, confirming new bond formation between Cu and N, which in turn lowers the strength of N=N and C=N bonds. In addition, a bathochromic shift has been observed for UV-visible spectra of complexes (1), (2), (3), and (4). Furthermore, elemental analysis data have been useful to obtain empirical formulas of these complexes and to establish the purity of each complex. Complexes (1) and (2) have shown antibacterial activity for both *S. aureus* (ATCC® 25923) and *E. coli* (ATCC® 25922) at 1 mg/disc concentration, and ferrozine has shown a larger inhibition zone against the clinical sample of *C. albicans* at 1 mg/disc concentration in comparison with the positive control, fluconazole.

1. Introduction

Transition metals have numerous and unique biological, chemical, and physical properties due to the availability of d electrons in valence shells. Much attention has been focused on copper complexes due to their various potential biological activities [1–4] out of which antimicrobial [5] and antiviral activities is paramount [6–15].

Since triazine is a well-known natural material which possesses many biological properties [16–21], it is not surprising that organometallic complexes of triazine with first row transition metals (Mn [22, 23], Co [24, 25], Ni [24, 25], Cu [22, 24–28], and Zn [25]), with second row transition metals (Ru [29], Pd [30], Ag [31], and Cd [32]), and with third row transition metals (Re [33] and Pt [34–36]) have

been synthesized, and their activities explored as catalysts [37] and biological agents such as antibacterial [25], anticancer [29, 36], antifouling [24], antifungal [33], anti-HIV [35], antimicrobial [25], antiproliferative [26, 34], antiviral [28, 35], and DNA binding [26, 29, 30] agents.

Even though many reports exist of metal complexes of triazine derivatives as detailed above, metal complexes containing the pyridyl-1,2,4-triazine core are relatively unexplored. Platinum(II) complexes of sulphonated 2-pyridyl-1,2,4-triazine have been reported to possess anti-HIV activity [35]. A copper(II) complex bearing 2,4,6-tris(2-pyridyl)-1,3,5-triazine ligand has been reported to bind DNA in a moderately strong way exhibiting significantly better anticancer activity against breast cancer in comparison with cisplatin [26]. An octahedral complex of rhenium(V), ML1L2L3L4

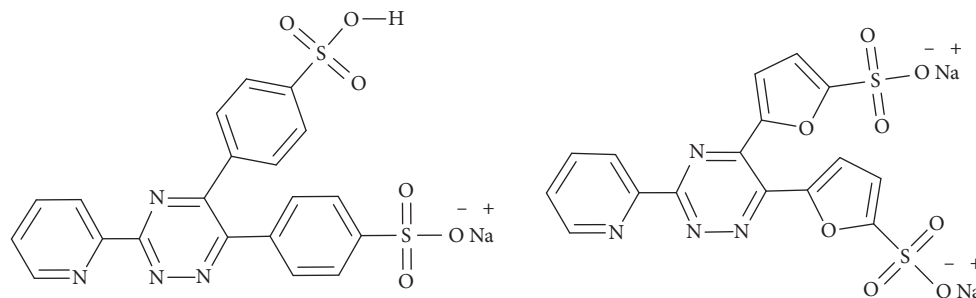


FIGURE 1: Structure of 3-(2-pyridyl)-5,6-diphenyl-1,2,4-triazine-*p,p'*-disulfonic acid monosodium salt (L1) (a) and 3-(2-pyridyl)-5,6-di(2-furyl)-1,2,4-triazine-5,5'-disulfonic acid disodium salt (L2) (b).

(where L1 = oxo, L2 = chloride, L3 = triphenylphosphine, and L4 = 3-hydrazino-5,6-diphenyl-1,2,4-triazine), has shown comparable antifungal activity against *Alternaria alternata* and *Aspergillus niger* [33]. We ourselves have explored the potential of using rhenium complexes of ferene and ferrozine (Figure 1) as biological imaging agents [38]. In our most recent work, we have commented on the possible use of the scaffold of sulfonated pyridyl triazine complexes being utilized as serum albumin transporters [39]. As such, it seems prudent to now explore its binding towards copper.

Thus, the current study explores the synthesis of four novel water-soluble complexes of the type, ML_nCl_2 (Figure 2) (where $M = Cu^{2+}$, $L = 3-(2\text{-pyridyl})\text{-}5,6\text{-diphenyl}\text{-}1,2,4\text{-triazine}\text{-}4',4''\text{-disulfonic acid sodium salt}/3-(2\text{-pyridyl})\text{-}5,6\text{-di}(2\text{-furyl})\text{-}1,2,4\text{-triazine}\text{-}5',5''\text{-disulfonic acid disodium salt}$, and $n = 1/2$), their chemical characterization, and preliminary tests to assess antimicrobial activity of above synthesized complexes as well as of the ligands.

2. Experimental

2.1. Materials Used. All chemicals and reagents used for the synthesis were commercially available and used without further purification. 3-(2-Pyridyl)-5,6-diphenyl-1,2,4-triazine-4,4'-disulfonic acid monosodium salt (ferrozine), 3-(2-pyridyl)-5,6-di(2-furyl)-1,2,4-triazine-5,5'-disulfonic acid disodium salt (ferene), and methanol ACS reagent (assay $\geq 99.8\%$) were purchased from Sigma-Aldrich, and copper (II) chloride dihydrate was purchased from Research-Lab Fine Chem Industries. Mueller-Hinton agar was purchased from Hardy Diagnostics, USA. Sodium chloride, sodium hydroxide, and dextrose were purchased from HiMedia Laboratories. The bacteria were obtained by the Industrial Technology Institute, Colombo.

2.2. Instrumentation. Elemental analysis was carried out on PerkinElmer 2400 Series II CHNS/O Elemental Analyzer at Atlantic Microlabs, USA. IR spectra were recorded using Thermo Scientific NICOLET iS10 spectrophotometer in the spectral range $4000\text{--}650\text{ cm}^{-1}$ for both ligands and complexes. Thermo Spectronic Helios alpha UV-Vis double-beam spectrophotometer was used to measure the absorbance in the range of $190\text{--}1100\text{ nm}$, and baseline correction was performed using matched quartz cuvettes. High-resolution

mass spectra were recorded on an Agilent 6210 ESI TOF LCMS mass spectrometer.

2.3. Synthesis

2.3.1. Preparation of $[CuCl_2(\text{ferrozine})]\cdot 7H_2O\cdot MeOH$ (1). A solution of ferrozine (0.25 mmol, 0.1269 g) in methanol (8.0 cm^3) was added to copper chloride dihydrate (0.25 mmol, 0.0435 g) in methanol (2.0 cm^3). Then the resulting mixture was stirred for 2 hours at room temperature and progression of reaction checked using TLC. A light green colour crystalline precipitate was obtained after 2 days and collected by filtration (yield: 0.1264 g, 64%). IR (ATR; ν/cm^{-1}): 1596.84(m) and 1498.22(s), $\nu_{C=N}$ and $\nu_{N=N}$. UV-Vis (MeOH; λ_{max} [nm]): 205, 242, 298, and 327. Anal. Calc. for $C_{20}H_{13}Cl_2CuN_4NaO_6S_2\cdot 7H_2O\cdot CH_3OH$: C, 32.12; H, 3.98; N, 7.14. Found: C: 31.68%, H: 3.80%, and N: 7.42%. ESI-MS (m/z): $[M-H]^-$ calcd for $C_{20}H_{13}ClCuN_4O_6S_2$, 565.9179; found, 565.9188.

2.3.2. Preparation of $[CuCl_2(\text{ferrozine})_2]\cdot 5H_2O\cdot MeOH$ (2). A procedure similar to that given above was followed using copper chloride dihydrate (0.25 mmol, 0.0435 g) and ferrozine (0.50 mmol, 0.2538 g). The resulting mixture was stirred for 5 hours. A dark green colour crystalline precipitate was obtained after 2 days and collected by filtration (yield: 0.1937 g, 62%). IR (ATR; ν/cm^{-1}): 1595.69(m) and 1498.50(s), $\nu_{C=N}$ and $\nu_{N=N}$. UV-Vis (MeOH; λ_{max} [nm]): 213, 240, 301, and 334. Anal. Calc. for $C_{40}H_{26}Cl_2CuN_8Na_2O_{12}S_4\cdot 5H_2O\cdot CH_3OH$: C, 39.66; H, 3.25; N, 9.03. Found: C: 39.29%, H: 3.76%, N: 9.23%. ESI-MS (m/z): $[M-H]^-$ calcd for $C_{40}H_{26}CuN_8O_{12}S_4$, 999.9833; found, 999.9776.

2.3.3. Preparation of $[CuCl_2(\text{ferene})]\cdot H_2O\cdot MeOH$ (3). A solution of ferene (0.25 mmol, 0.1236 g) in methanol (8.0 cm^3) was added to copper chloride dihydrate (0.25 mmol, 0.0435 g) in methanol (2.0 cm^3). Then the resulting mixture was stirred for 6 hours at room temperature and progression of reaction checked using TLC technique initially and at the end. A yellow colour crystalline precipitate was obtained after 1 day and collected by filtration (yield: 0.1183 g, 75%). IR (ATR; ν/cm^{-1}): 1567.49(m) and 1499.15(s), $\nu_{C=N}$ and $\nu_{N=N}$. UV-Vis (MeOH; λ_{max} [nm]): 202, 239, 338, and 371. Anal. Calc. for $C_{16}H_8Cl_2CuN_4O_8S_2\cdot H_2O\cdot CH_3OH$: C, 32.16; H, 2.54; N, 8.82.

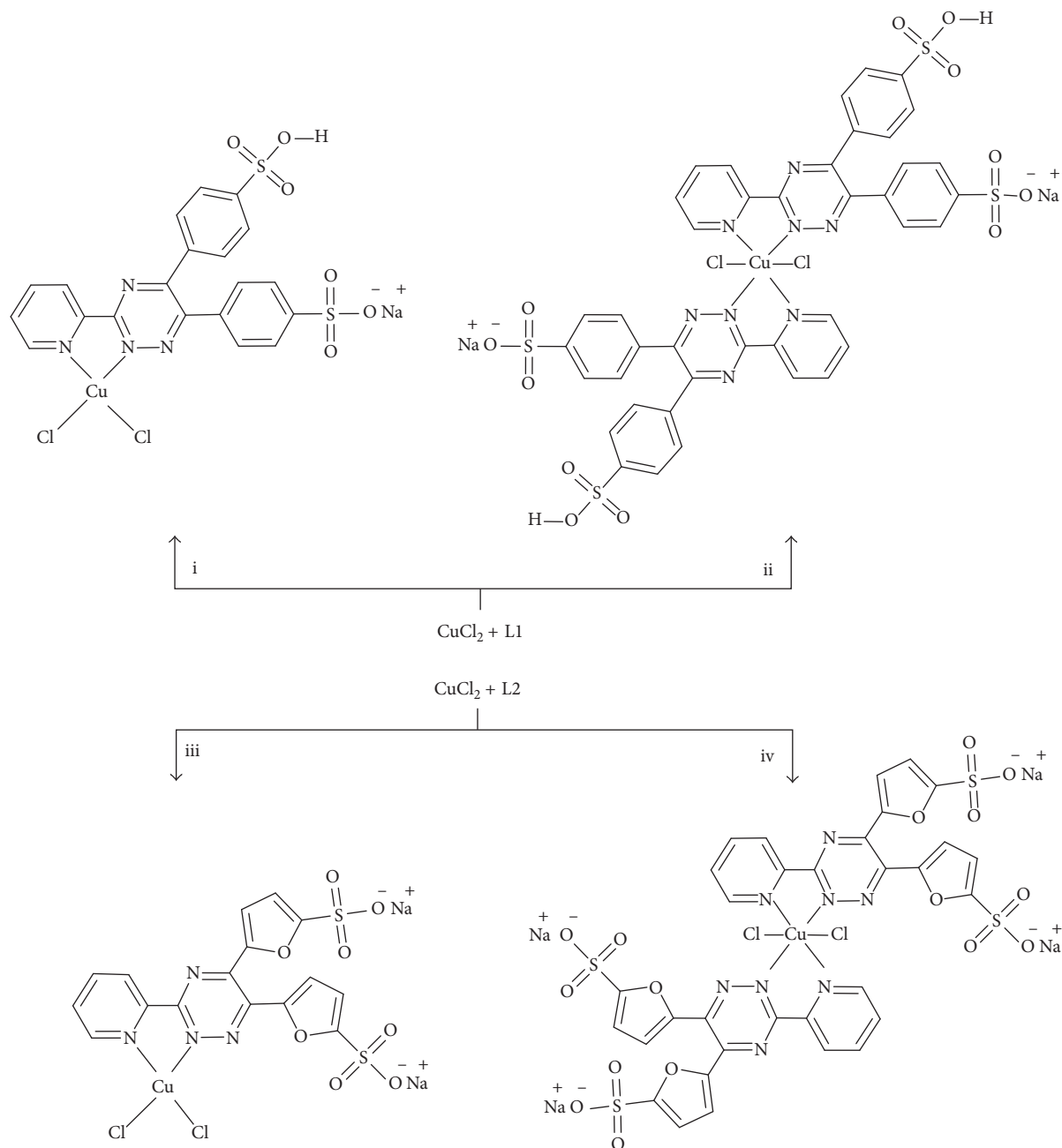


FIGURE 2: Synthetic routes for ML1Cl₂ (complex **(1)**) (i), M(L1)₂Cl₂ (complex **(2)**) (ii), ML2Cl₂ (complex **(3)**) (iii), and M(L2)₂Cl₂ (complex **(4)**) (iv) complexes. NB: L1 = 3-(2-pyridyl)-5,6-diphenyl-1,2,4-triazine-*p,p'*-disulfonic acid monosodium salt; L2 = 3-(2-pyridyl)-5,6-di(2-furyl)-1,2,4-triazine-5,5'-disulfonic acid disodium salt. Solvent molecules in complexes **(1)**–**(4)** have been omitted for clarity. Molar ratios of reactants: (i) CuCl₂:L1 = 1:1, (ii) CuCl₂:L1 = 1:2, (iii) CuCl₂:L2 = 1:1, and (iv) CuCl₂:L2 = 1:2.

Found: C, 32.12%, H, 2.76%, N, 9.29%. ESI-MS (*m/z*): [M]⁺ calcd for C₁₆H₈CuN₄O₈S₂, 510.9085; found, 510.9084.

2.3.4. Preparation of [CuCl₂(ferene)₂].H₂O.MeOH (4**).** A procedure similar to above was followed using copper chloride dihydrate (0.25 mmol, 0.0435 g) and ferene (0.50 mmol, 0.2472 g). The resulting mixture was stirred for 5 hours. A brown-yellow colour crystalline precipitate was obtained after 1 day and collected by filtration (yield: 0.1912 g, 65%). IR (ATR; ν/cm^{-1}): 1569.82(m) and 1494.40(s), $\nu_{\text{C=N}}$

and $\nu_{\text{N=N}}$. UV-Vis (MeOH; λ_{max} [nm]): 208, 246, 338 and 371. Anal. Calc. for C₃₂H₁₆Cl₂CuN₈Na₄O₁₆S₄.H₂O.CH₃OH: C, 33.78; H, 1.89; N, 9.56. Found: C, 33.76%; H, 2.42%; N, 9.58%.

2.4. Antimicrobial Assay. Compounds were tested against Gram-positive *Staphylococcus aureus* ATCC® 25923 and Gram-negative *Escherichia coli* ATCC® 25922 bacterial species and a clinical isolate of *Candida albicans* as a fungal species. Antimicrobial assay was performed by a standard disk diffusion assay [40] where the inhibition zones were

measured and expressed as a mean of three replicates. Gentamycin and flucanazole were used as positive controls, and methanol was used as the negative control.

3. Results and Discussion

3.1. Synthesis. Copper chloride and the relevant ligands were used in 1:1 and 1:2 ratios to synthesize the desired metal complexes (Figure 2). Thin-layer chromatography (TLC) was initially used to monitor the progress of reaction, and visualization of spots was done using an iodine bath.

3.2. FTIR Analysis. FTIR data were recorded for dried crystals of ligands and complexes (1)–(4), and literature values were utilized where relevant [41]. The stretching frequency of the pyridine ring ($\nu_{C=N}$) and stretching frequency of the triazine ring ($\nu_{N=N}$) are considered mostly, because their values change upon formation of new bonds serving as good indicators of complex formation.

Stretching frequencies of N=N and C=N in complexes (1) and (2) have shifted to lower frequencies as expected, compared to those values of the free ferrozine ligand, due to σ donation of N lone pair which lowers strength of N=N and C=N bonds (Table 1). Furthermore, a broad band around 3400–3300 cm^{-1} was observed due to OH groups from methanol or water.

Similarly, stretching frequencies of N=N and C=N in complexes (3) and (4) were observed at lower frequencies in comparison with those of the free ferrozine ligand (Table 1), and a broad band was observed around 3400–3300 cm^{-1} due to OH groups of solvent.

3.3. UV-Visible Spectroscopy. UV-Vis spectra of reactants and complexes (1, 2, 3, and 4) were recorded in methanol at room temperature (Figure 3, Table S1, Supplementary Materials). The absorption wavelengths of complexes (1)–(4) have shifted towards longer wavelengths (bathochromic shift) compared to the wavelengths of the reactants (copper, ferrozine, and ferene). Both ferrozine and ferene have aromatic ring systems, and $\pi-\pi^*$ transitions are thus possible [42]. These results are in agreement with those previously reported for zinc complexes of ferene and ferrozine [39] where a bathochromic shift was observed for both mono and bis complexes in comparison with that of the free ligand.

3.4. Elemental Analysis. Empirical formulas related to experimental values aided in obtaining the exact molecular formulas of all four complexes (Table 2). It can be seen that experimental values are within $\pm 0.4\%$ of expected values indicating purity of the synthesized complexes.

3.5. Antimicrobial Activity. All four complexes and ligands were studied *in vitro* for their antimicrobial activity against Gram-positive *Staphylococcus aureus* ATCC® 25923 and negative bacteria *Escherichia coli* ATCC® 25922 as well as the unicellular fungal species, *Candida albicans*. Inhibition zones were obtained by adding a concentration of 1 mg/disc, and the diameters of the zones are given in Table 3 for bacteria and Table 4 for fungi.

TABLE 1: FTIR data comparison chart of complexes (1)–(4) in comparison with those of free ligands.

	$\nu_{C=N}$ (cm^{-1})	$\nu_{N=N}$ (cm^{-1})
Ferrozine	1608	1503
Complex (1)	1596	1498
Complex (2)	1595	1498
Ferene	1589	1507
Complex (3)	1567	1499
Complex (4)	1570	1494

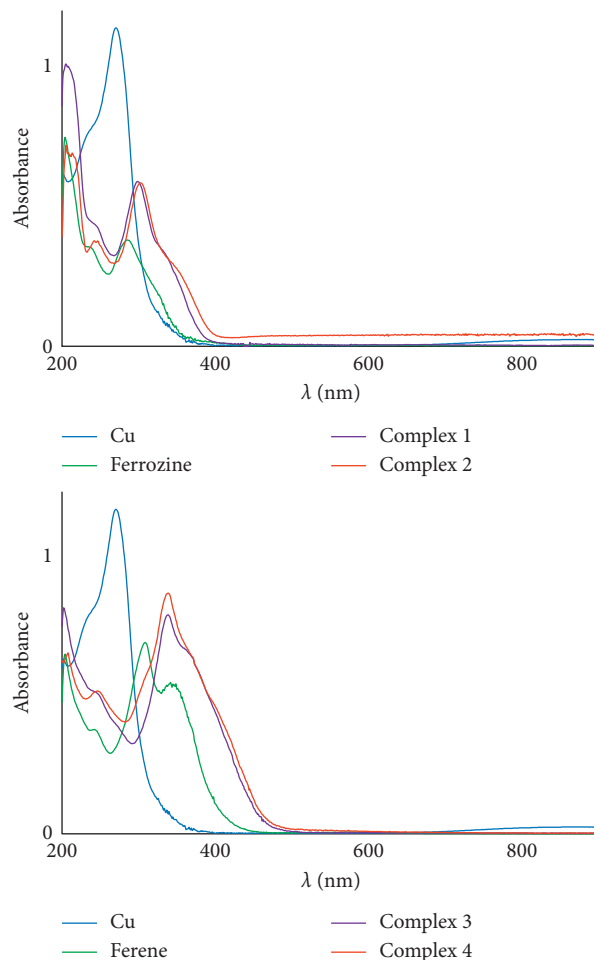


FIGURE 3: UV-visible spectra recorded in methanol of ferrozine, complexes (1) and (2) (a) and ferene, complexes (3) and (4) (b).

TABLE 2: Elemental analysis data of complexes.

Complex	Value	C (%)	H (%)	N (%)
(1)	Calculated	32.12	3.98	7.14
	Experimental	31.68	3.80	7.42
(2)	Calculated	39.66	3.25	9.03
	Experimental	39.29	3.76	9.23
(3)	Calculated	32.16	2.54	8.82
	Experimental	32.12	2.76	9.29
(4)	Calculated	33.78	1.89	9.55
	Experimental	33.76	2.42	9.58

TABLE 3: Mean inhibition zone diameter at 1 mg/disc of complexes (1) and (2) and at 20 μ g/disc of gentamicin.

	Mean inhibition zone diameter \pm SEM (mm)	
	<i>S. aureus</i> ATCC [®] 25923	<i>E. coli</i> ATCC [®] 25922
Complex (1)	8.75 \pm 0.75	7.50 \pm 1.00
Complex (2)	7.00 \pm 0.00	7.75 \pm 0.25
Positive control (gentamicin)	26.00 \pm 1.50	30.75 \pm 0.75
Negative control	ND	ND

ND, not detected.

TABLE 4: Mean inhibition zone diameter for *Candida albicans* at 1 mg/disc of ferrozine and at 1 mg/disc of fluconazole.

	Mean inhibition zone diameter \pm SEM (mm)
Ferrozine	13.00 \pm 2.00
Fluconazole	29.75 \pm 0.25

Analysis of the inhibition zone diameter revealed that only complex (1) and complex (2) show moderate antibacterial activity when compared to the positive control. It is interesting to see that ferrozine ligand demonstrates antifungal activity.

Antimicrobial activity reported here is of moderate value. Further studies are warranted to optimize this system for greater activity.

4. Conclusions

We have described the synthesis of four novel water-soluble copper complexes bearing sulfonated pyridyl triazine ligands. FTIR spectroscopic data have confirmed the existence of Cu-N bonds in all four complexes because stretching frequencies of N=N and C=N complexes have been shifted towards lower frequencies in comparison with that of the ligands. In UV-Vis spectra, a bathochromic shift has been observed for complexes (1)–(4). Furthermore, elemental analysis data have been useful to obtain empirical formulas of these complexes and to establish the purity of each complex.

Preliminary bioassays in antimicrobial activity showed moderate antibacterial activity with complexes (1) and (2) whereas ferrozine showed antifungal activity against *Candida albicans*. To the best of our knowledge, we are the first to report on the antifungal activity of ferrozine. These findings provide a potential lead for antimicrobial drug development.

Data Availability

The data used to support the findings of this study are included within the article and within the Supplementary Information file.

Conflicts of Interest

The authors declare that they have no conflicts of interest.

Acknowledgments

Financial assistance from the University of Sri Jayewardenepura (Grant no. ASP/01/RE/SCI/2015/19) is gratefully acknowledged. Clinical sample of *Candida albicans* was provided by the Department of Microbiology, Faculty of Medicine, University of Colombo. An earlier version of this work with two of the complexes detailed here was presented as an abstract at Chemistry in Sri Lanka 2015 as found in the link <http://www.ichemc.edu.lk/wp-content/uploads/2015/10/vol-31-no.-2.pdf>. The authors also acknowledge the Centre for Advanced Material Research of the University of Sri Jayewardenepura.

Supplementary Materials

Table S1: comparison of UV-Vis data of ferrozine, ferene, and complexes (1)–(4) is presented in a tabulated form in Supplementary Materials. (*Supplementary Materials*)

References

- [1] A. Valent, M. Melník, D. Hudecová, B. Dudová, R. Kivekäs, and M. R. Sundberg, "Copper(II) salicylidene-glycinate complexes as potential antimicrobial agents," *Inorganica Chimica Acta*, vol. 340, pp. 15–20, 2002.
- [2] M. Ibrahim, F. Wang, M. M. Lou et al., "Copper as an antibacterial agent for human pathogenic multidrug resistant *Burkholderia cepacia* complex bacteria," *Journal of Bioscience and Bioengineering*, vol. 112, no. 6, pp. 570–576, 2011.
- [3] A. Latif Abuhijleh and C. Woods, "Synthesis, characterization, and oxidase activities of copper(II) complexes of the anti-convulsant drug valproate," *Journal of Inorganic Biochemistry*, vol. 64, no. 1, pp. 55–67, 1996.
- [4] B. S. Creaven, B. Duff, D. A. Egan et al., "Anticancer and antifungal activity of copper(II) complexes of quinolin-2(1H)-one-derived Schiff bases," *Inorganica Chimica Acta*, vol. 363, no. 14, pp. 4048–4058, 2010.
- [5] H. I. Cervantes, J. A. Alvarez, J. M. Munoz, V. Arreguin, J. L. Mosqueda, and A. E. Macias, "Antimicrobial activity of copper against organisms in aqueous solution: a case for copper-based water pipelines in hospitals?," *American Journal of Infection Control*, vol. 41, no. 12, pp. e115–e118, 2013.
- [6] N. Shionoiri, T. Sato, Y. Fujimori et al., "Investigation of the antiviral properties of copper iodide nanoparticles against feline calicivirus," *Journal of Bioscience and Bioengineering*, vol. 113, no. 5, pp. 580–586, 2012.
- [7] G. Betanzos-Cabrera, F. J. Ramirez, J. L. Munoz, B. L. Barron, and R. Maldonado, "Inactivation of HSV-2 by ascorbate-Cu (II) and its protecting evaluation in CF-1 mice against encephalitis," *Journal of Virological Methods*, vol. 120, no. 2, pp. 161–165, 2004.
- [8] J. L. Sagripanti, L. B. Routson, A. C. Bonifacino, and C. D. Lytle, "Mechanism of copper-mediated inactivation of herpes simplex virus," *Antimicrobial Agents and Chemotherapy*, vol. 41, no. 4, pp. 812–817, 1997.
- [9] L. A. White, C. Y. Freeman, B. D. Forrester, and W. A. Chappell, "In vitro effect of ascorbic acid on infectivity of herpesviruses and paramyxoviruses," *Journal of Clinical Microbiology*, vol. 24, no. 4, pp. 527–531, 1986.
- [10] G. Borkow, S. S. Zhou, T. Page, and J. Gabbay, "A novel anti-influenza copper oxide containing respiratory face mask," *PLoS One*, vol. 5, no. 6, p. e11295, 2010.

- [11] M. Horie, H. Ogawa, Y. Yoshida et al., "Inactivation and morphological changes of avian influenza virus by copper ions," *Archives of Virology*, vol. 153, no. 8, pp. 1467–1472, 2008.
- [12] J. O. Noyce, H. Michels, and C. W. Keevil, "Inactivation of influenza A virus on copper versus stainless steel surfaces," *Applied and Environmental Microbiology*, vol. 73, no. 8, pp. 2748–2750, 2007.
- [13] J. I. Nieto-Juarez, K. Pierzchla, A. Sienkiewicz, and T. Kohn, "Inactivation of MS2 coliphage in Fenton and Fenton-like systems: role of transition metals, hydrogen peroxide and sunlight," *Environmental Science & Technology*, vol. 44, no. 9, pp. 3351–3356, 2010.
- [14] M. T. Yahya, T. M. Straub, and C. P. Gerba, "Inactivation of coliphage MS-2 and poliovirus by copper, silver, and chlorine," *Canadian Journal of Microbiology*, vol. 38, no. 5, pp. 430–435, 1992.
- [15] F. X. Abad, R. M. Pinto, J. M. Diez, and A. Bosch, "Disinfection of human enteric viruses in water by copper and silver in combination with low levels of chlorine," *Applied and Environmental Microbiology*, vol. 60, no. 7, pp. 2377–2383, 1994.
- [16] R. Menicagli, S. Samaritani, G. Signore, F. Vaglini, and L. Dalla Via, "In vitro cytotoxic activities of 2-alkyl-4,6-diheteroalkyl-1,3,5-triazines: new molecules in anticancer research," *Journal of Medicinal Chemistry*, vol. 47, no. 19, pp. 4649–4652, 2004.
- [17] S. Melato, D. Prospero, P. Coghi, N. Basilico, and D. Monti, "A combinatorial approach to 2,4,6-trisubstituted triazines with potent antimalarial activity: combining conventional synthesis and microwave-assistance," *ChemMedChem*, vol. 3, no. 6, pp. 873–876, 2008.
- [18] C. Zhou, J. Min, Z. Liu et al., "Synthesis and biological evaluation of novel 1,3,5-triazine derivatives as antimicrobial agents," *Bioorganic & Medicinal Chemistry Letters*, vol. 18, no. 4, pp. 1308–1311, 2008.
- [19] K. Srinivas, U. Srinivas, K. Bhanuprakash, K. Harakishore, U. S. Murthy, and V. J. Rao, "Synthesis and antibacterial activity of various substituted s-triazines," *European Journal of Medicinal Chemistry*, vol. 41, no. 11, pp. 1240–1246, 2006.
- [20] A. Baliani, G. J. Bueno, M. L. Stewart et al., "Design and synthesis of a series of melamine-based nitroheterocycles with activity against trypanosomatid parasites," *Journal of Medicinal Chemistry*, vol. 48, no. 17, pp. 5570–5579, 2005.
- [21] Y. Z. Xiong, F. E. Chen, J. Balzarini, E. De Clercq, and C. Pannecouque, "Non-nucleoside HIV-1 reverse transcriptase inhibitors. Part 11: structural modulations of diaryl-triazines with potent anti-HIV activity," *European Journal of Medicinal Chemistry*, vol. 43, no. 6, pp. 1230–1236, 2008.
- [22] J. G. Małeck, B. Machura, and A. Świtlicka, "X-ray studies, spectroscopic characterisation and DFT calculations for Mn(II), Ni(II) and Cu(II) complexes with 5,6-diphenyl-3-(2-pyridyl)-1,2,4-triazine," *Structural Chemistry*, vol. 22, no. 1, pp. 77–87, 2010.
- [23] M. M. Najafpour, D. M. Boghaei, and V. McKee, "Synthesis, characterization, crystal structure and oxygen-evolution activity of a manganese(II) complex with 2,4,6-tris(2-pyridyl)-1,3,5-triazine," *Polyhedron*, vol. 29, no. 17, pp. 3246–3250, 2010.
- [24] H. A. E. Hemaida, A. A. E. Dissouky, and S. M. M. Sadek, "Potential antifouling agents: copper, cobalt, and nickel complexes of 3-(2-acetyl pyridylidene) hydrazino-5,6-diphenyl-1,2,4-triazine," *Egyptian Journal of Aquatic Research*, vol. 31, pp. 45–56, 2005.
- [25] K. Singh, Y. Kumar, P. Puri, C. Sharma, and K. R. Aneja, "Antimicrobial, spectral and thermal studies of divalent cobalt, nickel, copper and zinc complexes with triazole Schiff bases," *Arabian Journal of Chemistry*, vol. 10, pp. S978–S987, 2017.
- [26] K. Abdi, H. Hadadzadeh, M. Salimi, J. Simpson, and A. D. Khalaji, "A mononuclear copper(II) complex based on the polypyridyl ligand 2,4,6-tris(2-pyridyl)-1,3,5-triazine (tptz), [Cu(tptz)₂]²⁺: X-ray crystal structure, DNA binding and in vitro cell cytotoxicity," *Polyhedron*, vol. 44, no. 1, pp. 101–112, 2012.
- [27] B. Machura, A. Świtlicka, R. Kruszynski, J. Mroziński, J. Kłak, and J. Kusz, "Coordination studies of 5,6-diphenyl-3-(2-pyridyl)-1,2,4-triazine towards Cu²⁺ cation. X-ray studies, spectroscopic characterization and DFT calculations," *Polyhedron*, vol. 27, no. 13, pp. 2959–2967, 2008.
- [28] C. G. Palivan, H. M. N. Palivan, B. A. Goodman, and C. Cristescu, "ESR study of some asymmetric-triazine copper (II) complexes having high antiviral activity," *Applied Magnetic Resonance*, vol. 15, no. 3–4, pp. 477–488, 1998.
- [29] N. Busto, J. Valladolid, M. Martinez-Alonso et al., "Anticancer activity and DNA binding of a bifunctional Ru(II) arene aqua-complex with the 2,4-diamino-6-(2-pyridyl)-1,3,5-triazine ligand," *Inorganic Chemistry*, vol. 52, no. 17, pp. 9962–9974, 2013.
- [30] W. H. Al-Assy and M. M. Mostafa, "Comparative studies and modeling structures of two new isomers containing binuclear PdII complexes derived from 2,4,6-tri(2-pyridyl)-1,3,5-triazine (TPTZ)," *Spectrochimica Acta Part A: Molecular and Biomolecular Spectroscopy*, vol. 120, pp. 568–573, 2014.
- [31] M. M. Najafpour, M. Holyńska, M. Amini, S. H. Kazemi, T. Lis, and M. Bagherzadeh, "Two new silver(I) complexes with 2,4,6-tris(2-pyridyl)-1,3,5-triazine (tptz): preparation, characterization, crystal structure and alcohol oxidation activity in the presence of oxone," *Polyhedron*, vol. 29, no. 14, pp. 2837–2843, 2010.
- [32] F. Marandi, M. Jangholi, M. Hakimi, H. A. Rudbari, and G. Bruno, "Synthesis and crystal structures of the first cadmium complexes of 3,5,6-tris(2-pyridyl)-1,2,4-triazine ligand," *Journal of Molecular Structure*, vol. 1036, pp. 71–77, 2013.
- [33] M. M. Mashaly, H. F. El-Shafiy, S. B. El-Maraghy, and H. A. Habib, "Synthesis, properties and thermal studies of oxorhenium(V) complexes with 3-hydrazino-5,6-diphenyl-1,2,4-triazine, benzimidazolethione and 2-hydrazinobenzimidazole. Mixed ligand complexes, pyrolytical products and biological activity," *Spectrochimica Acta Part A: Molecular and Biomolecular Spectroscopy*, vol. 61, no. 8, pp. 1853–1869, 2005.
- [34] I. Łakomska, B. Golankiewicz, J. Wietrzyk et al., "Synthesis, spectroscopic characterization and the biological activity in vitro of new platinum(II) complexes with imidazo[1,5-a]-1,3,5-triazine derivatives and dimethylsulfoxide," *Inorganica Chimica Acta*, vol. 358, no. 6, pp. 1911–1917, 2005.
- [35] A. N. Vzorov, D. Bhattacharyya, L. G. Marzilli, and R. W. Compans, "Prevention of HIV-1 infection by platinum triazines," *Antiviral Research*, vol. 65, no. 2, pp. 57–67, 2005.
- [36] R. W. Sun, D. L. Ma, E. L. Wong, and C. M. Che, "Some uses of transition metal complexes as anti-cancer and anti-HIV agents," *Dalton Transactions*, no. 43, pp. 4884–4892, 2007.
- [37] C. J. Cramer and D. G. Truhlar, "Density functional theory for transition metals and transition metal chemistry," *Physical Chemistry Chemical Physics*, vol. 11, no. 46, pp. 10757–10816, 2009.

- [38] K. Ranasinghe, S. Handunnetti, I. C. Perera, and T. Perera, "Synthesis and characterization of novel rhenium(I) complexes towards potential biological imaging applications," *Chemistry Central Journal*, vol. 10, no. 1, p. 71, 2016.
- [39] N. Abeydeera, I. C. Perera, and T. Perera, "Synthesis, characterization, and BSA-binding studies of novel sulfonated zinc-triazine complexes," *Bioinorganic Chemistry and Applications*, vol. 2018, Article ID 7563820, 7 pages, 2018.
- [40] Institute CaLS, "Methods for dilution antimicrobial susceptibility tests for bacteria that grow aerobically; approved standard—seventh edition," in *M7-A7*, Clinical and Laboratory Standards Institute, Wayne, PA, USA, 2006.
- [41] V. Béreau and J. Marrot, "Coordination studies of 5,6-diphenyl-3-(2-pyridyl)-1,2,4-triazine towards Zn^{2+} cation. Synthesis and characterization by X-ray diffraction and spectroscopic methods," *Comptes Rendus Chimie*, vol. 8, no. 6-7, pp. 1087–1092, 2005.
- [42] D. Eastwood, R. L. Lidberg, and M. S. Dresselhaus, "Ultraviolet-visible fluorescence spectroscopy of selected polyaromatic hydrocarbons and organometallics on hexagonal graphite and boron nitride," *Chemistry of Materials*, vol. 6, no. 2, pp. 211–215, 1994.

Research Article

Exploration on the Interaction Ability of Antitumor Compound Bis-[2,6-difluoro-*N*-(hydroxyl- κ O)benzamidato- κ O] dibutyltin(IV) with Human Peroxisome Proliferator-Activated Receptor hPPAR γ

Jiaqi Mai ¹, Yunlan Li ^{1,2}, Xiaozhi Qiao,¹ Xiaoqing Ji,¹ and Qingshan Li ^{1,2}

¹School of Pharmaceutical Science, Shanxi Medical University, Taiyuan 030001, China

²Shanxi University of Traditional Chinese Medicine, Jinzhong 030619, China

Correspondence should be addressed to Yunlan Li; liyunlanrr@163.com and Qingshan Li; sxlqs2012@163.com

Received 27 February 2018; Accepted 29 April 2018; Published 10 June 2018

Academic Editor: Rais A. Khan

Copyright © 2018 Jiaqi Mai et al. This is an open access article distributed under the Creative Commons Attribution License, which permits unrestricted use, distribution, and reproduction in any medium, provided the original work is properly cited.

Diorganotin(IV) antitumor compound bis-[2,6-difluoro-*N*-(hydroxyl- κ O)benzamidato- κ O] (DBDF2,6T) was one of the novel patent organotin compounds with high antitumor activity and relatively low toxicity. In this study, several methods were used to study the interaction between DBDF2,6T and hPPAR γ protein, including fluorescence quenching, three-dimensional (3D) fluorescence, drug affinity responsive target stability (DARTS), ultrafiltration-LC, and molecular docking. According to the experimental results, the quenching process of the hPPAR γ protein was induced by static quenching mode to form a nonradiative ground-state complex with DBDF2,6T spontaneously, mainly through the hydrophobic force. DBDF2,6T could bind to the hPPAR γ protein directly and give the protein the ability of antienzymatic hydrolysis. And the binding mode of DBDF2,6T into hPPAR γ protein appeared to have an orientation towards residues of SER342 and GLY284. In conclusion, these methods could comprehensively reveal the interaction details of DBDF2,6T and the hPPAR γ protein and established a feasible way to preliminarily identify the agonist compounds for the hPPAR γ protein.

1. Introduction

Organotin compounds have many uses in our life, which could act as stabilizers in plastics, fungicides, industrial catalysts, and so on. [1]. Our research group had synthesized a series of organotin patent compounds which possessed high anticancer activity with low toxicity and devoted to clarify its mechanism of action [2]. From the results of proteomics data, these compounds might play the physiological role through the PPAR (peroxisome proliferator-activated receptor) signaling pathway, which was consistent with the reports that organotin compounds may function as endocrine-disrupting chemicals by affecting the function of the protein PPAR γ [3]. Consequently, a reasonable hypothesis was made to assume that these biologically active compounds might function through the PPAR signaling pathway as an agonist to the

protein PPAR γ and further influence the expressions of the target genes.

PPARs proteins belong to the most important members of the nuclear receptor superfamily and can act as the ligand-activated transcription factors [4]. When the PPARs proteins bind to a specific ligand, the ligand-binding domains of PPARs will encounter the conformational change followed by promoting the recruitment of nuclear receptor coregulators such as steroid receptor coactivator-1 (SRC-1) and eventually influence the transcription of downstream target genes [5]. The PPARs proteins have three isotypes which had been identified as PPAR α , PPAR β/δ , and PPAR γ . These three subtypes exhibit distinct tissue distributions and have unique biological functions [6, 7]. In particular, PPAR γ has received much focus these years for the important physiological functions played by its ligands. For example,

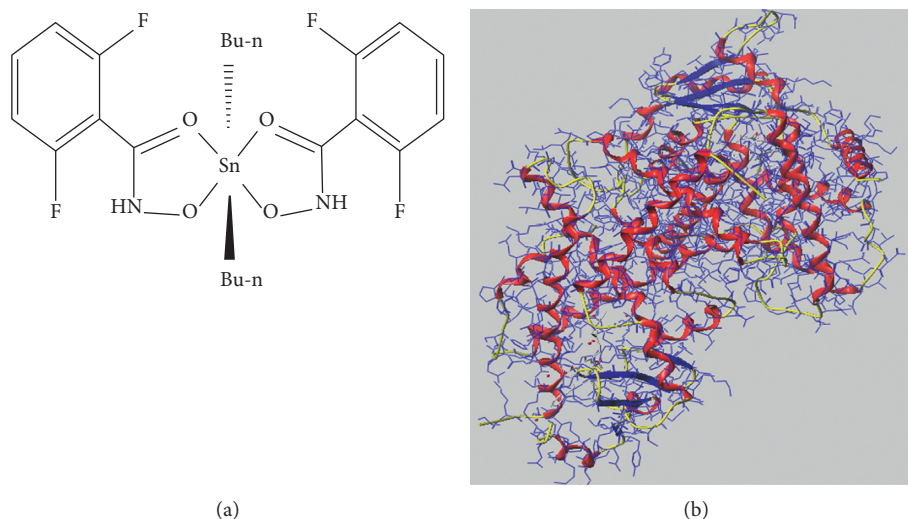


FIGURE 1: Structures of DBDF2,6T and hPPAR γ protein: (a) 2D structure of DBDF2,6T and (b) 3D structure of PPAR γ (4a4w.pdb).

thiazolidinediones (TZDs), a class of PPAR γ agonist compounds, had been used as a therapeutic compound for metabolic disorders such as type 2 diabetes and obesity [8], and it was also reported that the agonists to PPAR γ protein had a potential to be used as a new therapeutic approach to cancers, immune disorders, and so on. [9, 10]. Therefore, the experiments established to find ligands which could interact with the PPAR γ protein are promising works nowadays.

In this study, a patent organotin compound DBDF2,6T (bis-[2,6-difluoro-*N*-(hydroxyl-< κ >O)benzamidato-< κ >O]dibutyltin) (patent number: CN200910074795.X and ZL01135148.9 (P)) which showed a high antitumor activity was assumed as a potential agonist. Several different methods were adopted to test and verify the interaction between DBDF2,6T and the hPPAR γ protein. Spectroscopic study, one of the most widely used methods for analyzing the interaction between small molecule and protein, was applied to provide parameters such as binding constants and types of interaction forces. DARTS and ultrafiltration-LC were used to verify such interaction while molecular docking was used to evaluate affinity between receptors and ligands in a theoretical way. These methods meet the requirements of low cost and high feasibility and perfectly supplement and verify each other, which could be used to find the new agonists of the hPPAR γ protein preliminarily and offered references for the interaction analysis between synthesized compounds and proteins. The structures of DBDF2,6T and the hPPAR γ protein are shown in Figure 1.

2. Materials and Methods

2.1. Reagent. DBDF2,6T was synthesized by Shanxi Medical University with purity over 99%. The protein human PPAR γ (hPPAR γ) was purchased from Flarebio Company (Flarebio Biotech LLC, Wu Han, China) and stored at -20°C . Pronase was purchased from Roche Diagnostic GmbH (Mannheim, Germany) and stored at 4°C . The Coomassie Blue R-250 was purchased from Sigma Company (Shanghai, China), and the PageRuler Prestained Protein Ladder was made by Thermo

Fisher Scientific (Massachusetts, America). The solvent of organotin(IV) was configured by propanediol (Tianjin Fengchuan Chemical Reagent Science and Technology Co., Tianjin, China), ethylenediamine, and normal saline (Shijiazhuang Pharmaceutical, Shijiazhuang, China) (90:9:1, v/v/v). The disodium hydrogen phosphate dodecahydrate was purchased from Tianjin Fengchuan Chemical Reagent Company (Tianjin, China). The potassium phosphate monobasic was purchased from Tianjin Beichen Fangzheng Company (Tianjin, China).

All the other reagents used in this study were of analytical grade and were obtained commercially.

2.2. Fluorescence Quenching Spectrum. Amino acid residues such as tryptophan, tyrosine, and phenylalanine could empower the proteins with the ability to generate endogenous fluorescence. The fluorescence peaks of those three amino acids were located at 348 nm, 303 nm, and 282 nm, respectively. Actually, 95% of protein fluorescence was contributed to the tryptophan residue [11, 12]. Compared with other methods, fluorescence spectroscopy had many superior advantages including high sensitivity, selectivity, and easy operation [13]. Therefore, in this paper, the fluorescence quenching method was used to analyze the interaction between DBDF2,6T and the hPPAR γ protein.

The experiments were performed at 293 K and 310 K on a U-3900 spectrofluorophotometer (BaHens Instrument Co. Ltd., China). Protein hPPAR γ ($10\ \mu\text{g}$) was dissolved in a 2 mL PBS buffer. Several concentrations of DBDF2,6T (0.5×10^{-6} , 1.0×10^{-6} , 1.5×10^{-6} , 2.5×10^{-6} , 3.0×10^{-6} , and 3.5×10^{-6} mol/L) were, respectively, incubated with the certain concentration of the hPPAR γ protein. Samples of protein hPPAR γ and hPPAR γ -DBDF2,6T complexes were measured in a $1\ \text{cm}^2$ quartz cuvette. And the excitation and emission spectral slit widths were set as 10 nm. The emission spectra were recorded for light-scattering effects from 300 nm to 450 nm while the exciting wavelength was set as 280 nm.

2.3. Three-Dimensional Fluorescence Spectrum. The coordinate axes of the three-dimensional (3D) fluorescence spectrum were excitation wavelength, emission wavelength, and fluorescence intensity. It had been proved that the 3D fluorescence spectrum was an effective analytical technique to analyze the conformation changes of a protein in its solution state [14]. And this method could not only test the molecular structure change with much selectivity and sensitivity but also display fluorescent information of the sample solution comprehensively [15].

Experiments were performed at the temperature of 293 K. Protein hPPAR γ (10 μ g) was dissolved in a 2 mL PBS buffer and incubated with 2.0×10^{-6} mol/L DBDF2,6T for two minutes. Samples were tested on a U-3900 spectrofluorophotometer (BaHens Instrument Co. Ltd., China) with the parameters set as follows: excitation wavelength was from 200 nm to 300 nm; emission wavelength was from 320 nm to 450 nm; spectral slit width was 10 nm; and the gain value was 2.

2.4. DARTS with Pure hPPAR γ Protein. DARTS had been proved to be an efficient approach to efficiently verify drug-protein interactions when the protein was available in relatively pure form [16]. The basic principle of DARTS was that compounds were proposed to stabilize the combined protein globally or locally by reducing protease sensitivity of the target protein. This phenomenon was attributed to a specific conformational change caused by such a binding process, which would further induce protease recognition sites of the protein to be masked [17]. In this study, protein hPPAR γ regarded as target protein and pure hPPAR γ protein generated from recombinant plasmid were used in this experiment. Whether the presence of DBDF2,6T could reduce the proteolysis of the protein to validate the interaction between protein hPPAR γ and DBDF2,6T should be observed after incubating the hPPAR γ protein with DBDF2,6T.

Eight sample groups were set and divided into blank group, negative control group, and test group; each sample contained 0.5 μ g hPPAR γ protein. Except for the blank group, other samples were incubated with 2 μ L DMSO or 2 μ L DBDF2,6T with the concentration ranging from 1.0×10^{-2} mol/L to 1.0×10^{-4} mol/L for 60 min at 4°C and then digested with pronase (1 : 100) at room temperature for 30 min. The digestion was stopped by adding 5 \times SDS-PAGE sample loading buffer and boiling at 100°C for 10 min immediately. Samples were then subjected to electrophoresis on 8% SDS-PAGE. After electrophoresis, the gel was stained with Coomassie Brilliant Blue for 1 h and was observed after eluted overnight.

2.5. Ultrafiltration-Liquid Chromatography Experiment. Ultrafiltration-liquid chromatography (ultrafiltration-LC) was developed to verify the agonists of protein hPPAR γ . The main principle of ultrafiltration-LC was that the agonists of hPPAR γ had the ability to bind to the protein and would not be filtered out through the membrane of the ultrafiltration centrifuge tube, while after the protein denatured by dissolving in organic solvents, the compounds would be

unbound to the protein and could be washed out through the membrane of the ultrafiltration centrifuge tube. Based on the ultraviolet absorption of the compound, the DBDF2,6T which were bound to hPPAR γ could be detected through analyzing the washed solution by liquid chromatography. This method was first used in such confirmatory experiment and marked by its simplicity, generality, and applicability [18].

The recombination protein hPPAR γ (20 μ g) was incubated with compound DBDF2,6T (2μ L \cdot 10 $^{-3}$ mol/L) for 24 h at 4°C. After being filtered through a 10000 Da molecular weight cutoff ultrafiltration membrane (Millipore, UFC500396) by centrifugation at 13000 r/min for 8 min at 4°C, the sample was washed three times with 150 μ L PBS buffer (pH 7.4) and centrifuged at 13000 r/min for 12 min at 4°C to remove the unbound compounds. The washed solution was transferred to a new 10000 Da molecular weight cutoff ultrafiltration centrifuge tube and dissolved it in 400 μ L methanol. Centrifugation at 13000 r/min for 12 min was performed to wash out the compounds which were combined with the protein, and the washed solution was collected. Following reconstitution in 100 μ L of 50% aqueous methanol, the compound was analyzed using HPLC (Agilent Technologies). Denatured protein was used as a negative control, and in this experiment, the protein was heated at 98°C for 15 min to make it denatured.

The HPLC analysis was carried out using mobile phase methanol/0.5% phosphoric acid (28 : 72, v/v, pH 3.0) on a C18 column (Agilent TC-C18, 4.6 \times 250 mm i.d., 5 μ m) at a flow rate of 0.8 mL/min and at 25°C. The detection wavelength was set at 264 nm.

2.6. Molecular Docking. Surflex-Dock, docking module in SYBYL software (UCSF), was performed to determine the binding model of protein hPPAR γ (4a4w.pdb) and DBDF2,6T. It used prototype molecule (protomal) to represent protein binding pocket, utilizing probe to test the qualities of protein pocket such as surface hydrophobicity and could generate the invert transform of an active protein pocket. This method had high docking accuracy and could be used to research on the interaction between biomacromolecules and small molecular ligands [19].

Sybyl \times 2.0 was used to draw two-dimensional structure of DBDF2,6T with standard bonds and angles. In the process of optimizing the compound structure, minimize details and parameters of modify were set as follows. Minimize details: the iterations were set as 10000, and the color option was set as force. Parameters of modify: the force field was set as Tripos and the charges were set as Gasteiger-Marsili. In the docking process, A/YFB99 was chosen as extracted ligand structure and hydrogen molecules were added to the protein, and the modify details were set as follows: the force field was AMBER7 FF99 and the charge was AMBER. All other parameters were used the default value of SYBYL during the protein pocket generation and the molecular docking.

3. Results and Discussions

3.1. Fluorescence Spectrum of Protein hPPAR γ and hPPAR γ -DBDF2,6T Complexes. Fluorescence curves of the protein

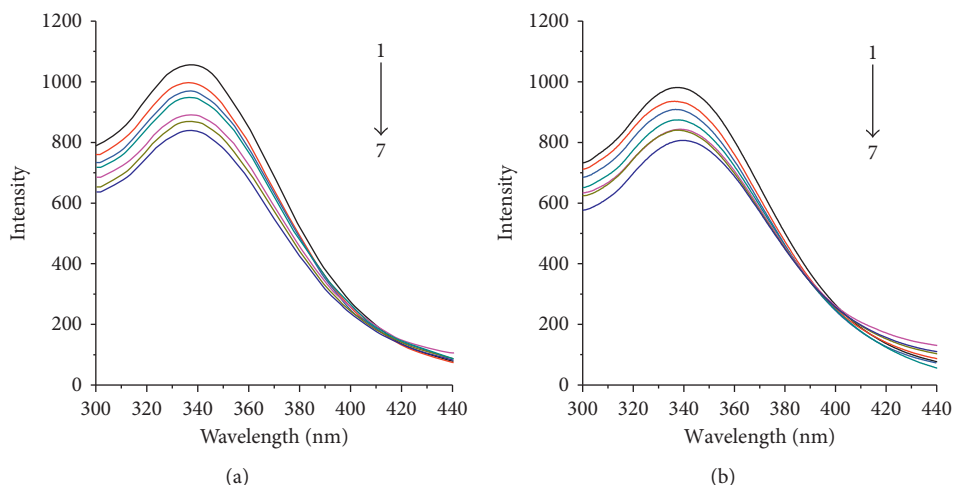


FIGURE 2: Fluorescence quenching spectra of protein hPPAR γ with series concentrations of DBDF2,6T at different temperatures: (a) 293 K and (b) 310 K. DBDF2,6T(a \rightarrow): 0, 0.5×10^{-6} , 1.0×10^{-6} , 1.5×10^{-6} , 2.5×10^{-6} , 3.0×10^{-6} , and 3.5×10^{-6} mol/L; hPPAR γ protein: $5 \mu\text{g/mL}$.

hPPAR γ and hPPAR γ -DBDF2,6T complexes are shown in Figure 2. The experiments were carried out in two temperatures with other experimental conditions unchanged. It can be observed from Figure 2 that, in both the experimental system of 273 K and 310 K, the intensity of fluorescence of the hPPAR γ protein was decreased while increasing the concentration of DBDF2,6T which was incubated with the hPPAR γ protein. And the highest fluorescent intensity values of hPPAR γ were recorded for next step of theoretical calculation.

3.2. Mechanism of Fluorescence Quenching. While the pH, temperature, and ionic strength were kept as constants, the types of fluorescence quenching could be classified into two categories: dynamic quenching and static quenching [20]. Dynamic quenching was caused by the fluorescent chromophore interacted with a quencher in excitation state, while the causes of static quenching were of three types: the first one, the fluorescent chromophore interacted with a quencher in ground state and came into being a nonfluorescent compound; the second one, the medium near the fluorescent chromophore had a polarity change, which caused by the conformational change of the protein attributing to the combination with the quencher; and the third one, a radiationless energy transfer between the fluorescent chromophore and the quencher [21].

The dynamic quenching obeyed the Stern–Volmer equation, and the formulas are shown as follows:

$$\frac{F_0}{F} = 1 + K_q \tau_0 c[Q] = 1 + K_{SV} c[Q], \quad (1)$$

$$K_q = \frac{K_{SV}}{\tau_0},$$

where K_{SV} is the Stern–Volmer quenching constant, K_q is the bimolecular quenching constant, and τ_0 is the average lifetime of the molecule which always be considered as 1.0×10^{-8} s [22, 23]. $c[Q]$ is the concentration of the quencher. F and F_0

correspondingly represent the intensity of the fluorescence of the protein added with the quencher or not.

The Stern–Volmer quenching curves were drawn according to the data obtained from fluorescence quenching spectra, and the corresponding linear regression equations and correlation coefficients are shown in Table 1.

When a quencher interacted with a biomacromolecule, the maximum value of diffusion collision rate constant was considered as 2.0×10^{10} L/mol/s. According to the computing results shown in Table 1, the dynamic quenching constant (K_q) between DBDF2,6T and the hPPAR γ protein was of the order of magnitude of 10^{12} , which was much bigger than the maximum value of diffusion collision rate constant. Consequently, the type of fluorescence quenching of the hPPAR γ protein induced by DBDF2,6T was preliminary defined as a kind of static quenching [24]. In dynamic quenching, which was associated with diffusion, quenching constant of fluorescent material was increasing as the temperature increased. But from the Figure 3, the slope of the Stern–Volmer lines was decreased while increasing the temperature of the experimental system, which further confirmed the quenching mechanism of DBDF2,6T with the hPPAR γ protein was static quenching.

3.3. Binding Constants and Binding Site Numbers. Equation (2) is the Lineweaver–Burk double-reciprocal equation, and (3) was deduced by (2) [25]:

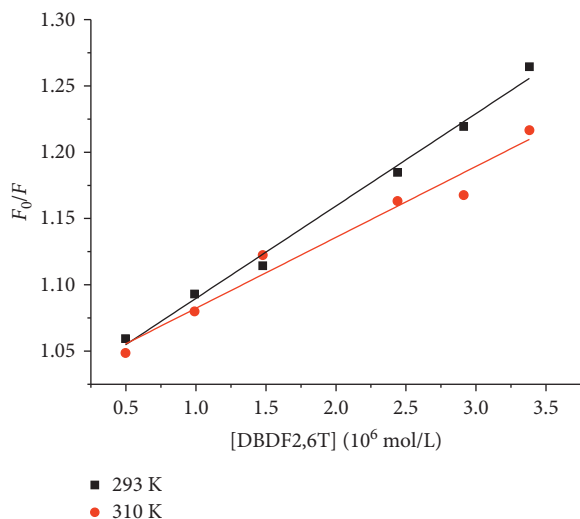
$$\frac{1}{F_0 - F} = \frac{1}{F_0} + \frac{1}{K_A F_0 c[Q]}, \quad (2)$$

$$\lg \left[\frac{F_0 - F}{F} \right] = \lg K_A + n \lg c[Q], \quad (3)$$

where K_A is the binding constant and n is the number of independent binding sites. When $-\lg[F_0 - F/F]$ were plotted against $\lg c(Q)$, a straight line could be drawn and is shown in Figure 4. The corresponding computing results are shown in Table 2.

TABLE 1: Linear regression equations and Stern–Volmer quenching rate constants at different temperatures.

Temperature T (K)	Linear regression equation	Correlation coefficient (r)	Dynamic quenching constant ($K_q/L\cdot\text{mol}^{-1}\cdot\text{s}^{-1}$)
293	$F_0/F = 0.0697 \times 10^6 c[Q] + 1.0201$	0.9926	6.97×10^{12}
310	$F_0/F = 0.0535 \times 10^6 c[Q] + 1.0288$	0.9679	5.35×10^{12}

FIGURE 3: Stern–Volmer plots of hPPAR γ interacted with DBDF2,6T at different temperatures.

In both the experimental temperatures (273 K and 310 K), the computing binding site numbers were near to 1, which meant that the hPPAR γ -DBDF2,6T complexes were formed by protein hPPAR γ and DBDF2,6T at the ratio approximately to 1 : 1. And the binding constants were of the order of magnitude of 10^3 , which meant that the binding ability between them was pretty strong.

3.4. Thermodynamic Parameters and Interaction Forces.

The interaction forces between small molecules and biomacromolecules were belonged to noncovalent force including hydrogen bond, van der Waals force, electrostatic attraction, and so on. The main acting force between hPPAR γ protein and DBDF2,6T could be judged according to the thermodynamic parameters which were calculated based on the Van't Hoff equation [26]. From the previous researches on interaction abilities, it was assumed that different proteins and compounds had different main acting force [27]. The thermodynamic parameters were calculated according to following equations:

$$\Delta H = \frac{2.303RT_1T_2}{T_2 - T_1} \lg \frac{K_2}{K_1}, \quad (4)$$

$$\Delta G = -RT \ln K, \quad (5)$$

$$\Delta S = \frac{\Delta H - \Delta G}{T}, \quad (6)$$

where R is the gas constant, ΔG is the Gibbs free energy change, ΔS is the entropy change, ΔH is the enthalpy change, and K is the Stern–Volmer quenching constant. ΔH could

be considered as a constant when the temperature changed in small range. And the Ross law indicated that, if $\Delta H > 0$ and $\Delta S > 0$, the main acting force between small molecules and biomacromolecules would be hydrophobic force; if $\Delta H < 0$ and $\Delta S < 0$, it would be hydrogen bond and van der Waals force; and if $\Delta H \approx 0$ and $\Delta S > 0$, it would be electrostatic force [28].

According to the computing results shown in Table 3, ΔH was 19.03 kJ/mol, ΔS was 3.92 J/mol·K and 3.90 J/mol·K correspondingly at 293 K and 310 K, and ΔG was -20.18 kJ/mol and -20.24 kJ/mol correspondingly at 293 K and 310 K. Based on the Ross law, the main acting force between hPPAR γ protein and DBDF2,6T was hydrophobic force. In addition, the regulator effect of several kinds of interaction forces and relevant microenvironments were both responsible for the macroscopic consequence [29].

3.5. Conformational Change of hPPAR γ Protein. The 3D fluorescence spectrum is shown in Figure 5 in the form of intensive contour map. The related data are shown in Table 4.

It can be observed from Figure 5 that two typical fluorescence peaks of proteins were located approximately at $\lambda_{em} = 340$ nm. In order to observe the peaks of fluorescent groups more clearly, the excitation wavelength range was set smaller than emission wavelength range, so the spectra of Rayleigh scattering were not available on the picture [19]. After the hPPAR γ protein was incubated with DBDF2,6T, the location of both fluorescence peaks did not show a significant change, but the intensity of each peak was reduced at different degrees. From the 3D fluorescence spectra of the hPPAR γ protein (Figure 5(a)), the intensity ratio of the big peak to the small one was 7.97 : 1, while after the protein was incubated with DBDF2,6T (Figure 5(b)), the value was changed to 8.00 : 1, and the DBDF2,6T showed a strong quenching effect on the big peak which was located at about 290/340 ($\lambda_{ex}/\lambda_{em}$). The 3D fluorescence spectrum indicated a conformational change of the specific structures of the hPPAR γ protein, which could further validate the interaction between the hPPAR γ protein and DBDF2,6T [30].

3.6. Confirmation of the Interaction Ability Using DARTS Technique.

To identify the binding targets for small molecules, the key advantage of DARTS method was no sample pretreatments such as labeling the ligand [17]. And the method was particularly useful when a compound had a lower affinity with the target, even the binding constant was in micromolar range [31]. To confirm the feasibility of the DARTS applying to the hPPAR γ protein, a preliminary experiment had been performed to research the digestion effects of the protease on the hPPAR γ protein. And the

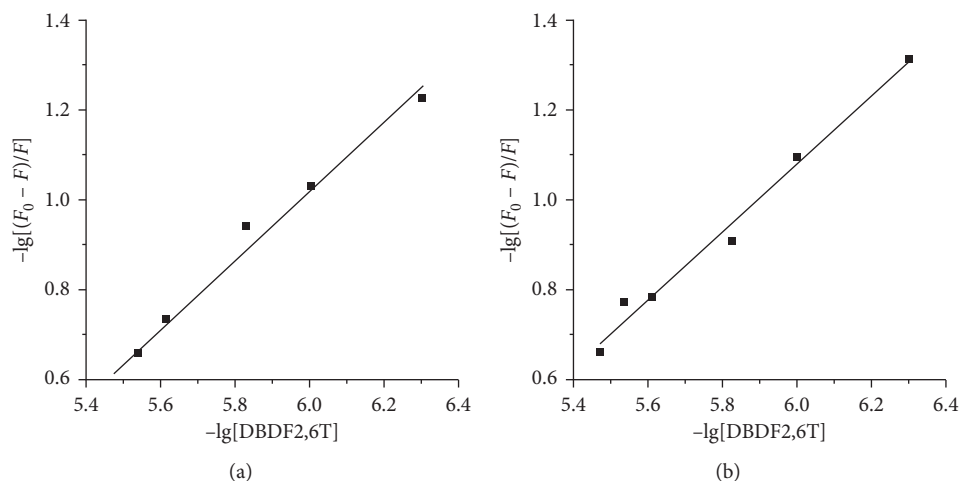


FIGURE 4: A plot of $-\lg[(F_0 - F)/F]$ versus $-\lg[\text{DBDF2,6T}]$ at different temperatures: (a) 293 K and (b) 310 K.

TABLE 2: Binding constants and the numbers of binding sites of hPPAR γ protein with DBDF2,6T at different temperatures.

Temperature T (K)	Numbers of binding sites	Binding constant, K_A (L/mol)	Correlation coefficient (r^2)
293	0.77	3.96×10^3	0.9841
310	0.75	2.58×10^3	0.9856

TABLE 3: Thermodynamic parameters of reaction system of hPPAR γ protein and DBDF2,6T.

Temperature T (K)	ΔH (kJ/mol)	ΔS (J/mol·K)	ΔG (kJ/mol)
293		3.92	-20.18
310	19.03	3.90	-20.24

pronase was used for digestion because it had been proved to be more useful for DARTS than any other protease [16]. In preliminary experiment, the digestion effects of time of enzymolysis and the concentration of pronase had been investigated.

After electrophoresis and staining, the protein bands of each sample are shown in Figure 6. Compared with the DMSO control, under certain conditions, the antienzymatic hydrolysis ability of hPPAR γ protein did exist and was closely related to the concentration of DBDF2,6T incubated with the protein. In 0.5×10^{-4} mol/L DBDF2,6T, the strongest antienzymatic hydrolysis ability of the hPPAR γ protein would appear, and such ability could be weakened with the change in the concentration. Although DBDF2,6T had shown hydrolysis ability to the hPPAR γ protein at relatively high concentration, the protective functions of DBDF2,6T to the hPPAR γ protein still could be observed and existed concentration-effect relationships in some extent. Consequently, the interaction between hPPAR γ protein and DBDF2,6T could be indirectly verified [32].

3.7. Confirmation of the Binding Ability Using Ultrafiltration-LC Technique. The results of ultrafiltration-LC experiment are shown in Figure 7. It can be observed from the chromatograms that both the sample and the negative control

had an obvious peak at location about 8.75 min which belongs to compound DBDF2,6T. Significant signal enhancement of the peak of compound DBDF2,6T between the sample and the negative control indicated a specific binding between DBDF2,6T and the recombinant protein hPPAR γ , while the signal of DBDF2,6T in the negative control was attributed to the nonspecific binding [33]. The big impurity peak was located at about 7 min attributed to the solution of recombination protein hPPAR γ . Therefore, the experiment of ultrafiltration-LC did verify that compound DBDF2,6T could bind to pure protein hPPAR γ directly in physiological environment [34].

3.8. Exploration of the Theoretical Binding Details Using Molecular Docking. In order to further understand the interaction between DBDF2,6T and hPPAR γ protein, molecular docking was used to explore the theoretical binding details of them [35]. Among the docking of 12 conformers of DBDF2,6T to generate pocket of the hPPAR γ protein, the highest total score was 7.14 and the corresponding crash score and polar score were -1.86 and 0.00, respectively, which meant that DBDF2,6T had a pretty strong affinity to hPPAR γ protein, and such docking process was under a relatively comfortable level of molecules [36]. The generated pocket of hPPAR γ is shown in Figure 8(a), and the hydrogen bond graph is shown in Figure 8(b). In conclusion, DBDF2,6T could theoretically bind to hPPAR γ protein with pretty strong binding strength, and it could directly interact with SER342 and GLY284 of hPPAR γ protein by hydrogen bond. The hydrogen bond lengths between DBDF2,6T and SER342 were 2.50 Å and 2.42 Å, and that between DBDF2,6T and GLY284 was 2.74 Å.

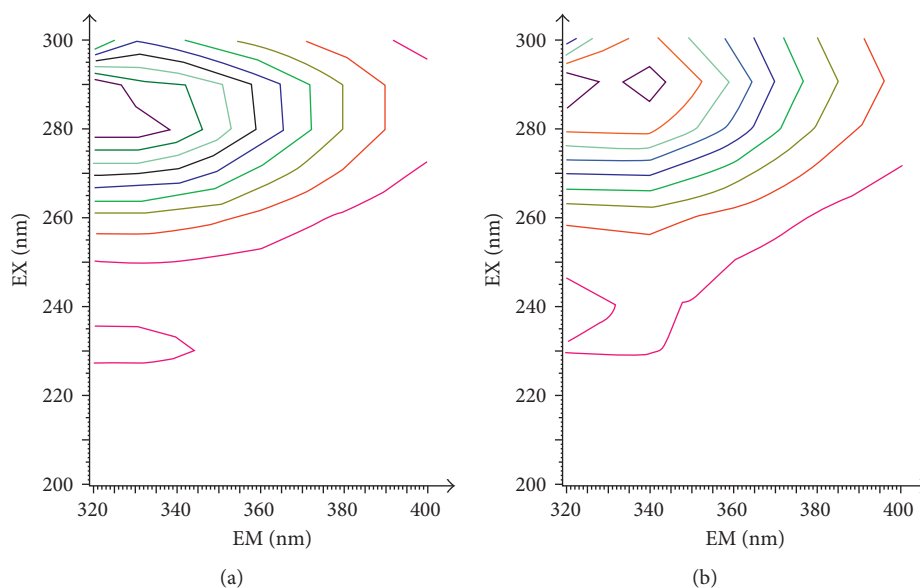


FIGURE 5: The contour maps of two fluorescent systems: (a) hPPAR γ and (b) hPPAR γ -DBDF2,6T system ($T = 293$ K).

TABLE 4: Several characteristic parameters of 3D fluorescence experiments.

System and parameters	PPAR γ		PPAR γ + DBDF2,6T	
	Peak 1	Peak 2	Peak 1	Peak 2
Fluorescence peak				
Peak position ($\lambda_{ex}/\lambda_{em}$ nm/nm)	283/337	230/328	290/340	231/332
Relative intensity (I)	1275	160	1200	150
I_1/I_2		7.97 : 1		8.00 : 1
Stokes shift ($\Delta\lambda$ /nm)	48	107	50	109

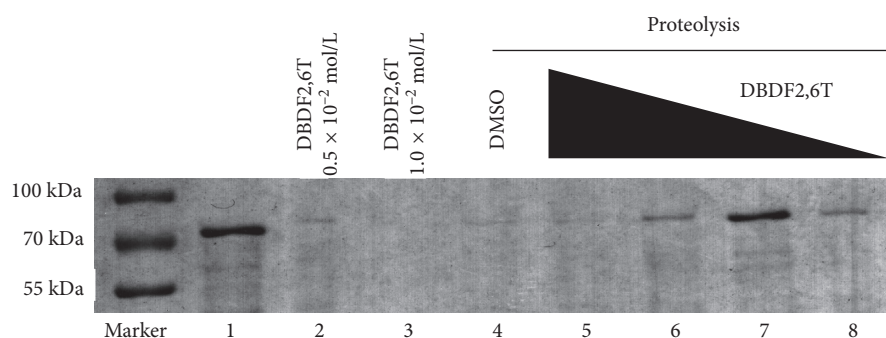


FIGURE 6: DARTS detection via SDS-PAGE. Band 1 was pure hPPAR γ protein without incubation with DBDF2,6T or proteolysis; bands 2 and 3 were hPPAR γ protein incubated with 0.5×10^{-2} mol/L and 1.0×10^{-2} mol/L DBDF2,6T, respectively, and without proteolysis; bands 4 to 8 were hPPAR γ protein incubated with DMSO and different concentrations of DBDF2,6T (5 \rightarrow 8: 0.5×10^{-2} mol/L, 0.5×10^{-3} mol/L, 0.5×10^{-4} mol/L, and 0.5×10^{-5} mol/L), respectively, and with proteolysis.

4. Conclusions

This study analyzed the interaction between the novel patent organotin compound DBDF2,6T and the hPPAR γ protein under physiological condition with the methods of fluorescence quenching, 3D fluorescence, DARTS, ultrafiltration-LC, and computer molecular docking. According to the spectroscopic experimental data, DBDF2,6T could interact with the hPPAR γ protein and formed a nonradiative

ground-state complex of hPPAR γ -DBDF2,6T, mainly through hydrophobic force. Such a reaction was spontaneous and could cause a conformational change of the hPPAR γ protein. And the experiments of DARTS and ultrafiltration-LC preliminarily proved the possibility of DBDF2,6T to be an agonist compound to hPPAR γ protein. Considering the anticancer activity of DBDF2,6T and various physiological functions performed by agonists of PPAR γ protein, the conclusion could be drawn that

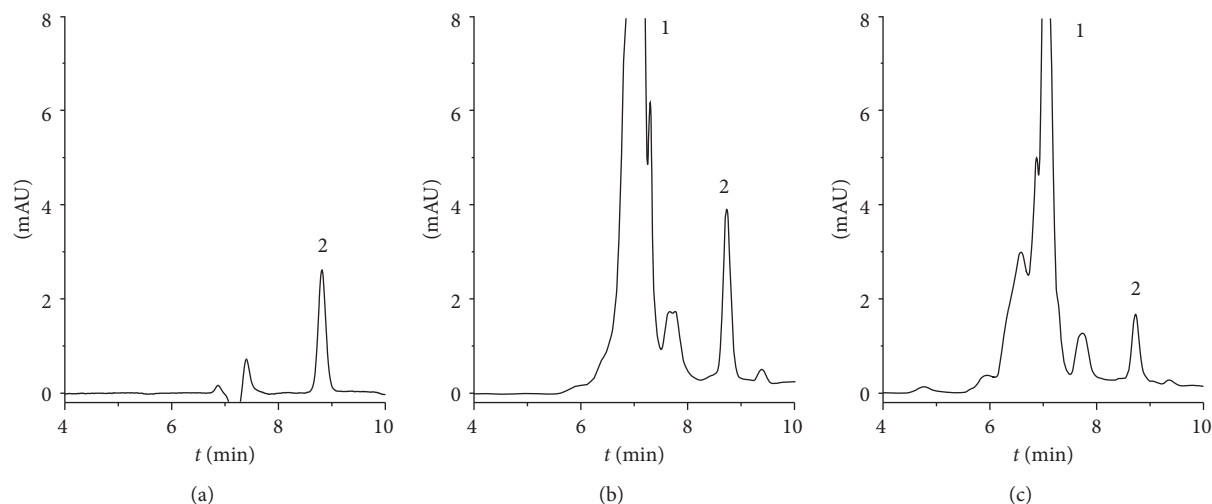


FIGURE 7: The results of ultrafiltration-LC experiment: (a) compound DBDF2,6T dissolved in 50% aqueous methanol; (b) the sample which was prepared using natural protein; (c) the negative control which was prepared using denatured protein. 1: the peak of impurities from solvent of protein hPPAR γ ; 2: the peak of compound DBDF2,6T.

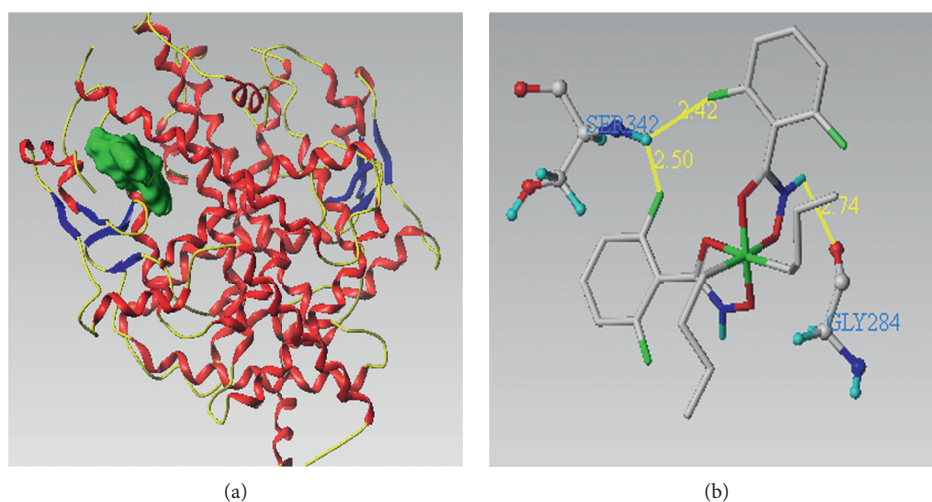


FIGURE 8: The docking results of DBDF2,6T to hPPAR γ protein: (a) the generated pocket of hPPAR γ protein; (b) hydrogen bond graph of DBDF2,6T to the interacted residues of the hPPAR γ protein. The yellow lines in the picture represent the hydrogen bond.

DBDF2,6T had a possibility to interact with the hPPAR γ protein as an agonist and finally inducing physiological effects such as anticancer activity. This work successfully revealed the interaction of DBDF2,6T with hPPAR γ protein and established a feasible way to validate the agonist compounds for hPPAR γ protein.

Abbreviations

DBDF2,6T:	Bis-[2,6-difluoro- <i>N</i> -(hydroxyl- κ O)benzamidato- κ O]dibutyltin
hPPAR γ :	Human peroxisome proliferator-activated receptor gamma
3D fluorescence:	Three-dimensional fluorescence
DARTS:	Drug affinity responsive target stability
LC:	Liquid chromatography.

Data Availability

The data used to support the findings of this study are available from the corresponding author upon request.

Conflicts of Interest

The authors declare that they have no conflicts of interest.

Acknowledgments

Financial supports funded by the Shanxi Key Laboratory of Innovative Drug for the Treatment of Serious Diseases Basing on the Chronic Inflammation Shanxi University of Chinese Medicine, Program for the Natural Science Foundation of Shanxi Province (no. 2014011027-1), the Fund for Shanxi Key Subjects Construction (2016), the

Program for Science and Technology of Shanxi Province (no. 20130313021-9), the Top Science and Technology Innovation Teams of Higher Learning Institutions of Shanxi Province, the Program for the Top Young and Middle-aged Innovative Talents of Higher Learning Institutions of Shanxi Province (2015), the Foundation of Young Academic Leader in Shanxi Province, the Project of Shanxi Key Laboratory for Innovative Drugs on Inflammation-Based Major Disease (2018), and the Project of Center of Comprehensive Development, Utilization and Innovation of Shanxi Medicine (2017-JYXT-18) are gratefully acknowledged.

References

- [1] H. K. Okoro, O. S. Fatoki, F. A. Adekola, B. J. Ximba, R. G. Snyman, and B. Opeolu, "Human exposure, biomarkers, and fate of organotin in the environment," *Reviews of Environmental Contamination and Toxicology*, vol. 213, pp. 27–54, 2011.
- [2] C. Yan, J. Zhang, T. Liang, and Q. Li, "Diorganotin(IV) complexes with 4-nitro-N-phthaloyl-glycine: synthesis, characterization, antitumor activity and DNA-binding studies," *Biomedicine and Pharmacotherapy*, vol. 71, pp. 119–127, 2015.
- [3] A. le Maire, M. Grimaldi, D. Roecklin et al., "Activation of RXR-PPAR heterodimers by organotin environmental endocrine disruptors," *EMBO Reports*, vol. 10, no. 4, pp. 367–373, 2009.
- [4] M. C. Cho, D. H. Lee, E. J. Kim et al., "Novel PPAR γ partial agonists with weak activity and no cytotoxicity; identified by a simple PPAR γ ligand screening system," *Molecular and Cellular Biochemistry*, vol. 358, no. 1-2, pp. 75–83, 2011.
- [5] S. Chen, B. A. Johnson, Y. Li et al., "Both coactivator LXXLL motif-dependent and-independent interactions are required for peroxisome proliferator-activated receptor gamma (PPAR γ) function," *Journal of Biological Chemistry*, vol. 275, no. 6, pp. 3733–3736, 2000.
- [6] M. C. Cho, H. E. Yoon, J. W. Kang et al., "A simple method to screen ligands of peroxisome proliferator-activated receptor delta," *European Journal of Pharmaceutical Sciences*, vol. 29, no. 5, pp. 355–360, 2006.
- [7] A. Kadivar, H. H. Khoei, H. Hassanpour et al., "Peroxisome proliferator-activated receptors (PPAR α , PPAR γ and PPAR β/δ) gene expression profile on ram spermatozoa and their relation to the sperm motility," *Veterinary Research Forum*, vol. 7, pp. 27–34, 2016.
- [8] K. L. Houseknecht, B. M. Cole, and P. J. Steele, "Peroxisome proliferator-activated receptor gamma (PPAR γ) and its ligands: a review," *Domestic Animal Endocrinology*, vol. 22, no. 1, pp. 1–23, 2002.
- [9] V. Vella, M. L. Nicolosi, S. Giuliano, M. Bellomo, A. Belfiore, and R. Malaguarnera, "PPAR- γ agonists as antineoplastic agents in cancers with dysregulated IGF axis," *Frontiers in Endocrinology*, vol. 8, pp. 8–31, 2017.
- [10] Z. Xu, G. Wang, Y. Zhu et al., "PPAR- γ agonist ameliorates liver pathology accompanied by increasing regulatory B and T cells in high-fat-diet mice," *Obesity*, vol. 25, no. 3, pp. 581–590, 2018.
- [11] Z. Tian, F. Zang, W. Luo et al., "Spectroscopic study on the interaction between mononaphthalimide spermidine (MINS) and bovine serum albumin (BSA)," *Journal of Photochemistry and Photobiology B: Biology*, vol. 142, pp. 103–109, 2015.
- [12] M. M. Khan and S. Tayyab, "Understanding the role of internal lysine residues of serum albumins in conformational stability and bilirubin binding," *Biochimica et Biophysica Acta (BBA)-Protein Structure and Molecular Enzymology*, vol. 1545, no. 1-2, pp. 263–277, 2011.
- [13] E. L. Gelamo and M. Tabak, "Spectroscopic studies on the interaction of bovine (BSA) and human (HSA) serum albumins with ionic surfactants," *Spectrochimica Acta Part A: Molecular and Biomolecular Spectroscopy*, vol. 56, no. 11, pp. 2255–2271, 2000.
- [14] L. E. Borissevitch, T. T. Tominaga, H. Imasato et al., "Fluorescence and optical absorption study of interaction of two water soluble porphyrins with bovine serum albumin. The role of albumin and porphyrin aggregation," *Journal of Luminescence*, vol. 69, no. 2, pp. 65–76, 1999.
- [15] X. J. Liu, X. Y. Wu, C. Y. Qi, and J. S. Cui, "Applications of three-dimensional fluorescent spectroscopy analysis technology," *Hebei Journal of Industrial and Technology*, vol. 6, pp. 422–425, 2012.
- [16] M. Y. Pai, B. Lomenick, H. Hwang et al., "Drug affinity responsive target stability (DARTS) for small-molecule target identification," *Methods in Molecular Biology*, vol. 1263, pp. 287–298, 2015.
- [17] M. M. Derry, R. R. Somasagara, K. Raina et al., "Target identification of grape seed extract in colorectal cancer using drug affinity responsive target stability (DARTS) technique: role of endoplasmic reticulum stress response proteins," *Current Cancer Drug Targets*, vol. 14, no. 4, pp. 323–336, 2014.
- [18] Y. Choi, Y. Jung, and S.-N. Kim, "Identification of eupatilin from *Artemisia argyi* as a selective PPAR α agonist using affinity selection ultrafiltration LC-MS," *Molecules*, vol. 20, no. 8, pp. 13753–13763, 2015.
- [19] Y. Wei, L. Niu, X. Liu et al., "Spectroscopic studies and molecular docking on the interaction of organotin antitumor compound bis[2,4-difluoro-N-(hydroxy- κ O)benzamido- κ O]diphenyltin(IV) with human cytochrome P450 3A4 protease," *Spectrochimica Acta Part A: Molecular and Biomolecular Spectroscopy*, vol. 163, pp. 154–161, 2016.
- [20] M. P. Brown and C. Royer, "Fluorescence spectroscopy as a tool to investigate protein interactions," *Current Opinion in Biotechnology*, vol. 8, no. 1, pp. 45–49, 1997.
- [21] G. Z. Chen, Z. X. Huang, and J. G. Xu, *Fluorescence Spectrometry*, Science Press, Beijing, China, 2nd edition, 1990.
- [22] S. M. T. Shaikh, J. Seetharamappa, S. Ashoka, and P. B. Kandagal, "A study of the interaction between bromopyrogallol red and bovine serum albumin by spectroscopic methods," *Dyes and Pigments*, vol. 73, no. 2, pp. 211–216, 2007.
- [23] W. Sun, Y. Du, J. Chen, J. Kou, and B. Yu, "Interaction between titanium dioxide nanoparticles and human serum albumin revealed by fluorescence spectroscopy in the absence of photoactivation," *Journal of Luminescence*, vol. 129, no. 8, pp. 778–783, 2009.
- [24] M. Kathiravan, R. Chandramohan, S. Renganathan, and S. Sekar, "Spectroscopic studies on the interaction between phycocyanin and bovine serum albumin," *Journal of Molecular Structure*, vol. 919, no. 1–3, pp. 210–214, 2009.
- [25] S. Bi, D. Song, Y. Tian, X. Zhou, Z. Liu, and H. Zhang, "Molecular spectroscopic study on the interaction of tetracyclines with serum albumins," *Spectrochimica Acta Part A: Molecular and Biomolecular Spectroscopy*, vol. 61, no. 4, pp. 629–636, 2005.
- [26] L. N. Zhang, X. Chen, Y. Xia et al., "Study on interaction mechanism between meso-tetra-(4-hydroxyphenyl)-Zn

- porphyrin and bovine serum albumin by fluorescence method," *Spectroscopy and Spectral Analysis*, vol. 3, pp. 773–776, 2009.
- [27] L. Gao, H. Y. Cao, and G. Liu, "Spectroscopy on the interaction between four metalloporphyrin complexes and serum albumin," *Chemical Reagents*, vol. 2, pp. 108–112, 2012.
- [28] M. R. Ganjali, F. Faridbod, A. Divsalar et al., "Nano-composite carbon paste electrode used for biophysical study of Ho3 ion interaction with human serum albumin V," *International Journal of Electrochemical Science*, vol. 5, pp. 852–866, 2010.
- [29] J. Gonzalez-Jimencz, H. Jacquotte, and J. Cayre, "Fluorescence quenching studies on binding fluoreno-9-spiro-oxazolidinedione to human serum albumin," *Chemico-Biological Interactions*, vol. 84, no. 3, pp. 221–228, 1992.
- [30] Q. Q. Zhang, S. H. Lei, X. L. Wang, L. Wang, and C.-J. Zhu, "Discrimination of phytoplankton classes using characteristic spectra of 3D fluorescence spectra," *Spectrochimica Acta Part A Molecular and Biomolecular Spectroscopy*, vol. 63, no. 2, pp. 361–369, 2006.
- [31] F. Dal Piaz, M. B. Vera Saltos, S. Franceschelli et al., "Drug affinity responsive target stability (DARTS) identifies laurifolioside as a new clathrin heavy chain modulator," *Journal of Natural Products*, vol. 79, no. 10, pp. 2681–2692, 2016.
- [32] C. Rodriguez-Furlan, C. Zhang, N. Raikhel et al., "Drug affinity responsive target stability (DARTS) to resolve protein–small molecule interaction in arabidopsis," *Current Protocols in Plant Biology*, vol. 2, no. 4, pp. 287–298, 2017.
- [33] P. Tang, S. Si, and L. Liu, "Analysis of bovine serum albumin ligands from *Puerariae flos* using ultrafiltration combined with HPLC-MS," *Journal of Chemistry*, vol. 2015, Article ID 648361, 6 pages, 2015.
- [34] Z. Liu, Z. Lin, S. Chen, L. Wang, and S. Xian, "Rapid screening of potential phosphodiesterase inhibitors from the roots of *Ilex pubescens* hook. et arn. Using a combination of ultrafiltration and LC-MS," *Evidence-Based Complementary and Alternative Medicine*, vol. 2017, Article ID 2749643, 8 pages, 2017.
- [35] G. Hou, R. Zhang, X. Hao, and C. Liu, "An exploration of the effect and the interaction mechanism of bisphenol A on waste sludge hydrolysis with multi-spectra, isothermal titration microcalorimetry and molecule docking," *Journal of Hazardous Materials*, vol. 333, pp. 32–41, 2017.
- [36] R. Spitzer and A. N. Jain, "Surflex-dock: docking benchmarks and real-world application," *Journal of Computer-Aided Molecular Design*, vol. 26, no. 6, pp. 687–699, 2012.

Research Article

Synthesis, Structural Analysis, and Biological Activities of Some Imidazolium Salts

Gühergül Uluçam  and Murat Turkyilmaz

Department of Chemistry, Trakya University, 22030 Edirne, Turkey

Correspondence should be addressed to Gühergül Uluçam; gulergul@trakya.edu.tr

Received 11 February 2018; Revised 11 April 2018; Accepted 17 April 2018; Published 22 May 2018

Academic Editor: Rais A. Khan

Copyright © 2018 Gühergül Uluçam and Murat Turkyilmaz. This is an open access article distributed under the Creative Commons Attribution License, which permits unrestricted use, distribution, and reproduction in any medium, provided the original work is properly cited.

Four newly synthesized imidazolium salts were characterized by nuclear magnetic resonance, vibrational spectra, and mass spectra. Then, the density functional theory calculations were performed to obtain the molecular configurations on which the theoretical nuclear magnetic resonance and infrared spectra were consequently obtained. The comparison of calculated spectra with the experimental spectra for each molecule leads to the conclusion that the theoretical results can be assumed to be a good approach to their molecular configurations. The *in vitro* biological activities of the salts on the selected bacteria and cancer cell lines were determined by using the broth dilution method according to Clinical and Laboratory Standards Institute guidelines. The 1,3-bis(2-hydroxyethyl) imidazolidinium bromide and 3-(2-ethoxy-2-oxoethyl)-1-(3-aminopropyl)-1H-imidazol-3-ium bromide showed efficiency on *Bacillus cereus* ATCC 11778. The 3-bis(2-carboxyethyl)-4-methyl-1H-imidazol-3-ium bromide was effective on HeLa while a similar effect was observed on Hep G2 with 3-(2-carboxyethyl)-1-(3-aminopropyl)-1H-imidazol-3-ium bromide.

1. Introduction

Imidazole rings are building blocks in amino acids [1] together with the fact that their membership in the development of new antifungal drugs [2, 3] and antibiotics [4, 5] are crucial. Its derivatives are widely used in other medicinal applications [6]. The pregnane derivatives with imidazole moiety and triazole moiety, for example, were tested on the prostate, breast, and lung cancer cell lines, and dose-effective proliferation of the cells was determined [7]. Similarly, the novel hybrid compounds of imidazole scaffold-based 2-benzylbenzofloran have been prepared and used in cytotoxic activity studies on various cancer cell lines [8].

As a five-membered aromatic ring containing two nonadjacent nitrogen atoms [9], imidazole is also subjected to various computational chemistry research beyond its biological applications. Its ability to capture CO₂ was determined in the investigations of the greenhouse effect compensation in the framework of van der Waals bonded host-guest relation [10]. The hydroxyl conductivity in

polymembranes based on imidazole salts was simulated using radial distribution functions and found that the imidazole groups provide better conductivity than that of water and methanol [11]. Moreover, the specific imidazole derivatives exhibited good cross section values for two-photon absorption [12]. The detoxification of phosphotriesters by imidazole rings was clarified comparing the same effects with methyl-imidazoles depending on the methyl positioning [13].

N-Heterocyclic carbenes (NHCs) are the imidazole-based carbene groups which are isolated and crystallized by the deprotonation of imidazole salts [14]. Also, the imidazole salts naturally transform into NHCs over metal complex building reactions, as exemplified on the synthesis and characterization of the silver-NHC complexes [15] and the iron-imidazole salts [16].

The constitution and functions of imidazole ligands in organometallic chemistry and inorganic chemistry have been widely studied, and these particular researches have been evaluated as a scientific competition field due to its importance in the related industry [17]. Also, they are set as

alternative to usual ligands in the carbon-carbon coupling reactions of the pharmaceutical reagents [18]. The synthesis and spectroscopic characterizations of four new NHC ligands, namely, 1,3-bis(2-hydroxyethyl) imidazolidinium bromide (L_A), 3-(2-ethoxy-2-oxoethyl)-1-(3-aminopropyl)-1H-imidazol-3-ium bromide (L_B), 1,3-bis(2-carboxyethyl)-4-methyl-1H-imidazol-3-ium bromide (L_C), and 3-(2-carboxyethyl)-1-(3-aminopropyl)-1H-imidazol-3-ium bromide (L_D) were exhibited in this study. Using their nuclear magnetic resonance (NMR) and infrared (IR) spectra, the molecular properties of the ligands were obtained. Also, the *in vitro* biological activities of the synthesized molecules were presented.

2. Materials and Methods

2.1. Instrumentation and Methods. The ^1H and ^{13}C NMR spectra of the compounds in deuterium oxide (D_2O) were recorded on Varian 300 MHz and Varian 75.5 MHz, respectively. The IR spectra by KBr pellets were recorded in the range $450\text{--}4000\text{ cm}^{-1}$ by a PerkinElmer BXII spectrometer. The mass spectra were acquired by the electron impact technique using a Thermo Finnegan Trace DSQ GC/MS. Elemental analyses for C, H, and N were realized on the dried samples using a PerkinElmer 2400 CHN analyzer. The absorbance measurements in determining the biological activities of the material were carried out in Thermo Scientific Multiskan Go multiplate spectrophotometer.

2.2. Synthesis

2.2.1. 1,3-Bis(2-hydroxyethyl) Imidazolidinium Bromide, L_A . Imidazole (10 mmol, 0.68 g) was dissolved in tetrahydrofuran (THF), and bromoethanol (22 mmol, 2.75 g) was added as the mixture was stirred for 20 hours. The completion of the reaction was monitored by thin-layer chromatography (TLC) in ethyl acetate/hexane (1 : 5) analyses, and the solid residue was filtered out with a sintered glass funnel. The solvent in the filtrate was evaporated using a rotary evaporator, and the product was dried in a vacuum desiccator. After that, the product was purified by column chromatography (ethyl acetate/hexane, 1 : 5). The best yield was obtained when the reaction was carried out at room temperature with a 1 : 2 mole ratio of the reagents. 1.54 g of the final product was obtained with 65% yield. It was in yellowish liquid form. The elemental analyses result for L_A with the chemical formula $\text{C}_7\text{H}_{13}\text{BrN}_2\text{O}_2$ are C, 35.46%; H, 5.53%; and N, 11.82%; found: C, 35.35%; H, 5.43%; and N, 11.73%. The mass spectroscopy reads (m/z) 158.22 ($\text{M} + \text{H}$)⁺ which is consistent with the expected molecular weight.

2.2.2. 3-(2-Ethoxy-2-oxoethyl)-1-(3-aminopropyl)-1H-imidazol-3-ium Bromide, L_B . 3-(1H-imidazol-1-yl)propan-1-amine (10 mmol, 1.27 g) was dissolved in THF and stirred at room temperature, and then, ethyl bromoacetate (11 mmol, 1.837 g) was added with a 1 : 1 mole ratio. The mixture was stirred for 15 hr. The completion of the reaction was monitored by thin layer chromatography (TLC) in ethyl acetate/hexane (1 : 5) analyses. The solvent was evaporated in

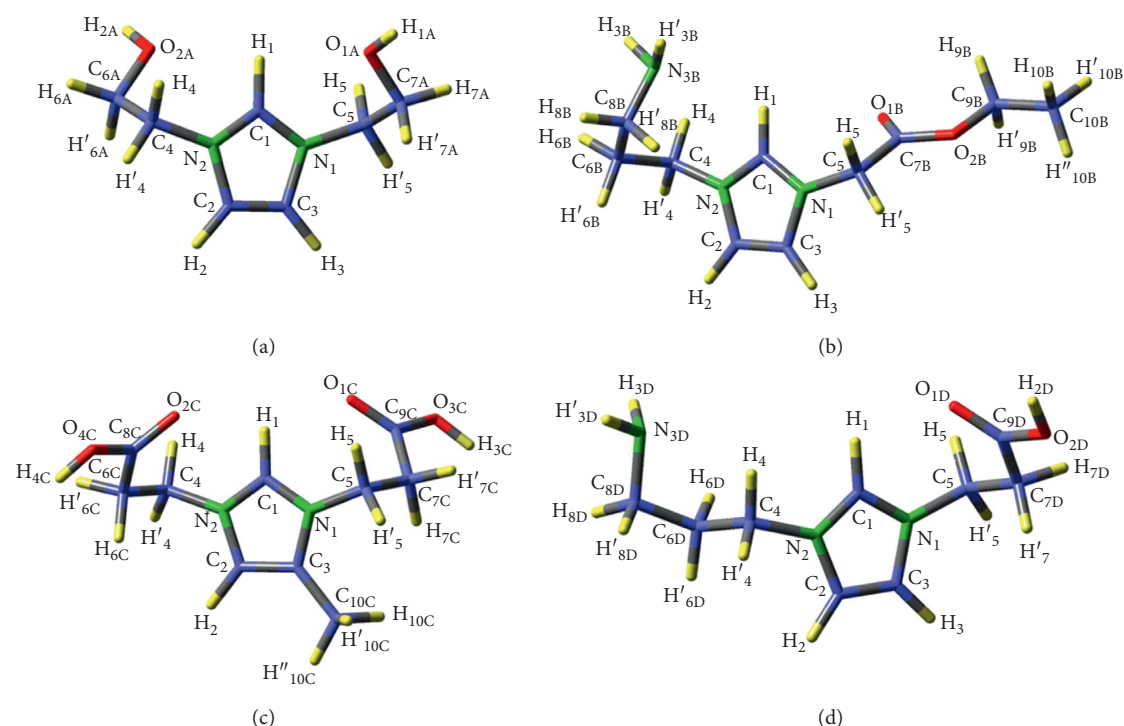
a rotary evaporator, and the substance was kept under vacuum in a desiccator. After that, the product was purified by column chromatography (ethyl acetate/hexane, 1 : 5). It was pale brown oily liquid. 0.94 g of the final product was obtained with 32% yield. The elemental analyses result for L_B with the chemical formula $\text{C}_{10}\text{H}_{18}\text{BrN}_3\text{O}_2$ are C, 41.11%; H, 6.21%; and N, 14.38%; found: C, 39.93%; H, 6.35%; N, and 14.21%. The mass spectroscopy result reads (m/z) 213.12 ($\text{M} + \text{H}$)⁺ which is consistent with the expected molecular weight.

2.2.3. 1,3-Bis(2-carboxyethyl)-4-methyl-1H-imidazol-3-ium Bromide, L_C . The procedure applied in the synthesis of L_A was also used for the synthesis of L_C by replacing imidazole and bromoethanol with 4-methylimidazole (10 mmol, 0.82 g) and 3-bromopropionic acid (22 mmol, 3.366 g), respectively. After that, the product was purified by column chromatography (ethyl acetate/hexane, 1 : 5). It was in white solid form. 1.48 g of the final product was obtained with 48% yield. The elemental analyses result for L_C with the chemical formula $\text{C}_{10}\text{H}_{15}\text{BrN}_2\text{O}_4$ are C, 39.10%; H, 4.92%; and N, 9.12%; found: C, 38.97%; H, 4.77%; and N, 19.22%. The mass spectroscopy result reads (m/z) 227.68 ($\text{M} + \text{H}$)⁺ which is consistent with the expected molecular weight.

2.2.4. 3-(2-Carboxyethyl)-1-(3-aminopropyl)-1H-imidazol-3-ium Bromide, L_D . The procedure applied in the synthesis of L_B was also used for the synthesis of L_D by replacing ethyl bromoacetate with 3-bromopropanoic acid (11 mmol, 1.683 g), respectively. The product was purified by column chromatography (ethyl acetate/hexane, 1 : 5). It was pale brown oily liquid. 1.22 g of the final product was obtained with 44% yield. The elemental analyses result for L_D with the chemical formula $\text{C}_9\text{H}_{16}\text{BrN}_3\text{O}_3$ are C, 38.86%; H, 5.80%; and N, 15.11%; found: C, 38.77%; H, 5.63%; and N, 15.23%. The mass spectroscopy result reads (m/z) 198.25 ($\text{M} + \text{H}$)⁺ which is consistent with the expected molecular weight.

2.3. Biological Activities

2.3.1. Antibacterial Activity. Broth microdilution method as in the guidelines of Clinical Laboratory Standards Institute was applied to determine the antibacterial activities of the L_A , L_B , L_C , and L_D on the Gram-negative bacteria (*Escherichia coli* ATCC 25922, *Escherichia coli* 0157:H7, and *Salmonella typhimurium* ATCC 14028), Gram-positive bacteria (*Bacillus cereus* ATCC 11778, *Staphylococcus aureus* ATCC 25923, and *Listeria monocytogenes* ATCC 19115), and standard yeast *Candida albicans* ATCC 10231. The bacteria and yeast were obtained from the American Type Culture Collection. The incubations were done in Tryptic Soy Broth medium at 37°C for 24 hr in the scale of McFarland 0.5. The antibiotic controls were carried by gentamicin on *Bacillus cereus* ATCC 1177 and amphotericin-b on *Candida albicans* ATCC 10231, while ampicillin was used on the other bacteria samples. For sterilization purposes, the antibiotic solutions and the stock solution of the chemicals were filtered through a $0.45\text{ }\mu\text{m}$ sterile filter. The solvent in which the test compounds



SCHEME 1: Optimized conformers of the synthesized imidazole molecules with their labeled and numbered atoms: (a) 1,3-bis(2-hydroxyethyl)imidazolidinium bromide, (b) 3-(2-ethoxy-2-oxoethyl)-1-(3-aminopropyl)-1H-imidazol-3-ium bromide, (c) 1,3-bis(2-carboxyethyl)-4-methyl-1H-imidazol-3-ium bromide, and (d) 3-(2-carboxyethyl)-1-(3-aminopropyl)-1H-imidazol-3-ium bromide.

TABLE 1: Some selected geometrical parameters of the common properties of the investigated molecules.

	L_A	L_B	L_C	L_D	L
<i>Selected bond lengths</i> (Å)					
C ₁ -H ₁	1.102	1.043	1.061	1.095	0.976
C ₁ -N ₁	1.295	1.301	—	—	1.312 (7)
C ₃ -N ₁	1.403	1.398	1.335	1.396	1.374 (8)
C ₂ -C ₃	1.297	1.332	1.366	1.314	1.312 (10)
C ₄ -N ₂	1.464	1.437	1.418	1.523	1.444 (8)
N ₁ -C ₅	1.464	1.474	1.429	1.505	1.444 (8)
C _{7B} -O _{1B}	—	1.204	—	—	1.241 (8)
N _{3B(D)} -H _{3B(D)}	—	1.015	—	1.013	1.010
<i>Selected bond angles</i> (°)					
N ₁ -C ₁ -N ₂	108.7	112.6	111.7	108.9	109.2 (6)
C ₁ -N ₁ -C ₃	108.9	105.7	108.9	108.6	107.9 (5)
C ₁ -N ₁ -C ₅	125.1	127.6	126.0	126.0	126.2 (5)
C ₄ -N ₂ -C ₁	125.1	126.5	126.9	125.2	126.2 (5)
H ₂ -C ₂ -N ₂	122.6	121.8	121.8	122.3	123.4
C ₃ -C ₂ -H ₂	130.6	129.4	129.9	130.5	128.2
<i>Selected dihedral angles</i> (°)					
C ₄ -N ₂ -C ₁ -N ₁	177.5	179.2	179.6	178.6	178.4 (5)
N ₂ -C ₂ -C ₃ -N ₁	0.2	0.4	0.3	0.1	0.9 (8)
C ₅ -N ₁ -C ₁ -N ₂	177.5	175.1	179.1	179.6	178.4 (5)
C ₅ -N ₁ -C ₃ -C ₂	177.7	175.2	179.8	179.7	177.9 (6)

The data of the molecule showed by L in the last column reflect the X-ray diffraction measurements and calculated values on 1,3-bis(acetamide)imidazol-3-ium bromide as given in [22]. The numbers in the parenthesis indicates the experimental error margins on the specific measurements. The labeled and numbered atoms in the first column are presented for each molecule in Scheme 1.

dissolved was dimethyl sulfoxide (DMSO) which did not show any inhibition effect on the bacteria. The pure L_A , L_B , L_C , and L_D solutions and the pure microorganism planted mediums were used as the sterility and the growth controls,

respectively. The six different concentrations of the each compound were applied to the cells starting from 32 μm and diluting to half each time. Each of the 96 microplates was planted in 150 μl of Tryptic Soy Broth medium, 30 μl of the

TABLE 2: Proton and carbon nuclear magnetic resonance spectral data of the molecules.

Assignment	Proton chemical shift (ppm)		Assignment	Carbon chemical shift (ppm)	
	Experimental	Theory		Experimental	Theory
<i>1,3-Bis(2-hydroxyethyl) imidazolidinium bromide (L_A)</i>					
s, 1H, NCHN	9.06	9.06	NCHN	136.33	137.66
d, 2H, HC=CH	7.70	7.32	HC=CH	122.60	123.06
t, 4H, N-CH ₂	3.93	4.01	O-CH ₂	59.75	61.68
t, 4H, O-CH ₂	3.82	3.87	N-CH ₂	51.98	52.59
s, 2H, OH	—	1.73	—	—	—
<i>3-(2-Ethoxy-2-oxoethyl)-1-(3-aminopropyl)-1H-imidazol-3-ium bromide (L_B)</i>					
s, 1H, NCHN	7.79	7.73	CO	171.85	172.23
d, 1H, HC=CH	7.25	7.23	NCHN	136.78	137.10
d, 1H, HC=CH	7.02	7.00	HC=CH	125.13	124.74
s, 2H, N-CH ₂ CO	4.23	4.22 (2)	HC=CH	120.73	121.34
q, 2H, CH ₂ -CH ₃	3.23	3.21 (3)	O-CH ₂ -CH ₃	60.78	57.36
t, 2H, N-CH ₂ -C	2.95	2.96 (3)	N-CH ₂	54.97	54.10
t, 2H, NH ₂ -CH ₂	2.55	2.54 (2)	N-CH ₂ -CH ₂ -	44.97	38.64
m, 2H, C-CH ₂ -C	2.20	2.18 (2)	NH ₂ -CH ₂ -	36.84	36.61
t, 3H, CH ₃	2.02	2.04 (3)	C-CH ₂ -C	28.72	31.52
NH ₂	—	0.5 (3)	CH ₃	13.64	17.70
<i>1,3-Bis(2-carboxyethyl)-4-methyl-1H-imidazol-3-ium bromide (L_C)</i>					
s, 1H, NCHN	8.84	8.83	COOH	173.03	170.3 (1)
s, 1H, HC=C-CH ₃	7.33	7.34	NCHN	133.30	132.96
s, OH	—	5.95 (2)	C-CH ₃	129.94	130.93
t, 4H, N-CH ₂	3.64	3.62 (5)	C=C-CH ₃	116.01	119.67
t, 4H, CH ₂ -COOH	2.91	3.10 (2)	N-CH ₂	37.53	39.7 (9)
s, 3H, -CH ₃	2.38	2.37	CH ₂ -COOH	26.79	33.8 (5)
			CH ₃	9.01	10.26
<i>3-(2-Carboxyethyl)-1-(3-aminopropyl)-1H-imidazol-3-ium bromide (L_D)</i>					
s, 1H, NCHN	9.11	9.11	COOH	170.21	177.74
d, 1H, HC=CH	7.72	7.71	NCHN	137.16	137.47
d, 1H, HC=CH	7.65	7.63	HC=CH	123.94	124.97
s, OH	—	6.39	HC=CH	121.50	124.69
t, 4H, N-CH ₂	4.45	4.47 (1)	N-CH ₂	60.01	60.29
t, 2H, COOH-C	3.33	3.34	N-CH ₂	52.02	53.30
t, 2H, NH ₂ -CH ₂	3.05	3.03	NH ₂ -CH ₂	45.42	45.41
m, 2H, C-CH ₂ -C	2.33	2.31	C-CH ₂ -C	36.18	40.05
NH ₂	—	0.7 (3)	COOH-CH ₂	27.76	34.43

bacteria or the yeast culture, and 20 μ l of the chemical compound solution. All microplates were incubated at 37°C for 24 hr. The absorbance was measured at 600 nm.

2.3.2. Cytotoxicity. 3-(4,5-Dimethylthiazol-2-yl)-2,5-diphenyl tetrazolium bromide (MTT) assay was used to observe the cytotoxicity of synthesized compounds on human cervical cancer cell line (HeLa), human liver cancer cell line (Hep G2), and healthy mouse embryonic fibroblast cell line (MEF). All cell lines were provided with American Type Culture Collection (ATCC, Manassas, VA, USA). A certain population of the cells were incubated in Dulbecco's modified Eagle's Medium (DMEM) provided with Life Technologies GIBCO, Grand Island, NY, USA involving 1% penicillin streptomycin and 1% L-glutamine and HAMS F12 (1:1) broth medium at 37°C under 5% CO₂. The cells were planted in 96-multiwell plates with approximately equal numbers of 10⁵, and they were allowed further incubation for 24 hr. The seven different doses of each compound were applied to the cancer cell lines and the MEF cells. The applied

doses were 400 μ m, 200 μ m, 100 μ m, 50 μ m, 25 μ m, 12.5 μ m, and 6.25 μ m, and the dose application time was 24 hr. The surviving control for each cell was carried out against the cells not exposed to any dose. Then, 20 μ l/plate of 5 mg/ml MTT solution was added into the each well and left to further incubation between 2 and 4 hr. The excess MTT solutions were removed from the wells, and 200 μ l of ultra-pure DMSO was added. The set was left in dark for 5 min before measuring the color intensities on a 492 nm spectrophotometer.

2.4. Computational Modeling. All calculations were carried out in the framework of Gaussian 09 package. The molecules were optimized in their ground state using Becke3-Lee-Yang-Parr (B3LYP) exchange correlation functional method and 6-311G+(2d, p) basis set within density functional theory (DFT). Then, the NMR spectra and the IR spectra were calculated on the optimized geometries using the same method and the same basis set. The gauge-independent atomic orbital (GIAO) method was adopted to acquire theoretical ¹H and ¹³C NMR shifts, which were

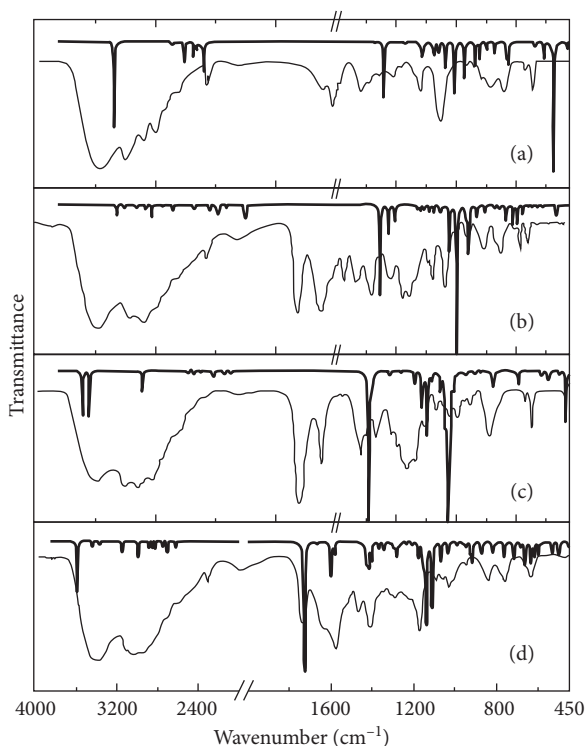


FIGURE 1: Calculated (bold lines) and experimental (pale lines) infrared spectra of the synthesized imidazole molecules: (a) *1,3-bis(2-hydroxyethyl) imidazolidinium bromide*, (b) *3-(2-ethoxy-2-oxoethyl)-1-(3-aminopropyl)-1H-imidazol-3-ium bromide*, (c) *1,3-bis(2-carboxyethyl)-4-methyl-1H-imidazol-3-ium bromide*, and (d) *3-(2-carboxyethyl)-1-(3-aminopropyl)-1H-imidazol-3-ium bromide*.

converted to that of tetramethylsilane scale. The IR spectra were scaled by the factor 0.9613 due to the theoretical miscalculations [19–21]. The vibrational modes were assigned by observing the animation property of the frequency calculations provided with Gaussian 09 package.

3. Result and Discussion

NMR and IR spectra are reliable methods to elucidate an organic material or some of metal complexes. They can also be used to verify calculated molecular structure by comparing calculated spectra with corresponding experimental spectra and thus determining structural parameters and complete description of chemicals investigated.

3.1. Molecular Structures. The NMR measurements were taken in dilute D_2O solution, while the IR spectra were recorded in the solid KBr pellet. Therefore, NMR and infrared spectra may reflect different molecular structures as the molecule surrounded by D_2O molecules in NMR spectra while the intermolecular interactions exist in the IR spectra, especially on -CH and -OH bonds [22]. On the theoretical calculation side, the crystalline phase calculations were excluded due to the single crystal form of the molecules obtained for X-ray analysis. The gas phase calculations were adopted considering differences with other phases with 2%

maximum error margin which were especially on the -CH and -OH bond lengths.

The process of the theoretical modeling of the molecules has initially been realized by using the potential energy surface scanning method for the selected dihedral angles of each molecule, thus obtaining the lowest energy conformers in the gas phase, and the resulting optimized conformers are given in Scheme 1. The imidazole rings except that of L_C with its CH_3 attachment and the CH_2 groups directly bonded to the nitrogen of the rings are common in the all molecules.

L_A has the point group symmetry C_2 as the other molecules were found to have C_1 symmetry. The lower point group symmetry of the L_B , L_C , and L_D in comparison with the C_2 symmetry of L_A is because of the attachment of the different aliphatic chains to their imidazole rings. The calculated optimized energies and the dipole moments of L_A , L_D , L_B , and L_C are, respectively, -534.4, -667.3, -706.6, and -800.5 in units of a.u. and 2.11, 3.41, 4.54, and 7.78 in units of Debye.

The calculated parameters of the common properties of the molecules are presented in Table 1. Although the molecules differ from each other by their moieties bonded to the imidazole rings, the bond lengths, the bond angles, and the dihedral angles belong to the ring, and its immediate vicinity are in good agreement with each other and with the corresponding X-ray diffractometer (XRD) results of previously investigated similar molecule *1,3-bis(acetamide) imidazol-3-ium bromide* which was crystallized successfully [22]. The dihedral angles chosen on the imidazole ring are either about 0° or 180° , implying the aromatic structure as expected. The C-N bond lengths which bind the rings and the aliphatic moieties, that is, C_4-N_2 and N_1-C_5 are equal in L_A reflecting the symmetric structure of the molecule. However, these are different in L_B , L_C , and L_D because of the different moieties on the both side of their aromatic rings. Although the symmetry of L_C was broken by the C- CH_3 group instead of C-H in the ring, no drastic changes were observed in the concerning ring parameters. It can be inferred that the common geometrical parameters are consistent with each other with a priori theoretical confirmations before NMR and IR spectra clarifications of the calculated molecular structures.

3.2. Nuclear Magnetic Resonance Spectra. The experimental and theoretical chemical shifts of 1H NMR and ^{13}C NMR spectra of L_A , L_B , L_C , and L_D molecules are given in Table 2. The calculations were carried out in the gas phase considering their optimized geometries given in Scheme 1. The proton signals for $-NH_2$ and $-OH$ in all were absent in the experimental 1H NMR spectra because the solvent was D_2O concerning the solubility of the specimens which exchanged NH_2 and OH protons with deuterium. Although their detailed analysis left to the IR spectra in the following section, the calculated shifts δ 1.73 ppm of OH in L_A and δ 0.5 ppm and δ 0.7 ppm of NH_2 in L_B and L_D , respectively, are in the typical chemical shift range of R- NH_2 and R-OH groups.

The imidazole proton ($NCHN$, H_1) shifts of L_A , L_C , and L_D with 9.06 ppm, 8.84 ppm, and 9.11 ppm, respectively, are noticeably bigger than that of L_B with 7.79 ppm. That can be due to the intramolecular interactions of the $NCHN$

TABLE 3: The experimental and theoretical vibrational wave numbers for the infrared spectra of 1,3-bis(2-hydroxyethyl) imidazolidinium bromide (L_A) with its symbolled and numbered atoms in Figure 1(a).

Vibrational assignments/vibrating atoms	Theory	Experiment
$\nu_s(\text{OH})/(O_{1A}-H_{1A}, H_{2A}-O_{2A})$	3477	
$\nu_{as}(\text{OH})/(O_{1A}-H_{1A}, H_{2A}-O_{2A})$	3477	3358
$\nu_{as}(\text{CH}_2)/(C_4-H_4, H'_4-C_4), (C_5-H_5, H'_5-C_5)$	3093	
$\nu_{as}(\text{CH}_2)/(C_{6A}-H_{6A}, H'_{6A}-C_{6A}), (C_{7A}-H_{7A}, H'_{7A}-C_{7A})$	3011	
$\nu(\text{NCHN})/(C_1-H_1)$	2949	
$\nu_s(\text{CH})/(C_2-H_2, H_3-C_3)$	2928	3114–2822
$\nu_s(\text{CH}_2)/(C_4-H_4, H'_4-C_4), (C_5-H_5, H'_5-C_5)$	2914	
$\nu_{as}(\text{CH})/(C_2-H_2, H_3-C_3)$	2899	
$\nu_s(\text{CH}_2)/(C_{6A}-H_{6A}, H'_{6A}-C_{6A}), (C_{7A}-H_{7A}, H'_{7A}-C_{7A})$	2880	2808
$\nu_{as}(\text{CN})/(C_1-N_1, N_2-C_1)$	1682	1630
$\nu_s(\text{CN})/(C_1-N_1, N_2-C_1)$	1543	1592
$\delta_{sc}(\text{CH}_2)/(C_{6A}-H_{6A}, H'_{6A}-C_{6A}), (C_{7A}-H_{7A}, H'_{7A}-C_{7A})$	1452	
$\delta_{sc}(\text{CH}_2)/(C_4-H_4, H'_4-C_4), (C_5-H_5, H'_5-C_5)$	1428	1463
$\delta(\text{OH})/(O_{1A}-H_{1A}), (O_{2A}-H_{2A})$	1411	
$\gamma_t(\text{CH}_2) + \delta_r(\text{CH}) + \delta(\text{NCHN})/(C_4-H_4, H'_4-C_4), (C_2-H_2, C_3-H_3), (C_1-H_1)$	1375	1373
$\gamma_w(\text{CH}_2) + \nu_s(\text{CN})/(C_5-H_5, H'_5-C_5), (C_{7A}-H_{7A}, H'_{7A}-C_{7A}), (C_4-N_2, N_1-C_5)$	1355	1330
$\delta_r(\text{CH})/(C_2-H_2, H_3-C_3)$	1345	
$\gamma_t(\text{CH}_2) + \delta(\text{NCHN}) + \delta_r(\text{CH})/(C_{6A}-H_{6A}, H'_{6A}-C_{6A}), (C_1-H_1), (C_2-H_2, H_3-C_3)$	1323	
$\gamma_t(\text{CH}_2) + \delta(\text{NCHN}) + \delta_r(\text{CH})/(C_4-H_4, H'_4-C_4), (C_1-H_1), (C_2-H_2, H_3-C_3)$	1313	1301
$\delta(\text{NCHN}) + \gamma_w(\text{OH})/(C_1-H_1), (O_{1A}-H_{1A}, H_{2A}-O_{2A})$	1274	
$\gamma_t(\text{CH}_2) + \delta_r(\text{OH})/(C_4-H_4, H'_4-C_4), (C_5-H_5, H'_5-C_5), (O_{1A}-H_{1A}, O_{2A}-H_{2A})$	1212	1265
$\gamma_t(\text{CH}_2) + \delta_r(\text{OH})/(C_{6A}-H_{6A}, H'_{6A}-C_{6A}), (C_{7A}-H_{7A}, H'_{7A}-C_{7A}), (O_{1A}-H_{1A}, O_{2A}-H_{2A})$	1209	
$\delta_{sc}(\text{CH})/(C_2-H_2, H_3-C_3)$	1149	
$\nu_{as}(\text{CN})/(C_3-N_1, N_2-C_2) + (C_4-N_2, N_1-C_5)$	1143	1179
$\nu_{as}(\text{CO}) + \nu_{as}(\text{CC})/(C_{6A}-O_{2A}, O_{1A}-C_{7A}), (C_{6A}-C_4, C_5-C_{7A})$	1077	
$\nu_s(\text{CO}) + \nu_s(\text{CC})/(C_{6A}-O_{2A}, O_{1A}-C_{7A}), (C_{6A}-C_4, C_5-C_{7A})$	1076	1080
$\delta_r(\text{CH}_2) + \nu_s(\text{CO})/(C_4-H_4, H'_4-C_4), (C_5-H_5, H'_5-C_5), (C_{6A}-O_{2A}, C_{7A}-O_{1A})$	1047	
$\delta_r(\text{CH}_2) + \nu_s(\text{CN})/(C_{6A}-H_{6A}, H'_{6A}-C_{6A}), (C_{7A}-H_{7A}, H'_{7A}-C_{7A}), (C_3-N_1, N_2-C_2)$	997	
$\nu(\text{NCHN})/(C_1-H_1)$	946	956
$\nu_s(\text{CC})/(C_{6A}-C_4, C_5-C_{7A})$	930	917
$\delta_r(\text{CH}_2) + \nu_{as}(\text{CO})/(C_4-H_4, H'_4-C_4), (C_5-H_5, H'_5-C_5), (C_{6A}-O_{2A}, O_{1A}-C_{7A})$	867	
$\delta_r(\text{CH}_2)/(C_4-H_4, H'_4-C_4), (C_{6A}-H_{6A}, H'_{6A}-C_{6A})$	861	875
$\gamma_w(\text{CH}) + \nu(\text{NCHN})/(C_2-H_2, H_3-C_3), (C_1-H_1)$	853	840
$\nu_{as}(\text{CN}) + \delta_r(\text{CH}_2)/(N_2-C_4, N_1-C_5), (C_{6A}-H_{6A}, H'_{6A}-C_{6A}), (C_{7A}-H_{7A}, H'_{7A}-C_{7A})$	677	673
$\nu(\text{NCHN})/(C_1-H_1)$	617	639

ν , stretching; δ , in-plane bending; γ , out-of-plane bending; s, symmetric; as, asymmetric; sc, scissoring; r, rocking; t, twisting; w, wagging.

hydrogen with the close oxygen atoms since the oxygen reduces the electron density on the hydrogen depending on the distance between them, thus causing higher NMR shifts. Indeed, the H_1-O_{1A} in L_A , the H_1-O_{1C} in L_C , and the H_1-O_{1D} in L_D are 2.61 Å, 2.42 Å, and 2.41 Å, respectively. These distances which were measured from the theoretical models of the molecules are quite longer than that 2.85 Å distance of the H_1-O_{1B} measured in L_B which results in small shifts for the H_1 of L_B . This is supported by the fact that the other imidazole proton shifts of H_2 and H_3 are all in close values about 7.7 ppm for all molecules as no distinct intermolecular interactions possible on H_2 and H_3 in any of them. In addition, the NMR signals of CH_2 protons in the aliphatic chains of all molecules and the smallest proton shifts of CH_3 protons in L_B and L_C molecules are theoretically and experimentally in agreement with the expected NMR results. These NMR data are in accordance with the previous study on a similar imidazole salt [23, 24] in which the protons belong to the aliphatic chain found in 4.15 ppm–2.08 ppm, the carbons belong to the imidazole ring, and the aliphatic

chain is found in 139.2 ppm–123 ppm and 62.5 ppm–33.9 ppm as in this study.

The eight R -squared tests using the data in Table 2 provide least 99.8% agreement between the experimental and the theoretical ^1H and ^{13}C NMR for L_A , L_B , L_C , and L_D . The theoretical results for NMR are in very good agreement with the experimental results as well as the observation of the expected specific values. Thus, one can infer that the calculated atomic configurations of the all molecules are good estimations except the exclusion of the interchangeable hydrogens.

3.3. Infrared Spectra. In Figure 1, the experimental infrared spectra of L_A , L_B , L_C , and L_D in the 450–4000 cm^{-1} region are given against their IR spectra calculations. The detailed account of the IR spectra including the in-plane vibrations of the stretching, scissoring, and rocking and the out-of-plane vibrations of the wagging and twisting for each molecule is presented for L_A , L_B , L_C , and L_D in Tables 3–6, respectively.

TABLE 4: The experimental and theoretical vibrational wave numbers for the infrared spectra of 3-(2-ethoxy-2-oxoethyl)-1-(3-aminopropyl)-1H-imidazol-3-ium bromide (L_B) with its symbolled and numbered atoms in Figure 1(b).

Vibrational assignments/vibrating atoms	Theory	Experiment
$\nu(\text{NCHN})/(\text{C}_1\text{-H}_1)$	3460	
$\nu_{\text{as}}(\text{NH}_2)/(\text{N}_{3\text{B}}\text{-H}_{3\text{B}}, \text{H}'_{3\text{B}}\text{-N}_{3\text{B}})$	3412	3400
$\nu_{\text{s}}(\text{NH}_2)/(\text{N}_{3\text{B}}\text{-H}_{3\text{B}}, \text{H}'_{3\text{B}}\text{-N}_{3\text{B}})$	3345	
$\nu_{\text{as}}(\text{CH}_2)/(\text{C}_{9\text{B}}\text{-H}_{9\text{B}}, \text{H}'_{9\text{B}}\text{-C}_{9\text{B}})$	3327	
$\nu_{\text{s}}(\text{CH}_2) + \nu_{\text{s}}(\text{CH}_2)/(\text{C}_1\text{-H}_5, \text{H}'_5\text{-C}_1), (\text{C}_{9\text{B}}\text{-H}_{9\text{B}}, \text{H}'_{9\text{B}}\text{-C}_{9\text{B}})$	3270	
$\nu(\text{CH}_2)/(\text{C}_4\text{-H}'_4)$	3263	
$\nu(\text{CH}_2)/(\text{C}_{8\text{B}}\text{-H}_{8\text{B}})$	3226	
$\nu_{\text{as}}(\text{CH}_2)/(\text{C}_5\text{-H}_5, \text{H}'_5\text{-C}_5)$	3221	
$\nu_{\text{s}}(\text{CH}_2)/(\text{C}_5\text{-H}_5, \text{H}'_5\text{-C}_5)$	3157	
$\nu(\text{CH})/(\text{C}_3\text{-H}_3)$	3087	3192–2720
$\nu(\text{CH})/(\text{C}_2\text{-H}_2)$	2946	
$\nu_{\text{as}}(\text{CH}_2)/(\text{C}_{6\text{B}}\text{-H}_{6\text{B}}, \text{H}'_{6\text{B}}\text{-C}_{6\text{B}})$	2843	
$\nu_{\text{s}}(\text{CH}_2)/(\text{C}_{6\text{B}}\text{-H}_{6\text{B}}, \text{H}'_{6\text{B}}\text{-C}_{6\text{B}})$	2795	
$\nu_{\text{as}}(\text{CH}_3)/(\text{C}_{10\text{B}}\text{-H}_{10\text{B}}, \text{H}'_{10\text{B}}\text{-C}_{10\text{B}})$	2784	
$\nu_{\text{as}}(\text{CH}_3)/(\text{C}_{10\text{B}}\text{-H}_{10\text{B}}, \text{H}''_{10\text{B}}\text{-C}_{10\text{B}})$	2783	
$\nu_{\text{s}}(\text{CH}_3)/(\text{C}_{10\text{B}}\text{-H}_{10\text{B}}, \text{H}'_{10\text{B}}\text{-C}_{10\text{B}}, \text{H}''_{10\text{B}}\text{-C}_{10\text{B}})$	2731	
$\nu(\text{CH}_2)/(\text{C}_{8\text{B}}\text{-H}'_{8\text{B}})$	2606	2618
$\nu(\text{CO})/(\text{C}_{7\text{B}}\text{-O}_{1\text{B}})$	1707	1753
$\nu(\text{CN}) + \delta(\text{CH}) + \nu(\text{C}=\text{C})/(\text{C}_1\text{-N}_2), (\text{C}_2\text{-H}_2), (\text{C}_2\text{-C}_3)$	1652	
$\nu(\text{CN}) + \nu(\text{C}=\text{C})/(\text{C}_1\text{-N}_1), (\text{C}_2\text{-C}_3)$	1619	1645
$\delta_{\text{sc}}(\text{NH}_2)/(\text{C}_{3\text{B}}\text{-H}_{3\text{B}}, \text{H}'_{3\text{B}}\text{-C}_{3\text{B}})$	1606	
$\nu_{\text{s}}(\text{CN}) + \nu(\text{NC})/(\text{N}_2\text{-C}_1, \text{C}_1\text{-N}_1), (\text{N}_2\text{-C}_2)$	1494	1561
$\delta_{\text{sc}}(\text{CH}_3) + \delta(\text{CH}_3)/(\text{C}_{10\text{B}}\text{-H}_{10\text{B}}, \text{C}_{10\text{B}}\text{-H}''_{10\text{B}}), (\text{C}_{10\text{B}}\text{-H}'_{10\text{B}})$	1464	
$\delta_{\text{sc}}(\text{CH}_2)/(\text{C}_{8\text{B}}\text{-H}_{8\text{B}}, \text{H}'_{8\text{B}}\text{-C}_{8\text{B}})$	1462	1528
$\delta_{\text{sc}}(\text{CH}_3) + \delta(\text{CH}_3)/(\text{C}_{10\text{B}}\text{-H}'_{10\text{B}}, \text{C}_{10\text{B}}\text{-H}''_{10\text{B}}), (\text{C}_{10\text{B}}\text{-H}_{10\text{B}})$	1451	
$\delta_{\text{sc}}(\text{CH}_2)/(\text{C}_{6\text{B}}\text{-H}_{6\text{B}}, \text{H}'_{6\text{B}}\text{-C}_{6\text{B}})$	1441	1473
$\delta_{\text{sc}}(\text{CH}_2) + \gamma_{\text{w}}(\text{CH}_3)/(\text{C}_{9\text{B}}\text{-H}_{9\text{B}}, \text{H}'_{9\text{B}}\text{-C}_{9\text{B}}), (\text{C}_{10\text{B}}\text{-H}_{10\text{B}}, \text{C}_{10\text{B}}\text{-H}'_{10\text{B}})$	1415	1465
$\delta_{\text{sc}}(\text{CH}_2)/(\text{C}_5\text{-H}_5, \text{H}'_5\text{-C}_5)$	1381	
$\gamma_{\text{w}}(\text{CH}_2) + \delta_{\text{sc}}(\text{CH}_2)/(\text{C}_{8\text{B}}\text{-H}_{8\text{B}}, \text{H}'_{8\text{B}}\text{-C}_{8\text{B}}), (\text{C}_4\text{-H}_4, \text{H}'_4\text{-C}_4)$	1372	1458
$\gamma_{\text{w}}(\text{CH}_2) + \delta_{\text{sc}}(\text{CH}_2)/(\text{C}_{6\text{B}}\text{-H}_{6\text{B}}, \text{H}'_{6\text{B}}\text{-C}_{6\text{B}}), (\text{C}_4\text{-H}_4, \text{H}'_4\text{-C}_4)$	1352	1394
$\nu_{\text{s}}(\text{CN}) + \gamma_{\text{t}}(\text{CH}_2)/(\text{C}_4\text{-N}_2, \text{N}_1\text{-C}_5), (\text{C}_{6\text{B}}\text{-H}_{6\text{B}}, \text{H}'_{6\text{B}}\text{-C}_{6\text{B}}), (\text{C}_5\text{-H}_5, \text{H}'_5\text{-C}_5)$	1319	1300
$\gamma_{\text{w}}(\text{CH}_2)/(\text{C}_{9\text{B}}\text{-H}_{9\text{B}}, \text{H}'_{9\text{B}}\text{-C}_{9\text{B}})$	1309	
$\gamma_{\text{t}}(\text{NH}_2) + \gamma_{\text{t}}(\text{CH}_2)/(\text{N}_{3\text{B}}\text{-H}_{3\text{B}}, \text{H}'_{3\text{B}}\text{-N}_{3\text{B}}), (\text{C}_{6\text{B}}\text{-H}_{6\text{B}}, \text{H}'_{6\text{B}}\text{-C}_{6\text{B}})$	1296	
$\delta(\text{NCHN}) + \delta_{\text{r}}(\text{CH})/(\text{C}_1\text{-H}_1), (\text{C}_2\text{-H}_2, \text{C}_3\text{-H}_3)$	1282	1242
$\nu_{\text{as}}(\text{CO}) + \gamma_{\text{w}}(\text{CH}_2)/(\text{C}_{7\text{B}}\text{-O}_{2\text{B}}, \text{O}_{2\text{B}}\text{-C}_{9\text{B}}), (\text{C}_5\text{-H}_5, \text{H}'_5\text{-C}_5), (\text{C}_{9\text{B}}\text{-H}_{9\text{B}}, \text{H}'_{9\text{B}}\text{-C}_{9\text{B}})$	1248	1214
$\nu_{\text{as}}(\text{CO}) + \gamma_{\text{w}}(\text{CH}_3)/(\text{C}_{7\text{B}}\text{-O}_{2\text{B}}, \text{O}_{2\text{B}}\text{-C}_{9\text{B}}), (\text{C}_{10\text{B}}\text{-H}_{10\text{B}}, \text{C}_{10\text{B}}\text{-H}''_{10\text{B}})$	1198	1183
$\nu_{\text{as}}(\text{CC}) + \nu(\text{CO}) + \nu_{\text{s}}(\text{CN})/(\text{C}_{8\text{B}}\text{-C}_{6\text{B}}, \text{C}_{6\text{B}}\text{-C}_4), (\text{C}_{3\text{B}}\text{-O}_{2\text{B}}), (\text{C}_4\text{-N}_2, \text{N}_1\text{-C}_5)$	1123	1118
$\nu_{\text{s}}(\text{CO}) + \nu(\text{CC}) + \delta(\text{NCHN})/(\text{C}_{7\text{B}}\text{-O}_{2\text{B}}, \text{O}_{2\text{B}}\text{-C}_{9\text{B}}), (\text{C}_{9\text{B}}\text{-C}_{10\text{B}}), (\text{C}_7\text{B}\text{-C}_5), (\text{C}_1\text{-H}_1)$	1069	1097
$\gamma_{\text{w}}(\text{NH}_2) + \delta_{\text{r}}(\text{CH}_2)/(\text{N}_{3\text{B}}\text{-H}_{3\text{B}}, \text{H}'_{3\text{B}}\text{-N}_{3\text{B}}), (\text{C}_{8\text{B}}\text{-H}_{8\text{B}}, \text{H}'_{8\text{B}}\text{-C}_{8\text{B}})$	1011	1039
$\gamma_{\text{w}}(\text{NH}_2) + \nu(\text{CC})/(\text{N}_{3\text{B}}\text{-H}_{3\text{B}}, \text{H}'_{3\text{B}}\text{-N}_{3\text{B}}) + (\text{C}_{6\text{B}}\text{-C}_4)$	869	931
$\nu(\text{CC}) + \gamma_{\text{w}}(\text{CH}_3) + \nu(\text{CO})/(\text{C}_5\text{-C}_{7\text{B}}), (\text{C}_{10\text{B}}\text{-H}_{10\text{B}}, \text{C}_{10\text{B}}\text{-H}'_{10\text{B}}), (\text{C}_7\text{B}\text{-O}_{2\text{B}})$	860	852
$\gamma_{\text{w}}(\text{NH}_2) + \nu(\text{CC})/(\text{N}_{3\text{B}}\text{-H}_{3\text{B}}, \text{H}'_{3\text{B}}\text{-N}_{3\text{B}}), (\text{C}_4\text{-C}_{6\text{B}})$	824	787
$\nu(\text{NCHN}) + \gamma_{\text{w}}(\text{CH})/(\text{C}_1\text{-H}_1), (\text{C}_2\text{-H}_2, \text{C}_3\text{-H}_3)$	797	765
$\gamma_{\text{w}}(\text{CH}) + \gamma_{\text{t}}(\text{NH}_2) + \gamma_{\text{t}}(\text{CN})/(\text{C}_2\text{-H}_2, \text{C}_3\text{-H}_3), (\text{N}_{3\text{B}}\text{-H}_{3\text{B}}, \text{H}'_{3\text{B}}\text{-N}_{3\text{B}}), (\text{N}_1\text{-C}_5)$	759	700
$\gamma_{\text{t}}(\text{NH}_2) \gamma_{\text{t}}(\text{CN}) + \nu(\text{NCHN})/(\text{N}_{3\text{B}}\text{-H}_{3\text{B}}, \text{H}'_{3\text{B}}\text{-N}_{3\text{B}}), (\text{N}_2\text{-C}_4), (\text{C}_1\text{-H}_1)$	722	652
$\gamma_{\text{t}}(\text{CH}_2) + \delta(\text{CC})/(\text{C}_{8\text{B}}\text{-H}_{8\text{B}}, \text{H}'_{8\text{B}}\text{-C}_{8\text{B}}), (\text{C}_{6\text{B}}\text{-H}_{6\text{B}}, \text{H}'_{6\text{B}}\text{-C}_{6\text{B}}), (\text{C}_5\text{-C}_{7\text{B}})$	665	636
$\gamma_{\text{t}}(\text{CH}_2) + \delta(\text{CC})/(\text{C}_{6\text{B}}\text{-H}_{6\text{B}}, \text{H}'_{6\text{B}}\text{-C}_{6\text{B}}) + (\text{C}_{6\text{B}}\text{-C}_4) + (\text{C}_5\text{-C}_{7\text{B}})$	626	592
$\gamma_{\text{t}}(\text{C}=\text{C})/(\text{N}_2\text{-C}_2, \text{C}_3\text{-N}_1)$	603	
$\Gamma(\text{NCHN})/(\text{C}_1\text{-H}_1)$	534	534

ν , stretching; δ , in-plane bending; γ , out-of-plane bending; s, symmetric; as, asymmetric; sc, scissoring; r, rocking; t, twisting; w, wagging.

The R -square test results exhibit 99.8%, 99.5%, 99.5%, and 99.7% agreement between the experimental and the theoretical IR spectra of L_A , L_B , L_C , and L_D , respectively.

The intermolecular interactions and the correlations of close frequency IR signals cause the -OH, -CH, -CH₂, -CH₃, and -NH₂ stretching vibrations to appear under broad peaks in the experimental spectra. These broad peaks are in very

well-defined frequency region. The vibrations coming from the other functional groups of the imidazole rings and the aliphatic chains including the other vibrations of the hydrogenic groups in all modes appeared in 1750–450 cm⁻¹ region.

The first vibration signals observed in the 1800–1700 cm⁻¹ region of the experimental spectra of L_B , L_C , and L_D are distinct peaks arising from $\nu(\text{C}=\text{O})$ stretching as their values

TABLE 5: The experimental and theoretical vibrational wave numbers for the infrared spectra of 1,3-bis(2-carboxyethyl)-4-methyl-1H-imidazol-3-ium bromide (L_C) with its symbolled and numbered atoms in Figure 1(c).

Vibrational assignments/vibrating atoms	Theory	Experiment
$\nu(\text{OH})/(\text{O}_{3\text{C}}-\text{H}_{3\text{C}})$	3685	
$\nu(\text{OH})/(\text{O}_{4\text{C}}-\text{H}_{4\text{C}})$	3643	3416
$\nu(\text{CH}_2)/(\text{C}_5-\text{H}_5)$	3328	
$\nu(\text{CH}_2)/(\text{C}_4-\text{H}_4)$	3311	
$\nu(\text{NCHN})/(\text{C}_1-\text{H}_1)$	3292	
$\nu(\text{CH}_3)/(\text{C}_{10}-\text{H}''_{10\text{C}})$	3046	
$\nu(\text{CH}_2)/(\text{C}_5-\text{H}'_5)$	2983	
$\nu(\text{CH}_2)/(\text{C}_4-\text{H}'_4)$	2949	3268–2677
$\nu_{\text{as}}(\text{CH}_3)/(\text{C}_{10\text{C}}-\text{H}_{10\text{C}}, \text{H}'_{10\text{C}}-\text{C}_{10\text{C}})$	2904	
$\nu_{\text{as}}(\text{CH}_2)/(\text{C}_{7\text{C}}-\text{H}_{7\text{C}}, \text{H}'_{7\text{C}}-\text{C}_{7\text{C}})$	2836	
$\nu_{\text{as}}(\text{CH}_2)/(\text{C}_{6\text{C}}-\text{H}_{6\text{C}}, \text{H}'_{6\text{C}}-\text{C}_{6\text{C}})$	2828	
$\nu_{\text{s}}(\text{CH}_2)/(\text{C}_{6\text{C}}-\text{H}_{6\text{C}}, \text{H}'_{6\text{C}}-\text{C}_{6\text{C}})$	2752	
$\nu_{\text{s}}(\text{CH}_2)/(\text{C}_{7\text{C}}-\text{H}_{7\text{C}}, \text{H}'_{7\text{C}}-\text{C}_{7\text{C}})$	2739	
$\nu(\text{CH})/(\text{C}_2-\text{H}_2)$	2706	2663
$\nu_{\text{s}}(\text{COOH}) + \nu_{\text{s}}(\text{OH})/(\text{C}_{9\text{C}}-\text{O}_{1\text{C}}, \text{O}_{2\text{C}}-\text{C}_{8\text{C}}), (\text{O}_{3\text{C}}-\text{H}_{3\text{C}}, \text{H}_{4\text{C}}-\text{O}_{4\text{C}})$	1785	
$\nu_{\text{as}}(\text{COOH}) + \nu_{\text{as}}(\text{OH})/(\text{C}_{9\text{C}}-\text{O}_{1\text{C}}, \text{O}_{2\text{C}}-\text{C}_{8\text{C}}), (\text{O}_{3\text{C}}-\text{H}_{3\text{C}}, \text{H}_{4\text{C}}-\text{O}_{4\text{C}})$	1783	1774
$\nu_{\text{as}}(\text{CN})/(\text{C}_1-\text{N}_1, \text{N}_2-\text{C}_1)$	1756	
$\nu_{\text{as}}(\text{CN}) + \nu(\text{CC}) + \nu(\text{CN})/(\text{C}_1-\text{N}_1, \text{N}_2-\text{C}_5), (\text{C}_{6\text{C}}-\text{C}_4), (\text{N}_2-\text{C}_4)$	1679	
$\nu_{\text{s}}(\text{CN}) + \nu(\text{C}=\text{C}) + \nu(\text{CC})/(\text{C}_1-\text{N}_1, \text{N}_2-\text{C}_1), (\text{C}_2-\text{C}_3), (\text{C}_3-\text{C}_{10\text{C}}), (\text{C}_4-\text{N}_2)$	1642	1662
$\gamma_{\text{t}}(\text{CH}_2) + \nu(\text{CN})/(\text{C}_5-\text{H}_5, \text{H}'_5-\text{C}_5), (\text{N}_1-\text{C}_3)$	1510	1576
$\gamma_{\text{t}}(\text{CH}_2) + \nu(\text{CN})/(\text{C}_4-\text{H}_4, \text{H}'_4-\text{C}_4), (\text{N}_2-\text{C}_2)$	1476	1561
$\delta_{\text{sc}}(\text{CH}_2) + \delta_{\text{sc}}(\text{CH}_3)/(\text{C}_4-\text{H}_4, \text{H}'_4-\text{C}_4), (\text{C}_{6\text{C}}-\text{H}_{6\text{C}}, \text{H}'_{6\text{C}}-\text{C}_{6\text{C}}), (\text{C}_{10\text{C}}-\text{H}_{10\text{C}}, \text{C}_{10\text{C}}-\text{H}''_{10\text{C}})$	1434	1468
$\nu(\text{CH}_3)/(\text{C}_{10\text{C}}-\text{H}'_{10\text{C}})$	1398	1393
$\delta(\text{CH}) + \gamma_{\text{t}}(\text{CH}_2) + \delta(\text{NCHN})/(\text{C}_2-\text{H}_2) + (\text{C}_4-\text{H}_4, \text{H}'_4-\text{C}_4) + (\text{C}_5-\text{H}_5, \text{H}'_5-\text{C}_5) + (\text{C}_1-\text{H}_1)$	1305	1317
$\delta(\text{OH}) + \nu(\text{CO})/(\text{O}_{4\text{C}}-\text{H}_{4\text{C}}), (\text{C}_{8\text{C}}-\text{O}_{4\text{C}})$	1259	1282
$\delta(\text{CH}) + \nu(\text{CC}) + \nu(\text{CN})/(\text{C}_1-\text{H}_1), (\text{C}_2-\text{H}_2), (\text{C}_3-\text{C}_{10\text{C}}), (\text{N}_2-\text{C}_4)$	1239	
$\delta(\text{CH}) + \nu(\text{CC}) + \nu_{\text{s}}(\text{CN})/(\text{C}_1-\text{H}_1), (\text{C}_2-\text{H}_2), (\text{C}_3-\text{C}_{10\text{C}}), (\text{N}_2-\text{C}_4, \text{C}_5-\text{N}_1)$	1221	1235
$\gamma_{\text{t}}(\text{CH}_2)/(\text{C}_4-\text{H}_4, \text{H}'_4-\text{C}_4), (\text{C}_{6\text{C}}-\text{H}_{6\text{C}}, \text{H}'_{6\text{C}}-\text{C}_{6\text{C}})$	1191	1199
$\gamma_{\text{t}}(\text{CH}_2)/(\text{C}_5-\text{H}_5, \text{H}'_5-\text{C}_5), (\text{C}_{7\text{C}}-\text{H}_{7\text{C}}, \text{H}'_{7\text{C}}-\text{C}_{7\text{C}})$	1181	
$\gamma_{\text{w}}(\text{CH}_2) + \delta(\text{OH})/(\text{C}_{6\text{C}}-\text{H}_{6\text{C}}, \text{H}'_{6\text{C}}-\text{C}_{6\text{C}}), (\text{O}_{4\text{C}}-\text{H}_{4\text{C}})$	1149	
$\gamma_{\text{w}}(\text{CH}_2) + \delta(\text{OH})/(\text{C}_{7\text{C}}-\text{H}_{7\text{C}}, \text{H}'_{7\text{C}}-\text{C}_{7\text{C}}), (\text{O}_{3\text{C}}-\text{H}_{3\text{C}})$	1139	1157
$\nu(\text{CC})/(\text{C}_5-\text{C}_{7\text{C}})$	1086	
$\nu(\text{CC})/(\text{C}_4-\text{C}_{6\text{C}})$	1074	
$\delta(\text{CH}_3)/(\text{C}_{10}-\text{H}_{10\text{C}}, \text{C}_{10}-\text{H}'_{10\text{C}}, \text{C}_{10}-\text{H}''_{10\text{C}})$	1046	1031
$\nu(\text{CH}_3) + \nu(\text{NCHN}) + \nu(\text{CH})/(\text{C}_{10}-\text{H}_{10\text{C}}, \text{C}_{10}-\text{H}'_{10\text{C}}, \text{C}_{10}-\text{H}''_{10\text{C}}), (\text{C}_1-\text{H}_1), (\text{C}_2-\text{H}_2)$	953	990
$\gamma_{\text{w}}(\text{CH}_2) + \delta_{\text{t}}(\text{CH}_2)/(\text{C}_{6\text{C}}-\text{H}_{6\text{C}}, \text{H}'_{6\text{C}}-\text{C}_{6\text{C}}), (\text{C}_4-\text{H}_4, \text{H}'_4-\text{C}_4)$	940	931
$\nu(\text{CC}) + \delta_{\text{t}}(\text{CH}_2)/(\text{C}_3-\text{C}_{10}, (\text{C}_{7\text{C}}-\text{C}_{9\text{C}}), (\text{C}_4-\text{H}_4, \text{H}'_4-\text{C}_4), (\text{C}_{6\text{C}}-\text{H}_{6\text{C}}, \text{H}'_{6\text{C}}-\text{C}_{6\text{C}})$	807	
$\nu(\text{NCHN})/(\text{C}_1-\text{H}_1)$	786	836
$\gamma_{\text{t}}(\text{C}=\text{C}) + \delta(\text{OH})/(\text{N}_2-\text{C}_2, \text{C}_3-\text{N}_1) + (\text{O}_{4\text{C}}-\text{H}_{4\text{C}})$	624	629
$\delta(\text{OH})/(\text{O}_{4\text{C}}-\text{H}_{4\text{C}})$	470	
$\delta(\text{OH})/(\text{O}_{3\text{C}}-\text{H}_{3\text{C}})$	424	462

ν , stretching; δ , in-plane bending; γ , out-of-plane bending; s, symmetric; as, asymmetric; sc, scissoring; r, rocking; t, twisting; w, wagging.

in agreement with the previously observed $\nu(\text{C}=\text{O})$ stretching [25] and theoretically calculated values as reflected in Table 3. The imidazole $\nu(\text{C}=\text{N})$ stretching of L_A appears as individual signals while they are coupled under broad peaks with L_B , L_C , and L_D molecules as seen about 1650 cm^{-1} while the frequencies for $\nu(\text{C}=\text{N})$ stretching are in agreements with the corresponding data as given in [26]. The aliphatic $\nu(\text{C}-\text{N})$ stretching in $1069\text{--}1235 \text{ cm}^{-1}$ interval and the aliphatic $\nu(\text{C}-\text{C})$ stretching in $917\text{--}1099 \text{ cm}^{-1}$ are consistent with the previous corresponding measurements [27].

Beyond the consistency of the common imidazole properties of the molecules, we also give unique infrared signals of molecules in Table 3. C-O stretching belong to the $\text{H}_2\text{C}-\text{OH}$ group in L_A , in-plane δ vibrations of CH_3 at the end of the aliphatic chain of L_B , and at the attachment of the

imidazole ring of L_C are such unique vibrations. The calculated and observed wave numbers of these vibrations are consistent with the concerning previous studies [28, 29].

The molecules in consideration analyzed by infrared spectrum because of the lack of exchangeable protons of -OH and -NH₂ in the NMR spectra of the chemicals and the existence of these groups is proved in the molecules. Also, the IR spectra of the molecules reverifies the theoretically obtained configurations of them as they were first verified by the comparison the theoretical NMR spectra with that of the experimental NMR spectra.

3.4. Antibacterial and Cytotoxic Activities. The antibacterial tests of the synthesized four molecules were run on the six

TABLE 6: The experimental and theoretical vibrational wave numbers for the infrared spectra of 3-(2-carboxyethyl)-1-(3-aminopropyl)-1H-imidazol-3-ium bromide (L_D) with its symbolled and numbered atoms in Figure 1(d).

Vibrational assignments/vibrating atoms	Theory	Experiment
$\nu(\text{OH})/(\text{O}_{2D}\text{-H}_{2D})$	3590	
$\nu_{\text{as}}(\text{NH}_2)/(\text{N}_{3D}\text{-H}_{3D}, \text{H}'_{3D}\text{-N}_{3D})$	3446	3423
$\nu(\text{CH}_2)/(\text{C}_4\text{-H}_4)$	3381	
$\nu_{\text{s}}(\text{NH}_2)/(\text{N}_{3D}\text{-H}_{3D}, \text{H}'_{3D}\text{-N}_{3D})$	3370	3222–2666
$\nu(\text{CH}_2)/(\text{C}_5\text{-H}_5)$	3154	
$\nu(\text{CH}_2)/(\text{C}_{8D}\text{-H}_{8D})$	3152	
$\nu(\text{NCHN})/(\text{C}_1\text{-H}_1)$	2995	
$\nu(\text{CH}_2)/(\text{C}_{6D}\text{-H}_{6D})$	2890	
$\nu_{\text{s}}(\text{CH})/(\text{C}_2\text{-H}_2, \text{H}_3\text{-C}_3)$	2857	
$\nu_{\text{as}}(\text{CH}_2)/(\text{C}_{7D}\text{-H}_{7D}, \text{H}'_{7D}\text{-C}_{7D})$	2850	—
$\nu_{\text{as}}(\text{CH}) + \nu_{\text{s}}(\text{CH}_2)/(\text{C}_2\text{-H}_2, \text{H}_3\text{-C}_3), (\text{C}_5\text{-H}_5, \text{H}'_5\text{-C}_5)$	2828	
$\nu_{\text{s}}(\text{CH}_2)/(\text{C}_{7D}\text{-H}_{7D}, \text{H}'_{7D}\text{-C}_{7D})$	2789	
$\nu(\text{CH}_2)/(\text{C}_4\text{-H}'_4)$	2752	
$\nu(\text{CH}_2)/(\text{C}_{8D}\text{-H}'_{8D})$	2709	
$\nu(\text{COOH})/(\text{C}_{9D}\text{-O}_{1D})$	1728	1745
$\nu_{\text{s}}(\text{CN}) + \nu(\text{C}=\text{C})/(\text{C}_1\text{-N}_1, \text{N}_2\text{-C}_1), (\text{C}_2\text{-C}_3)$	1668	1642
$\nu_{\text{as}}(\text{CN}) + \delta_{\text{r}}(\text{CH})/(\text{C}_1\text{-N}_1, \text{N}_2\text{-C}_1), (\text{C}_2\text{-H}_2, \text{H}_3\text{-C}_3)$	1601	1585
$\delta_{\text{sc}}(\text{NH}_2)/(\text{N}_{3D}\text{-H}_{3D}, \text{H}'_{3D}\text{-N}_{3D})$	1582	
$\nu_{\text{s}}(\text{CN})/(\text{C}_1\text{-N}_1, \text{N}_2\text{-C}_1)$	1468	
$\delta_{\text{sc}}(\text{CH}_2)/(\text{C}_{6D}\text{-H}_{6D}, \text{H}'_{6D}\text{-C}_{6D})$	1454	1470
$\delta_{\text{sc}}(\text{CH}_2)/(\text{C}_{8D}\text{-H}_{8D}, \text{H}'_{8D}\text{-C}_{8D})$	1443	
$\delta_{\text{sc}}(\text{CH}_2) + \gamma_{\text{w}}(\text{CH}_2)/(\text{C}_5\text{-H}_5, \text{H}'_5\text{-C}_5), (\text{C}_{7D}\text{-H}_{7D}, \text{H}'_{7D}\text{-C}_{7D})$	1430	1419
$\delta_{\text{sc}}(\text{CH}_2)/(\text{C}_4\text{-H}_4, \text{H}'_4\text{-C}_4)$	1423	
$\gamma_{\text{w}}(\text{CH}_2) + \nu(\text{CC}) + \nu(\text{CO})/(\text{C}_{7D}\text{-H}_{7D}, \text{H}'_{7D}\text{-C}_{7D}), (\text{C}_{7D}\text{-C}_{9D}) + (\text{C}_{9D}\text{-O}_{2D})$	1417	
$\delta_{\text{sc}}(\text{CH}_2)/(\text{C}_{7D}\text{-H}_{7D}, \text{H}'_{7D}\text{-C}_{7D})$	1404	
$\delta(\text{NCHN}) + \delta_{\text{r}}(\text{CH})/(\text{C}_1\text{-H}_1), (\text{C}_2\text{-H}_2, \text{H}_3\text{-C}_3)$	1372	1354
$\gamma_{\text{w}}(\text{CH}_2) + \nu(\text{CC})/(\text{C}_4\text{-H}_4, \text{H}'_4\text{-C}_4), (\text{C}_{6D}\text{-H}_{6D}, \text{H}'_{6D}\text{-C}_{6D}), (\text{C}_{6D}\text{-C}_{8D})$	1369	
$\gamma_{\text{w}}(\text{CH}_2) + \gamma_{\text{t}}(\text{NH}_2)/(\text{C}_4\text{-H}_4, \text{H}'_4\text{-C}_4), (\text{C}_{6D}\text{-H}_{6D}, \text{H}'_{6D}\text{-C}_{6D}), (\text{N}_{3D}\text{-H}_{3D}, \text{H}'_{3D}\text{-N}_{3D})$	1348	
$\gamma_{\text{w}}(\text{CH}_2)/(\text{C}_5\text{-H}_5, \text{H}'_5\text{-C}_5), (\text{C}_{7D}\text{-H}_{7D}, \text{H}'_{7D}\text{-C}_{7D})$	1344	1318
$\delta_{\text{r}}(\text{CH}) + \gamma_{\text{t}}(\text{CH}_2) + \gamma_{\text{w}}(\text{CH}_2)/(\text{C}_2\text{-H}_2, \text{H}_3\text{-C}_3), (\text{C}_5\text{-H}_5, \text{H}'_5\text{-C}_5), (\text{C}_{8D}\text{-H}_{8D}, \text{H}'_{8D}\text{-C}_{8D})$	1314	
$\delta(\text{NCHN}) + \delta_{\text{r}}(\text{CH}) + \delta(\text{OH})/(\text{C}_1\text{-H}_1), (\text{C}_2\text{-H}_2, \text{H}_3\text{-C}_3), (\text{O}_{2D}\text{-H}_{2D})$	1298	1297
$\gamma_{\text{w}}(\text{CH}_2) + \delta(\text{OH})/(\text{C}_{7D}\text{-H}_{7D}, \text{H}'_{7D}\text{-C}_{7D}), (\text{O}_{2D}\text{-H}_{2D})$	1283	
$\gamma_{\text{t}}(\text{NH}_2) + \gamma_{\text{t}}(\text{CH}_2)/(\text{N}_{3D}\text{-H}_{3D}, \text{H}'_{3D}\text{-N}_{3D}), (\text{C}_{6D}\text{-H}_{6D}, \text{H}'_{6D}\text{-C}_{6D})$	1266	1225
$\gamma_{\text{t}}(\text{NH}_2)/(\text{N}_{3D}\text{-H}_{3D}, \text{H}'_{3D}\text{-N}_{3D})$	1209	
$\delta_{\text{sc}}(\text{CH}) + \delta(\text{CH}) + \gamma_{\text{t}}(\text{CH}_2)/(\text{C}_2\text{-H}_2, \text{H}_3\text{-C}_3), (\text{C}_1\text{-H}_1), (\text{C}_4\text{-H}_4, \text{H}'_4\text{-C}_4)$	1178	1174
$\delta_{\text{sc}}(\text{CH})/(\text{C}_2\text{-H}_2, \text{H}_3\text{-C}_3)$	1148	
$\delta(\text{NCHN}) + \gamma_{\text{w}}(\text{CH}_2) + \delta(\text{OH})/(\text{C}_1\text{-H}_1), (\text{C}_{7D}\text{-H}_{7D}, \text{H}'_{7D}\text{-C}_{7D}), (\text{O}_{2D}\text{-H}_{2D})$	1139	1119
$\delta(\text{NCHN}) + \gamma_{\text{t}}(\text{CH}_2) + \gamma_{\text{t}}(\text{NH}_2)/(\text{C}_1\text{-H}_1), (\text{C}_5\text{-H}_5, \text{H}'_5\text{-C}_5), (\text{N}_{3D}\text{-H}_{3D}, \text{H}'_{3D}\text{-N}_{3D})$	1111	1098
$\gamma_{\text{t}}(\text{NH}_2) + \delta_{\text{sc}}(\text{CH}) + \nu_{\text{as}}(\text{CN})/(\text{N}_{3D}\text{-H}_{3D}, \text{H}'_{3D}\text{-N}_{3D}), (\text{C}_2\text{-H}_2, \text{H}_3\text{-C}_3), (\text{C}_4\text{-N}_2, \text{N}_1\text{-C}_5)$	1070	1069
$\nu(\text{CC})/(\text{C}_5\text{-C}_{7D})$	1037	
$\gamma_{\text{w}}(\text{NH}_2) + \nu(\text{CC}) + \nu(\text{CN})/(\text{N}_{3D}\text{-H}_{3D}, \text{H}'_{3D}\text{-N}_{3D}), (\text{C}_{6D}\text{-C}_4), (\text{C}_4\text{-N}_2)$	1034	1033
$\gamma_{\text{t}}(\text{CH})/(\text{C}_2\text{-H}_2, \text{H}_3\text{-C}_3)$	973	
$\gamma_{\text{w}}(\text{CH}_2) + \delta_{\text{r}}(\text{CH}_2) + \delta(\text{OH})/(\text{C}_{7D}\text{-H}_{7D}, \text{H}'_{7D}\text{-C}_{7D}), (\text{C}_5\text{-H}_5, \text{H}'_5\text{-C}_5), (\text{O}_{2D}\text{-H}_{2D})$	960	976
$\gamma_{\text{t}}(\text{NH}_2) + \nu(\text{CC})/(\text{N}_{3D}\text{-H}_{3D}, \text{H}'_{3D}\text{-N}_{3D}), (\text{C}_{6D}\text{-C}_{8D})$	948	
$\nu(\text{NCHN}) + \gamma_{\text{w}}(\text{CH})/(\text{C}_1\text{-H}_1), (\text{C}_2\text{-H}_2, \text{H}_3\text{-C}_3)$	918	954
$\gamma_{\text{t}}(\text{NH}_2) + \nu(\text{CN}) + \delta_{\text{r}}(\text{CH}_2)/(\text{N}_{3D}\text{-H}_{3D}, \text{H}'_{3D}\text{-N}_{3D}), (\text{N}_{3D}\text{-C}_{8D}), (\text{C}_{6D}\text{-H}_{6D}, \text{H}'_{6D}\text{-C}_{6D})$	818	846
$\nu_{\text{s}}(\text{CC}) + \nu(\text{CO}) + \delta(\text{OH})/(\text{C}_5\text{-C}_{7D}, \text{C}_{7D}\text{-C}_{9D}), (\text{C}_{9D}\text{-O}_{2D}), (\text{O}_{2D}\text{-H}_{2D})$	801	767
$\gamma_{\text{t}}(\text{C}=\text{C}) + \delta(\text{OH})/(\text{C}_2\text{-C}_3), (\text{O}_{2D}\text{-H}_{2D})$	663	637
$\delta(\text{OH}) + \delta_{\text{r}}(\text{CH}_2)/(\text{O}_{2D}\text{-H}_{2D}), (\text{C}_{7D}\text{-H}_{7D}, \text{H}'_{7D}\text{-C}_{7D})$	530	—

ν , stretching; δ , in-plane bending; γ , out-of-plane bending; s, symmetric; as, asymmetric; sc, scissoring; r, rocking; t, twisting; w, wagging.

different bacteria and yeast, as mentioned in Section 2.3.1. Figures 2(a) and 3(b) show the inhibitory effects of the various concentrations of the L_A and L_B on *Candida albicans* ATCC 10231 and *Bacillus cereus* ATCC 11778 (Gram positive) together with that of the antibiotic controls. Their effects on *Escherichia coli* O157:H7 (Gram negative), *Escherichia coli* ATCC 25922, *Salmonella typhimurium*

ATCC 14028, *Staphylococcus aureus* ATCC 25923, and *Listeria monocytogenes* ATCC 19115 are excluded because of their very weak efficacy in comparison with that of the antibiotic control. Although the absorbance measurements involve some statistical errors, L_A showed better inhibition than the antibiotic on *Bacillus cereus* ATCC 11778, while both chemicals are effective on the selected bacteria and

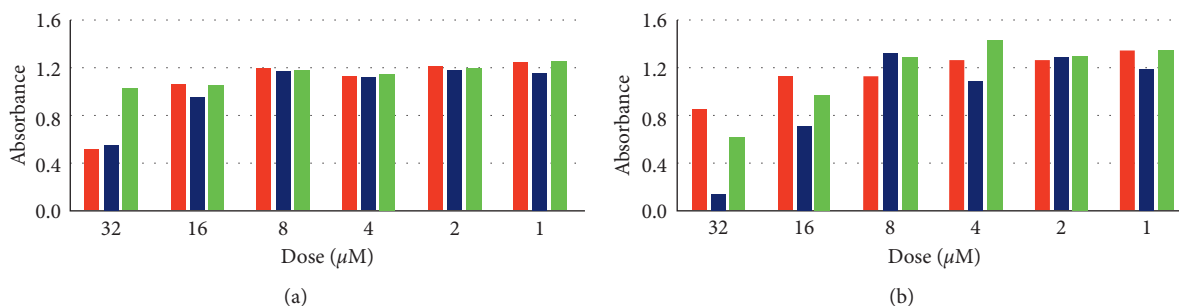


FIGURE 2: (a) The antibacterial activity on *Candida albicans*. The first bars on the left are for the commercial antibiotic inhibition for each dose. The second bars are for 1,3-bis(2-hydroxyethyl) imidazolidinium bromide (L_A), and the third bars are for 3-(2-ethoxy-2-oxoethyl)-1-(3-aminopropyl)-1H-imidazol-3-ium bromide (L_B), (b) same as in Figure 2(a), but for the antibacterial activity on *Bacillus cereus*.

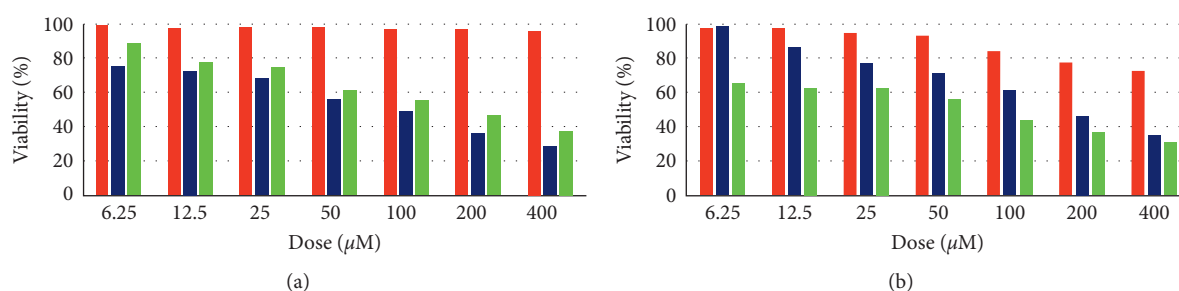


FIGURE 3: (a) The cytotoxicity of 1,3-bis(2-carboxyethyl)-4-methyl-1H-imidazol-3-ium bromide. The first bars represent the effect on healthy mouse embryonic fibroblast cell line for each dose, as do the second bars on human cervical cancer cell line, and the third bars on human liver cancer cell line, (b) same as in Figure 3(a), but for the cytotoxicity of 3-(2-carboxyethyl)-1-(3-aminopropyl)-1H-imidazol-3-ium bromide.

TABLE 7: Half inhibition concentrations of the molecules on the selected bacteria and cancer cell lines.

	Antibacterial activity IC_{50} (μM)			Cytotoxic activity IC_{50} (μM)		
	<i>Escherichia coli</i> O157:H7	<i>Candida albicans</i>	<i>Bacillus cereus</i>	HeLa	Hep G2	MEF
L_A	32	30	17	316	100	—
L_B	39	156	29	141	182	—
L_C	—	—	—	81	150	—
L_D	—	—	—	167	57	—
Antibiotic	10	30	56	—	—	—

L_A , 1,3-bis(2-hydroxyethyl) imidazolidinium bromide; L_B , 3-(2-ethoxy-2-oxoethyl)-1-(3-aminopropyl)-1H-imidazol-3-ium bromide; L_C , 1,3-bis(2-carboxyethyl)-4-methyl-1H-imidazol-3-ium bromide; L_D , 3-(2-carboxyethyl)-1-(3-aminopropyl)-1H-imidazol-3-ium bromide; IC_{50} , half inhibitory concentrations; HeLa, human cervical cancer cell line; Hep G2, human liver cancer cell line; MEF, healthy mouse embryonic fibroblast cell line.

yeast as much as the antibiotics. L_C and L_D show no noticeable inhibitory effects on the target bacteria, and thus, their absorbance values as function of their concentration were not given for the sake of brevity.

Figure 3(a) shows the cytotoxic activity of L_C on HeLa and Hep G2 cell lines against healthy MEF cell lines, as does Figure 3(b) for the cytotoxic activity of L_D . The cytotoxic activities of L_A and L_B are not exhibited as they showed lesser cytotoxic activities in comparison with L_C and L_D . The percentage cell viability of HeLa and Hep G2 cell lines was significantly reduced by L_C and L_D at the end of 24 hr application of the doses. In addition, L_C did not harm the healthy MEF cell lines for any dose so that its half inhibitory concentrations (IC_{50}) cannot be calculated. Meantime, L_D

showed some activity on the MEF cells with the high doses together with the fact that the activity was not as strong as it did on the cancer cell lines.

The antibacterial and cytotoxic effectiveness of the synthesized molecules are summarized in Table 7 by presenting their IC_{50} concentrations in the units of μM on the bacteria together with the IC_{50} values of the antibiotics and on the cancer cell lines. The lack of the IC_{50} values of L_C and L_D for antibacterial activity in Table 7 indicates that the IC_{50} values of them cannot be calculated due to their very weak effect on the bacteria sample within the dose range considered. L_A and L_B were, respectively, thrice and twice more effective on *Bacillus cereus* than the antibiotic (gentamicin) as the L_A equals the antibiotic (amphotericin-b) effect on *Candida albicans*.

The cell viability assay of the chemicals exhibits no harmful effect on the healthy MEF cell lines as their IC_{50} values cannot be calculated within the dose range considered. The L_C inhibition on HeLa and the L_D inhibition on Hep G2 are distinctive when they are compared with the inhibition of the other imidazole-based chemicals on different cancer cell lines in the concerning studies. The IC_{50} values of the L_C on HeLa and the L_D on Hep G2 were $81 \mu M$ and $57 \mu M$, respectively. The similar imidazole compounds which have alkyl moieties were tested on the cancer cells different from the cells used in this study [8]. The IC_{50} values of 1-(benzofuran-2-yl(phenyl)methyl)-3-allyl-2-ethyl-1H-imidazol-3-ium bromide and 1-(benzofuran-2-yl(phenyl)methyl)-3-butyl-2-ethyl-1H-imidazol-3-ium iodide on leukemia (HL-60), lung carcinoma (A549), colon carcinoma (SW480), breast carcinoma (MCF-7), and myeloid liver carcinoma (SMMC-7721) cancer lines have been detected over $40 \mu M$. Additionally, the IC_{50} activity of 3β -hydroxy-21-(1H-imidazol-1-yl)pregna-5,16-dien-20-one on prostate cancer (PC-3), breast cancer (MCF7), and lung cancer (SK-LU-1) were $20 \mu M$, $19 \mu M$, and $18 \mu M$, respectively [7]. These results are quantitatively better than $81 \mu M$ and $57 \mu M$ on Hep G2 and HeLa. However, this is compensated by the fact that the L_C and L_D have not any harmful effect on the healthy MEF cell lines.

4. Conclusions

Novel imidazole salts, or *N*-heterocyclic carbene ligands, namely, 1,3-bis(2-hydroxyethyl) imidazolidinium bromide L_A , 3-(2-ethoxy-2-oxoethyl)-1-(3-aminopropyl)-1H-imidazol-3-ium bromide L_B , 1,3-bis(2-carboxyethyl)-4-methyl-1H-imidazol-3-ium bromide L_C , and 3-(2-carboxyethyl)-1-(3-aminopropyl)-1H-imidazol-3-ium bromide L_D were synthesized, and they were preliminary confirmed by GC-MS and elemental analysis methods. Their molecular structures were theoretically determined, and they were confirmed by comparing calculated 1H , ^{13}C NMR, and IR spectra with those of experimentally observed data. Also, the calculated structures were verified by the XRD results on a similar imidazole salt [22].

The antimicrobial and cytotoxic activities of the synthesized ligands on some specific bacteria and cancer cell lines were measured using spectrophotometric methods. It is seen that L_A showed better inhibition than the selected antibiotic on *Bacillus cereus* ATCC 11778 while it is effective on the selected bacteria and the yeast together with L_B . On the cytotoxicity evaluation, L_C showed considerable inhibition effect on HeLa, as does L_D on Hep G2. Although their IC_{50} doses are quite high in comparison with the similar chemicals in the literature, the cytotoxicity of L_C and L_D is affirmed by not causing harmful effect on the healthy MEF cells as much as they do on the cancel cell lines.

Data Availability

The data used to support the findings of this study are available from the corresponding author upon request.

Conflicts of Interest

The authors declare that they have no conflicts of interest.

References

- [1] X. Chen, Y. Zou, M. Han et al., "Solubilisation of myosin in a solution of low ionic strength L-histidine: significance of the imidazole ring," *Food Chemistry*, vol. 196, pp. 42–49, 2016.
- [2] R. I. Benhamou, K. B. Steinbuch, and M. Fridman, "Anti-fungal imidazole-decorated cationic amphiphiles with markedly low hemolytic activity," *Chemistry*, vol. 22, no. 32, pp. 11148–11151, 2016.
- [3] M. Y. Wani, A. Ahmad, R. A. Shiekh, K. J. Al-Ghamdi, and A. J. Sobral, "Imidazole clubbed 1,3,4-oxadiazole derivatives as potential antifungal agents," *Bioorganic and Medicinal Chemistry*, vol. 23, no. 15, pp. 4172–4180, 2015.
- [4] K. Krowicki and J. W. Lown, "Synthesis of novel imidazole-containing DNA minor groove binding oligopeptides related to the antiviral antibiotic netropsin," *Journal of Organic Chemistry*, vol. 52, no. 16, pp. 3493–3501, 1987.
- [5] W.-N. Lee, A. Y.-C. Lin, and X.-H. Wang, "The occurrence of quinolone and imidazole antibiotics in rivers in Central Taiwan," *Desalination and Water Treatment*, vol. 52, no. 4–6, pp. 1143–1152, 2013.
- [6] G. Castanedo, Y. Liu, J. J. Crawford, and M. G. Braun, "Synthesis of fused imidazole-containing ring systems via dual oxidative amination of C(sp³)-H bonds," *Journal of Organic Chemistry*, vol. 81, no. 18, pp. 8617–8624, 2016.
- [7] A. V. Silva-Ortiz, E. Bratoeff, M. T. Ramirez-Apan et al., "Synthesis and biological activity of two pregnane derivatives with a triazole or imidazole ring at C-21," *Journal of Steroid Biochemistry and Molecular Biology*, vol. 159, pp. 8–18, 2016.
- [8] X.-Q. Wang, L.-X. Liu, Y. Li et al., "Design, synthesis and biological evaluation of novel hybrid compounds of imidazole scaffold-based 2-benzylbenzofuran as potent anticancer agents," *European Journal of Medicinal Chemistry*, vol. 62, pp. 111–121, 2013.
- [9] A. Mrozek, J. Karolak-Wojciechowska, and K. Kieć-Kononowicz, "Five-membered heterocycles. Part III. Aromaticity of 1,3-imidazole in 5+n hetero-bicyclic molecules," *Journal of Molecular Structure*, vol. 655, no. 3, pp. 397–403, 2003.
- [10] R. Boussefi, S. Dalbouha, V. Timón, N. Komiha, N. Jaïdane, and M. L. Senent, "Stability of Van der Waals complexes of the greenhouse effect gases CH₄ and SF₆ with imidazole in gas mixtures containing CO₂," *Computational and Theoretical Chemistry*, vol. 1094, pp. 82–91, 2016.
- [11] L. Feng, X. Zhang, C. Wang et al., "Effect of different imidazole group positions on the hydroxyl ion conductivity," *International Journal of Hydrogen Energy*, vol. 41, no. 36, pp. 16135–16141, 2016.
- [12] G.-C. Zheng, Z.-B. Cai, Y.-L. Pan et al., "Synthesis and two-photon absorption properties of novel 2-substituted-4,5-diphenyl-1H-imidazoles," *Tetrahedron*, vol. 72, no. 22, pp. 2988–2996, 2016.
- [13] R. B. Campos, L. R. A. Menezes, A. Barison, D. J. Tantillo, and E. S. Orth, "The importance of methyl positioning and tautomeric equilibria for imidazole nucleophilicity," *Chemistry—A European Journal*, vol. 22, no. 43, pp. 15521–15528, 2016.
- [14] A. J. Arduengo, R. L. Harlow, and M. Kline, "A stable crystalline carbene," *Journal of the American Chemical Society*, vol. 113, no. 1, pp. 361–363, 1991.
- [15] M. O. Karatas, B. Olgundeniz, S. Gunal, I. Ozdemir, B. Alici, and E. Cetinkaya, "Synthesis, characterization and antimicrobial activities of novel silver(I) complexes with coumarin substituted *N*-heterocyclic carbene ligands," *Bioorganic and Medicinal Chemistry*, vol. 24, no. 4, pp. 643–650, 2016.

- [16] H. A. Özbek, P. S. Aktaş, J.-C. Daran, M. Oskay, F. Demirhan, and B. Çetinkaya, "Synthesis, structure, electrochemical and antimicrobial properties of N,N'-bis(ferrocenylmethyl)imidazolium salts," *Inorganica Chimica Acta*, vol. 423, pp. 435–442, 2014.
- [17] W. A. Herrmann, "N-heterocyclic carbenes: a new concept in organometallic catalysis," *Angewandte Chemie International Edition*, vol. 41, no. 8, pp. 1290–1309, 2002.
- [18] N. Hadei, E. A. Kantchev, C. J. O'Brien, and M. G. Organ, "Electronic nature of N-heterocyclic carbene ligands: effect on the Suzuki reaction," *Organic Letters*, vol. 7, no. 10, pp. 1991–1994, 2005.
- [19] J. S. Al-Otaibi and R. I. Al-Wabli, "Vibrational spectroscopic investigation (FT-IR and FT-Raman) using ab initio (HF) and DFT (B3LYP) calculations of 3-ethoxymethyl-1,4-dihydroquinolin-4-one," *Spectrochimica Acta Part A: Molecular and Biomolecular Spectroscopy*, vol. 137, pp. 7–15, 2015.
- [20] J. B. Foresman and A. E. Frisch, *Exploring Chemistry with Electronic Structure Methods*, Gaussian, Inc., Wallingford, CT, USA, 2nd edition, 1996.
- [21] G. Uluçam, S. E. Okan, Ş. Aktaş, and G. P. Öğretmen, "Characterization of dinaphthosulfoxide molecule," *Journal of Molecular Structure*, vol. 1102, pp. 146–152, 2015.
- [22] M. Turkyilmaz, G. Uluçam, Ş. Aktaş, and S. E. Okan, "Synthesis and characterization of new N-heterocyclic carbene ligands: 1,3-Bis(acetamide)imidazol-3-ium bromide and 3-(acetamide)-1-(3-aminopropyl)-1H-imidazol-3-ium bromide," *Journal of Molecular Structure*, vol. 1136, pp. 263–270, 2017.
- [23] X. Mi, S. Luo, and J.-P. Cheng, "Ionic liquid-immobilized quinuclidine-catalyzed Morita–Baylis–Hillman reactions," *Journal of Organic Chemistry*, vol. 70, no. 6, pp. 2338–2341, 2005.
- [24] X. Mi, S. Luo, H. Xu, L. Zhang, and J.-P. Cheng, "Hydroxyl ionic liquid (HIL)-immobilized quinuclidine for Baylis–Hillman catalysis: synergistic effect of ionic liquids as organocatalyst supports," *Tetrahedron*, vol. 62, no. 11, pp. 2537–2544, 2006.
- [25] J. Sasaki, J. K. Lanyi, R. Needleman, T. Yoshizawa, and A. Maeda, "Complete identification of C:O stretching vibrational bands of protonated aspartic acid residues in the difference infrared spectra of M and N intermediates versus bacteriorhodopsin," *Biochemistry*, vol. 33, no. 11, pp. 3178–3184, 1994.
- [26] L. Clougherty, J. Sousa, and G. Wyman, "Notes-C=N stretching frequency in infrared spectra of aromatic azomethines," *Journal of Organic Chemistry*, vol. 22, no. 4, p. 462, 1957.
- [27] S. Gunasekaran, E. Sailatha, S. Seshadri, and S. Kumaresan, "FTIR, FT Raman spectra and molecular structural confirmation of isoniazid," *Indian Journal of Pure and Applied Physics*, vol. 47, no. 1, pp. 12–18, 2009.
- [28] M. Schwanninger, J. C. Rodrigues, H. Pereira, and B. Hinterstoisser, "Effects of short-time vibratory ball milling on the shape of FT-IR spectra of wood and cellulose," *Vibrational Spectroscopy*, vol. 36, no. 1, pp. 23–40, 2004.
- [29] J. S. Singh, "FT-IR and Raman spectra, ab initio and density functional computations of the vibrational spectra, molecular geometries and atomic charges of uracil and 5-methyluracil (thymine)," *Spectrochimica Acta Part A: Molecular and Biomolecular Spectroscopy*, vol. 137, pp. 625–640, 2015.